Scuola Internazionale Superiore di Studi Avanzati – Trieste

Development and Characterization of scaffold based three-dimensional neuronal cultures

Thesis submitted for the degree of Doctor Philosophiae

Neuroscience Area

PhD in Neurobiology

November 2017

Candidate

Francesco Paolo Ulloa Severino

Supervisor

Vincent Torre

SISSA – Via Bonomea 265 – 34136 TRIESTE - Italy

This page was intentionally left blank

The good thing about science is that it's true whether or not you believe in it.

Neil deGrasse Tyson

TABLE OF CONTENTS

LIST OF PUBLICATIONS 1

1. ABSTRACT 2

2. INTRODUCTION 5

2.1. Three-dimensional *in vitro* models of nervous system 6

2.2. Carbon based material and neural interaction: carbon nanotubes and graphene 11

2.3. Spontaneous Activity of neuronal networks 16

3. REFERENCES 21

4. RESULTS 29

4.1 Patch method for culture of primary hippocampal neurons 30

4.2 Fabrication of PDMS microlattices for three-dimensional cell culture 37

4.3 The role of dimensionality in neuronal network dynamics 57

5. CONCLUSION AND PERSPECTIVES 80

6. SUPPLEMENTARY PUBLICATIONS 84

6.1 Graphene oxide nanosheets reshape synaptic function in cultured brain networks 85

6.2 Effective motor neuron differentiation of human induced pluripotent stem cells on a patch made of crosslinked monolayer gelatin nanofibers 111

6.3 Fabrication of PLGA nanofibers on PDMS micropillars for neuron culture studies 120

LIST OF PUBLICATIONS

Peer reviewed publications:

- **F.P. Ulloa Severino[+],** J. Ban[+], M. Tang, Q. Song, G. Bianconi, G. Cheng and V. Torre. *The role of dimensionality in neuronal network dynamics.* Sci.Rep. 2016.

- R. Rauti, N. Lozano, V. León, D. Scaini, M. Musto, I. Rago, **F. P. Ulloa Severino**, A. Fabbro, L. Casalis, E. Vázquez, K. Kostarelos, M. Prato, and L. Ballerini. *Graphene oxide nanosheets reshape synaptic function in cultured brain networks*. ACS Nano, 2016.

- Y. Tang，L. Liu，J. Li，L. Yu, **F. P. Ulloa Severino**, L. Wang，J. Shi, X. Tu, V. Torre, Y. Chen. *Effective motor neuron differentiation of human induced pluripotent stem cells on a patch made of crosslinked monolayer gelatin nanofibers.* Journal of Materials Chemistry B., 2016.

- Y. Tang[+], **F. P. Ulloa Severino[+]**, F. Iseppon, V. Torre and Y. Chen. *Patch method for primary hippocampal neuron culture.* Microelectronic Engineering, 2017.

- J. Wei[+], D. Pozzi[+], **F.P. Ulloa Severino**, V. Torre, Y. Chen. *Fabrication of PLGA nanofibers on PDMS micropillars for neuron culture studies.* Microelectronic Engineering, 2017.

Papers in preparation:

- M. Xiao[+], **F.P. Ulloa Severino[+]**, X. Li, Q. Song, M. Lazzarino, G. Cheng & V. Torre*. Graphene-Carbon Nano Tubes scaffold: a new 3D cortical in vitro model for brain tumors infiltration.*

- S. Li[+], **F.P. Ulloa Severino[+]**, J. Ban, L. Wang, G. Pinato, V. Torre and Y. Chen. *Fabrication of PDMS microlattices for three-dimensional cell culture.*

1. ABSTRACT

Tissue engineering, through different approaches, strives to create functional components of organs and cell types *in vitro*. A major bottle neck in recreating *in vivo*-like phenotypes in these *in vitro* systems is to find biocompatible materials to scaffold both as an interface with living tissues, and also to support the survival and function of the cells during *in vitro* culture.

It is clear nowadays that 2D *in vitro* models poorly reflect the complexity of the body organs. This is particularly true for the brain, and many research group are working, using different approaches, to have a more appropriate system to investigate developmental processes, neuronal network dynamics and molecular pathways, as well as for drug screening.

In my Ph.D., I aimed to circumvent these major bottlenecks by developing and carefully characterizing 3D neural cultures. To do so, I used optical imaging methods, particularly calcium imaging, to investigate the neuronal network dynamics of reconstructed 3D primary cultures from rats. In particular, I developed and tested new scaffolds for these culture systems.

In the brain both conductivity and stiffness are important parameters that help shape neural networks. To mimick these properties of the brain, I tested the scaffolding properties of elastic organic polymers like Polydimethylsiloxane (PDMS) and gelatin. In addition, I used graphene-based materials as electrically conductive scaffolds. Through these studies, I developed a number of functional 3D-neural networks using different scaffolds with distinct structure, topology and compositions.

In particular I determined that:

1) Patch substrate with a monolayer of gelatin nanofibers electrospun and crosslinked on a honeycomb microframe of poly (ethylene glycol) diacrylate (PEGDA) are suitable substrates for neuronal studies in a 3D environment. This method allows us to minimize exogenous material contact of cells and largely increase the exposure area of cells to the culture medium. Even though there are no connections in vertical dimension, I found that neurons, and especially astrocytes, have a more *in vivo* like morphology comparing to that on culture dish or on glass slide. We also found that neurons were preferentially located in the suspended areas of the monolayer nanofibers. Finally, calcium imaging revealed that primary neurons have a higher degree of neural activity on the patch than on glass.

These results suggest that crosslinked and monolayer gelatin nanofibers closely mimic the extracellular matrix structure and allow more effective culture of primary neurons than conventional methods, thus facilitating advanced studies of neural functions as well as cell-based assays.

2) PDMS microlattices scaffolds, produced by conventional photolithography techniques, can be used as a soft scaffold for *in vitro* cell culture for both cell lines and primary neuronal cultures. The photomask with micro-scale dots array spin coated with photoresist is downward mounted on a rotating stage with a 45°angle to UV irradiated direction. After three irradiation times the UV exposed area could be developed to form a three dimensional (3D) porous photoresist template. PDMS is poured in and cured and a 3D PDMS lattice is obtained after etching. I determined that our 3D PDMS lattices are suitable for:
    a. Culturing NIH-3T3 cell line into the microlattices. We observed homogenously cell adhesion and extension to form a 3D *in vitro* culture. Cell nuclear shape could also be controlled by adjusting the unit-cell architecture of the lattice.
    b. Easy cell observation. This 3D scaffold is biocompatible and also transparent and it can be applied to study the differences between 2D and 3D cell cultures *in vitro* and enable cells maintain their *in vivo* morphology of tissue-like structures within an *in vitro* platform.
    c. Culturing primary hippocampal cells from rats. We observed a great cell-material interaction. Neurons and astrocytes grow over and among the pillars creating a 3D *in vitro* neuronal network.

These results show that adjusting the size of 3D structure it is not only possible to control the cell growth and shape, but also to allow primary hippocampal cells to be cultured on a softer substrates and have suspended connection among the pillars reaching an unexpected three-dimensionality.

3) Graphene foam scaffold is particularly suitable for 3D-neural cultures as it permitted the formation of a modular network between cultured neurons, which is characterized by a higher firing frequency and synchronization. I was able to culture through the whole scaffolds (1-1.5 mm in heights) a viable neuronal network which, because of its third dimension, has many connections among distant neurons leading to small-world networks and their characteristic dynamics. This new *in vitro* model reflects

some of the observation done on the nervous system dynamics *in vivo*. More in details, I defined:

a. The presence of a Moderately Synchronized (MS) regime and a Highly Synchronized (HS) regime. The HS regime was never observed in 2D networks and was observed in the cases of highly connected portion of the network. During the MS regime, neuronal assemblies in synchrony changed with time as observed in mammalian brains. After two weeks, the degree of synchrony in 3D networks decreased, as observed *in vivo*.
b. The absence of a disequilibrium between excitatory and inhibitory neurons by staining the culture for the GABA neurotransmitter.
c. The presence of astrocytes with a ramified shape that resemble the *in vivo* shape that allows the engulfment of many neuronal terminals.
d. The maturation of the network follow the pattern of maturation observed in vivo with a decrease synchronization and frequency.

These results show that dimensionality determines properties of neuronal networks and that several features of brain dynamics are a consequence of its 3D topology. Moreover this scaffold allows to have a 3D neuronal network *in vitro* that has similar *in vivo* dynamics and could represent a better *in vitro* model to study some of the aspects of the nervous system.

All together, these results show that to achieve complex connectivity among neurons, 3D-scaffolds with distinct electrical and mechanical properties can be applied. What makes the difference is the aim that every research group wants to achieve. In the future it could be useful to compare a 3D scaffold based *in vitro* model to a positive control, such as organotipic slices or acute slices, in order to understand how close we are to the network dynamics of an *ex-vivo* preparation. Moreover, it could be interesting to investigate the reasons behind the more elevated frequency and synchronization of the 3D neuronal networks. It could be possible that the different morphology of astrocytes affects the on-going activity of neurons or that there is a different speed of maturation of the network since we have another growing dimension (the z-plane).

Beyond the basic research, it would be interesting to apply this new *in vitro* model to study the progression of some diseases like tumours, and in particular brain tumours, in a 3D environment and in a 3D brain culture.

2. INTRODUCTION

The attempt to improve the self-healing capacity of human body is one of the aim of the regenerative medicine according to the National Institute of Health (NIH). In this framework, a large subfield called tissue engineering strives to create functional tissues or unit of tissues *in vitro* through different approaches[1] (**Fig. 1**).

Two-dimensional (2D) *in vitro* cell cultures remain the predominant culture method and has been proven indispensable for a variety of applications. The first example of 2D culture in neuroscience dates back to the 1907, when Rose Harrison was able to maintain a tissue explant from a frog embryo and observing the outgrowth of nerve cells up to four weeks[2]. Since then, there has been great progress in neuroscience and these models have provided important insights into neuronal network activity patterns, cellular dynamics and drug screening. Even though the simplicity of 2D culture allows to easily screen the cell samples, it has some drawbacks. In 2D culture, cells are forced to adhere to a flat surface, such as plastic or glass, with a completely different stiffness compared to their original tissues (i.e. <1KPa for brain slices and single brain cells), that affects cell growth and differentiation[3,4]. Hence, the complex 3D architecture of natural Central Nervous System (CNS) is not represented in this *in vitro* model with consequences on connectivity and activity. These unfamiliar mechanical cues and lack of 3D extracellular matrix (ECM) support can have a significant impact on cellular behaviour,

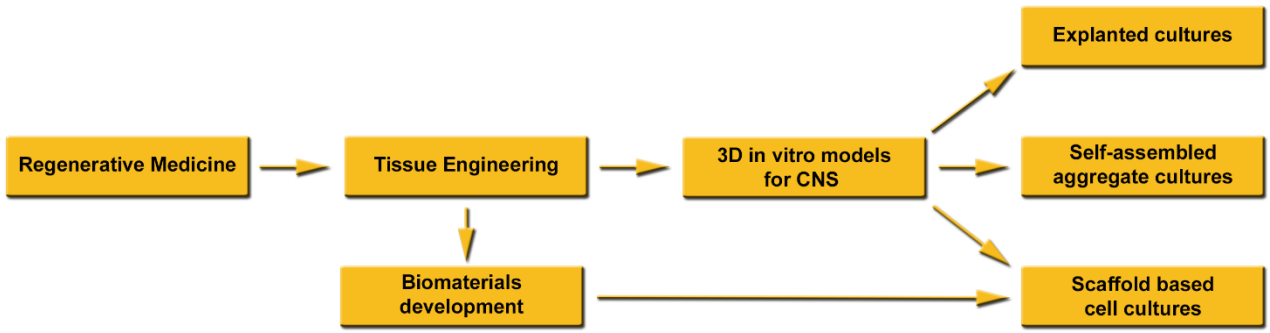

Figure 1: 3D in vitro model for CNS. *Graphical representation of the synergistic efforts of two fields of research for the scaffold based cell cultures development and application. Modified from Ref.1.*

function, growth, and morphology[5,6]. When, for instance, a matrigel-embedded 3D cortical culture is stained for neuronal markers, spherical somata with processes extending in vertical dimension can be observed. Within 2D culture, instead, neurites are forced to grow in a planar region and changes in the excitability of the neurons has also been reported[7].

The necessity of three-dimensionality brought to the conclusion that new *in vitro* strategies are necessary to have a more reliable model of the natural connectivity and cell behaviour for the nervous system, filling the gap between 2D *in vitro* models and complex *in vivo* studies.

2.1. Three-dimensional *in vitro* models of nervous system

The main approaches to have 3D models of the CNS can be broadly categorized as *explanted cultures, self-assembled aggregate cultures* and *scaffold based cell cultures*[8](**Fig 1**). The latter and their use for *in vitro* studies of the neuronal network activity will be the leading topic of this thesis.

2.1.1. Explanted cultures and self-assembled aggregate culture

Explanted cultures can be obtained through techniques that allow to grow intact tissues *in vitro*. Slices of brain tissues dissected from the animal body can be freshly used (acute slices) for experimental purposes that need cells which cannot be harvested; otherwise they can be cultured using supporting membrane insert (organotypic cultures). These approaches aim at retaining the complex 3D organization of tissues *in vitro*. However, one of the limitations

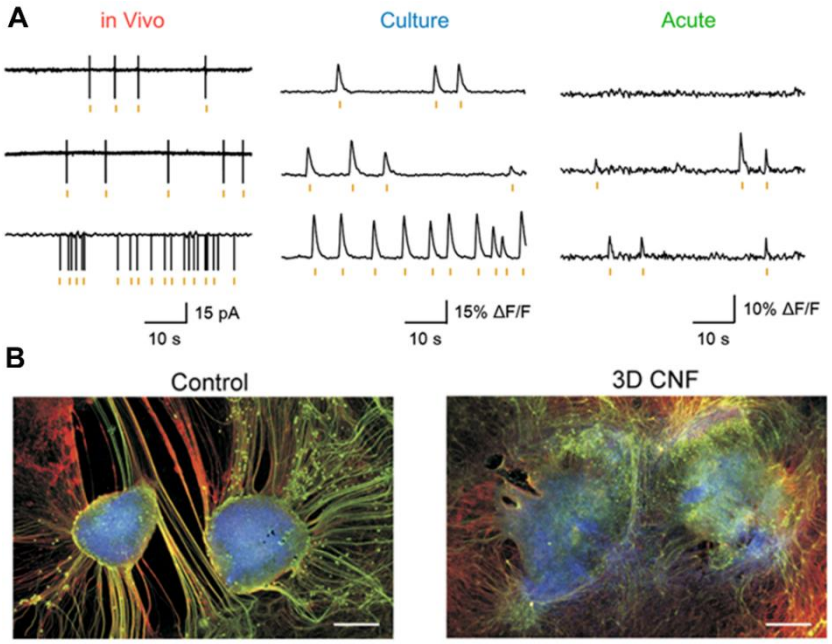

Figure 2: Explanted cultures. *The activity of the organotipic cultures resemble to the in vivo one more than acute slices do* (A). *The ability to regrow their processes in vitro is used to study strategies for brain repair* (B). *See Ref. 9, 10.*

is the loss of function after removal from the body (**Fig. 2A**). For instance, it has been demonstrated that, in hippocampal acute slices preparation, several neurites are cut,

resulting in a destroyed neural network with predominant GABAergic inhibition over glutamatergic excitation. On the other hand, organotypic slices have the time to regrow pruned neurites and establish new synaptic connections showing an *in vivo*-like activity[9](**Fig. 2A**). In addition, the ability to regrow their connections *in vitro* has been used in tissue engineering to study, for instance, the reconnection of segregated spinal explants through the application of biocompatible materials as neuronal prostheses for possible *in vivo* application and injury repair[10,11] (**Fig. 2B**).

Self-assembled aggregated cultures rely on the use of stem cell technology to develop 3D *in vitro* models. This approach is advantageous as it uses the natural tendency of cells to aggregate, the cell guided assembly of 3D environment and the possibility to obtain induced neurons (iN) in different ways[12] (**Fig. 3A**). There are spheroids, embryonic bodies, neurospheres and, recently, cerebral organoids[13–16] that can be obtained by hanging drop technique, in suspension or using spinning bioreactor[17,18] (**Fig. 3B**).

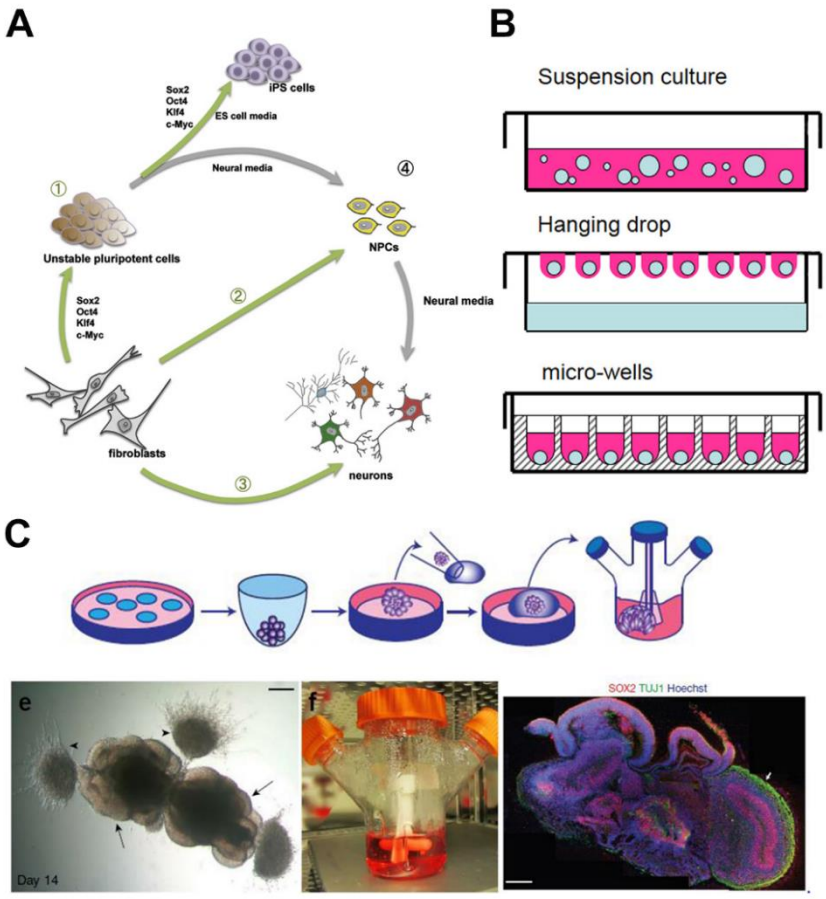

Figure 3: Stem Cell for Self assembled cultures.
Neurons can be obtained in a variety of ways, direct and indirect (A). Spheroids, Embryonic bodies and neurospheres can be cultured in suspension, hanging drop or micro-wells (B) to obtain spherical aggregates. The recent cortical organoids were cultured using spinning bioreactors to minimize the lack of oxygen and nutrients and formation of necrotic spots(C). See Ref. 10, 12, 14,15.

However, they tend to suffer from high variability, due to the stem cell clone-ability, and size limitation and formation of necrotic cores due to the insufficient oxygen and nutrient diffusion.

Lancaster and collaborators recently showed that human induced pluripotent stem cells (hiPSCs) encapsulated in Matrigel, result in spontaneous development of cerebral organoids that can model and recapitulate the distinct characteristics of microcephaly, a disorder that has been difficult to obtain with *in vivo* rodent models. Moreover, they can form structures anatomically comparable to the organization of the progenitor zone in human brain[16]. All together, these techniques offer useful models to investigate different aspects of the nervous system, but still they have limitations. Another approach that tries to overcome these limitations (i.e. loss of connectivity, low oxygen diffusion) is to use biocompatible materials to develop scaffolds as support for cell growth and development.

2.1.2. Scaffold-Based Cell Cultures

The concept of 3D scaffold-based cell culture was developed 40 years ago, via the use of floating collagen gels that helped maintain cellular differentiation and organization[19]. This work was an important contribution for the “closer-to-in vivo” behaviour of cells when grown as 3D cultures. Nowadays, an overwhelming number of biomaterials have been developed to engineer a 3D environment and reconstruct a particular cellular phenotype. There are either natural polymers (e.g. agarose, collagen, fibronectin, gelatin, laminin, hyaluronic acid and vitronectin) or synthetic polymers (e.g. polycaprolactone, polyethylene glycol, polystyrene and polydimethylsiloxane)[8,20]. The main differences among these two groups is the biodegradability. Moreover, particular care should be taken to select the appropriate crosslinking when we need a polymerization reaction to avoid negative effects on cell viability.

Cell properties modification can be accomplished by working on micropatterned substrates that control cell adhesion and spreading on a flat surface[21]. There are different methods for the fabrication of these substrates, such as lithography, electrospinning or electrospray (**Fig. 4A**) and the interaction with cells can change their degree of differentiation, maturation and activity[22–26]. hiPSC, for example, were grown and differentiated in motoneurons on gelatin nanofibers patch with polyethylene glycol diacrylate (PEGDA) honeycomb microframe showing an increase in specific protein expression and spontaneous neuronal activity that were not observed in conventional dish method[23]. Even if this approach is an improvement of the 2D culture systems that allows investigation of different biophysical aspects of cell behaviour and morphology, there is still a lack of growth in the vertical dimension that drastically changes the cell properties (**Fig. 4B**).

This is one of the reason why there is so much interest in the development of 3D matrices[27], and hydrogels have got so much attention for neuroscience applications[28–30]. These scaffolds need to be not only biocompatible for implantation, but should also have an appropriate pore size (>40 μm) that allows cell infiltration, migration, growth and adequate oxygen, nutrient and waste circulation, which is achieved primarily by diffusion[28,31]. The most common methods to obtain macroporous scaffolds are based on the use of a template that can be removed generally by heating or dissolution[32,33] (**Fig 4C**).

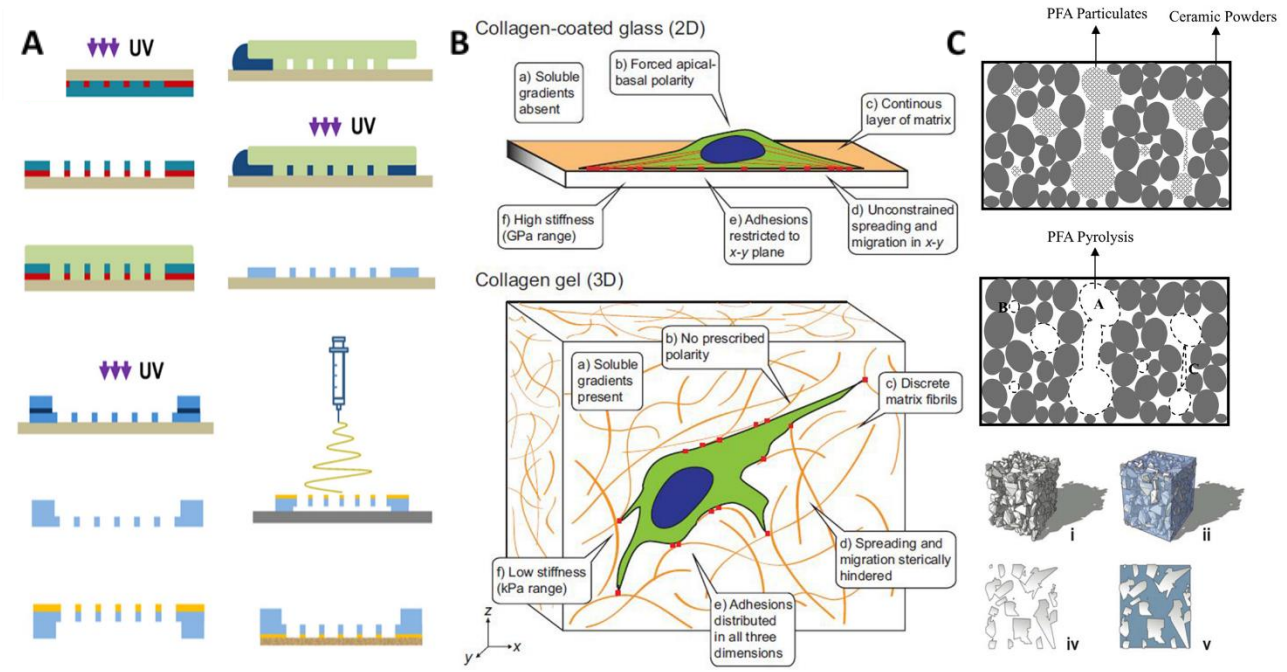

Figure 4: Scaffold based culture formation and properties: Lithography and electrospinning are two techniques applied to build patterned substrates to mimic the ECM microenvironment in which cells develop. Tang et al. applied these two fabrications system in combination to build gelatin nanofibers patch and grow primary hippocampal neurons in vitro (A). Three-dimensional environment is anyway necessary to obtain an in vivo-like cellular culture and 3D hydrogels or synthetic scaffolds can help reconstructing it (B). In C are shown two examples of thermo sensitive and soluble materials for pore formation in three-dimensional scaffolds. From Ref. 23, 26, 31, 32.

All these efforts in biomaterial development and fabrication strategies are made to mimic the natural nano-environment where neural cells grow and develop *in vitro*. However, there is another aim pursued by the tissue engineering that is to apply nanotechnology strategies to develop neural interfaces for research and biomedical application (**BOX 1**). To this aim, electrically active nanomaterials (EANs) such as conductive polymers, carbon nanotubes or graphene structures, are tested as neural interfaces.

BOX 1: Possible applications of 3D cultures: Neural interfaces

Brain-machine interfaces have been used to build prosthetic devices[34] or to treat neurological disorders[35] by recording and stimulating neural tissues in animals and humans[36]. These neural interfaces communicate with the nervous system through implantable electrodes made of either organic or inorganic biomaterials[37] that often do not well integrate with neural tissues. Once implanted, the mechanical trauma of electrode insertion cause an acute inflammation at the lesion core where a number of cytokines are released by active glia cells (**Fig B1**) following the cell death and liquid movement[37,38]. When the acute inflammation declines, a chronic response cause a glia scar formation with isolation of the exogenous material resulting in inefficient neural interface. Many strategies are used to reduce tissue damage, glia reaction and scar formation to improve the electrode performances and stability. An emerging concept is the fabrication of the "organic electrode" coated with molecules and encapsulated neurons (**Fig B1**). These is an idea based on the progress in conductive materials applications, molecules delivery systems and NSC technology[39,40] that is already been used, partially, for tissue reconstruction and functional recovery after cortical insult[41]. This device, indeed, does not contain the properties of an electrode (i.e. charge transfer, flexibility). There are few examples of integrated 3D electronics with biomaterials and synthetic tissues. Key points that must be addressed to achieve this goal include: i) the electronic structures must be macroporous, not planar, to enable 3D interpenetration with biomaterials; ii) the electronic network should have nanometre to micrometre scale features comparable to biomaterial scaffolds; and iii) the electronic network must have 3D interconnectivity and mechanical properties similar to biomaterials. An example that respect these points is the construction of 3D macroporous, flexible and free-standing nanowire nanoelectronic scaffolds (nanoES)[42] (**Fig B1**). This devices have a robust electronic properties and have been used to electrically record and stimulate cardiomyocytes, neurons and muscle cells activity. However, more studies need to provide information about the maturation and activity of neuronal cultures interacting with these conductive structures.

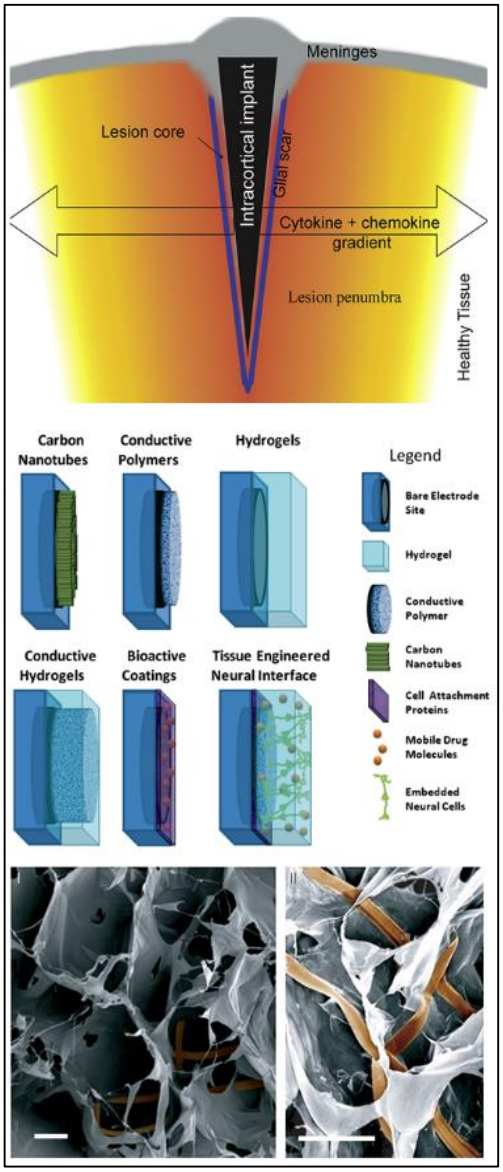

Figure B1: Electrodes for neural tissues interface: *Schematic representation of the lesion zones upon intracortical implant. Cytokines create a gradient after delivery by reactive glia cells (A). In B there are examples of possible organic electrodes construct for neural interfaces to integrate better the exogenous and synthetic material in the brain. From Ref. 37, 39.*

2.2. Carbon based material and neural interaction: carbon nanotubes and graphene

2.2.1. Carbon nanotubes

Carbon nanotubes (CNTs) are made of wrapped graphite sheet(s) composed of either single or multi-walled (SWCNTs and MWCNTs) (**Fig. 5A**). The single shell or single walled nanotubes (SWCNT) are made of single graphene cylinders and have a very narrow size distribution. In contrast, multi walled CNTs (MWCNT) consists of two or more concentric cylindrical shells of graphene sheets coaxially arranged around a central hollow area with a spacing between the layers which is close to that of the interlayer separation as in graphite[43]. Because of their remarkable properties, like high electrochemically accessible surface area, high mechanical strength and high electronic current, CNTs are extremely useful for the fabrication of electronic devices (e.g. super-capacitors)[37]. CNTs have attracted a lot of attention as a possible scaffold to help the reconnection among neurons *in vitro*[44–46] and are becoming relevant in neuroscience research for their possible biomedical applications[10]. CNTs have been studied as scaffold for neural cell adhesion, proliferation and differentiation[47,48] supporting their use for neural applications. They can be used to regulate neuronal structures or functions[47,48] and are biocompatible[49], even if their possible applications in human health-care need to be deeply investigated due to the possible cytotoxic effect.

However, the excellent electrical conductivity, biocompatibility and large surface area of carbon nanotubes favour their interactions with distal dendrites making them a good candidate for long-lasting brain machine interfaces[46,49,50]. For example, hippocampal neurons on glass surfaces modified with MWCNTs can reconstruct a functional network with enhanced firing frequency compared to the pure glass control[46]. This effect has been demonstrated to be a CNT-induced modification that create electrical shortcut with cell membranes[44](**Fig. 5B**). That is, when neurons were cultured on a different material with comparable roughness, or comparable electrical conductivity, the same effect has not been observed[44]. Moreover, CNTs can promote action potential-independent increase in connectivity and induce synaptogenesis with new synapses displaying different short-term dynamics that need the presence of action potentials (APs) and spike back-propagation also favoured by CNTs[45].

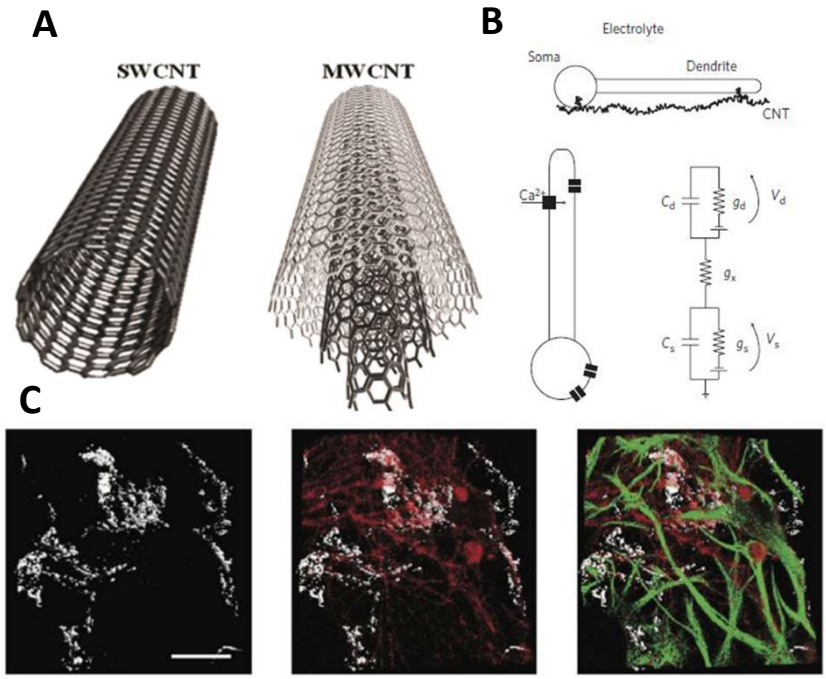

Figure 5. Carbon nanotubes and neural interaction:
A) Schematic representation of Single and Multi-Wall Carbon Nanotubes. In B is reported the proposed model for the electrical short-cutting effect of CNT on the membrane voltage. C) 3D hippocampal culture growth on a PDMS-MWCNT scaffold. The carbon nanotubes are reported in grey and acquired using the reflection mode of a confocal microscope; in red there are the neurons and in green the astrocytes. From Ref. 33, 43, 44

CNTs have also been used to enhance the functional reconnections of separated spinal explants[10] and reconstruct 3D hippocampal network *in vitro*[33](**Fig. 5C**). Bosi and collaborators were able to fabricate 3D PDMS scaffolds with pores layered by an irregular carbon nanotube carpet stably entrapped in the PDMS matrix. These mixed 3D scaffolds were applied not only to study the activity of primary hippocampal neurons *in vitro*[33], but also as scaffolds for the growth and functional reconnection of separated spinal cord organotypic slices and *in vivo* implant in the adult rats visual cortex ,where they show a limited tissue reaction[11].

2.2.2. Graphene

The existence of graphene as a two-dimensional single layer sheet of sp^2 hybridized carbon atoms organized in a hexagonal arrangement was theoretically known since the 1960s[37]. However, it has been impossible to obtain graphene until the 2004. In those years Andre Geim and Kostya Novoselov, simply using tape, were able to obtain and characterize for the first time a single layer of carbon atoms. This is the first two-dimensional atomic crystal available and for their discovery Geim and Novoselov were awarded the Nobel Prize in physics in the 2010.

One of the reasons why graphene is a very attractive material is that the laboratory procedures to obtain high quality material are relatively easy and cheap. Moreover,

graphene has many exceptional properties such as a Young's module of 1 TPa, high electrical conductivity (1 S m^{-1}) as well as a very low resistivity (10^{-6} Ω) and can be chemically functionalized[37,51,52]. Together with its biocompatibility, all these characteristics make graphene a unique material which can find many applications in the industries, for instance to build electronic devices, as well as in biomedical research and tissue engineering.

There are a dozens of methods for producing graphene that affect very much the purity and, in turn, all the properties of the final product and so the application it can have (**Fig. 6A**). Among the different techniques, there are the liquid phase and thermal exfoliation, epitaxial growth by chemical vapour deposition (CVD) and epitaxial growth on silicon carbide (SiC)[52,53].

Liquid phase exfoliation of graphite is based on the exposure to an organic solvent that increases the surface area of graphite crystallites. Using sonication, graphite disrupts into individual platelets and prolonged sonication originate monolayer flakes in suspension that can be enriched by centrifugation. A similar method is based on the ultrasonic exfoliation of graphite oxide in aqueous solution, centrifugation and finally *in situ* (partial) reduction to have pristine graphene. Moreover, is possible to use a shear mixer or a ball milling process for large scale production of defect-free and highly conductive graphene by exfoliation[52,54,55]. An important variation for industrial mass production is the thermal-shock procedure to achieve exfoliation and reduction simultaneously with a final product that have the same characteristics of single layer graphene, even if it is composed by multiple layers[52].

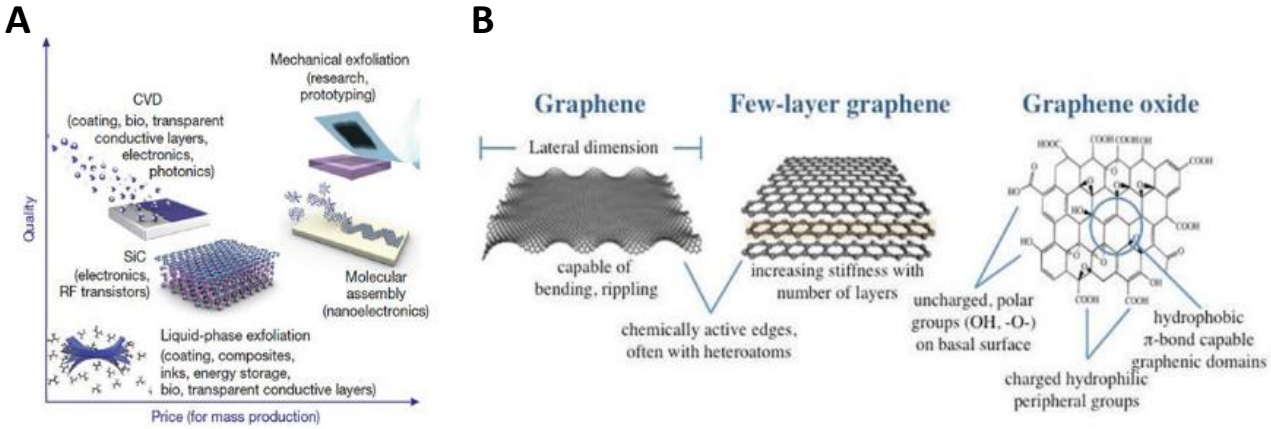

Figure 6. Graphene production and properties: *A) The different techniques for the mass production of graphene are shown in a graph that correlates the quality of the product and the price of production. B) Schematic rapresentation of the basic properties of graphene and some of its different types. From Ref. 52, 61.*

Another technique to grow graphene is the **chemical vapour deposition (CVD)**. The CVD

allows the growth of large area and uniform graphene film on a 2D copper film[56,57] or 3D nickel structure[58–60] that can find a lot of different applications. Even if the presence of a metal layer could be advantageous for some electronic applications, once the graphene has been grown is necessary the etching process to remove the metal template that could be toxic, for example, in biomedical applications. However, the growth phase, as well as the etching process, make the CVD expensive owing to the energy consumption and the removal of the metal layer. A breakthrough would be to use CVD to grow graphene on an arbitrary surface or at low temperatures minimizing the number of defects[52].

The **growth of graphene on Silicon Carbide (SiC)**, a common material used in high-power electronic, is another approach to obtain high quality graphene. A controlled number of graphitic layers can be grown either on the Si or the C surface of the SiC wafer by sublimation of Si atoms. There are some drawbacks of this method such as the high cost of the wafers and the high temperatures used (above 1000°C). Due to its disadvantages, this technique will probably be limited to niche applications[52].

All these fabrication techniques can originate different graphene structures that are grouped as “Graphene Family Nanomaterials” (GFN), which are: single layer graphene (SLG), few-layer graphene (FLG), ultrathin graphite, graphene oxide (GO), reduced graphene oxide (rGO) and nano-GO. All the members of the GFN group vary in layer number, lateral dimension, surface chemistry and purity[61](**Fig. 6B**). The large differences in the available graphene types determine another level of complexity that is the interaction of graphene with living cells and compartments[53].

Two major concerns about the application of graphene for neural interfaces are the graphene biocompatibility as well as the interaction between cells and graphene. Many groups are studying the biocompatibility and cytotoxicity of graphene *in vitro* and they aim to use it for neuronal regeneration, activity recording and stimulation and delivery system[56,58,62–65]. Bendali and Lorenzoni studied, on different brain cells and using different approaches, the biocompatibility of graphene by examining the neuronal growth on 2D SLG. They demonstrated that neurons prefer to grow over a graphene patterned area using stripes of graphene and showing how both neuronal cell bodies and neurites orientate themselves onto the pattern with or without coating[62,63](**Fig. 7A**). Studies of the cytotoxicity of graphene *in vitro* were carried out also using flakes of pristine graphene (GR) and graphene oxide (GO) with a small lateral dimension. Rauti et al. demonstrated that small-GO flakes do not affect the hippocampal cells viability, but down-regulate their activity by impairing the excitatory pathway and synaptic release kinetics[64]. Using different

approaches, Bramini et al. showed similar results on cortical cultures; they described an up-regulation of the inhibitory pathway and alterations in the expression of membrane phospholipids and in a multiplicity of molecules involved in Ca^{2+} homeostasis and dynamics[65](**Fig. 7B**).

Trying to take advantages from the electrical conductivity of the graphene and its ability to be affected by the electric field[66], Hess et al developed graphene transistor arrays for the extracellular detection of electric signals from cardiomyocytes-like cells[67](**Fig. 7C**). More studies exploited the ability of electrically stimulated graphene to enhance the maturation of Mesenchymal Stem Cells and accelerate nerve growth and development[68–70].

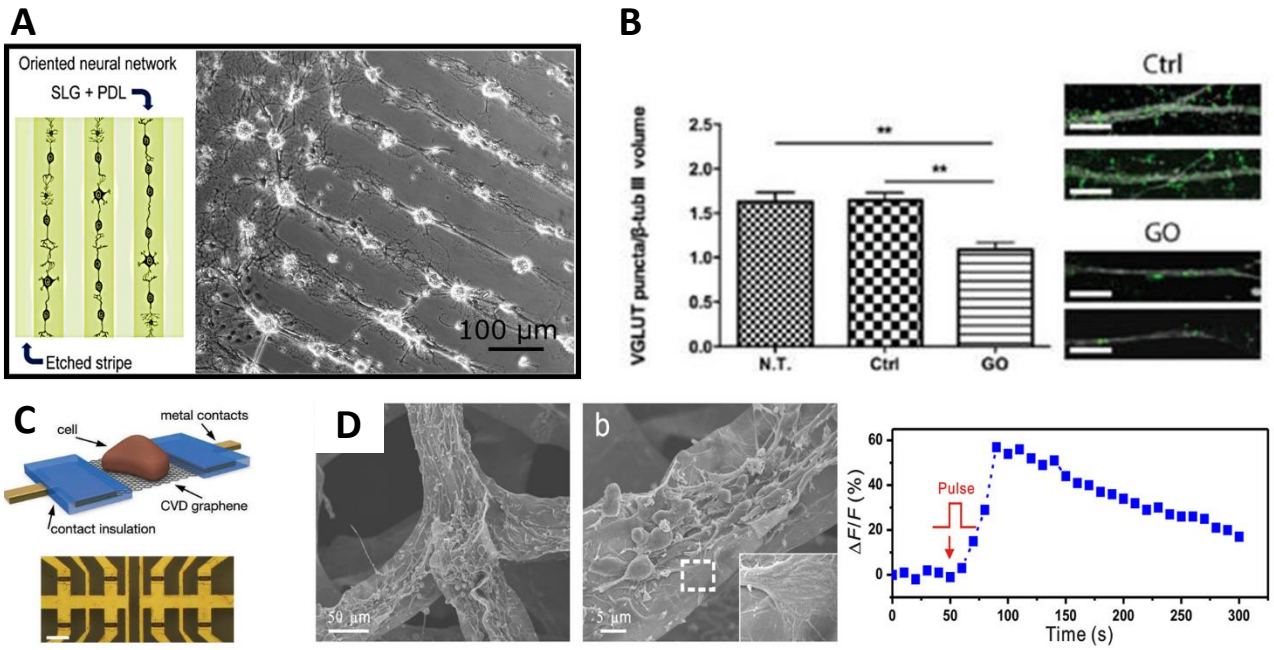

Figure 7. Biocompatibility and citotoxicity of graphene: *A) Dissociated hippocampal neurons prefer to grow over coated graphene stripes and form an highly ordered neuronal network. B) Graphene oxide flakes exposed to cortical neurons impair the formation of excitatory synapses in vitro. C) Cartoon of the graphene transistor arrays used for the detection of electric signals from electrogenic cells. D) Graphene foams are biocompatible 3D scaffolds for NSC growth and differentiation and can be stimulated to evoke activity in differentiated neurons. From Ref. 63, 65, 67, 58.*

With an increasing interest in using 3D structures to culture dissociated cells *in vitro*, the use of 3D graphene structures increased as well[71,72]. One of the first test of biocompatibility of a 3D graphene structure was made by the group of Guosheng Cheng. They build 3D Graphene Foams (GFs) using the CVD technique and grew Neural Stem Cell (NSC) on them, observing cellular adhesion, maturation and differentiation in a 3D environment[58](**Fig. 7D**). In this paper it is also shown that the GFs can be electrically stimulated to elicit activity in the mature neurons. Another evidence of the biocompatibility of this structures was

published one year after by the same group. They showed the anti-inflammatory effect of the GFs studying cytokine production of cultured microglia upon insult with LPS[59].

2.3. Spontaneous Activity of neuronal networks

The spontaneous activity is an important dynamic process that underlies many developmental events in the nervous system[73,74], including migration and dendrites formation. It has been showed, indeed, that post-migratory neurons in layer II/III have a more frequent spontaneous calcium activity and its elevation blocks cell migration and induces a premature branching[75](**Fig. 8A**).

An interesting feature of the on-going activity of developing neurons and circuits is the presence of highly synchronized activity[76]. An example is the presence of giant depolarizing potentials (GDPs) that are responsible for most of the spontaneous activity of a developing hippocampus and are generated in the early stages of development thanks to an initial depolarizing effect of GABAergic synapses and their interplay with the developing glutamatergic counterpart[77]. This phenomenon has been described also in other brain regions like the cortex[78]. This high level of activity during network maturation is also responsible for a large rise of $[Ca^{2+}]_i$ that represents an important signal for growth and maturation, as well as for many other cellular processes[79]. The expression of the transcription factor Npas4 in neurons, for instance, is activity-dependent and is selectively induced by the Ca^{2+} influx. Its expression regulates the number of active inhibitory synapses that excitatory neurons receive[80]. Another example of the importance of the synchronized activity is synaptic plasticity. Synapses that are “out of sync” with their neighbours are depressed in their transmission efficiency[81] and this is completely in line with the finding of a higher synchronized activity in strongly paired neurons[82](**Fig. 8B**). However, even though highly correlated activity is necessary for the development of the nervous system, it should not last longer in order to properly propagate information through brain areas[83]. There are theoretical evidences that de-correlated and fluctuating activity is important in the adulthood to integrate incoming stimuli[84]. The study of spontaneous activity of cortical neurons in mice has shown that there is a transition to a much more desynchronized state after the second post-natal week[85](**Fig. 8C**). What we can conclude is that de-correlated background activity can improve the coding of natural stimuli and perturbation of this step of maturation could result in network dysrhythmias that may underlie brain disorders[86].

All the information about the spontaneous activity of developing neuronal networks needs to be considered when we choose or develop an *in vitro* model to study the dynamic

properties of a neuronal ensemble. Systematic studies of dissociated 2D neuronal networks showed similar things. Hippocampal cultures from rats have a spontaneously synchronized activity starting from the third day *in vitro* (DIV) until the second week in culture. They show an increase in the firing frequency, but there is no decrease in terms of burst correlation[87]. In another study on cortical neurons dissociated from rats it has been reported a high degree of correlation of spike trains up to 35 DIV[88]. Both studies are not in line with what has been observed *in vivo*[83,85].

However, when studies of dynamical properties of neuronal networks are carried out on dissociated cells, many parameters can affect the network properties, such as cell density[87] and glial percentage[89].

2.3.1. Spontaneous activity of scaffold-based 3D neuronal network models

The most used 3D models of brain tissues are acute and organotypic slices. It has been show that only the organotypic slices have a spontaneous activity similar to the one observed *in vivo*. This is due to the regrowth of pruned processes during the days *in vitro*, a phenomenon that does not happen in acute slices preparations and causes a reduction in the activity[9]. However, neocortical acute slices have been used to describe the dynamics of the spontaneous activity[90] and it has been show that ensembles of synchronized neurons exist that can overlap each other and share same elements. Once accepted that 2D *in vitro* models do not represent the *in vivo* dynamics of cells growth and development, another approach is to integrate tissue engineering and biomaterials(**Fig. 1**) to improve many morphological and dynamic parameters that were poorly mimicked, or completely absent, in 2D models. As expected, together with a cell morphological and viability assessment, researchers started to investigate the neuronal spontaneous activity of these networks to understand their dynamics and properties. A higher and more complex degree of connectivity seems to lead to a more complex on-going activity, but there is still little information about this. A first example was given by a paper published by Irons and collaborators in which, using a technique modified from traditional acute slice whole-cell

patch clamp recordings, the authors showed that neurons in co-culture, embedded in a matrigel matrix, have the same resting membrane potential of neurons growth in conventional way (**Fig. 9A**). The differences are in the larger amplitude of action potentials of neurons in 3D and in their higher firing frequency after K^+ stimulation[7].

Other studies, using both hippocampal and cortical neurons, were conducted using synthetic scaffolds, such as glass microbeads and the commercially available polystyrene Alvetex[91,92]. By implementing a Multi Electrodes Array (MEA) system to these engineered 3D cultures it was possible to describe the spontaneous activity of co-cultured neuron/glia

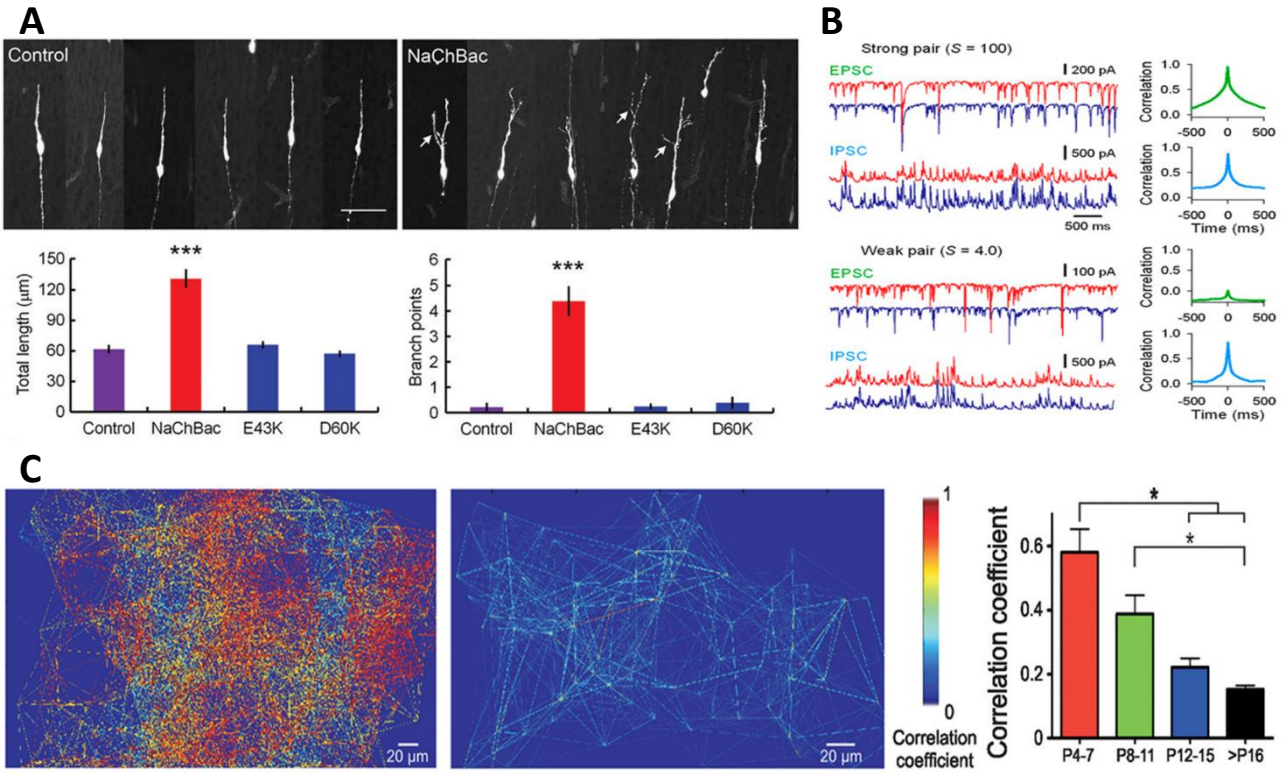

Figure 8. Spontaneous activity of developing networks: *A) Constitutive increase of the spontaneous activity using ectopic expression of prokaryotic voltage-gated sodium channel (NaChBac) cause an increase in the process length and in the number of branch points. B) Strongly paired neurons show a higher correlation coefficient compared to the weaker paired ones. However, it seems that excitatory neurons are specifically wired to ensure synchronized activity. C) The correlation coefficient of paired neurons in vivo is very high at P4 (left panel) and drastically decreases at P14 (meddle panel). This drop of synchronization happens gradually during development and reflects a mature state of the network (right panel). From Ref.75, 82, 85.*

population after 3-4 weeks *in vitro* (**Fig. 9B**). Both groups reported a significant lower firing frequency compared to the standard 2D controls at this stage of maturation[91,92] (**Fig. 9B**). Moreover, Frega et al reported that 3D cultures have a bursting activity which is highly synchronized and a random activity with lower correlation[91], but overall the activity is less correlated.

Even though electrophysiological techniques have provided important insights into the function of neural circuits both *in vitro* and *in vivo*, they lack of spatial resolution and there

are many technical issues behind their application in scaffold-based 3D *in vitro* models. In the previously described cases it was possible to record the activity either from single neuron or from the outside layer of the 3D culture by limiting the investigation possibilities. The use of calcium as a reporter of action potentials[93] and the increasing improvement in microscopy techniques[91–93] opened the door to a less invasive way of measuring the neuronal activity on a larger spatial scale and deep inside the engineered 3D culture.

Bosi et al. were able to obtain a 3D scaffold made of PDMS with holes layered by an irregular carbon nanotube carpet. Using the calcium imaging technique, they showed that hippocampal

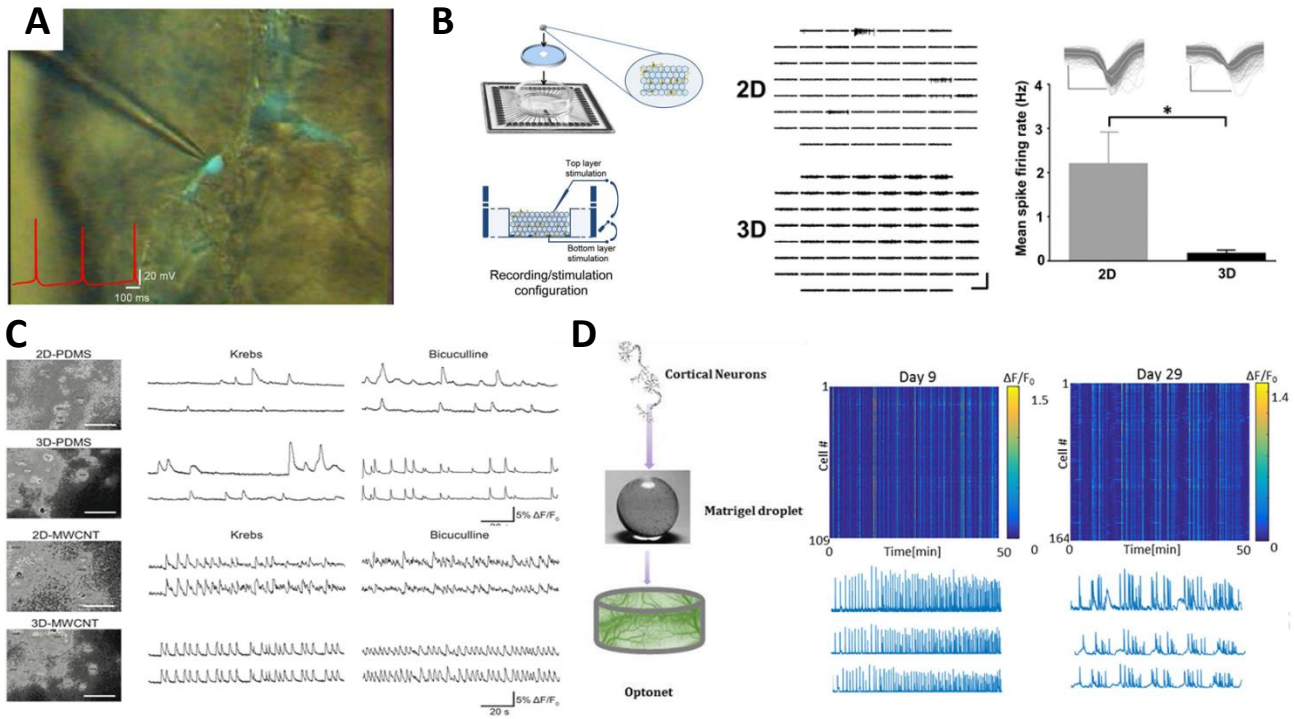

Figure 9. Spontaneous activity of scaffold based 3D models: *A) The first example of electrophysiological recording from a neuron embedded in a 3D matrix. B) Integration of a 3D network grown on microbeads with a MEA recording system. C) Extracellular recording obtained with a MEA system showing that the activity of mature 3D scaffold-based neuronal networks have a lower frequency compared to the 2D networks. D) Different degree of activity described comparing 2D and 3D cultures on PDMS and PDMS+MWCNT showing the effects of MWCNT on the level of the activity also in 3D. E) Using the "Optonet", optically transparent 3D in vitro neuronal networks, was described the degree of activity during maturation in vitro. See Ref. 7, 91, 92, 33, 30.*

neurons growth on the scaffolds with only PDMS had a spontaneous activity characterized by a higher frequency and a higher correlation compared with their 2D PDMS counterpart. When neurons were interfaced with MWCNT, either in 2D or 3D, their spontaneous activity showed an increased Inter Event Interval (IEI) and correlation (**Fig. 9C**). However, no differences were reported between the two conditions, in presence of bicuculline[33].

Recently, the maturation of a 3D neuronal culture was also described. Using embryonic cortical rat neurons, Marom and co-workers build up an optical transparent 3D neuronal network using matrigel as matrix scaffold; they called this system “optonet”[30] (**Fig. 9D**). Taking advantage of the last version of a Genetically Encoded Calcium Indicator (GECI) GCaMP6m, they studied the activity of the network during development from 5 DIV to 4 weeks *in vitro* using a 3D scanning system associated with the epifluorescence microscopy and a deconvolution step to improve the image sequences and get rid of out of focus light[30]. Alongside the innovative approach, they describe networks with an increased activity during the first 2 weeks of culture where the peak of frequency was observed, while the activity started to decline from day 21-23 (**Fig. 9D**).

All together these information create a new road for further investigation on the dynamics of scaffold-based 3D neuronal networks and for the creation of new scaffolds for different applications in basic and applied neuroscience. These will be the main topic of this thesis and detailed results will be provided about the work I did during my Ph.D. studies together with my collaborators.

3. REFERENCES

1. Hopkins, A. M., DeSimone, E., Chwalek, K. & Kaplan, D. L. 3D in vitro modeling of the central nervous system. *Progress in Neurobiology* **125,** 1–25 (2015).
2. Harrison, R. G., Greenman, M. J., Mall, F. P. & Jackson, C. M. Observations of the living developing nerve fiber. *Anat. Rec.* **1,** 116–128 (1907).
3. Migliorini, E. *et al.* Nanomechanics controls neuronal precursors adhesion and differentiation. *Biotechnol. Bioeng.* **110,** 2301–2310 (2013).
4. Chen, W.-H., Cheng, S.-J., Tzen, J. T. C., Cheng, C.-M. & Lin, Y.-W. Probing Relevant Molecules in Modulating the Neurite Outgrowth of Hippocampal Neurons on Substrates of Different Stiffness. *PLOS ONE* **8,** e83394 (2013).
5. Bikbaev, A., Frischknecht, R. & Heine, M. Brain extracellular matrix retains connectivity in neuronal networks. *Scientific Reports* **5,** 14527 (2015).
6. Barros, C. S., Franco, S. J. & Müller, U. Extracellular matrix: functions in the nervous system. *Cold Spring Harb Perspect Biol* **3,** a005108 (2011).
7. Irons, H. R. *et al.* Three-dimensional neural constructs: a novel platform for neurophysiological investigation. *J Neural Eng* **5,** 333–341 (2008).
8. Ko, K. R. & Frampton, J. P. Developments in 3D neural cell culture models: the future of neurotherapeutics testing? *Expert Rev Neurother* **16,** 739–741 (2016).
9. Okamoto, K. *et al.* Ex vivo cultured neuronal networks emit in vivo-like spontaneous activity. *J Physiol Sci* **64,** 421–431 (2014).
10. Usmani, S. *et al.* 3D meshes of carbon nanotubes guide functional reconnection of segregated spinal explants. *Science Advances* **2,** e1600087 (2016).
11. Aurand, E. R. *et al.* Nanostructures to Engineer 3D Neural-Interfaces: Directing Axonal Navigation toward Successful Bridging of Spinal Segments. *Adv. Funct. Mater.* n/a-n/a doi:10.1002/adfm.201700550
12. Yang, N., Ng, Y. H., Pang, Z. P., Südhof, T. C. & Wernig, M. Induced Neuronal Cells: How to Make and Define a Neuron. *Cell Stem Cell* **9,** 517–525 (2011).

13. Dingle, Y.-T. L. *et al.* Three-Dimensional Neural Spheroid Culture: An In Vitro Model for Cortical Studies. *Tissue Eng Part C Methods* **21,** 1274–1283 (2015).
14. LIYANG, G., ABDULLAH, S., ROSLI, R. & NORDIN, N. Neural Commitment of Embryonic Stem Cells through the Formation of Embryoid Bodies (EBs). *Malays J Med Sci* **21,** 8–16 (2014).
15. Brewer, G. J. & Torricelli, J. R. Isolation and culture of adult neurons and neurospheres. *Nat. Protocols* **2,** 1490–1498 (2007).
16. Lancaster, M. A. *et al.* Cerebral organoids model human brain development and microcephaly. *Nature* **501,** 373–379 (2013).
17. Lancaster, M. A. & Knoblich, J. A. Generation of cerebral organoids from human pluripotent stem cells. *Nat Protoc* **9,** 2329–2340 (2014).
18. Kadoshima, T., Sakaguchi, H. & Eiraku, M. Generation of Various Telencephalic Regions from Human Embryonic Stem Cells in Three-Dimensional Culture. *Methods Mol. Biol.* **1597,** 1–16 (2017).
19. Emerman, J. T. & Pitelka, D. R. Maintenance and induction of morphological differentiation in dissociated mammary epithelium on floating collagen membranes. *In Vitro* **13,** 316–328 (1977).
20. Ravi, M., Paramesh, V., Kaviya, S. R., Anuradha, E. & Solomon, F. D. P. 3D cell culture systems: advantages and applications. *J. Cell. Physiol.* **230,** 16–26 (2015).
21. Yu, L. M. Y., Leipzig, N. D. & Shoichet, M. S. Promoting neuron adhesion and growth. *Materials Today* **11,** 36–43 (2008).
22. Limongi, T. *et al.* Nanostructured superhydrophobic substrates trigger the development of 3D neuronal networks. *Small* **9,** 402–412 (2013).
23. Tang, Y. *et al.* Effective motor neuron differentiation of human induced pluripotent stem cells on a patch made of crosslinked monolayer gelatin nanofibers. *J. Mater. Chem. B* (2016). doi:10.1039/C6TB00351F
24. Tang, Y., Ulloa Severino, F. P., Iseppon, F., Torre, V. & Chen, Y. Patch method for culture of primary hippocampal neurons. *Microelectronic Engineering* **175,** 61–66 (2017).

25. Wei, J., Pozzi, D., Ulloa Severino, F. P., Torre, V. & Chen, Y. Fabrication of PLGA nanofibers on PDMS micropillars for neuron culture studies. *Microelectronic Engineering* **175,** 67–72 (2017).
26. Lau, C. L. *et al.* 3D Electrospun scaffolds promote a cytotrophic phenotype of cultured primary astrocytes. *J. Neurochem.* **130,** 215–226 (2014).
27. Baker, B. M. & Chen, C. S. Deconstructing the third dimension – how 3D culture microenvironments alter cellular cues. *J Cell Sci* **125,** 3015–3024 (2012).
28. Li, H., Wijekoon, A. & Leipzig, N. D. 3D differentiation of neural stem cells in macroporous photopolymerizable hydrogel scaffolds. *PLoS ONE* **7,** e48824 (2012).
29. Hanson Shepherd, J. N. *et al.* 3D Microperiodic Hydrogel Scaffolds for Robust Neuronal Cultures. *Adv Funct Mater* **21,** 47–54 (2011).
30. Marom, A., Shor, E., Levenberg, S. & Shoham, S. Spontaneous Activity Characteristics of 3D 'Optonets'. *Front Neurosci* **10,** (2017).
31. Ahn, G. *et al.* Effect of pore architecture on oxygen diffusion in 3D scaffolds for tissue engineering. *J Biomech Eng* **132,** 104506 (2010).
32. Zhang, H. L., Li, J.-F. & Zhang, B.-P. Microstructure and electrical properties of porous PZT ceramics derived from different pore-forming agents. *Acta Materialia* **55,** 171–181 (2007).
33. Bosi, S. *et al.* From 2D to 3D: novel nanostructured scaffolds to investigate signalling in reconstructed neuronal networks. *Scientific Reports* **5,** 9562 (2015).
34. Velliste, M., Perel, S., Spalding, M. C., Whitford, A. S. & Schwartz, A. B. Cortical control of a prosthetic arm for self-feeding. *Nature* **453,** 1098–1101 (2008).
35. McConnell, G. C., So, R. Q., Hilliard, J. D., Lopomo, P. & Grill, W. M. Effective deep brain stimulation suppresses low-frequency network oscillations in the basal ganglia by regularizing neural firing patterns. *J. Neurosci.* **32,** 15657–15668 (2012).
36. Perlmutter, J. S. & Mink, J. W. Deep Brain Stimulation. *Annu Rev Neurosci* **29,** 229–257 (2006).
37. Fattahi, P., Yang, G., Kim, G. & Abidian, M. R. A Review of Organic and Inorganic Biomaterials for Neural Interfaces. *Adv. Mater.* **26,** 1846–1885 (2014).

38. Gilmour, A. D., Woolley, A. J., Poole-Warren, L. A., Thomson, C. E. & Green, R. A. A critical review of cell culture strategies for modelling intracortical brain implant material reactions. *Biomaterials* **91,** 23–43 (2016).
39. Fang, Y., Li, X. & Fang, Y. Organic bioelectronics for neural interfaces. *J. Mater. Chem. C* **3,** 6424–6430 (2015).
40. Aregueta-Robles, U. A., Woolley, A. J., Poole-Warren, L. A., Lovell, N. H. & Green, R. A. Organic electrode coatings for next-generation neural interfaces. *Front. Neuroeng.* **7,** 15 (2014).
41. Vaysse, L., Beduer, A., Sol, J. C., Vieu, C. & Loubinoux, I. Micropatterned bioimplant with guided neuronal cells to promote tissue reconstruction and improve functional recovery after primary motor cortex insult. *Biomaterials* **58,** 46–53 (2015).
42. Tian, B. *et al.* Macroporous nanowire nanoelectronic scaffolds for synthetic tissues. *Nat Mater* **11,** 986–994 (2012).
43. Choudhary, V. & Gupta, A. Polymer/Carbon Nanotube Nanocomposites. (2011). doi:10.5772/18423
44. Cellot, G. *et al.* Carbon nanotubes might improve neuronal performance by favouring electrical shortcuts. *Nat Nano* **4,** 126–133 (2009).
45. Cellot, G. *et al.* Carbon Nanotube Scaffolds Tune Synaptic Strength in Cultured Neural Circuits: Novel Frontiers in Nanomaterial–Tissue Interactions. *J. Neurosci.* **31,** 12945–12953 (2011).
46. Lovat, V. *et al.* Carbon Nanotube Substrates Boost Neuronal Electrical Signaling. *Nano Lett.* **5,** 1107–1110 (2005).
47. Jan, E. *et al.* Layered Carbon Nanotube-Polyelectrolyte Electrodes Outperform Traditional Neural Interface Materials. *Nano Lett.* **9,** 4012–4018 (2009).
48. Jan, E. & Kotov, N. A. Successful Differentiation of Mouse Neural Stem Cells on Layer-by-Layer Assembled Single-Walled Carbon Nanotube Composite. *Nano Lett.* **7,** 1123–1128 (2007).

49. Schipper, M. L. *et al.* A pilot toxicology study of single-walled carbon nanotubes in a small sample of mice. *Nat Nano* **3,** 216–221 (2008).
50. Silva, G. A. Shorting neurons with nanotubes. *Nat Nanotechnol* **4,** 82–83 (2009).
51. Georgakilas, V. *et al.* Functionalization of Graphene: Covalent and Non-Covalent Approaches, Derivatives and Applications. *Chem. Rev.* **112,** 6156–6214 (2012).
52. Novoselov, K. S. *et al.* A roadmap for graphene. *Nature* **490,** 192–200 (2012).
53. Kostarelos, K. & Novoselov, K. S. Exploring the Interface of Graphene and Biology. *Science* **344,** 261–263 (2014).
54. Paton, K. R. *et al.* Scalable production of large quantities of defect-free few-layer graphene by shear exfoliation in liquids. *Nat Mater* **13,** 624–630 (2014).
55. Teng, C. *et al.* Ultrahigh Conductive Graphene Paper Based on Ball-Milling Exfoliated Graphene. *Adv. Funct. Mater.* **27,** n/a-n/a (2017).
56. Li, N. *et al.* The promotion of neurite sprouting and outgrowth of mouse hippocampal cells in culture by graphene substrates. *Biomaterials* **32,** 9374–9382 (2011).
57. Li, X. *et al.* Large-area synthesis of high-quality and uniform graphene films on copper foils. *Science* **324,** 1312–1314 (2009).
58. Li, N. *et al.* Three-dimensional graphene foam as a biocompatible and conductive scaffold for neural stem cells. *Sci Rep* **3,** 1604 (2013).
59. Song, Q. *et al.* Anti-inflammatory effects of three-dimensional graphene foams cultured with microglial cells. *Biomaterials* **35,** 6930–6940 (2014).
60. Ulloa Severino, F. P. *et al.* The role of dimensionality in neuronal network dynamics. *Scientific Reports* **6,** 29640 (2016).
61. Sanchez, V. C., Jachak, A., Hurt, R. H. & Kane, A. B. Biological Interactions of Graphene-Family Nanomaterials: An Interdisciplinary Review. *Chem. Res. Toxicol.* **25,** 15–34 (2012).
62. Bendali, A. *et al.* Purified Neurons can Survive on Peptide-Free Graphene Layers. *Advanced Healthcare Materials* **2,** 929–933 (2013).
63. Lorenzoni, M., Brandi, F., Dante, S., Giugni, A. & Torre, B. Simple and effective graphene laser processing for neuron patterning application. *Scientific Reports* **3,** srep01954 (2013).

64. Rauti, R. *et al.* Graphene Oxide Nanosheets Reshape Synaptic Function in Cultured Brain Networks. *ACS Nano* **10,** 4459–4471 (2016).
65. Bramini, M. *et al.* Graphene Oxide Nanosheets Disrupt Lipid Composition, Ca2+ Homeostasis, and Synaptic Transmission in Primary Cortical Neurons. *ACS Nano* **10,** 7154–7171 (2016).
66. Novoselov, K. S. *et al.* Electric Field Effect in Atomically Thin Carbon Films. *Science* **306,** 666–669 (2004).
67. Hess, L. H. *et al.* Graphene Transistor Arrays for Recording Action Potentials from Electrogenic Cells. *Adv. Mater.* **23,** 5045–5049 (2011).
68. Guo, W. *et al.* Self-Powered Electrical Stimulation for Enhancing Neural Differentiation of Mesenchymal Stem Cells on Graphene–Poly(3,4-ethylenedioxythiophene) Hybrid Microfibers. *ACS Nano* **10,** 5086–5095 (2016).
69. Lim, K.-T. *et al.* Pulsed-Electromagnetic-Field-Assisted Reduced Graphene Oxide Substrates for Multidifferentiation of Human Mesenchymal Stem Cells. *Adv. Healthcare Mater.* **5,** 2069–2079 (2016).
70. Feng, Z.-Q., Wang, T., Zhao, B., Li, J. & Jin, L. Soft Graphene Nanofibers Designed for the Acceleration of Nerve Growth and Development. *Adv. Mater.* **27,** 6462–6468 (2015).
71. Ji, H. *et al.* Preparation, microstructure, and compressive strength of carbon foams derived from sucrose and kaolinite. *Journal of Materials Research* **29,** 1018–1025 (2014).
72. Zhu, C. *et al.* Highly compressible 3D periodic graphene aerogel microlattices. *Nature Communications* **6,** 6962 (2015).
73. O'Donovan, M. J. The origin of spontaneous activity in developing networks of the vertebrate nervous system. *Current Opinion in Neurobiology* **9,** 94–104 (1999).
74. Spitzer, N. C. Electrical activity in early neuronal development. *Nature* **444,** 707–712 (2006).
75. Bando, Y. *et al.* Control of Spontaneous Ca2+ Transients Is Critical for Neuronal Maturation in the Developing Neocortex. *Cereb. Cortex* (2014). doi:10.1093/cercor/bhu180
76. Feller, M. B. Spontaneous Correlated Activity in Developing Neural Circuits. *Neuron* **22,** 653–656 (1999).

77. Ben-Ari, Y. Developing networks play a similar melody. *Trends in Neurosciences* **24,** 353–360 (2001).

78. Opitz, T., Lima, A. D. D. & Voigt, T. Spontaneous Development of Synchronous Oscillatory Activity During Maturation of Cortical Networks In Vitro. *Journal of Neurophysiology* **88,** 2196–2206 (2002).

79. Berridge, M. J., Lipp, P. & Bootman, M. D. The versatility and universality of calcium signalling. *Nat Rev Mol Cell Biol* **1,** 11–21 (2000).

80. Lin, Y. *et al.* Activity-dependent regulation of inhibitory synapse development by Npas4. *Nature* **455,** 1198–1204 (2008).

81. Winnubst, J., Cheyne, J. E., Niculescu, D. & Lohmann, C. Spontaneous Activity Drives Local Synaptic Plasticity In Vivo. *Neuron* **87,** 399–410 (2015).

82. Takahashi, N., Sasaki, T., Matsumoto, W., Matsuki, N. & Ikegaya, Y. Circuit topology for synchronizing neurons in spontaneously active networks. *PNAS* **107,** 10244–10249 (2010).

83. Bondy, A. & Cumming, B. Synchronous Spikes Are More Effective (but Not for Long). *Neuron* **87,** 676–678 (2015).

84. Ostojic, S. Two types of asynchronous activity in networks of excitatory and inhibitory spiking neurons. *Nat Neurosci* **17,** 594–600 (2014).

85. Golshani, P. *et al.* Internally Mediated Developmental Desynchronization of Neocortical Network Activity. *J. Neurosci.* **29,** 10890–10899 (2009).

86. Gonçalves, J. T., Anstey, J. E., Golshani, P. & Portera-Cailliau, C. Circuit level defects in the developing neocortex of Fragile X mice. *Nat. Neurosci.* **16,** 903–909 (2013).

87. Cohen, E., Ivenshitz, M., Amor-Baroukh, V., Greenberger, V. & Segal, M. Determinants of spontaneous activity in networks of cultured hippocampus. *Brain Research* **1235,** 21–30 (2008).

88. Chiappalone, M., Bove, M., Vato, A., Tedesco, M. & Martinoia, S. Dissociated cortical networks show spontaneously correlated activity patterns during in vitro development. *Brain Research* **1093,** 41–53 (2006).

89. Feldt, S. *et al.* Functional clustering in hippocampal cultures: relating network structure and dynamics. *Phys. Biol.* **7,** 046004 (2010).
90. Mao, B.-Q., Hamzei-Sichani, F., Aronov, D., Froemke, R. C. & Yuste, R. Dynamics of Spontaneous Activity in Neocortical Slices. *Neuron* **32,** 883–898 (2001).
91. Frega, M., Tedesco, M., Massobrio, P., Pesce, M. & Martinoia, S. Network dynamics of 3D engineered neuronal cultures: a new experimental model for in-vitro electrophysiology. *Scientific Reports* **4,** srep05489 (2014).
92. Smith, I. *et al.* Neuronal-glial populations form functional networks in a biocompatible 3D scaffold. *Neurosci. Lett.* **609,** 198–202 (2015).
93. Cossart, R., Ikegaya, Y. & Yuste, R. Calcium imaging of cortical networks dynamics. *Cell Calcium* **37,** 451–457 (2005).
94. Göbel, W., Kampa, B. M. & Helmchen, F. Imaging cellular network dynamics in three dimensions using fast 3D laser scanning. *Nat Meth* **4,** 73–79 (2007).
95. Dana, H. *et al.* Hybrid multiphoton volumetric functional imaging of large-scale bioengineered neuronal networks. *Nature Communications* **5,** ncomms4997 (2014).
96. Yang, W. *et al.* Simultaneous Multi-plane Imaging of Neural Circuits. *Neuron* **89,** 269–284 (2016).

4. RESULTS

This section is the sum of experiments carried out by different people I collaborated with during my Ph.D. course.

For what concerns me:

- In the first article, I set the culture protocol of primary neurons and performed the immuno cytochemical analysis and calcium imaging experiments. I carried out the data analysis and prepared the figures concerning my experimental part;
- In the second article, I fabricated the PDMS pillars, I set the culture protocol and performed SEM and immunofluorescence together with my collaborators. I also carried out data analysis and figure preparation.
- In the third article, I set the culture protocol and performed calcium imaging experiments. I carried out data analysis and figure preparation;

I actively participated in writing and designing all these works.

4.1.

Patch method for culture of primary hippocampal neurons

Y. Tang[+], F. P. Ulloa Severino[+], F. Iseppon, V. Torre and Y. Chen

Microelectronic Engineering

Microelectronic Engineering 175 (2017) 61–66

Contents lists available at ScienceDirect

Microelectronic Engineering

journal homepage: www.elsevier.com/locate/mee

Research paper

Patch method for culture of primary hippocampal neurons

Yadong Tang [a,1], Francesco Paolo Ulloa Severino [b,1], Federico Iseppon [b], Vincent Torre [b,*], Yong Chen [a,c,d,**]

[a] Ecole Normale Supérieure-PSL Research University, Département de Chimie, Sorbonne Universités - UPMC Univ Paris 06, CNRS UMR 8640 PASTEUR, 24, rue Lhomond, 75005 Paris, France
[b] Scuola Internazionale Superiore di Studi Avanzati, via Bonomea, 265, 34136 Trieste, Italy
[c] Institute for Integrated Cell-Material Sciences, Kyoto University, Kyoto 606-8507, Japan
[d] Institute for Interdisciplinary Research, Jianghan University, Wuhan, China

ARTICLE INFO

Article history:
Received 12 October 2016
Received in revised form 9 January 2017
Accepted 13 January 2017
Available online 18 January 2017

Keywords:
Nanofiber
Patch
Hippocampal neuron
Calcium imaging

ABSTRACT

Culture of primary neurons, and especially hippocampal neurons, is important for understanding cellular mechanisms in neurobiology. Actually, this is achieved by using culture dish or glass slide with surface coated proteins. Here, we proposed a patch method for culture of primary neurons on a monolayer of gelatin nanofibers electrospun and crosslinked on a honeycomb microframe of poly (ethylene glycol) diacrylate (PEGDA). This method allows us to minimize exogenous material contact of cells and largely increase the exposure area of cells to the culture medium. We found that neurons, and especially astrocytes, have a more *in vivo* like morphology comparing to that on culture dish or on glass slide. We also found that neurons were preferentially located in the suspended areas of the monolayer nanofibers. Finally, calcium imaging revealed that primary neurons have a higher degree of neural activity on the patch than on glass. These results suggest that crosslinked and monolayer gelatin nanofibers closely mimic the extracellular matrix structure and allow more effective culture of primary neurons than conventional methods, thus facilitating advanced studies of neural functions as well as cell-based assays.

1. Introduction

Primary neurons, especially the hippocampal neurons, are widely used for *in vitro* studies due to the relative simple nerve cell population and the expression of key neural phenotypic features as well as the involvement of the hippocampus in learning and memory [1–4]. In most of these studies, the primary neurons were cultured in culture dish or on glass slides with or without astrocytes [5]. It has been shown, however, that the neural growth and its functional performance are critically dependent on the culture conditions, especially the mechanical and biochemical properties of the substrate [6,7]. While the optimal culture should recapitulate the *in vivo* organization of extracellular matrix (ECM) of primary neurons [8,9], the conventional culture methods are not flexible to achieve this ultimate goal.

Electrospun nanofibers are *in vivo* ECM like, which are promising for advanced applications in tissue engineering and regenerative medicine [10,11]. Gertz et al. showed that electrospun nanofibers can significantly enhance neuritogenesis, maturation and the polarity formation of neurons compared to the conventional two-dimensional (2D) culture using glass substrates [12]. Our previous studies demonstrated that gelatin nanofibres could be used for long-term expansion of human induced pluripotent stem cells (hiPSCs) [13]. Although nanofibers made of different types of synthetic polymers can also be used for cell culture, natural bio-polymers such as gelatin, which is produced by hydrolyzing collagen, should be more relevant for cell based assays [14]. More recently, we used monolayer gelatin nanofibers in form of culture patch to differentiate hiPSCs towards mature motor neurons and cardiomyocytes [15,16]. Our results showed a number of advantages of this patch method over the conventional culture dish methods, including up-regulated expression of neural specific genes, accelerated neuron maturation as well as plug-and-play monitoring of neuron spikes by extracellular potential recording.

In this work, we extend the patch method to culture primary hippocampal neurons. We show that hippocampal cells, especially astrocytes, have *in vivo* like morphology on the culture patch. Our results also showed that most of neurons were found in the porous areas inside the honeycomb compartments and that primary neurons have a higher degree of neural activity on the patch than on glass.

2. Experimental

2.1. Fabrication of culture patch

The culture patch was fabricated as described previously [15,16]. Briefly, honeycomb microframe of 500 μm pitch size and 50 μm band

* Corresponding author.
** Correspondence to: Y. Chen, Ecole Normale Supérieure-PSL Research University, Département de Chimie, Sorbonne Universités - UPMC Univ Paris 06, CNRS UMR 8640 PASTEUR, 24, rue Lhomond, 75005 Paris, France.
E-mail addresses: torre@sissa.it (V. Torre), yong.chen@ens.fr (Y. Chen).
[1] Authors contributed equally to this work.

http://dx.doi.org/10.1016/j.mee.2017.01.012
0167-9317/

width was patterned on a Chrome mask with a micro pattern generator (μPG 101, Heidelberg Instruments). A 50 μm thick photoresist layer (AZ 40XT, MicroChem) was then spun coated on the mask and backside exposed with UV light. After development, the mask with resist pattern was treated in trimethylchlorosilane (TMCS) vapor for *anti*-sticking treatment. Polydimethylsiloxane (PDMS) pre-polymer and cross-linker (GE RTV 615) at weight ratio of 10:1 was mixed and then poured on the resist layer. After curing at 80 °C for 2 h, the PDMS layer was peeled off and placed on a glass slide. The PDMS-glass assembly was then degassed for 10 min in a desiccator. Afterwards, a PEGDA (average Mn = 250, Sigma) solution containing 1 v/v% Irgacure 2959 as photo-initiator was dropped on the edge of PDMS mould to fill the cavity between PDMS and glass with the help of degassing based micro-aspiration. After UV curing for 30 s at 9.1 mW/cm^2, the PDMS mould was release. In parallel, a 100 μm thick PEGDA ring with outer and inner diameter of 13 mm and 9 mm respectively was prepared with the similar method. This PEGDA ring was then mounted on the honeycomb microframe using PEGDA solution as binder and UV curing.

Gelatin nanofibers were prepared by electrospinning using the same protocol as described previously [8]. For easy collection of the nanofibers, 10 nm thick Au layer was sputtered on the PEGDA frame and the PEGDA frame was fixed on a silicon wafer (collector). 10 wt% gelatin was dissolved in a solvent mixture containing distilled water, ethylacetate acid and acetic acid at a volume ratio of 10:14:21. The gelatin solution was then ejected from a syringe to the collector at a distance of 10 cm and a pumping speed of 0.2 ml/h through a stainless steel needle (23-gauge) under a bias voltage of 11 kV. After electrospinning for 15 min, the sample was removed in a desiccator to remove the residual solvent overnight. An ethanol solution containing 0.2 M 1-ethyl-3-(3-dimethylaminopropyl) carbodiimide hydrochloride (EDC) and 0.2 M N-hydroxysuccinimide (NHS) was used for crosslinking the gelatin nanofibers during 4 h. Finally, the samples was rinsed with ethanol three times and dried completely in a desiccator overnight to eliminate the remaining solvent.

2.2. Cell culture

Human glioblastoma cell line U-87 was cultured in Dulbecco's Modified Eagle Medium (DMEM) completed with 10% FBS and 1% penicillin/streptomycin at 37 °C with 5% CO_2 supplementation for 3– 4 days to reach 80% confluence. Then cells were dissociated by Trypsin at 37 °C for 3 min. Then without any additional coating, 10^5 cells in 50 μl medium were seeded on the patch in the center of the ring. After incubation at 37 °C for 1 h for cell attachment, more medium was added gently around the patch, which was then transferred back to the incubator for continued culture.

Hippocampal neurons from Wistar rats (P2-P3) were prepared in accordance with the guidelines of the Italian Animal Welfare Act, and their use was approved by the Local Veterinary Service, the SISSA Ethics Committee board and the National Ministry of Health (Permit Number: 630-III/14) in accordance with the European Union guidelines for animal care (d.1.116/92; 86/609/C.E.). The animals were anaesthetized with CO_2 and sacrificed by decapitation, and all efforts were made to minimize suffering. All substrates (Glass and patch nanofibers) were sterilized under UV light (15 min each side), soaked for 2 days in PBS and other 2 days in 100 units/ml Penicillin and 100 μg/ml Streptomycine. Finally, they were coated with 20 μg/ml Laminin (Sigma-Aldrich, St. Louis, MO, USA) overnight and washed with water before Matrigel coating (1:50 diluted in the Culture Medium) (Corning, Tewksbury MA, USA) and cell seeding. Dissociated cells were resuspended in Culture Medium: minimum essential medium (MEM) with GlutaMAX™ supplemented with 10% dialyzed fetal bovine serum (FBS, all from Thermo Fisher Scientific, Waltham, MA, USA), 0.6% D-glucose, 15 mM Hepes, 0.1 mg/ml apo-transferrin, 30 μg/ml insulin, 0.1 μg/ml D-biotin, 1 μM vitamin B12 and 2.5 μg/ml gentamycin (all from Sigma-Aldrich). A drop containing 200.000 cells was deposited per each substrate and incubated for 30 min at 37 °C. The cells were then resuspended in Astrocyte Conditioned Medium (ACM) in 1:1 ratio with Neurobasal/B27 medium. After 48 h, 2 μM cytosine-β-D-arabinofuranoside (Ara-C; Sigma-Aldrich) was added to the culture medium to block glial cell proliferation. Half of the medium was changed every 2–3 days. The neuronal cultures were maintained in an incubator at 37 °C, 5% CO_2 and 95% relative humidity.

2.3. Scanning electron microscopy (SEM) observation

For the samples with cells, they were firstly fixed with 4% formaldehyde for 30 min, and rinsed three times with PBS. Then the samples were immersed in 30% ethanol solution (in distilled water) for 30 min. Afterward, the samples were dehydrated using graded ethanol solutions with concentrations of 50%, 70%, 80%, 90%, 95%, and 100%, respectively, each for 10 min and dried by nitrogen gas flow. Before observation, both dehydrated cell samples and samples without cells were deposited with a 2 nm thick Au layer by sputtering. Finally the samples was observed with a scanning electron microscope (Hitachi S-800) operated at 10 kV.

2.4. Calcium imaging

The cells were loaded with 4 μM of a cell-permeable calcium dye Fluo4-AM (Life Technologies) dissolved in anhydrous DMSO (Sigma-Aldrich), stock solution 4 mM, and Pluronic F-127 20% solution in DMSO (Life Technologies) at a ratio of 1:1 in Ringer's solution (145 mM NaCl, 3 mM KCl, 1.5 mM $CaCl_2$, 1 mM $MgCl_2$, 10 mM glucose and 10 mM Hepes, pH 7.4) at 37 °C for 1 h. After incubation, the cultures were washed and then transferred to the stage of a Nikon Eclipse Ti-U inverted microscope equipped with a piezoelectric table (Nano-ZI Series 500 μm range, Mad City Labs), an HBO 103 W/2 mercury short arc lamp (Osram, Munich, Germany), a mirror unit (exciter filter BP 465-495 nm, dichroic 505 nm, emission filter BP 515-555) and an Electron Multiplier CCD Camera C9100-13 (Hamamatsu Photonics, Japan). The experiments were performed at RT, and images were acquired using the NIS Element software (Nikon, Japan) with an S-Fluor 20×/0.75 NA objective at a sampling rate of 3–10 Hz with a spatial resolution of 256 × 256 pixels for 10 min. To avoid saturation of the signals, excitation light intensity was attenuated by ND4 and ND8 neutral density filters (Nikon).

2.4.1. Ca^{2+} imaging processing and analysis

The initial video was processed with the ImageJ (U. S. National Institutes of Health, Bethesda, MA) software. The image sequences were then analysed as described previously [17]. Appropriate ROIs around the cells bodies were then selected. The time course of the fluorescence intensity, $I_f(t)$, in this ROI was displayed, and any decay, which is a consequence of dye bleaching, was evaluated. The Ca^{2+} transients of each cell signal were extracted in a semi-automatic manner by selecting a threshold for the smallest detectable peak that was equal to three times the standard deviation of the baseline. $I_f(t)$ was then fitted to the original optical signal to compensate for dye bleaching, and the fractional optical signal was calculated as follows: $DF/F = (Y(t) + I_f(t))/I_f(0)$, where $I_f(0)$ is the fluorescence intensity at the beginning of the recording.

2.4.2. Computation of the correlation coefficient of Ca^{2+} transient occurrence

The times, t_i, at which transient peaks occurred were used to calculate the rate of activity. The correlation coefficient of the calcium transients for neuron i and neuron j (σ_{CTij}) was computed as follows: The total recording time, T_{tot}, was divided into N intervals (1,..,n, …,N) of a

duration Δt. Thus, if f_{in} and f_{jn} are the number of calcium transients of neuron i and neuron j in the time interval Δt_n, then

$$\sigma_{CT_{ij}} = \frac{\sum_n f_{in} f_{jn}}{\sqrt{\left(\sum_n f_{in}^2\right)\left(\sum_n f_{jn}^2\right)}} \quad (1)$$

such that σ_{CTij} depends on Δt and varies between 0 and 1. The range of explored values of Δt was 10 s.

2.5. Immunofluorescence

Cells were fixed in 4% paraformaldehyde containing 0.15% picric acid in phosphate-buffered saline (PBS), saturated with 0.1 M glycine, permeabilized with 0.1% Triton X-100, saturated with 0.5% BSA (all from Sigma-Aldrich) in PBS and then incubated for 1 h with primary antibodies: mouse monoclonal glial fibrillary acidic protein (GFAP)(Sigma-Aldrich) and *anti*-β-tubulin III (TUJ1) mouse monoclonal antibody (Covance, Berkeley, CA). The secondary antibodies were goat anti-mouse immunoglobulin (Ig) G1 Alexa Fluor® 488, goat anti-mouse IgG2a Alexa Fluor® 594, (all from Life Technologies) and the incubation time was 30 min. Nuclei were stained with 2 μg/ml in PBS Hoechst 33342 (Sigma-Aldrich) for 5 min. All the incubations were performed at room temperature (20–22 °C). The cells were examined using a Leica DM6000 fluorescent microscope equipped with DIC and fluorescence optics, CCD camera and Volocity 5.4 3D imaging software (PerkinElmer, Coventry, UK). The fluorescence images were collected with a 20× magnification and 0.5 NA objective. When necessary z-stack images were acquired with slice spacing of 0.5 μm. Image J by W. Rasband (developed at the U.S. National Institutes of Health and available at http://rsbweb.nih.gov/ij/) was used for image processing.

To assess the preferential localization of the cells inside the honeycomb compartment, the cell number inside the compartment, $nCell_{in}$, has been counted. In case of homogenous cell distribution, the cell number inside the compartment is given by

$$\mathrm{ExpCell} = (A_{in}/A_{tot}) \times \mathrm{n}Cell_{tot} \quad (2)$$

where A_{in} is the area of the compartment and A_{tot} is the total area including both the compartment and the frame, $nCell_{tot}$ being the cell

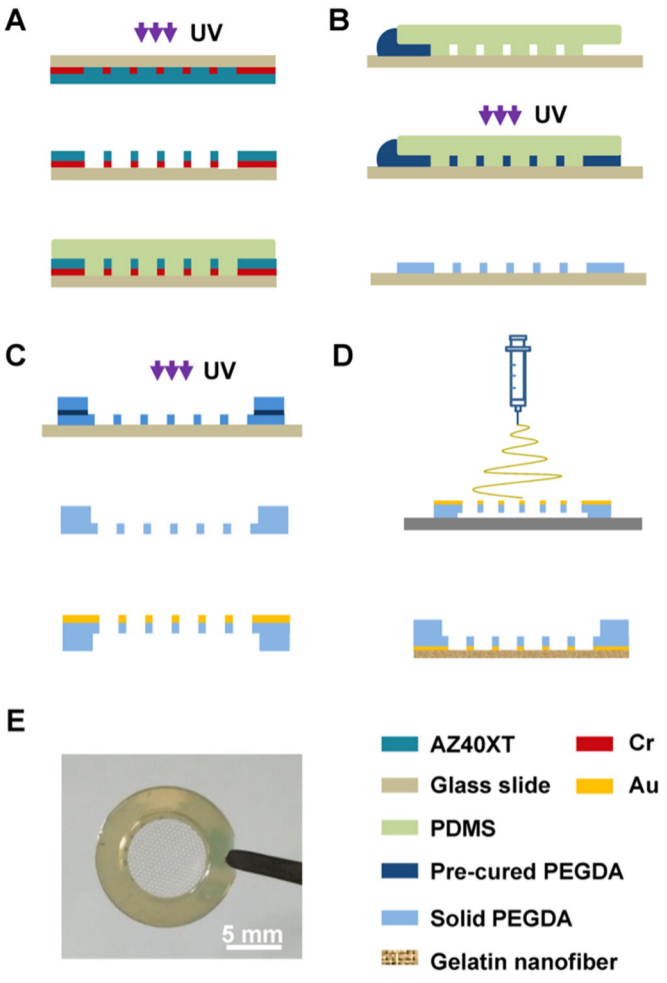

Fig. 1. Culture patch fabrication. (A) Mould fabrication by backside UV exposure and PDMS casting; (B) Fabrication of PEGDA honeycomb microframe by aspiration-assisted moulding. (C) PEGDA ring mounting and backside Au deposition. (D) Electrospinning of gelatin nanofibers. (E) Photograph of a culture patch handled with a tweezer.

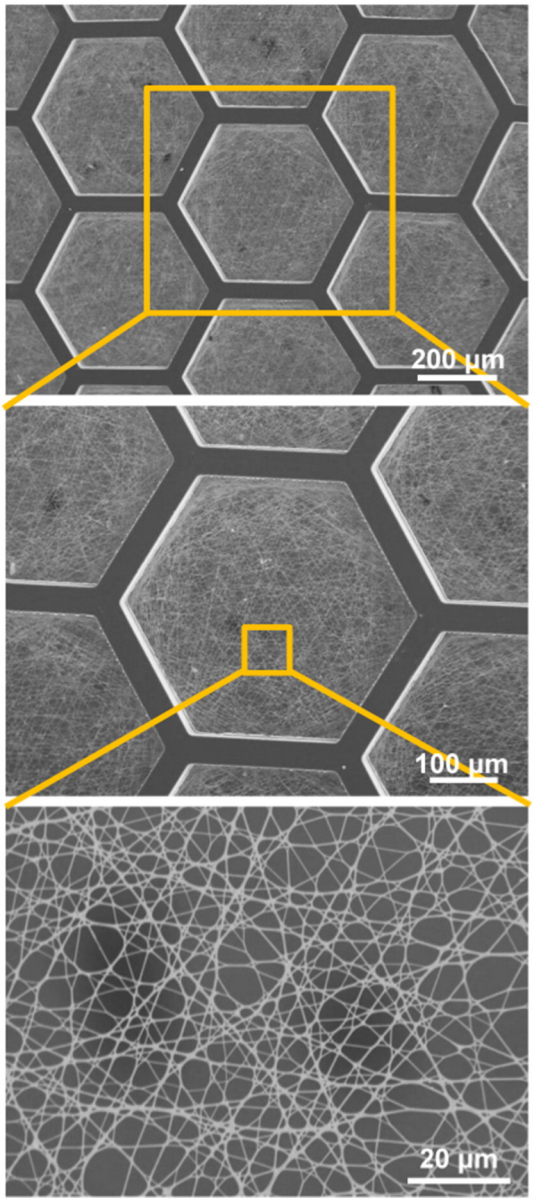

Fig. 2. SEM images of a culture patch. After electrospinning and crosslinking, the nanofibers on PEGDA microframe formed a high porosity nanonet with pore sizes smaller than 8 μm.

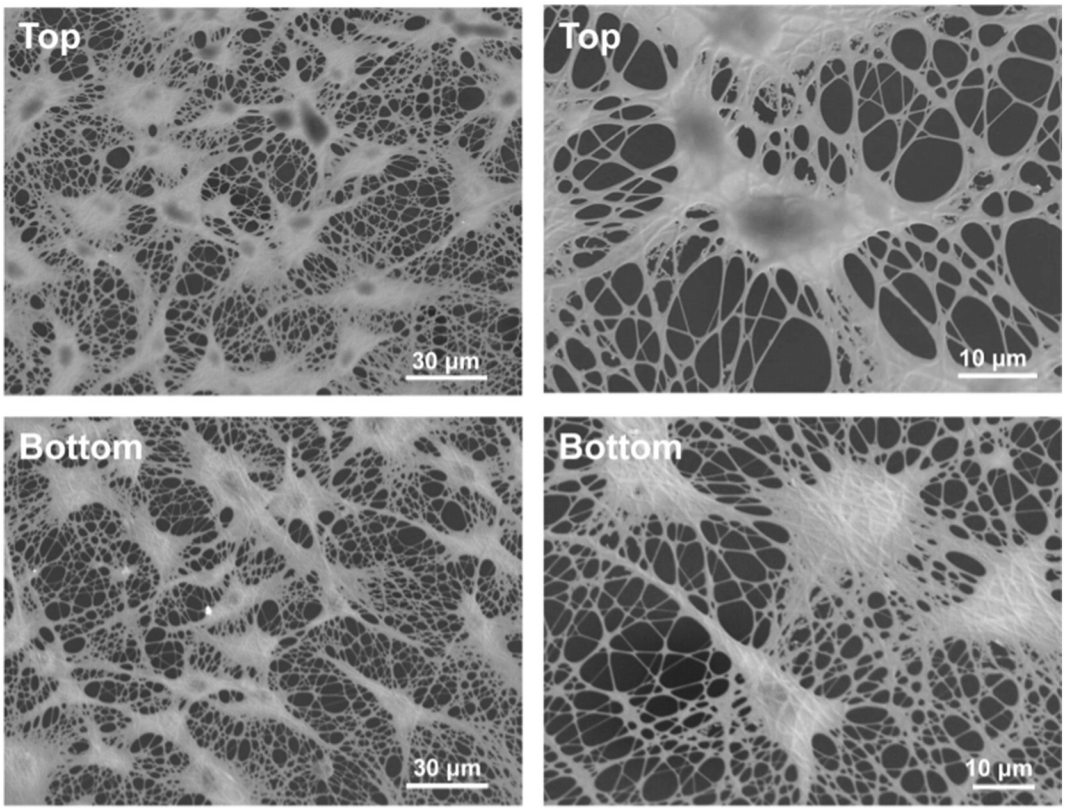

Fig. 3. Top- and bottom-view SEM images of U87 cells on a culture patch after 48 h culture, respectively.

number over the total area. In our case, the cell number inside the compartment deviated from the homogenously distributed one,

$$\%\Delta n_{cell} = \frac{nCell_{in} - ExpCell}{ExpCell} \times 100 \quad (3)$$

can then be used to estimate the preferential cell localization inside or outside the honeycomb compartment.

2.6. Statistical analysis

Data are shown as the mean ± s.e.m from at least three neuronal cultures. For the morphological analysis of immunofluorescence images, n refers to the number of images analysed, and the number in brackets refers to total number of cells analysed. All the cells were counted not in the entire field of view, but considering the hexagon of the patch as a unit. The quantified activity (frequency and Cross-correlation) and morphological data were analysed with Student's-*t*-test or Mann-Whitney test using the software SygmaPlot 10.0. The number of replicates and statistical tests used for each experiment are mentioned in the respective figure legends or in the Results. Significance was set to $^{*}p < 0.05$, $^{**}p < 0.01$ and $^{***}p < 0.001$.

3. Results and discussion

The culture patch can be easily handled with a tweezer (Fig. 1E), facilitating a large number of biological analyses. After crosslinking, the electrospun gelatin nanofibers exhibited a net structure (Fig. 2) with a nanofiber diameter of about 500 nm and pore sizes of <8 μm [15,16]. These pore sizes are sufficiently small to support cell growth but large enough to ensure a minimal exogenous material contact and a maximal exposure to the culture medium of the cells.

We firstly cultured brain-original glioblastoma U87-MG cells on the culture patch. Due to the comparable material density to the culture medium, the culture patch could be immerged in the medium but has no tight contact with the surface of the medium container, suggesting an off-ground culture condition. Fig. 3 shows SEM images of U87-MG cells after 2 days' culture on a patch. Unlike in conventional culture, the most of cells on the patch were entirely exposed to medium. We found, however, that the nuclei were mostly on the topside of the nanofibers, due probably to the fact that the pore sizes of the patch are smaller than that of nuclei so that no cell migrates to the bottom side of nanofibers. Interestingly, the spreading of cells was largely conditioned by the morphology of nanofibers, and the nanofibers could be wrapped due to cell-fiber interaction. This would suggest an outstanding compatibility of our culture patch to the cells.

Next, hippocampal neurons were isolated from postnatal wistar rats (P1-P3) and seeded on both Matrigel/laminin coated culture patch and glass slide for comparison. In order to examine the relative abundance of neurons and glial cells, cultures were stained with antibodies for neurons with TUJ1 and for glial cells with glial fibrillary acidic protein (GFAP) after 8– 10 days *in vitro* (DIV). Fig. 4A and B show GFAP staining images of the astrocytes cultured in normal FBS culture medium. Clearly, the morphology of the astrocytes on patch is significantly different from that on glass and the majority of the cells on patch show a stellate-shaped morphology, which looks *in vivo* like [18]. However, the astrocytes on glass have flat cell morphology with very few branches (Fig. 4C).

The results of primary neuron culture using ACM are shown in Fig. 5. Here, glial cells adhered well to both culture patch and glass on which neuron networks could be formed (Fig. 5A & B). Now, astrocytes on both culture patch and glass are more *in vivo* like, although some flat astrocytes were still observed on glass. It can also be noted that in such a case the percentage of other types of cells over neurons is significant larger on patch than on glass (Fig. 5C). Interestingly, we found that

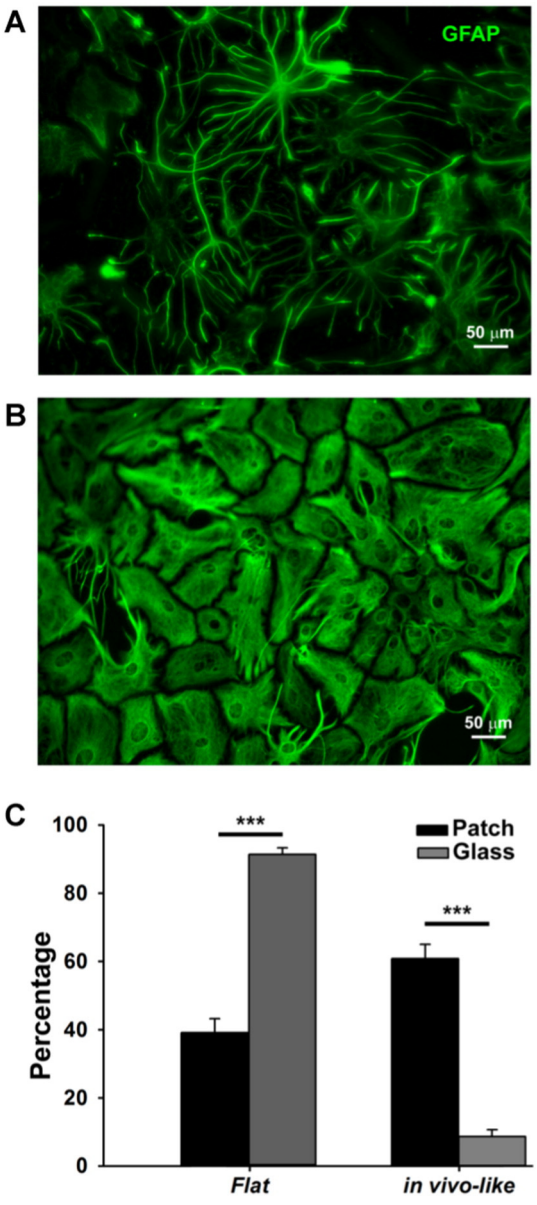

Fig. 4. (A, B) Immunofluorescence images of hippocampal neurons after 8– 10 DIV in FBS culture medium on a culture patch (A) and a glass (B) respectively, stained with glial fibrillary acidic protein (GFAP, green). (C) Percentage of astrocytes with flattened and *in vivo* like morphology on culture patch and on glass respectively (n = 130 cells on patch and n = 247 cells on glass from 4 experiments; p < 0.001 Student's-t-test). (For interpretation of the references to color in this figure legend, the reader is referred to the web version of this article.)

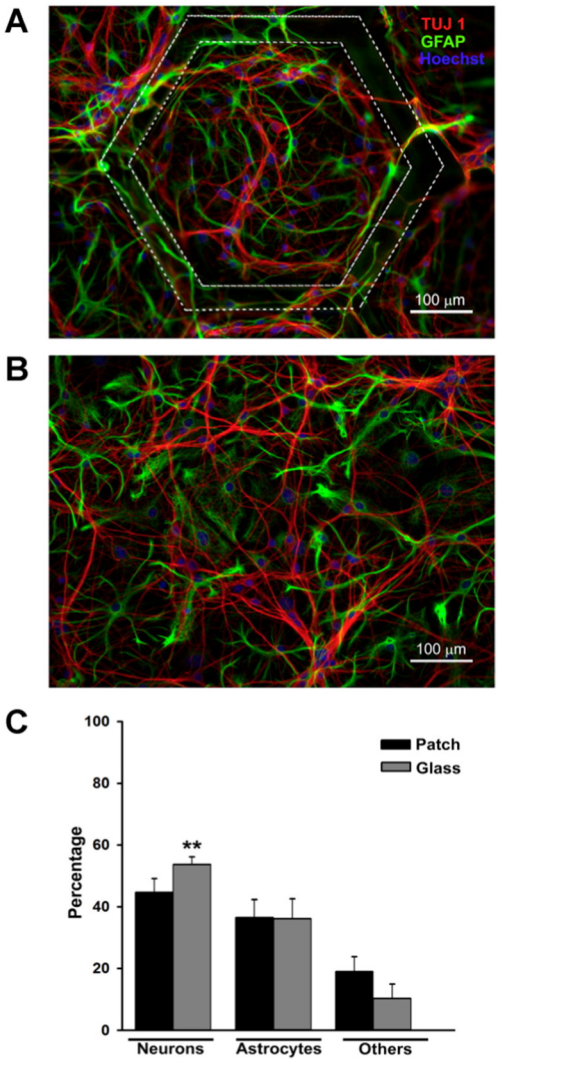

Fig. 5. (A, B) Immunofluorescence images of hippocampal neurons after 8– 10 DIV in astrocyte conditioned medium on culture patch (A) and on glass (B) respectively, stained with TUJ1 (red), GFAP (green) and Hoechst 33342 (blue). (C) Proportion of neurons (TUJ1-positive) and astrocytes (GFAP-positive) on culture patch and on glass respectively. TUJ1- and GFAP-negative cells are referred to as "other". ($n = 691$ cells from 8 experiments for culture patch; $n = 407$ cells from 7 experiments for glass; $p < 0.01$ Student's-*t*-test). (For interpretation of the references to color in this figure legend, the reader is referred to the web version of this article.)

neurons on patch are more likely located on the porous area of the honeycomb compartment than on the frame ($+12.4 \pm 3.9\%$ deviation of the cell number inside the honeycomb compartment from the expected value of homogenously distribution).

The spontaneous electrical activity of hippocampal neurons cultured on both type of substrates was recorded by Calcium imaging. The fluorescence images of Fluo-4-loaded neurons cultured on patch and on glass were shown in Fig. 6A and B respectively. Neural activity was evaluated by recording their calcium transients (DF/F) in fluorescence images at 3– 10 Hz for 10– 20 min (Fig. 6C and D). The neural activity on culture patch was ~20% more frequent than that on glass (Fig. 6E), even though the amount of neurons on patch was fewer (Fig. 5C). The synchronization of neural signals could be represented by the mean correlation coefficient of the calcium transients. However, the synchrony of neural activity did not show obvious difference on patch and on glass (Fig. 6F). Overall, we believe that the culture patch is reliable for primary neuron culture, due to its ECM like morphology and enhanced exposure of the cells to the culture medium.

4. Conclusion

We have demonstrated a culture patch method for culture of primary hippocampal neurons. This method is advantageous over the conventional culture dish methods since it allows not only minimizing the cell-exogenous materials contact but also maximizing the cell-medium exchange under off-ground culture conditions. We found that astrocytes on patch exhibited much more *in vivo* like morphologies comparing to that on a glass slide. We also found that neurons were more active on the patch than on glass. Finally, we believe that our culture patch method is flexible to sample manipulation, monitoring and other types of assays.

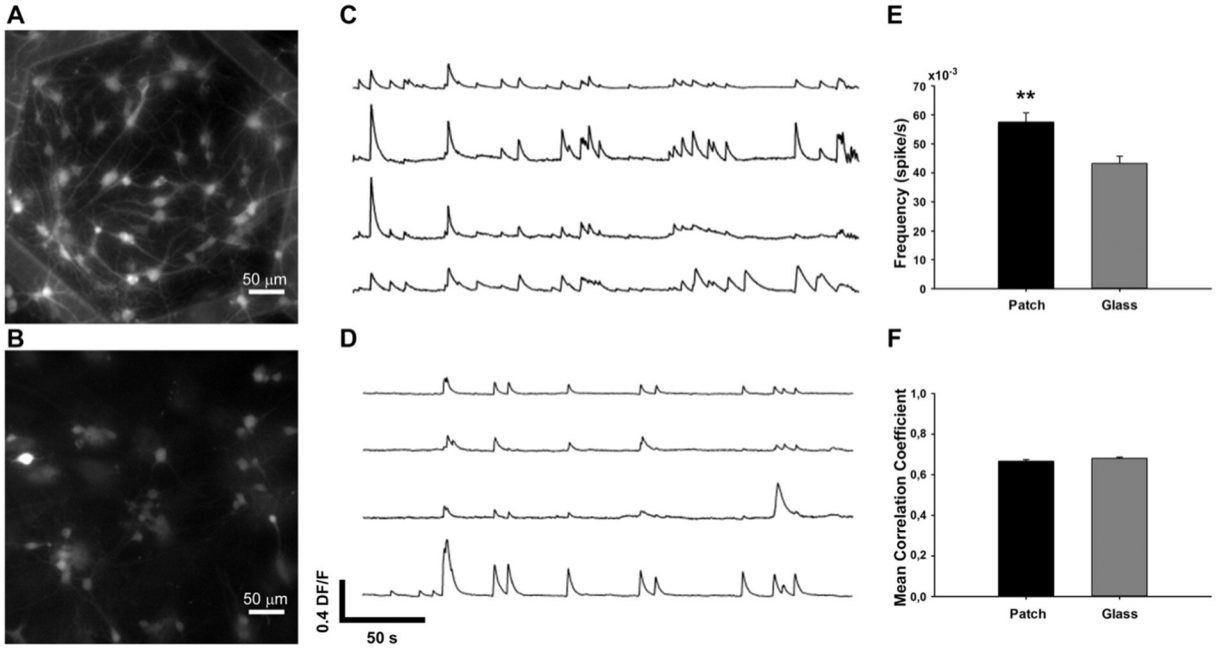

Fig. 6. (A, B) Fluorescence images of neuronal cultures loaded with 4 μM Fluo-4-AM calcium indicator on culture patch (A) and on glass (B), respectively. (C, D) Calcium transients on culture patch (C) and on glass (D) respectively, for 4 selected neurons. (E) Frequency of neural spikes on culture patch and on glass, respectively ($n = 110$ neurons from 8 experiments for culture patch; $n = 70$ neurons from 3 experiments for glass; $p < 0.01$ Mann-Whitney test). (F) Mean correlation coefficient of the calcium transients and slow calcium signals ($n = 599$ couple of neurons from 8 experiments for culture patch; $n = 782$ couple of neurons from 3 experiments for glass).

Acknowledgment

This work was supported by the European Commission under contract No.604263 (Neuroscaffolds) and Agence de Recherche Nationale under contract No ANR-13-NANO-0011-01 (Pillarcell) and ANR-12-RPIB-0015 (CardiacPatch).

References

[1] S. Kaech, G. Banker, Culturing hippocampal neurons, Nat. Protoc. 1 (5) (2006) 2406–2415.
[2] J. Ray, D.A. Peterson, M. Schinstine, F.H. Gage, Proliferation, differentiation, and long-term culture of primary hippocampal neurons, Proc. Natl. Acad. Sci. 90 (8) (1993) 3602–3606.
[3] K. Jayalakshmi, M. Sairam, S. Singh, S. Sharma, G. Ilavazhagan, P. Banerjee, Neuroprotective effect of *N*-acetyl cysteine on hypoxia-induced oxidative stress in primary hippocampal culture, Brain Res. 1046 (1) (2005) 97–104.
[4] J. Nunez, Primary culture of hippocampal neurons from P0 newborn rats, J. Vis. Exp. (19) (2008) e895.
[5] E.V. Jones, D. Cook, K.K. Murai, A Neuron-astrocyte co-culture System to Investigate Astrocyte-secreted Factors in Mouse Neuronal Development, Astrocytes: Methods and Protocols, 2012 341–352.
[6] J.L. Bourke, H.A. Coleman, V. Pham, J.S. Forsythe, H.C. Parkington, Neuronal electrophysiological function and control of neurite outgrowth on electrospun polymer nanofibers are cell type dependent, Tissue Eng. A 20 (5-6) (2013) 1089–1095.
[7] K. Saha, A.J. Keung, E.F. Irwin, Y. Li, L. Little, D.V. Schaffer, K.E. Healy, Substrate modulus directs neural stem cell behavior, Biophys. J. 95 (9) (2008) 4426–4438.
[8] C. Lutton, B. Goss, Caring about microenvironments, Nat. Biotechnol. 26 (6) (2008) 613–614.
[9] D.B. Edelman, E.W. Keefer, A cultural renaissance: in vitro cell biology embraces three-dimensional context, Exp. Neurol. 192 (1) (2005) 1–6.
[10] K.S. Rho, L. Jeong, G. Lee, B.-M. Seo, Y.J. Park, S.-D. Hong, S. Roh, J.J. Cho, W.H. Park, B.-M. Min, Electrospinning of collagen nanofibers: effects on the behavior of normal human keratinocytes and early-stage wound healing, Biomaterials 27 (8) (2006) 1452–1461.
[11] S.-J. Liu, Y.-C. Kau, C.-Y. Chou, J.-K. Chen, R.-C. Wu, W.-L. Yeh, Electrospun PLGA/collagen nanofibrous membrane as early-stage wound dressing, J. Membr. Sci. 355 (1) (2010) 53–59.
[12] C.C. Gertz, M.K. Leach, L.K. Birrell, D.C. Martin, E.L. Feldman, J.M. Corey, Accelerated neuritogenesis and maturation of primary spinal motor neurons in response to nanofibers, Dev. Neurobiol. 70 (8) (2010) 589–603.
[13] L. Liu, M. Yoshioka, M. Nakajima, A. Ogasawara, J. Liu, K. Hasegawa, S. Li, J. Zou, N. Nakatsuji, K.-i. Kamei, Nanofibrous gelatin substrates for long-term expansion of human pluripotent stem cells, Biomaterials 35 (24) (2014) 6259–6267.
[14] S. Li, J. Shi, L. Liu, J. Li, L. Jiang, C. Luo, K. Kamei, Y. Chen, Fabrication of gelatin nanopatterns for cell culture studies, Microelectron. Eng. 110 (2013) 70–74.
[15] Y. Tang, L. Liu, J. Li, L. Yu, F.P.U. Severino, L. Wang, J. Shi, X. Tu, V. Torre, Y. Chen, Effective motor neuron differentiation of hiPSCs on a patch made of crosslinked monolayer gelatin nanofibers, J. Mater. Chem. B 4 (19) (2016) 3305–3312.
[16] Y. Tang, L. Liu, J. Li, L. Yu, L. Wang, J. Shi, Y. Chen, Induction and differentiation of human induced pluripotent stem cells into functional cardiomyocytes on a compartmented monolayer of gelatin nanofibers, Nanoscale 8 (30) (2016) 14530–14540.
[17] F.P.U. Severino, J. Ban, Q. Song, M. Tang, G. Bianconi, G. Cheng, V. Torre, The role of dimensionality in neuronal network dynamics, Sci. Rep. 6 (2016).
[18] D.D. Wang, A. Bordey, The astrocyte odyssey, Prog. Neurobiol. 86 (4) (2008) 342–367.

4.2.

Fabrication of PDMS microlattices for three-dimensional cell culture

S. Li[+], F.P. Ulloa Severino[+], J. Ban, L. Wang, G. Pinato, V. Torre and Y. Chen

In Preparation

Improved neuron culture using scaffolds made of three-dimensional PDMS micro-lattices

Sisi Li[a‡], Francesco Paolo Ulloa Severino[b‡], Jelena Ban[b], Li Wang[a] , Giulietta Pinato[b], Vincent Torre[b] and Yong Chen[a*]

[a]*Ecole Normale Supérieure, PSL Research University, Département de Chimie, CNRS UMR 8640 PASTEUR, 75005 Paris, France*

[b]*Neurobiology Sector, International School for Advanced Studies (SISSA), via Bonomea, 265, 34136 Trieste, Italy*

[‡]*These authors contributed equally to this work*

Abstract: Tissue engineering strives to create functional components of organs with different cell types *in vitro*. One of the challenges is to fabricate scaffolds for three-dimensional (3D) cell culture under physiological conditions. Of particular interest is to investigate the morphology and function of the central nervous system (CNS) cultured using such scaffolds. Here, we used an elastomer, polydimethylsiloxane (PDMS), to produce 3D lattice-type scaffolds from a photolithography defined template. The photomask with antidot arrays was spin-coated with a thick resist layer and downward mounted on an inclined rotating stage. After exposure for three or more times at UV different incident angles and development, a 3D photoresist template was obtained. Then, it was casted with a pre-polymer mixture of PDMS and cured, resulting in lattice-type PDMS features after resist etching. Culture tests were performed with NIH-3T3 cells and rat primary hippocampal neurons, showing homogenously cell infiltration and 3D attachment as well as larger cell numbers than 2D cultures. We also found a higher neuron to astrocyte ratio and a better cell ramification in 3D comparing to the conventional culture, thereby improving the growth of neurons and the formation of neuronal networks.

Keywords: Biofabrication, Scaffold, PDMS, Neuron

* Corresponding author. Ecole Normale Supérieure, 24 rue Lhomond, 75231 Paris, France. Tel.: +33 1 44322421; Fax: +33 1 44322402. E-mail address: yong.chen@ens.fr (Y. Chen).

1. Introduction

Cell adhesion, migration, proliferation and differentiation are guided by topographic and biochemical cues, which can now be engineered *in vitro* by sophisticated technologies [1]. The previous studies, however, were mostly devoted to the two-dimensional (2D) patterns using photolithography, soft-lithography, nanoimprint lithography and similar techniques [2-4]. Alternatively, non-lithographic techniques such as electrospinning, solvent casting, particulate leaching, etc. have been used to produce stochastic scaffolds [5-7]. More recently, 3D plotting [8-11], fused deposition molding [12, 13], stereo-lithography [14-16], self-propagating photopolymer waveguide processing [17-20], etc., are emerged as rapid prototyping techniques. These techniques are promising but generally of low resolution [21], time-consuming [22], or not biocompatible for advanced cell assays [23].

In this work, we fabricated well-defined three-dimensional (3D) micro-lattice as scaffolds for neuronal cultures using conventional photolithography and soft-lithography techniques. Polydimethylsiloxane (PDMS), a widely used elastomer for casting and microfluidic device making, has been chosen because of its non-toxic and easy-processing properties [24-26]. In addition, the Young's module of PDMS is relatively low (0.4 - 4 MPa) and it can be regulated by changing the ratio between catalytic and basic components [27, 28]. Furthermore, the effective Young's module of the substrates made of PDMS micropillars or micro-tripods can be adjusted to match the tissue stiffness (e.g. <1KPa for brain slices) [29]. The fabrication of 3D PDMS scaffolds by layer-by-layer construction has already been reported, showing the relevance of the scaffolds for culture studies [30]. Our technique is straightforward and less time-consuming. The conventional photolithography is used to produce 3D templates in a thick layer of resist by backside exposure with an UV light at defined incident angles. Soft lithography is used to cast PDMS into the resist templates, resulting in lattice-type PDMS features after the resist etching. The lattice parameters, i.e. thickness, indication angle and node-to-node space of the lattice units, are adjustable to produce symmetrical and asymmetrical 3D features. The PDMS replica with different geometry parameters are then used to culture NIH-3T3 cell line and rat primary hippocampal neurons. We show that the 3D PDMS micro-lattices improved the survival and growth of cells as well as the formation of neuron networks.

2. Experimental methods

Chemicals and materials: AZ40XT photoresist and AZ developer 726MIF developer were purchased from MicroChemicals GmbH. Chrome photoplates coated with AZ1518 photoresist @ 5300 Å thickness were from Nanofilm Inc, USA. PDMS (RTV615 Kit) was from Momentive. Fibronectin (FN) was from Biopur AG. Dulbecco's minimum essential medium (DMEM), L-glutamine, penicillin/streptomycin (P/S), 0.05% Trypsin-EDTA, Dulbecco's modified phosphate-buffered saline (DPBS), PBS tablets, minimum essential medium (MEM), fetal bovine serum (FBS), gentamycin, goat anti mouse immunoglobulin (Ig) G1 Alexa Fluor® 488 and goat anti-mouse IgG2a Alexa Fluor® 594 were purchased from Life Technologies. Rhodamine B, fungizone, paraformaldehyde (PFA), Triton-X-100 (TX), bovine serum albumin (BSA), sodium azide, 4,6-diamidino-2-phenylindole (DAPI), Hoechst 33342, fluorescein isothiocyanate (FITC)-labelled Phalloidin, poly-L-ornithin, D-glucose, Hepes, apo-transferrin, insulin, D-biotin, vitamin B12, cytosine-β-D-arabinofuranoside (Ara-C), glial fibrillary acidic protein (GFAP) were all purchased from Sigma-Aldrich, Matrigel was purchased from Corning, anti-β-tubulin III (TUJ1) antibodies were purchased from Covance.

Fabrication of 3D templates: The photolithography process was described in **Fig. 1a**. A homemade rotating stage was fixed under collimated UV light with a 45° angle of inclination (**Fig. 1b**). An array of antidote was created on a chrome mask using a micro pattern generator (μPG 101, Heidelberg, Germany). Then, AZ40XT photoresist was spin-coated on the chrome mask at a speed of 1800 rpm for 20 s to reach a thickness of approximately 40 μm. After baking on a hot plate at 126 ℃ for 7 min, it was mounted on the rotation stage with the photoresist downward for backside UV exposure. Each exposure was performed for 90 s with a UV beam at 365 nm (9.2 mW/cm^2). The stage was rotated after each exposure along the major axis of the mask surface to have an equal incident angle. After soft baking at 105 ℃ for 2 min, the resist was developed in AZ726MIF developer for 2 min and rinsed with deionized (DI) water, resulting in a 3D porous template as shown in the inserted SEM image of **Fig. 1c.**

Pattern transfer: A pre-polymer of PDMS mixture at 1:5 ratio was poured on the porous template and degassed in vacuum to remove the bubbles. After solidification at 80 ℃ for 2 h, the AZ resist was dissolved in acetone with ultrasonic (80 mW, 20 min). PDMS layer was then separated from the Cr mask, resulting in a 3D truss structures adhered to the bottom substrate (**Fig.1d**).

SEM imaging: The fabricated AZ templates, the PDMS replica and the PDMS replica with cells

were sputter-coated (Quorum technologies Sputter K675XD) with 5 nm gold and observed under a scanning electron microscope (Hitachi S-800) operated at 10 kV.

NIH-3T3 cell culture: The 3D PDMS lattice was sterilized with autoclave at 120 ℃ for 30 min. After drying in an oven at 120 ℃ for 2 h, it was treated with plasma (Plasma Cleaner, Harrick) for 3 min and incubated in 50 μg/ml fibronectin in DPBS at room temperature for 30 min. NIH-3T3 cells were prepared in a culture flask in 37 ℃ incubator with 5% CO_2. The culture medium is DMEM consisting 10% FBS, 1% L-glutamine, 0.1% P/S and 0.01% fungizone. After dissociation in a 0.05% Trypsin-EDTA solution and centrifugation, cells were seeded on the surface of PDMS lattice at a density of 1×10^4 cells/cm^2.

Hippocampal neuron culture: Hippocampal neurons from Wistar rats (P2-P3) were prepared in accordance with the guidelines of the Italian Animal Welfare Act, and their use was approved by the Local Veterinary Service, the SISSA Ethics Committee board and the National Ministry of Health (Permit Number: 630-III/14) in accordance with the European Union guidelines for animal care (d.1.116/92; 86/609/C.E.). The animals were anaesthetized with CO_2 and sacrificed by decapitation, and all efforts were made to minimize suffering.

All substrates (2D glass coverslips, 2D PDMS and 3D PDMS) were treated with air plasma-cleaner in order to facilitate cell adhesion and at the end sterilized with an UV lamp. Soon after the substrates were coated with 50 μg/ml poly-L-ornithine overnight and coated with Matrigel just before cells seeding. Dissociated cells were plated at a concentration of 6×10^5 cells/ml on all the substrates in MEM with GlutaMAXTM supplemented with 10% FBS, 0.6% D-glucose, 15 mM Hepes, 0.1 mg/ml apo-transferrin, 30 μg/ml insulin, 0.1 μg/ml D-biotin, 1 μM vitamin B12, and 2.5 μg/ml gentamycin. After 48 hours, 2 μM Ara-C was added to the culture medium to block glial cell proliferation, and the concentration of FBS was decreased to 5%. Half of the medium was changed every 2–3 days. The neuronal cultures were maintained in an incubator at 37 ℃, 5% CO_2 and 95% relative humidity.

Confocal imaging of PDMS lattice and NIH-3T3 cells: Before cell loading, the PDMS lattice was treated with plasma for 3 min and immerged in 100 mM Rhodamine B in DI water for overnight. NIH-3T3 cells were fixed in 4% PFA for 30 min and then permeabilized in PBS containing 0.5% TX for 30 min. After blocked in blocking buffer (0.1% TX, 3% BSA, 0.1% sodium azide in PBS) for 30 min again, cell skeleton and nuclei were stained with 5 μg/mL phalloidin-FITC and 300 nM DAPI in PBS for 30min, respectively. All the procedures were operated at room temperature and there were

PBS rinsing three times between each solution change. The samples were imaged under the Carl Zeiss laser scanning microscopes LSM 710.

Morphological and immunocytochemical analysis. Cells were fixed in 4% paraformaldehyde containing 0.15% picric acid in PBS, saturated with 0.1 M glycine, permeabilized with 0.1% Triton X-100, saturated with 0.5% BSA in PBS and then incubated for 1 h with primary antibodies: mouse monoclonal GFAP and anti-β-tubulin III (TUJ1) antibodies. The secondary antibodies were goat anti mouse immunoglobulin (Ig) G1 Alexa Fluor® 488, goat anti-mouse IgG2a Alexa Fluor® 594, and the incubation time was 30 min. Nuclei were stained with 2 μg/ml in PBS Hoechst 33342 for 5 min. All the incubations were performed at room temperature (20–22 ℃). The cells were examined using a Leica DM6000 fluorescent microscope equipped with DIC and fluorescence optics, CCD camera and Volocity 5.4 3D imaging software (PerkinElmer, Coventry, UK). The fluorescence images were collected with a 40X magnification and 0.5 NA objective. Image J by W. Rasband (developed at the U.S. National Institutes of Health and available at http://rsbweb.nih.gov/ij/) was used for image processing.

3. Results and discussion

3.1 Fabrication of PDMS micro-lattices

Contact lithography is commonly used in research laboratories to replicate the 2D patterns by UV exposing a photoresist layer spin coated on a substrate through a photomask in direct contact with the resist. To reach the highest resolution and the best pattern stability, we spun coat a thick resist layer directly on the photomask and then performed the sequential steps with the same substrate until the release of the PDMS replica (**Fig. 1a**). Since all steps are bench process and the photomask can be used for many times, this fabrication technique remains straightforward and low cost.

The SEM image of the PDMS replica in **Fig.1d** shows a 3D lattice feature with tetrahedral-type unit-cell originated from the same aperture, defined by the antidote array on the 2D photomask and the three directional UV exposures. Since the symmetry, the porosity and the interconnectivity, may all affect the cell culture performance, we fabricated 3D lattices of PDMS with different parameters.

We firstly studied the pattern geometry by rotating 120 ° or 90 ° the sample stage after each exposure, resulting in a tripod structure (**Fig. 2a**) or a four-fold symmetry (**Fig. 2b**). Asymmetric

unit-cell can also be achieved by changing the rotation angle after each exposure. **Fig. 2c- 3e** show asymmetrical lattice structures by rotating the sample stage three times with angle of 60°-60°-240°, 90°-90°-180°, and 150°-150°-60° respectively. We also evaluated the fabrication performance by changing the resist thickness and the incident angle of the UV light. **Fig. 3a1** and **a2** show the SEM images of the PDMS lattices obtained with initial resist layer thickness of 40 μm and 25 μm, respectively. **Fig. 3b1** and **b2** show the SEM images of the PDMS lattices obtained with an UV incident angle is 60° and 45° respectively. As can be seen, the resulted beam angle of the structure is around 35° and 28°, respectively, which are in agreement with the calculation based on Snell' law.

The geometry of the PDMS lattices is primarily determined by the antidot diameter and pitch size of the photomask. **Fig. 4** shows the PDMS features obtained with triangle arrays of antidots with 4 μm diameter and three different pitch sizes: 11 μm (**Fig. 4a1** and **a2**), 14 μm (**Fig. 4b1** and **b2**) and 20 μm (**Fig. 4c1** and **c2**), respectively. For larger pitch sizes, the lattice feature collapses due to insufficient mechanical strength, as showed in **Fig. 4d**. By changing gradually the lattice spacing in the same mask, we could achieve a 3D gradient lattice as showed in **Fig. 4e**. Finally, the fabricated PDMS structures could be peeled off, making it possible to be used for other purposes such as microfluidic integration (**SI, Fig. S1**).

3.2 Biocompatibility test with NIH-3T3 cell line

We choose 40 μm-height and three-fold symmetric PDMS lattices with 6 μm diameter and 24 μm pitch size (**Fig. 5a**) for cell culture test. Before sterilization, we stained the PDMS lattice with Rhodamine (red) for easy structure observation under laser confocal microscopy. Then, we seeded NIH-3T3 cells on the lattice surface and cultured them for 2 days. We clearly observed adhesion and extension of actin filaments along the 3D lattice surface (**Fig. 5b and 5c)**. Here, actin filaments and nuclei were respectively stained by palloidin-FITC (green) and DAPI (blue). From **Fig. 5h-j**, we also observed the actin filaments crossed the free space of the 3D lattice features, which should be more tissue-like for *in vitro* studies. The 3D embedment of cell nuclei (**Fig. 5d**) and cell cytoskeleton (**Fig. 5e and 5f**) in the PDMS micro-lattice both provide the evidence of 3D cell features, not like often observed flatten features in 2D cultures. However, the shape of the nuclei could be deformed by reducing the pitch size of the lattice and this deformation is inversely proportional to the spacing between the lattice features **(Fig. 5g)**. Previously, it has been shown that both stem cell proliferation and differentiation were correlated to the cell shape [31, 32]. The PDMS lattices with defined geometry could be potentially applied in stem cell research.

3.3 Culture of primary hippocampal neurons

Primary hippocampal neurons are commonly used to study 3D network formation on substrates made by different materials [7, 33]. Here, we used hippocampal neurons from rats to co-culture neurons and astrocytes and show the possibility of a 3D neuronal network formation with the help of a PDMS lattice of 15 μm diameter, 18 μm pitch size and ~40 μm heights (**Fig. 6**). Cells were homogeneously distributed on the structure (**Fig. 6a**) and were able to form an interconnected and mature network after 8 days *in vitro* (DIV) (**Fig. 6b**). From the SEM images both glia cells (**Fig. 6c**) and neurons (**Fig. 6d**) showed a three-dimensional morphology characterized by rounder cell body and neurites projected in all the directions. Glia cells show a flat but ramified morphology whereas neurons have thinner processes (**Fig. 6e**) that, once contacted the surface either of other cells or of the PDMS, highly ramify. These details show a good interaction between cells and material that is extremely important in tissue engineering. Moreover, in **Fig. 6a** and 6**b** is possible to observe slightly bended pillars. This phenomenon appears only in presence of cells and is due to the adhesion forces that cells apply to the substrates. Once known the Young's module and all the parameters of the substrates, these can be used as a device to measure cell adhesion forces [34, 35].

Immunostaining for neuronal and astrocytes markers, TUJ-1 and GFAP respectively (**Fig. 7**), confirmed the observation made from the SEM images. Compared to the standard glass (**SI Fig.S2**) and to the flat 2D PDMS substrates (**Fig. 7a**), on the 3D PDMS substrates (**Fig. 7b**), we can observe a complex morphological ramification of both neurons and astrocytes. Besides, we found a higher number of cells (213 cell/mm^2, 223 cell/mm^2 and 1150 cell/mm^2 respectively) on 3D PDMS lattice and we can infer that this difference is due to the three-dimensionality of the substrates which offer more surfaces where cells can adhere. On the 3D PDMS the 59.6% of these cells are neurons and 26.9% are astrocytes, the remained part is not identified cells (e.g. microglia).

The significant difference in the number of neurons and astrocytes, compared to the 2D substrates (Glass: 33.3% of neurons, 59.2% of astrocytes; 2D PDMS: 40% of neurons, 58% of astrocytes) has a high degree of confidence (**Fig 6c-d**). Finally both neurons and astrocytes are visibly more ramified compared to the other 2D substrates. All these data show that 3D PDMS substrate offer a good platform to reconstruct a three-dimensional *in vitro* neuronal network with ramified, *in vivo*-like morphology, thanks to more appropriate topographical cues and elastic properties compared to the bare glass and flat 2D PDMS. Therefore, we can assess that the

3D-PDMS improve the survival and growth of the neurons and support the network formation and maturation. By controlling the lithography parameters, the PDMS lattice could be separated from the substrate (**Supp.Fig.2**), which shows its potential for the application in tissue engineering and transplantation.

4. Conclusion

We have studied the fabrication process of PDMS micro-lattices using backside photolithography at different incident angles and soft lithography for 3D casting. The fabricated 3D lattices were used to evaluate cell culture performance using NIH-3T3 cell line and primary hippocampal neurons of rats. Homogenously cell infiltration and 3D attachment were observed with increased cell number, increased neuron to astrocyte ratio, and improved cell ramification comparing to the 2D culture. Since the geometry and the interconnectivity of the PDMS lattice could be precisely controlled, more systematic studies can be developed. The proposed fabrication process is straightforward but yet simple and low cost, thereby holding a high potential for future cell-based assays.

Acknowledgments

This work was supported by European Commission through project contract No. 604263 (Neuroscaffolds) and Agence de Recherche Nationale under contract No. ANR-13-NANO-0011-01 (Pillarcell). We want to thank also Mattia Fanetti for his assistance during the SEM imaging sessions.

References

1. Théry, M., et al., *The extracellular matrix guides the orientation of the cell division axis*. Nature cell biology 2005, **7** (10): p. 947-953.
2. Kidambi, S., et al., *Cell adhesion on polyelectrolyte multilayer coated polydimethylsiloxane surfaces with varying topographies.* Tissue engineering, 2007. **13**(8): p. 2105-2117.
3. Karuri, N.W., et al., *Biological length scale topography enhances cell-substratum adhesion of human corneal epithelial cells.* Journal of cell science, 2004. **117**(15): p. 3153-3164.
4. Li, S., et al., *Fabrication of gelatin nanopatterns for cell culture studies.* Microelectronic Engineering, 2013. **110**: p. 70-74.
5. Shen, F., et al., *A study on the fabrication of porous chitosan/gelatin network scaffold for tissue engineering.* Polymer international, 2000. **49**(12): p. 1596-1599.
6. Sherwood, J.K., et al., *A three-dimensional osteochondral composite scaffold for articular cartilage repair.* Biomaterials, 2002. **23**(24): p. 4739-4751.
7. Tang, Y., et al., *Patch method for culture of primary hippocampal neurons.* Microelectronic Engineering, 2017. **175**: p. 61-66.
8. Landers, R. and R. Mülhaupt, *Desktop manufacturing of complex objects, prototypes and biomedical scaffolds by means of computer‐assisted design combined with computer‐guided 3D plotting of polymers and reactive oligomers.* Macromolecular Materials and Engineering, 2000. **282**(1): p. 17-21.
9. Landers, R., et al., *Fabrication of soft tissue engineering scaffolds by means of rapid prototyping techniques.* Journal of materials science, 2002. **37**(15): p. 3107-3116.
10. Ang, T., et al., *Fabrication of 3D chitosan–hydroxyapatite scaffolds using a robotic dispensing system.* Materials Science and Engineering: C, 2002. **20**(1): p. 35-42.
11. Landers, R., et al., *Rapid prototyping of scaffolds derived from thermoreversible hydrogels and tailored for applications in tissue engineering.* Biomaterials, 2002. **23**(23): p. 4437-4447.
12. Zein, I., et al., *Fused deposition modeling of novel scaffold architectures for tissue engineering applications.* Biomaterials, 2002. **23**(4): p. 1169-1185.
13. Hutmacher, D.W., et al., *Mechanical properties and cell cultural response of polycaprolactone scaffolds designed and fabricated via fused deposition modeling.* Journal of biomedical materials research, 2001. **55**(2): p. 203-216.
14. Bertsch, A., H. Lorenz, and P. Renaud, *3D microfabrication by combining microstereolithography and thick resist UV lithography.* Sensors and Actuators A: Physical, 1999. **73**(1): p. 14-23.
15. Melchels, F.P., et al., *Mathematically defined tissue engineering scaffold architectures prepared by stereolithography.* Biomaterials, 2010. **31**(27): p. 6909-6916.
16. Lee, K.-W., et al., *Poly (propylene fumarate) bone tissue engineering scaffold fabrication using stereolithography: effects of resin formulations and laser parameters.* Biomacromolecules, 2007. **8**(4): p. 1077-1084.
17. Schaedler, T.A., et al., *Ultralight metallic microlattices.* Science, 2011. **334**(6058): p. 962-965.
18. Kisailus, D., A.J. Jacobsen, and C. Zhou, *Three-dimensional biological scaffold and method of making the same*. 2013, Patent US8541015.

19. Jacobsen, A.J., *Optically oriented three-dimensional polymer microstructures*. 2010, Patent US7653279
20. Kisailus, D., A.J. Jacobsen, and C. Zhou, *Three-dimensional biological scaffold compromising polymer waveguides*. 2012, Patent US 8287895.
21. Zhang, B., et al., *3D printing of high-resolution PLA-based structures by hybrid electrohydrodynamic and fused deposition modeling techniques.* Journal of Micromechanics and Microengineering, 2016. **26**(2): 025015.
22. Bassoli, E., et al., *3D printing technique applied to rapid casting.* Rapid Prototyping Journal, 2007. **13**(3): p. 148-155.
23. Renbutsu, E., et al., *Preparation and biocompatibility of novel UV-curable chitosan derivatives.* Biomacromolecules, 2005. **6**(5): p. 2385-2388.
24. Kane, R.S., et al., *Patterning proteins and cells using soft lithography.* Biomaterials, 1999. **20**(23): p. 2363-2376.
25. Singhvi, R., et al., *Engineering cell shape and function.* Science, 1994. **264**(5159): p. 696-698.
26. Takayama, S., et al., *Patterning cells and their environments using multiple laminar fluid flows in capillary networks.* Proceedings of the National Academy of Sciences, 1999. **96**(10): p. 5545-5548.
27. Wang, Z., A.A. Volinsky, and N.D. Gallant, *Crosslinking effect on polydimethylsiloxane elastic modulus measured by custom‐built compression instrument.* Journal of Applied Polymer Science, 2014. **131**(22).
28. Johnston, I., et al., *Mechanical characterization of bulk Sylgard 184 for microfluidics and microengineering.* Journal of Micromechanics and Microengineering, 2014. **24**(3): p. 035017.
29. Migliorini, E., et al., *Acceleration of neuronal precursors differentiation induced by substrate nanotopography.* Biotechnology and bioengineering, 2011. **108**(11): p. 2736-2746.
30. Mata, A., et al., *A three-dimensional scaffold with precise micro-architecture and surface micro-textures.* Biomaterials, 2009. **30**(27): p. 4610-4617.
31. Kumar, G., et al., *The determination of stem cell fate by 3D scaffold structures through the control of cell shape.* Biomaterials, 2011. **32**(35): p. 9188-9196.
32. Kumar, G., et al., *Freeform fabricated scaffolds with roughened struts that enhance both stem cell proliferation and differentiation by controlling cell shape.* Biomaterials, 2012. **33**(16): p. 4022-4030.
33. Severino, F.P.U., et al., *The role of dimensionality in neuronal network dynamics.* Scientific Reports, 2016. **6**. 29640.
34. Li, J., et al., *Culture substrates made of elastomeric micro-tripod arrays for long-term expansion of human pluripotent stem cells.* Journal of Materials Chemistry B, 2017. **5**(2): p. 236-244.
35. Fu, J., et al., *Mechanical regulation of cell function with geometrically modulated elastomeric substrates.* Nature methods, 2010. **7**(9): p. 733-736.

Figure caption

Figure 1 Fabrication of the PDMS 3D lattice. (a) The fabrication process flow; (b) Backside UV exposure at incident angles; (c) SEM top view of the fabricated AZ40XT 3D template and; (d) SEM side view of the replicated PDMS 3D lattices. The diameter of antidots on Cr mask is 4 μm diameter and the period is 18 μm. Scale bar is 10 μm.

Figure 2 SEM images of symmetrical and asymmetrical PDMS 3D lattices. (a) 3-fold symmetry; (b) 4-fold symmetry; Asymmetry with three side vertex angles: (c) 60°-60°-240°; (d) 90°-90°-180°; (e) 150°-150°-60°. Scale bar is 10 μm.

Figure 3 SEM images of PDMS 3D lattices obtained with initial resist layer thickness of 40 μm (a1) and 25μm (a2) and member incident angles of 35° (b1) and 28° (b2), respectively. Scale bar is 10 μm.

Figure 4 SEM images of PDMS 3D lattices with 4 μm diameter but different pitch sizes: (a) 11 μm; (b) 14 μm; (c) 20 μm; (d) 24 μm. (e) pitch size changing from 8.5 μm to 14.5 μm. (a1), (b1), (c1), (d) and (e) are top view images. (a2), (b2) and (c2) are side view images. Scale bar is 10 μm.

Figure 5 NIH-3T3 cells in PDMS 3D lattices after culture for 2 days. (a) 3D view of a confocal Z-stack of PDMS lattice of 6 μm diameter, 22 μm pitch size and 40 μm height. (b) 3D view of a confocal Z-stack of cell actin filaments adhered on the lattice surface. (c) Merged image of (a) and (b). (d) 3D view of a confocal Z-stack of cell nuclei trapped in the PDMS lattice of (a). (e) Enlarged image of (d) but rotated in 3D space to clearly show the cell nuclei 3D distribution in the PDMS lattice. (f) Nuclei shape of the cells in (e). (g) Z-slice of cells in the PDMS lattice of 4 μm diameter, 14 μm pitch size and 40 μm height. (h) Z-slice of cells in the PDMS lattice of (a). (i)(j) SEM images of actin filaments crossing the free space of the PDMS lattice.

Figure 6 Primary hippocampal neuron culture in PDMS 3D lattices: (a-b) SEM images of the cell embedment. (c-f) Enlarged view of the SEM images showing glia cell (g) and neuron (n) as well as the dendritic arborization and neural attachment on the PDMS surface (e,f).

Figure 7 Morphological differences among 2D (a) and 3D (b) PDMS substrates. A two-sample t-test

between proportions was performed to determine whether there was a significant differences between the 2D-glass, 2D-PDMS, 3D-PDMS with respect to the percent of neurons (Fig. c) and astrocytes (Fig. d). The t-statistic was significant at the 0.05 critical alpha level for the comparison of 3D-PDMS cultures with the 2D cultures used as controls. (2D vs 3D-PDMS $p<0,01$; Glass vs 3D-PDMS $p<0,001$, 2D vs 3D-PDMS $p<0,001$; Glass vs 3D-PDMS $p<0,001$).

Figure1

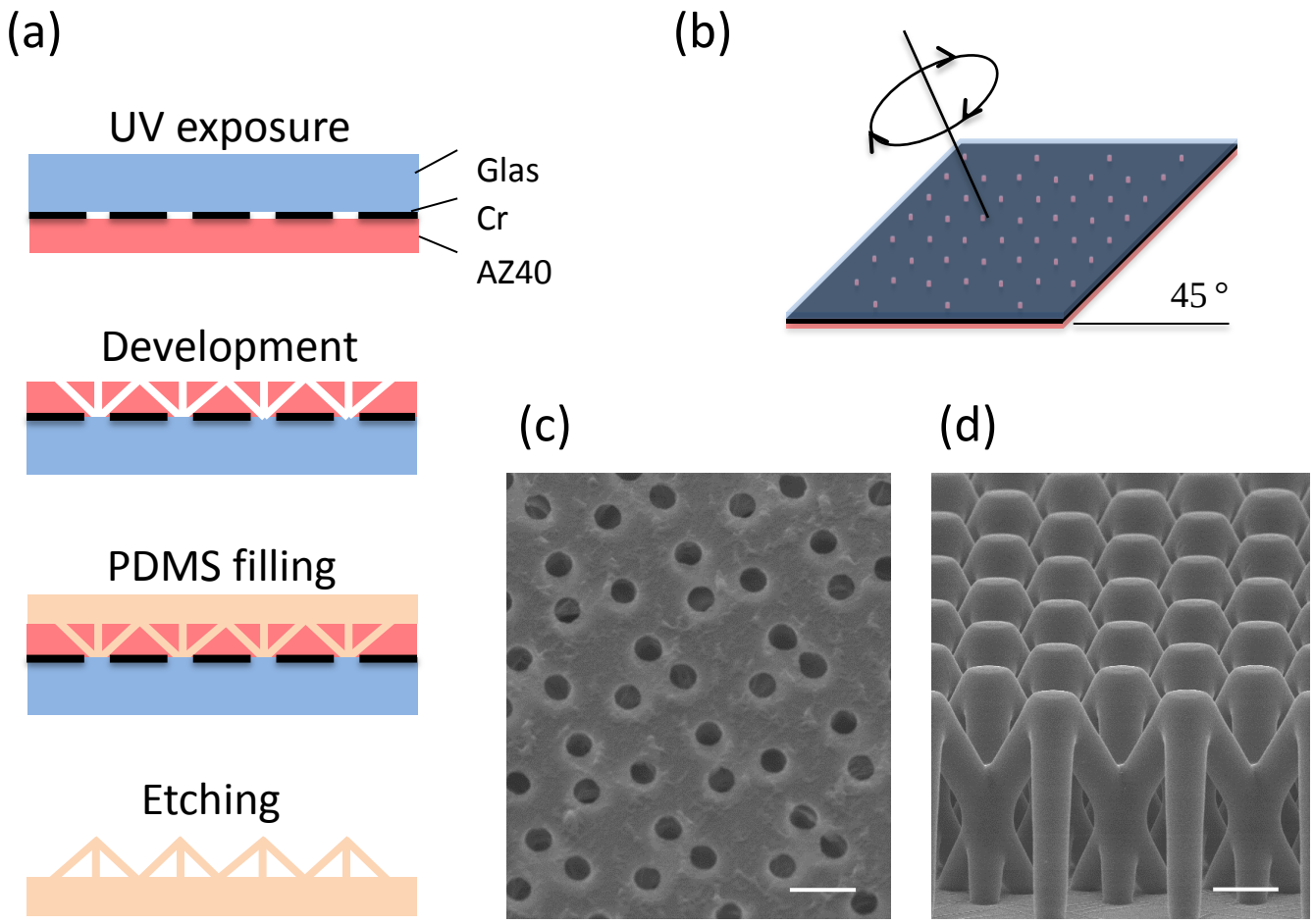
(a)
UV exposure
Glas
Cr
AZ40
Development
PDMS filling
Etching
(b)
45 °
(c)
(d)

Figure 2

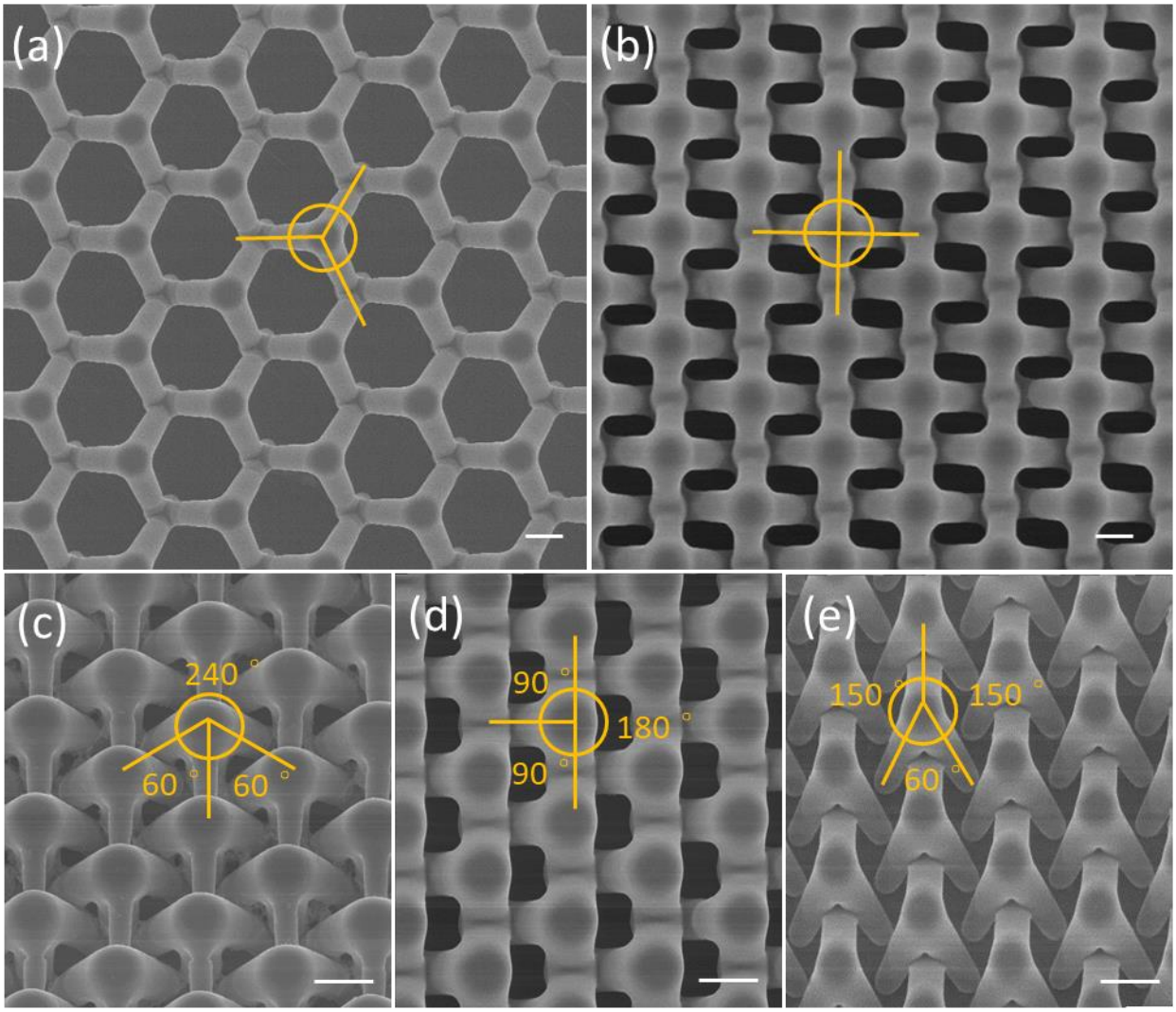

Figure 3

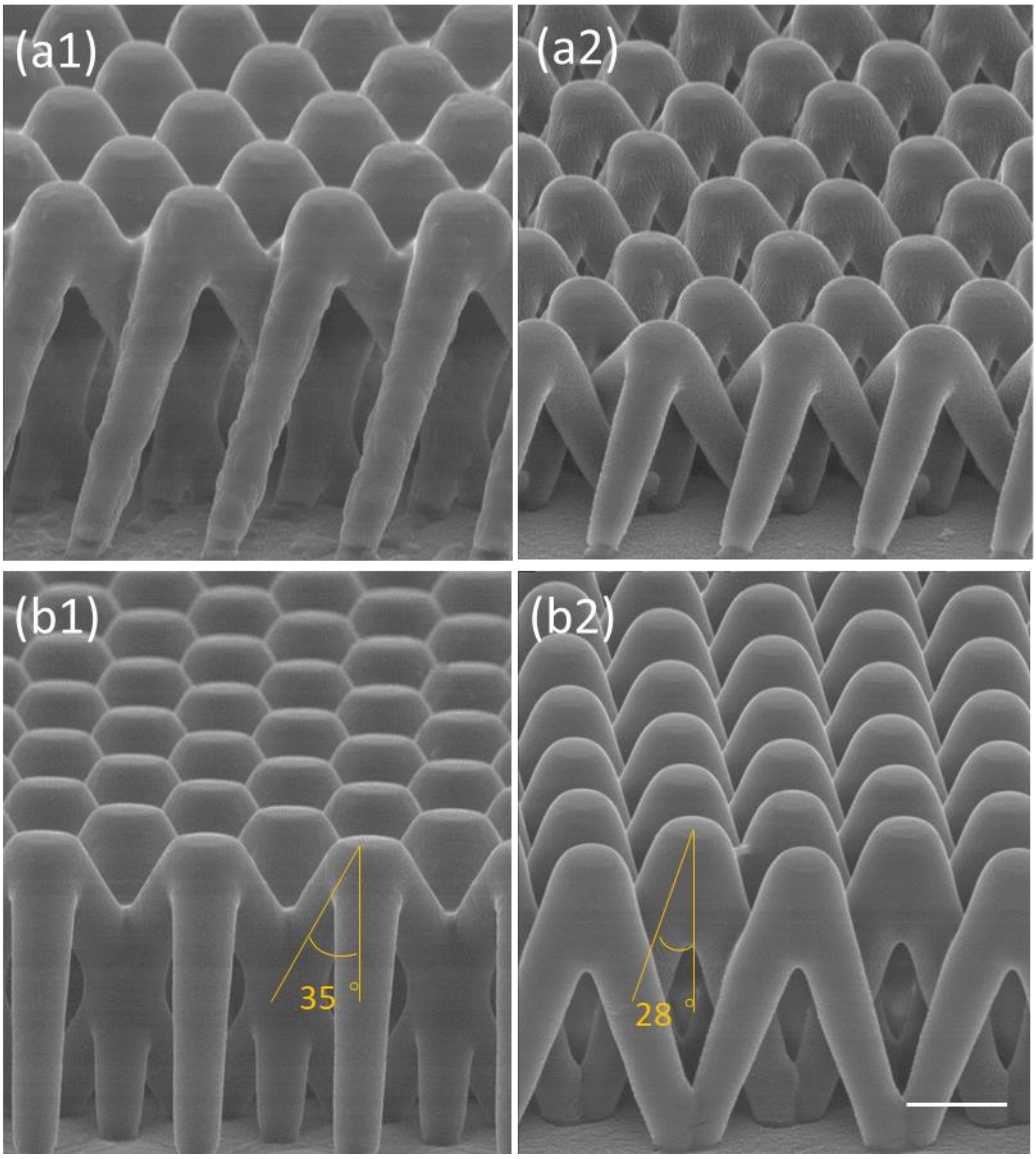

Figure 4

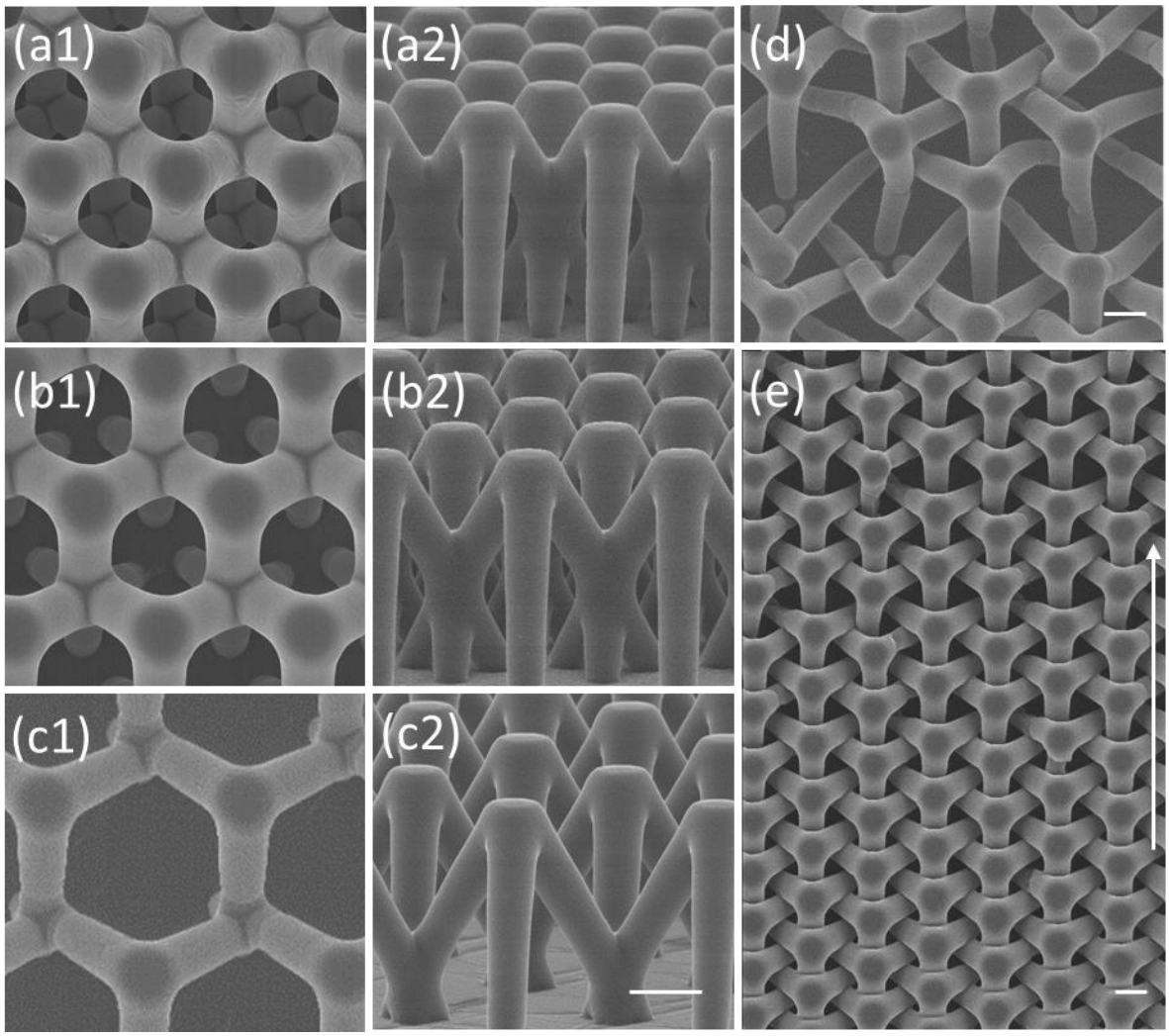

Figure 5

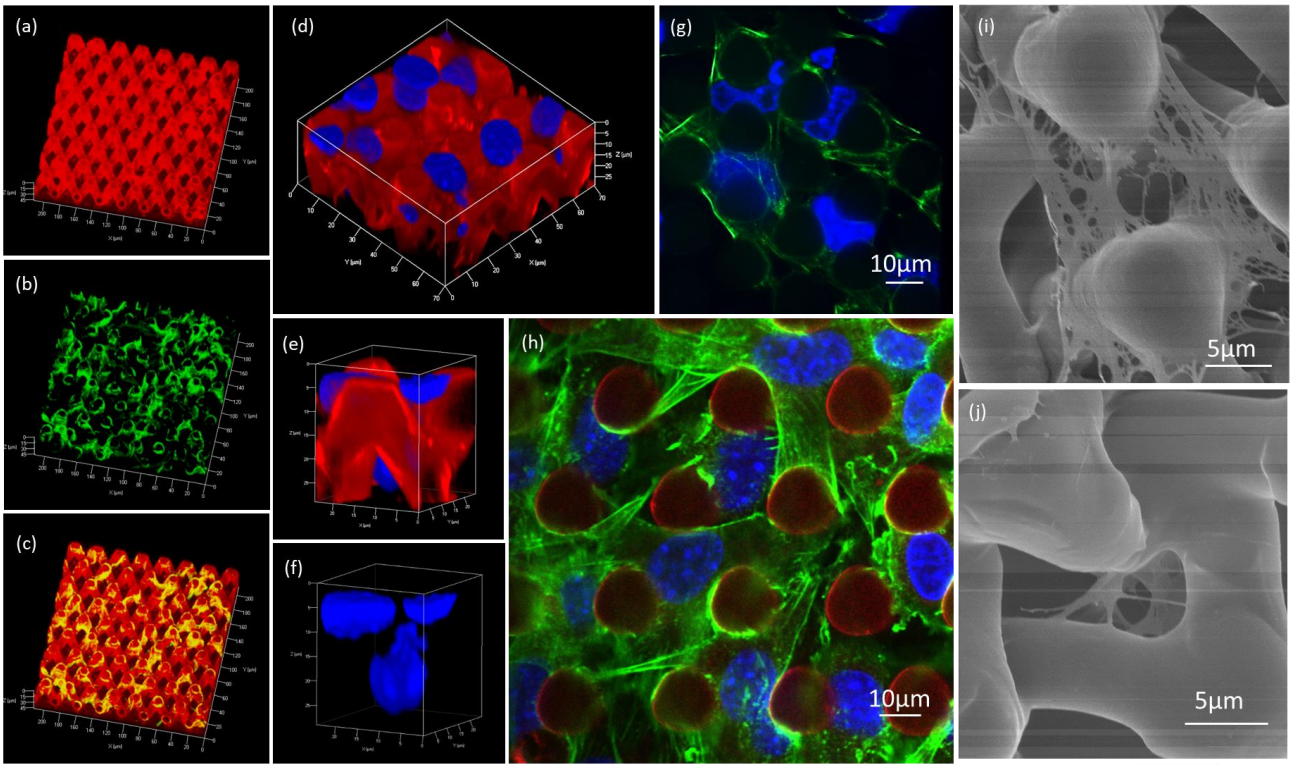

Figure 6

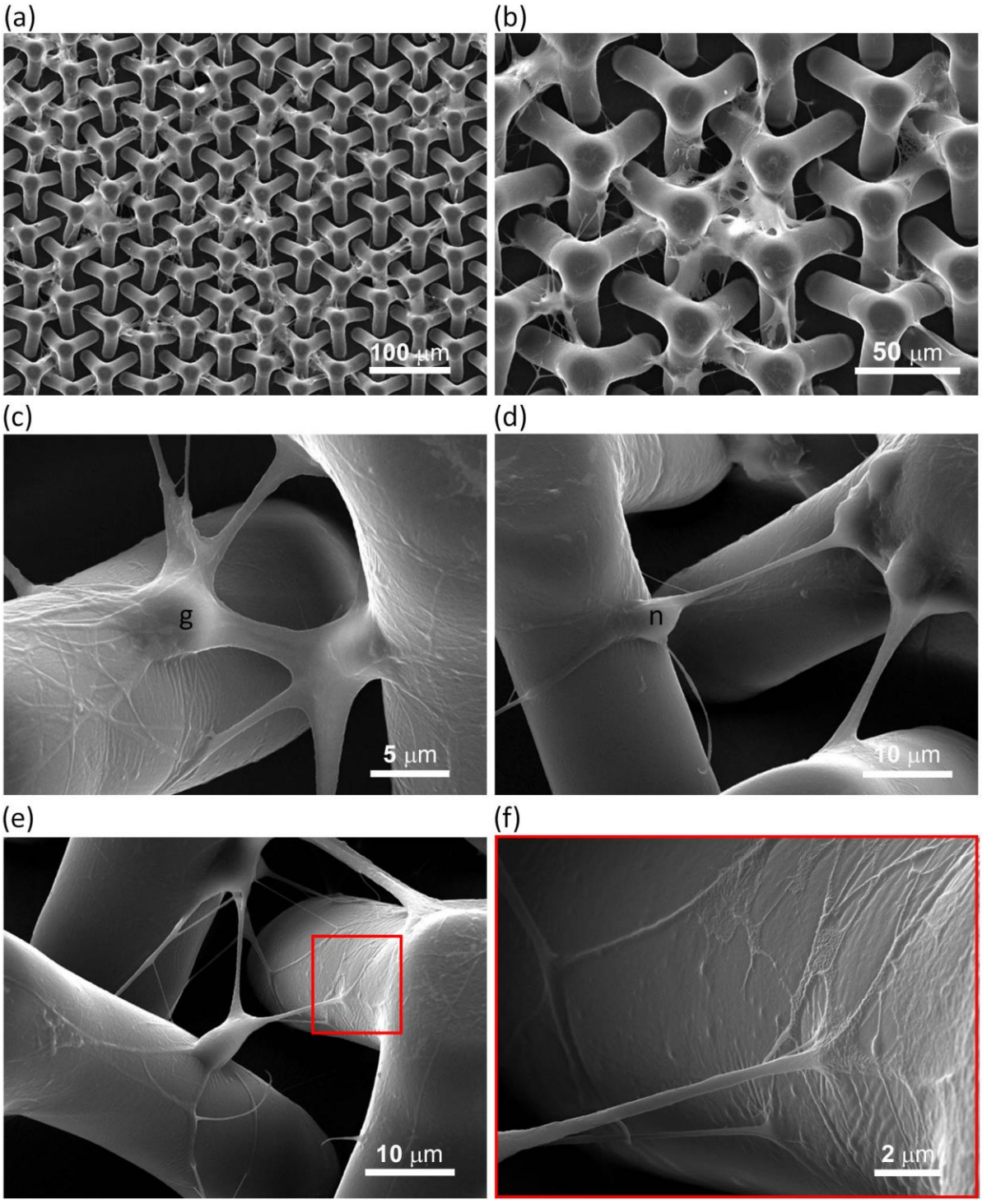

Figure 7

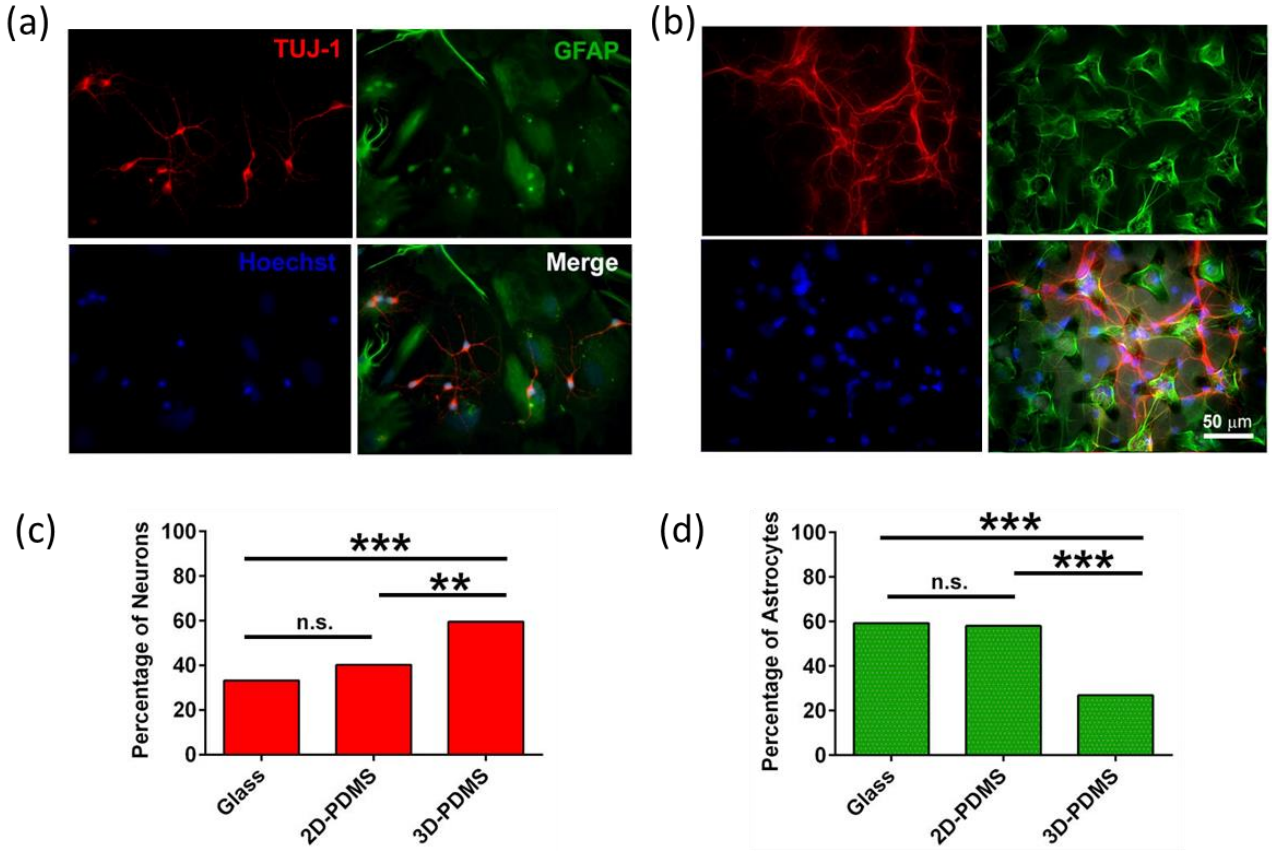
(a)
TUJ-1
GFAP
Hoechst
Merge
(b)
50 μm
(c)
Percentage of Neurons
100
80
60
40
20
0
***
**
n.s.
Glass
2D-PDMS
3D-PDMS
(d)
Percentage of Astrocytes
100
80
60
40
20
0
***
***
n.s.
Glass
2D-PDMS
3D-PDMS

Supplementary information

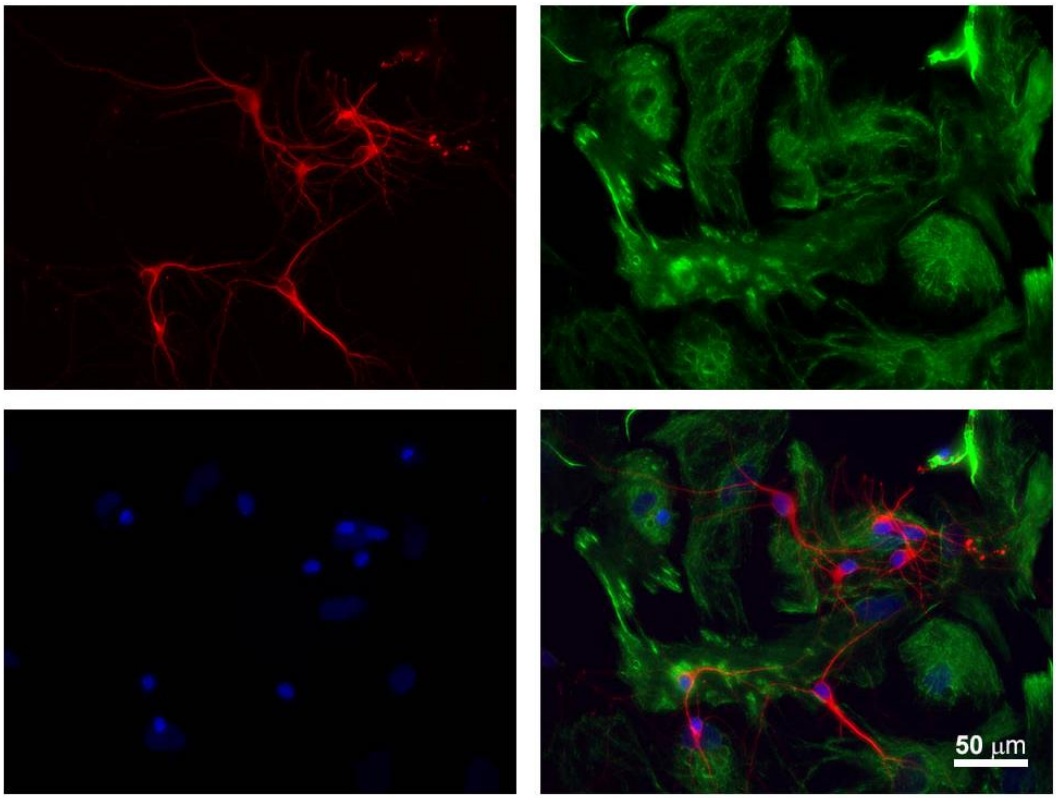

SI Figure S1 Hippocampal cell culture on glass.

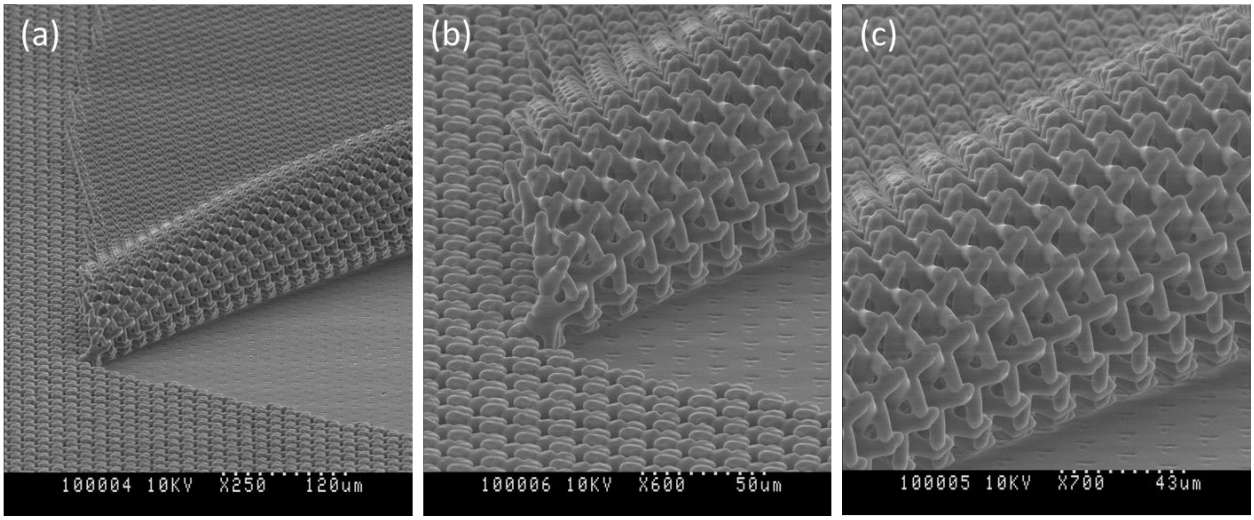

SI Figure S2 PDMS lattice peeling off from the substrate.

4.3.

The role of dimensionality in neuronal network dynamics

F.P. Ulloa Severino[+], J. Ban[+], M. Tang, Q. Song, G. Bianconi, G. Cheng and V. Torre

Scientific Reports

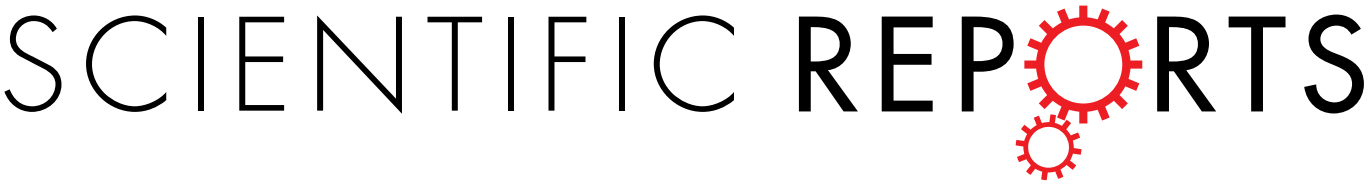

OPEN

The role of dimensionality in neuronal network dynamics

Francesco Paolo Ulloa Severino[1,*], Jelena Ban[1,*], Qin Song[2], Mingliang Tang[3], Ginestra Bianconi[4], Guosheng Cheng[2] & Vincent Torre[1]

Received: 30 March 2016
Accepted: 15 June 2016
Published: 11 July 2016

Recent results from network theory show that complexity affects several dynamical properties of networks that favor synchronization. Here we show that synchronization in 2D and 3D neuronal networks is significantly different. Using dissociated hippocampal neurons we compared properties of cultures grown on a flat 2D substrates with those formed on 3D graphene foam scaffolds. Both 2D and 3D cultures had comparable glia to neuron ratio and the percentage of GABAergic inhibitory neurons. 3D cultures because of their dimension have many connections among distant neurons leading to small-world networks and their characteristic dynamics. After one week, calcium imaging revealed moderately synchronous activity in 2D networks, but the degree of synchrony of 3D networks was higher and had two regimes: a highly synchronized (HS) and a moderately synchronized (MS) regime. The HS regime was never observed in 2D networks. During the MS regime, neuronal assemblies in synchrony changed with time as observed in mammalian brains. After two weeks, the degree of synchrony in 3D networks decreased, as observed *in vivo*. These results show that dimensionality determines properties of neuronal networks and that several features of brain dynamics are a consequence of its 3D topology.

Neuronal networks in the brain have connections extending in all 3 dimensions (3D), a characteristic that is lost in planar neuronal cultures grown on 2D supports[1–3]: these 2D networks exhibit cell-cell contacts that differ from the complex 3D interactions that occur *in vivo*. Several properties of brain dynamics have been identified and two of them are particularly relevant here: firstly, the coexistence of segregated and global processing, in which specific computations are carried out locally while information and signals are transmitted throughout the entire brain[4]; secondly, the existence of neuronal assemblies which change their degree of correlated activity both in time and in space, generating a variety of rhythms[5]. These basic properties[6–10] could be a consequence of the fact that neuronal networks in the brain are embedded in a 3D space. Indeed, dynamical properties of 3D brain networks could be significantly different from those of 2D cultures.

The understanding of the different dynamical properties of 2D and 3D neuronal networks is relevant not only for basic neuroscience but it is also important for the repair of the nervous system, especially the brain, and for the realization of what is referred to as the "organic electrode" used for chronic implants[11,12]. A first step towards this goal is the development of *in vitro* networks of neurons and/or neuronal stem cells grown in appropriate 3D supporting scaffolds. Graphene is a highly conductive hydrophobic material[13], therefore graphene scaffolds have been used to grow and to electrically stimulate neuronal networks[14]. Moreover, graphene promotes neurite outgrowth[15,16] and reduces the inflammatory response[17]. A second important step for the repair of the nervous system requires that the cultured 3D neuronal networks have physiological and dynamical properties -as close as possible- to those observed in the brain, allowing the transplantation of these 3D networks into the central nervous system.

The present manuscript has two main objectives: firstly, to understand the role of dimensionality in determining the dynamical properties of neuronal networks, and secondly, to make progress towards the repair of lesions in the nervous system. Therefore, we used 3D graphene foam (3D-GF) scaffolds to grow 3D networks of dissociated rat hippocampal neurons, and we compared the properties of 2D and 3D neuronal networks cultured on 2D

[1]Neurobiology Sector, International School for Advanced Studies (SISSA), via Bonomea, 265, 34136 Trieste, Italy. [2]Key Laboratory of Nano-Bio Interface, Suzhou Institute of Nano-tech and Nano-bionics, Chinese Academy of Sciences, 398 Ruoshui Road, Jiangsu 215123, China. [3]Institute of Life Sciences, Southeast University, Sipailou 2, Nanjing 210096, China. [4]School of Mathematical Sciences, Queen Mary University of London, Mile End Rd, London E1 4NS, United Kingdom. *These authors contributed equally to this work. Correspondence and requests for materials should be addressed to C.G. (email: gscheng2006@sinano.ac.cn) or V.T. (email: torre@sissa.it)

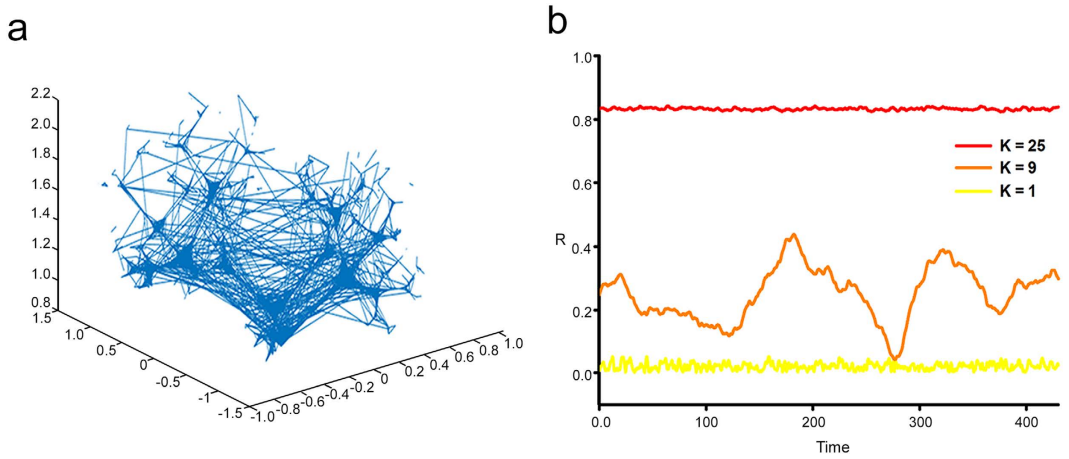

Figure 1. 3D network model. (**a**) Simulation of a 3D neuronal network which is modular and has short range connections and some long range connections (small-word network). The neurons are distributed along a fractal tree and primarily connected by short-range interactions; long-range interactions constitute a small proportion of the connections. The Kuramoto model of this network yields three dynamical regimes as a function of the strength of the coupling, K, between the oscillators. Large values of K result in a fully synchronized phase, whereas low values of K do not produce synchronization. Intermediate values of K produce a phase of frustrated synchronization. In panel (**b**), we plotted the order parameter, R, for the synchronization as a function of time, t, for different values of the coupling, K. The parameter R ranges from one (totally synchronized state) to zero (absence of synchronization). As a function of K, the plots indicate three different synchronization phases for the simulated 3D network.

Glass coverslip (2D Glass), 2D graphene films (2D G), and 3D-GFs. We show that 3D networks have dynamical properties that are quantifiably more similar to what is observed in the brain than 2D networks[4,5,18–20].

Results

Important features of networks depend on their connectivity, i.e. the number and properties of the connections between the units (neurons) composing the networks[21,22].

In order to determine differences between 2D and 3D neuronal networks, we plated hippocampal neurons on different substrates: 2D Glass, 2D G and 3D-GFs and examined their morphology and dynamics after 8–9 and 14–15 days *in vitro* (DIV) using immunocytochemistry and calcium imaging.

Dynamical properties of 2D and 3D networks. Mechanisms leading to the synchronization of coupled oscillators have been extensively studied for several decades and more recently using network theory[23–27]. Novel insights into the global dynamics of coupled oscillators on lattices, where coupling is restricted to the nearest neighbours, clarify the effect of dimensionality on the synchronization properties of these networks. In fact, using tools from mean-field analysis, scaling theory and numerical simulations[28,29] it is possible to investigate the role of the dimension d in network formed by the classical Kuramoto model. Indeed, fully entrained synchrony in an infinite hypercubic lattices is possible only for $d > 4$, whereas entrained states can form only locally for $2 < d \leq 4$. In addition, synchronization has been shown to be impossible for $d \leq 2$, i.e., global or local entrained states cannot occur for these dimensions[29]. These results provide a theoretical framework to explain why in 2D lattice no synchronization can occur while in 3D lattices some sort of weak synchronization is expected. Recent developments in network theory[23–25] have elucidated the role of long-range shortcuts, i.e., of a direct coupling between nodes (neurons) that are not physically near. The modularity of the network, i.e., the tendency of some units to be more densely connected to each other than to the rest of the network, together with the presence of short- and long-range connections (the small-world property) produce a rich phenomenology, including full synchronization and patches of synchronization that vary in time and space, such as frustrated synchronization[9,10].

We have developed models in which the 3D spatial distribution of neurons promotes the establishment of neuronal networks with small-world properties and high modularity. To this end we have modelled the 3D scaffold as a fractal tree, and we have sprinkled neurons on it uniformly, generating regions of different neuronal density. Then short distance links and a small density of long distance links were established forming a modular small-world network (Fig. 1a). The obtained networks exhibit three kinds of dynamical regimes (Fig. 1b) depending on the strength of coupling K: full synchronization (red line) was observed for high values of K, whereas low values of K resulted in the absence of synchronization (yellow); intermediate values of K yielded a time-varying degree of synchronization, usually referred as frustrated synchronization (orange). Frustrated synchronization is a consequence of the modularity of the network and of an intermediate value of K. All these results suggest a more complex dynamics in 3D than in 2D neuronal networks.

2D and 3D cultures grown on graphene substrates. 2D G and 3D graphene foams (Fig. 2a,b) were prepared using a chemical vapour deposition method using a Cu and Ni template respectively. Successive washing steps (Methods) then chemically removed the templates. Raman spectrum analysis obtained from these 3D-GFs

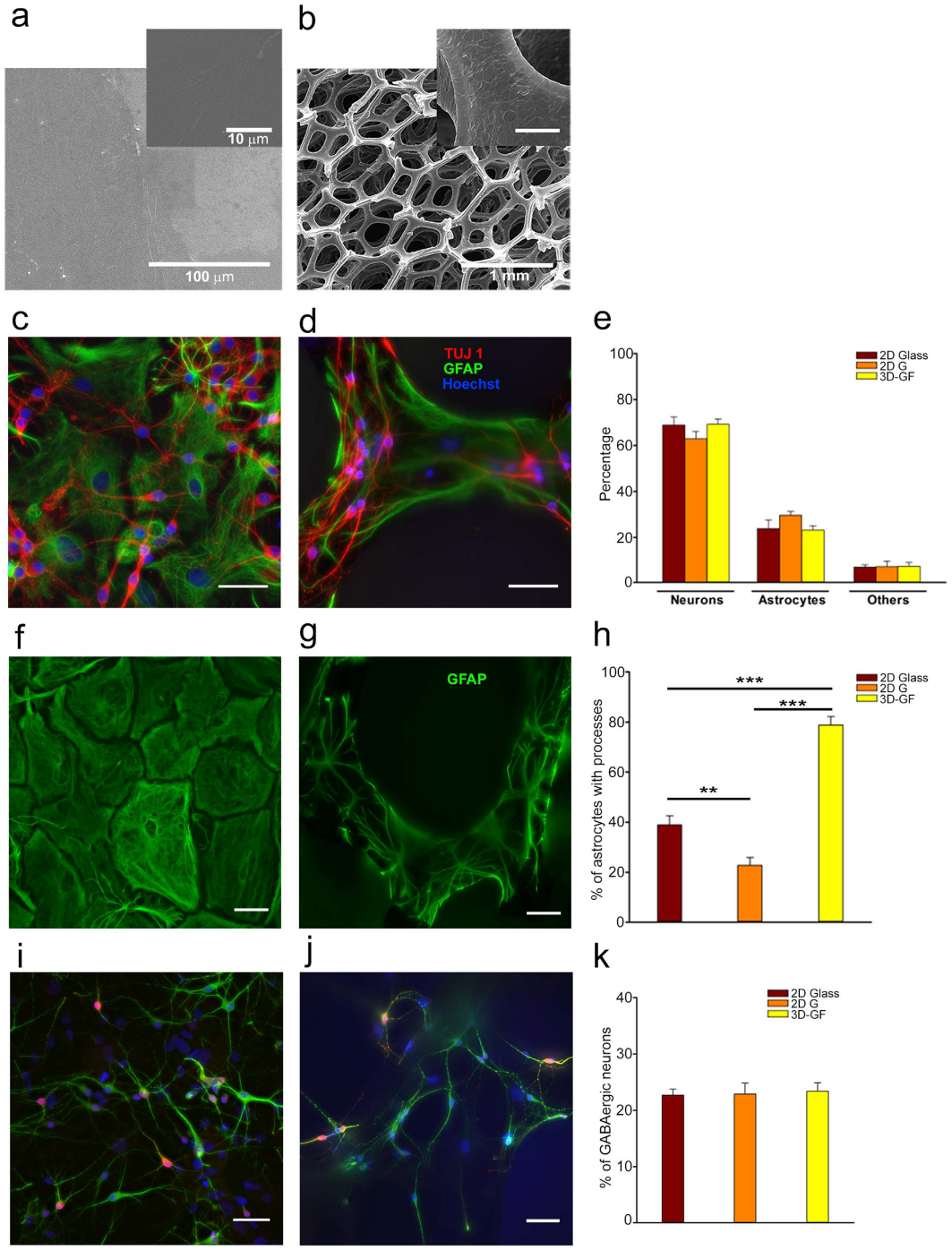

Figure 2. Cellular morphology of 2D and 3D cultures. (**a**) SEM image of a 2D graphene film. Darker areas present an higher number of layers compared to the brighter one; as shown in the inset the surface is flat. (**b**) SEM image of a 3D Graphene Foam scaffold (3D-GF); the surface presents ripples, as shown in the inset. (**c**) Hippocampal culture at 7 DIV on 2D Glass stained for β-tubulin III (TUJ1, red), glial fibrillary acidic protein (GFAP, green) and Hoechst 33342 nuclear stain (blue). (**d**) The same as (**c**) but for 3D-GFs. (**e**) Proportion of neurons (TUJ 1-positive) and glia (GFAP-positive) among different substrates tested. TUJ 1- and GFAP-negative cells are referred to as "other". (**f,g**) GFAP staining of astrocytes on 2D G and 3D-GF, respectively. (**h**) Percentage of astrocytes with processes for the different substrates tested (**$p < 0.01$ ***$p < 0.001$ One-way ANOVA, Holm-Sidak post-hoc test). (**i,j**) Neuronal cultures on 2D G and and 3D-GFs respectively. Cells were stained for MAP2 (green), GABA (red) and Hoechst 33342 nuclear marker (blue). (**k**) Percentage of GABAergic inhibitory neurons for three conditions tested. The images are the projections of a 20 μm z-stack for 2D samples and 35–50 μm for the 3D cultures, acquired with 0.5-μm slice spacing. Scale bar, 50 μm.

shows that these scaffolds are of high quality and consist of few graphene sheets[14]. 3D-GFs have holes with diameters ranging from 100 to 500 μm and the size of their backbone varied from 100 to 200 μm. Neurons survived well in all three tested conditions and formed functional networks after one week.

In order to examine the relative abundance of neurons and glial cells, cultures were stained with antibodies for neurons (β-tubulin III) and for glial cells with glial fibrillary acidic protein (GFAP), as shown in Fig. 2c,d. The proportion of β-tubulin III-positive neurons (68.89 ± 3.59% on 2D Glass, 63.01 ± 3.18% on 2D G and 69.29 ± 2.23% on 3D-GFs) and the percentage of GFAP-positive astrocytes (23.93 ± 3.66%, 29.67 ± 1.68% and 23.25 ± 1.84% on 2D Glass, 2D G and 3D-GFs, respectively) were similar among different cultures (Fig. 2e; n = 6(744), n = 5(436), n = 7(403)). Glial cells adhered to the 3D-GFs as well as to flat surfaces, forming a layer above which neurons formed a network. Both stellate-shaped and flattened ovoid morphologies were observed (Fig. 2f,g), which are typical of *in vitro* dissociated primary cultures[30,31]. Nevertheless, the majority of astrocytes on 3D-GFs extended processes (78.80 ± 3.37%, n = 8 (125)), whereas the ratio of astrocytes with extended processes was significantly lower for 2D cultures (Fig. 2h, 38.82 ± 3.69%, n = 9(432) for 2D Glass and 22.67 ± 3.2%, n = 5(160) for 2D G, one-way ANOVA tested with Holm Sidak test). These observations suggest that 3D cultures favour a more differentiated and *in vivo*-like morphology.

We compared the amount of inhibitory GABAergic neurons between 2D and 3D cultures after 7DIV with staining for microtubule-associated protein 2 (MAP2) and GABA (Fig. 2i,j). As shown in Fig. 2k, all cultures tested showed comparable percentages of GABA-positive neurons: 22.77 ± 1.07% for 2D Glass, 22.90 ± 1.92% for 2D G and 23.40 ± 1.49% for 3D-GFs (n = 5(566), n = 7(436) and n = 11(276) for glass, 2D G and 3D-GFs respectively). These data show that the ratio of excitatory and inhibitory neurons was not altered on 3D-GFs, but the composition of GABAergic subtypes[32,33] or the density of both pre- and post-synaptic GABA receptors could be different.

Neuronal culture on 3D-GFs extended continuously and uniformly along the scaffold backbone (Supplementary Fig. S1). After one week of culture, we counted the number of neurites emerging from each neuron and the average number of neurites was similar for glass, 2D G and 3D-GFs (2.99 ± 0.08, 3.06 ± 0.08 and 2.86 ± 0.08 neurites per neuron; n = 141, 149 and 140 neurons analysed for 2D Glass, 2D G and 3D-GFs respectively). The same analysis showed that frequency distribution of the neurites' number was similar for the three different supports (Supplementary Fig. S2). After two weeks of culture, axons approached a millimetre in length in both 2D and 3D cultures (Supplementary Fig. S3), but they only vertically extended several hundreds of micrometres on 3D-GFs, allowing a more extensive connectivity (Supplementary Video S1).

The spontaneous electrical activity of 3D networks is more synchronous. Fluorescence images of the Fluo-4-loaded neuronal cultures confirmed the formation of 2D neuronal networks (Fig. 3a) plated either on 2D Glass or on 2D G. Fluorescence images of 3D neuronal networks grown on 3D-GFs (Fig. 3b) showed that the scaffold backbone was entirely covered by neurons and glial cells. Cells could be visualized up to 500 μm deep in the scaffold because of the large size of the scaffold pores. Glial cells were present in all cultures and could be morphologically identified both in 2D and 3D cultures (Fig. 3c,d), because of their larger cell body and the shape of their processes. The spontaneous electrical activity of neurons was monitored by measuring their calcium transients (DF/F), obtained by acquiring fluorescence images at 3–10 Hz for 10–20 min. During this recording time, the emitted fluorescence was stable with negligible bleaching (Supplementary Video S2).

After one week of culture, it was possible to record clear calcium transients from both 2D and 3D neuronal cultures (Fig. 3e,f). The onset time of calcium transients was defined by detecting those events in the fluorescence signal that exceed at least three times the standard deviation of the noise (≈0.01 DF/F). Standard analysis of the percentage of active neurons, the mean amplitude of Ca^{2+}-transients and the frequency distribution of the amplitude, reveal that neuronal activity is significantly different for three-dimensional cultures (Supplementary Fig. S4). Indeed, calcium transients from 2D and 3D cultures had a different degree of synchrony, with 3D cultures appearing consistently more synchronous. Calcium waves from glial cells (Fig. 3g) were less frequent but longer and larger with amplitude approximately greater than 0.2 DF/F and propagated at a speed between 4 and 5 μm/s in 2D cultures and between 5 and 7 μm/s in 3D-GFs. By contrast, calcium transients in neurons appeared to propagate along neurites almost instantaneously. Superimposed smaller and rapidly propagating calcium transients were observed in calcium waves, these transients presumably originated from neurites grown over glial cells (Fig. 3g arrows). Calcium waves in glial cells propagated both inter- and intra-cellularly along glial processes[34,35].

Raster plots of detected calcium transients from 2D (Fig. 3h) and 3D neuronal networks (Fig. 3i) were constructed. The Δt interval between two successive calcium transients was computed to obtain an average inter events interval (IEI) for each neuron. The cumulative count (Fig. 3j) showed that the IEI for neurons in 3D-GFs was 32.8 ± 3.1 s, whereas this value was 51.5 ± 5.4 s and 57.3 ± 4.4 s for 2D Glass and 2D G, respectively. Therefore, the rate of firing was significantly higher in 3D networks compared to both the 2D cultures (ANOVA on ranks tested with Domm's post-hoc test. n = 114 neurons for 6 neuronal cultures on 3D-GF; n = 103 neurons for 6 neuronal cultures on 2D Glass; n = 127 neurons for 5 neuronal cultures on 2D G).

On the basis of these raster plots, we analyzed the degree of synchrony of 2D and 3D neuronal networks by computing the mean correlation coefficient (cc)[19]. We computed the cross-correlation matrix, $_{CT}\mathcal{M}$, for all neuron pairs with entries σ_{CTij}, varying between 0 and 1 (Methods) in 2D and 3D networks (Fig. 3k). We also computed the cross-correlation matrix, $_{S}\mathcal{M}$, among the entire optical signals including their slow component. The entries of the matrix $_{S}\mathcal{M}$ were σ_{SLOWij} and varied between −1 and 1 (Methods) in 2D and 3D conditions (Fig. 3l). In both cases, the cc was obtained by averaging all entries of the $_{CT}\mathcal{M}$ or $_{S}\mathcal{M}$ over all the experiments. The values of the cc for the calcium transients in 2D Glass and 2D G cultures were significantly lower (0.53 ± 0.006 and 0.59 ± 0.006, respectively) than that of the 3D-GF cultures (0.82 ± 0.005). We considered also

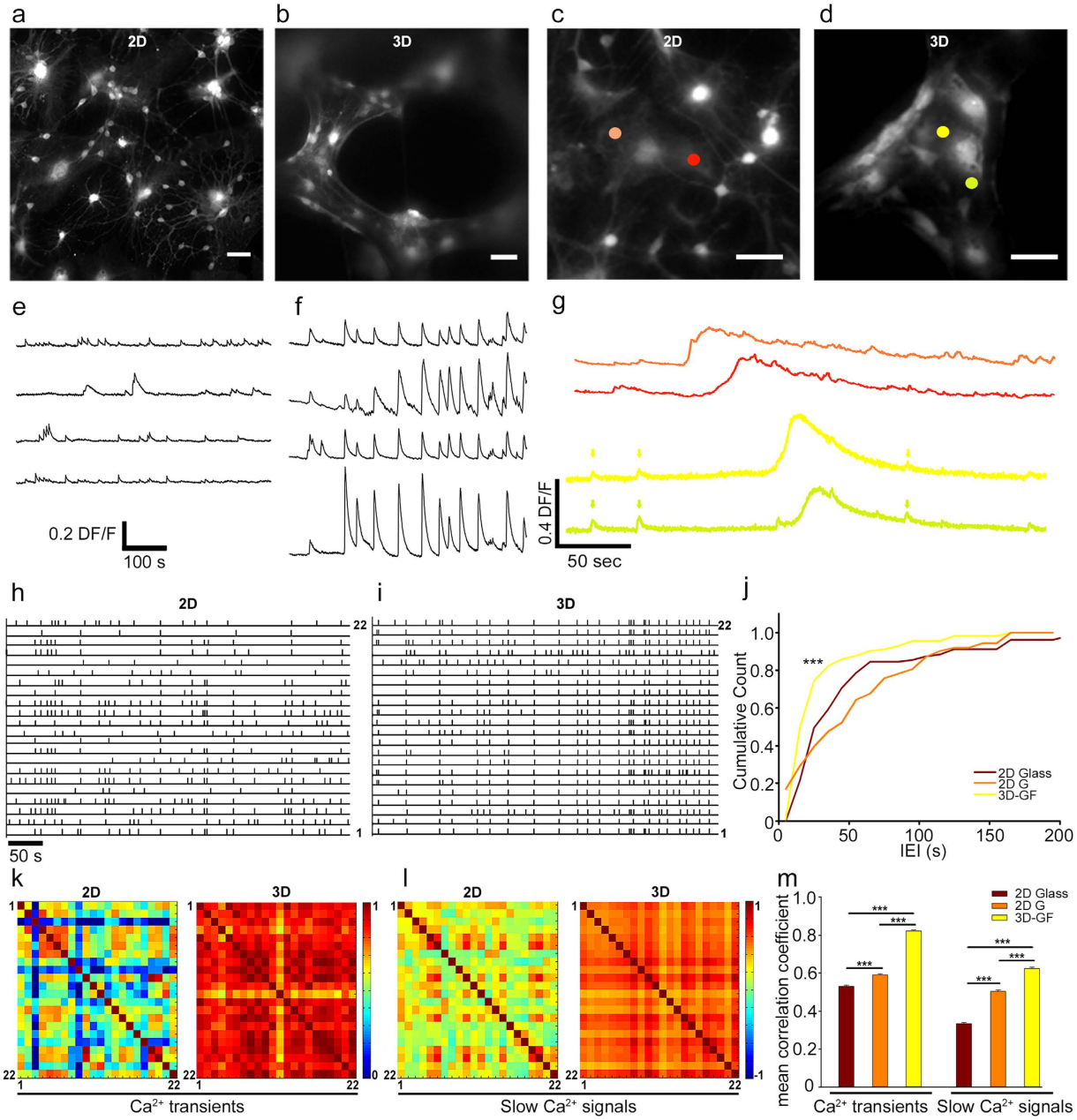

Figure 3. The spontaneous activity of 3D networks is more synchronous. (**a,b**) Neuronal cultures loaded with 4 μM Fluo-4-AM calcium indicator on 2D Glass and 3D-GF, respectively. (**c,d**) Glial cells on 2D G and 3D-GF respectively. Coloured circles indicate the ROIs where calcium waves were obtained. (**e,f**) Calcium transients on 2D Glass and 3D-GF, respectively, for 4 selected neurons. (**g**) Calcium waves from glial cells on 2D G (top traces) and 3D-GFs (bottom traces); arrows indicate signals from neurites projecting over glial cells. (**h**) Raster plot of 2D culture on glass and (**i**) 3D culture on 3D-GFs for 22 selected traces. (**j**) Cumulative count of the Inter Events Interval (IEI) for neuronal cultures grown on 2D Glass, 2D G and 3D-GF (**$p < 0.01$ ***$p < 0.001$ ANOVA on ranks, Domm's post-hoc test). (**k**) Cross-correlation matrices of calcium transients $_{CT}\mathcal{M}$ in 2D and 3D neuronal networks. (**l**) Cross-correlation matrices of slow calcium signals $_{S}\mathcal{M}$ for the same two conditions. (**m**) Mean correlation coefficient of the calcium transients and slow calcium signals (***$p < 0.001$ ANOVA on ranks, Domm's post-hoc test). Scale bar, 50 μm.

the cross-correlation between the slow Ca^{2+} signals, which is a possibly more accurate measure of the degree of synchronization: the value of cc – obtained from $_{S}\mathcal{M}$ -was lower for 2D Glass and 2D G cultures (0.33 ± 0.006 and 0.50 ± 0.007, respectively) than for 3D-GFs (0.62 ± 0.008) (Fig. 3m; ANOVA on ranks tested with Domm's post-hoc test. $n = 1497$ couples of neurons for 6 neuronal cultures on 2D Glass; $n = 1624$ couples of neurons for 5 neuronal cultures on 2D G; $n = 1093$ couples of neurons for 6 neuronal cultures on 3D-GF). We examined also whether the value of cc depended on the distance between neurons: there was no difference when cc was

computed among all active neurons in an image and for pairs of neurons separated by more than 200 μm (0.56 ± 0.009 for 2D Glass; 0.58 ± 0.008 for 2D G; 0.84 ± 0.007 for 3D-GF). These results show that the spontaneous firing of 3D networks is more synchronous than that of 2D networks and that the conductivity of graphene based materials, alone, does not affect the activity of neurons[36,37] (Supplementary Information).

Different degree of connectivity leads to different network regimes. After one week of culture, 3D networks exhibited two regimes: a highly synchronized (HS) regime, characterized by a very high synchrony of calcium transients (mean cc > 0.8), and a moderately synchronized (MS) regime, in which large synchronous transients coexisted with sparse smaller and uncorrelated transients (0.5 < mean cc < 0.8). The HS regime was very rarely observed in 2D networks grown on glass or 2D G obtained from the same batch of dissociated hippocampal neurons.

MS regime. In several experiments, we observed from the cell body of the same neuron small and large calcium transients. Therefore, we computed the amplitude histograms of these transients during a period of up to 10–20 min before the occurrence of dye bleaching (Methods). For many neurons, these histograms had two well-separated peaks (Fig. 4a) that allowed the identification of two classes of calcium transients (Fig. 4b), i.e. small (red) and large (black). The former had approximately the same amplitude and could originate either from a single action potential (AP) or from a burst of a small number of APs, whereas the latter were likely due to a burst of several APs occurring in a window of 200–500 ms[38]. Visual inspection of raster plots of these transients (Fig. 4c) suggests that large calcium transients (black bars) were more synchronous than small calcium transients (red bars). Therefore, we analysed the degree of correlation of these two classes. The cross-correlation matrices $_{CT}\mathcal{M}$, (Fig. 4d,e) show that the large calcium transients were more correlated ($cc = 0.69 \pm 0.010$) than the smaller ($cc = 0.45 \pm 0.009$; $n = 518$ couples of neurons. *Student's t-test*). Therefore, in the MS regime large synchronous bursts of electrical activity coexisted with sparse firing which was poorly correlated. The frequency of the two types of signals differed significantly; the mean IEI of large synchronized transients was 31.7 ± 0.7 s, whereas that of small, poorly correlated transients was 25.1 ± 0.6 s (Fig. 4f. *Mann Whitney test*. $n = 50$ cells for 3 neuronal cultures).

HS regime. 3D-GFs contained large pores with a diameter ranging from 100 to 500 μm. After 8–15 days of culture, we observed neurites able to cross the pores and bridge distances of 100–200 μm in the scaffold (Fig. 5a). Clear calcium transients that originated from crossing neurites were recorded (Fig. 5b red trace), and these transients were correlated with those that originated from neighbouring neurons (black traces). In some preparations, holes were not only filled with crossing neurites but also with the soma of neurons and glial cells, which appeared to be hanging in the pore (Fig. 5c).

3D-GFs with a high degree of connectivity, as indicated by the presence of the soma of neurons inside the holes and many crossing neurites (Fig. 5d), had calcium transients almost completely synchronous (Fig. 5e where 24 traces overlapped - top traces- and 3 isolated examples are reported - bottom traces). We defined this state as highly synchronous (HS) and the rising phase of these calcium transients matched perfectly (Fig. 5e, insets) within the limits of our time resolution (3–5 Hz). The falling phase of calcium transients from different neurons, however, had a different time course. This higher synchrony ($cc = 0.93 \pm 0.004$; $n = 483$ couples of neurons) is attributed to a more extensive connectivity associated to the presence of crossings (or shortcuts) across the holes and the long neurites extending in 3D along the scaffold backbone.

Transitions between HS and MS. Neuronal cultures grown on 3D-GFs often exhibited clear transitions between the MS and HS regimes (Fig. 5f). During the 10–20 min of network activity, the value of cc – computed over a time window of 2–4 minutes - fluctuated between 0.8 and 1.0 (HS regime, Fig. 5f, red trace) as well as between 0.6 and 0.8 (MS regime, Fig. 5f, orange traces). A network remained in a given state for 2–5 minutes and frequently changed its degree of synchrony – i.e., the value of the cc. When cultures obtained from the same hippocampal tissue were grown on a 2D flat substrate – either glass or a graphene film – the value of cc remained confined between 0.4 and 0.6 (Fig. 5f, yellow trace). Only neuronal networks with a high number of crossings or shortcuts across holes, as those in Fig. 5c,d, remained in the HS state for the entire duration of the optical recording (Fig. 5e). In several 3D neuronal networks, transitions between the HS and the MS state were observed (orange symbols in Fig. 5f), and there were episodes in which calcium transients were highly synchronous (Fig. 5g) and in other episodes the degree of correlation was significantly lower (Fig. 5h). In the great majority of 2D neuronal networks the degree of synchrony was lower (yellow symbols in Fig. 5f,i). The transition from the MS to the HS regime is reminiscent of a phenomenon observed in 2D cultures after the addition of inhibitors of GABAergic pathways[39].

Neuronal assemblies in synchrony change in time and space. 3D-GFs have holes with a diameter of 100–500 μm, allowing visualization of neurons on focal planes separated by 100–200 μm along the z-axis (Supplementary Fig. S1). In this way we followed the spontaneous activity of 3D neuronal assemblies and we could observe possible changes in space and in time of the degree of synchrony. Indeed, by using a stage controlled by a fast piezoelectric device, we collected fluorescence images at focal planes separated in the axial (vertical) direction by 100–200 μm. Fluorescence images were obtained by acquiring 3 frames per second at each plane with a time shift of 167 ms (corresponding to 100 ms of exposure time and 67 ms for the movement of the stage). This delay between images collected at different focal planes is small in comparison of the duration of calcium transients (10–20 s) and represents the time resolution for the determination of synchrony. Calcium transients obtained from neurons

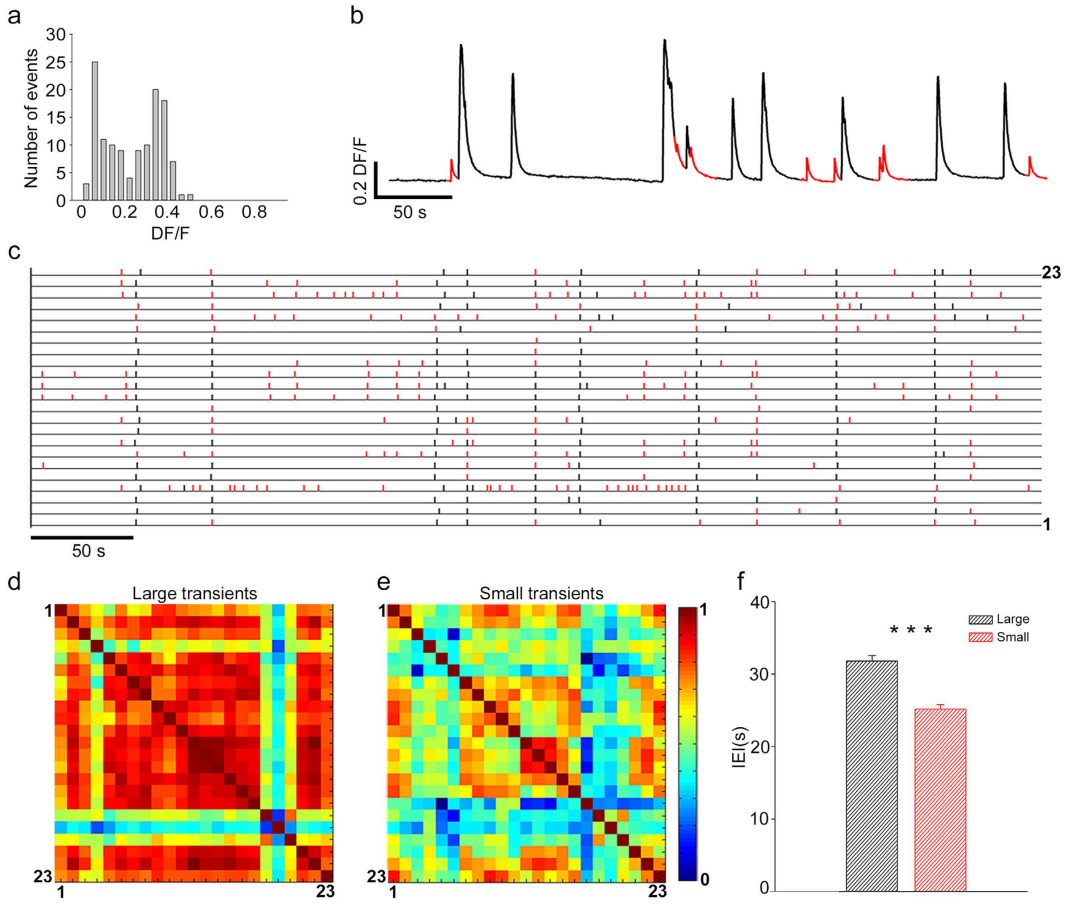

Figure 4. Small and large calcium transients. (**a**) Amplitude histograms of calcium transients obtained from one optical trace: two peaks are clearly present. (**b**) Representative optical trace with large (black) and small (red) calcium transients. (**c**) Raster plot of large (black dash) and small (red dash) transients for 23 different neurons. (**d,e**) Cross correlation matrices calculated for the large and small transients, respectively. (**f**) The mean value of IEI for large and small calcium transients; data from 3 experiments and a total of 50 neurons (***$p < 0.001$ Student t-test).

with the soma on one plane (Fig. 6a,b,e,f; red circles) could be synchronous (Fig. 6c,d,g,h; blue shadow bars) and not in synchrony with calcium transients from neurons on focal planes at a distance of some tens of microns. Often, however, calcium transients obtained from focal planes at a distance of 76 (Fig. 6a–d) and 110 μm (Fig. 6e–h) were synchronous (pink shadow bars). These episodes of high synchrony in 3D were interspersed with periods of less correlated electrical activity (also Fig. 5f).

These results have two important consequences: firstly, they show that in 3D neuronal networks neurons extend neurites along the z-axis for several hundreds of microns so to form long-range connections; secondly, that the assemblies of neurons in synchrony are highly dynamic and change both in space and time, reminiscent of what is usually referred as frustrated synchronization in network theories[9,10] and often observed in native 3D neuronal networks[19].

We computed the cross-correlation matrix $CT\mathcal{M}$ for all pairs of neurons positioned on both planes (Fig. 6i). Visual inspection of the matrix $CT\mathcal{M}$, show a high degree of synchronization for pairs of neurons from the same focal plane (z_1 or z_2) (entries framed in light blue and dark blue in Fig. 6i). Pairs of neurons from different focal planes have a lower degree of synchrony (entries framed in black in Fig. 6i). Collected data from 3 neuronal cultures show that the mean value of cc was 0.61 ± 0.02 among calcium transients measured from neurons in the same focal plane. When pairs of neurons from different focal planes were considered the value of cc decreased to 0.43 ± 0.01 which was smaller than that of all pairs of neurons ($cc = 0.51 \pm 0.01$). (Fig. 6j, ANOVA on ranks tested with Domm's post-hoc test; 79, 207 and 364 pairs of neurons for z_1 and z_2, $z_1 \cap z_2$ and $z_1 \cup z_2$ respectively). These values of cc were obtained from averaging data over a time window of 20 minutes, but a different and more dynamic picture is observed when the cross-correlation matrix $CT\mathcal{M}$ is computed on successive time windows of 60 s, as shown in Fig. 6k. The degree of synchrony of calcium transients among neurons on the same focal plane varies with time and when neurons on two different focal planes are considered there are episodes in which calcium transients are in phase or in anti-phase (Fig. 6k light and dark blue line). When pairs of neurons from different focal planes were considered, we observed episodes where calcium transients were highly synchronous (value

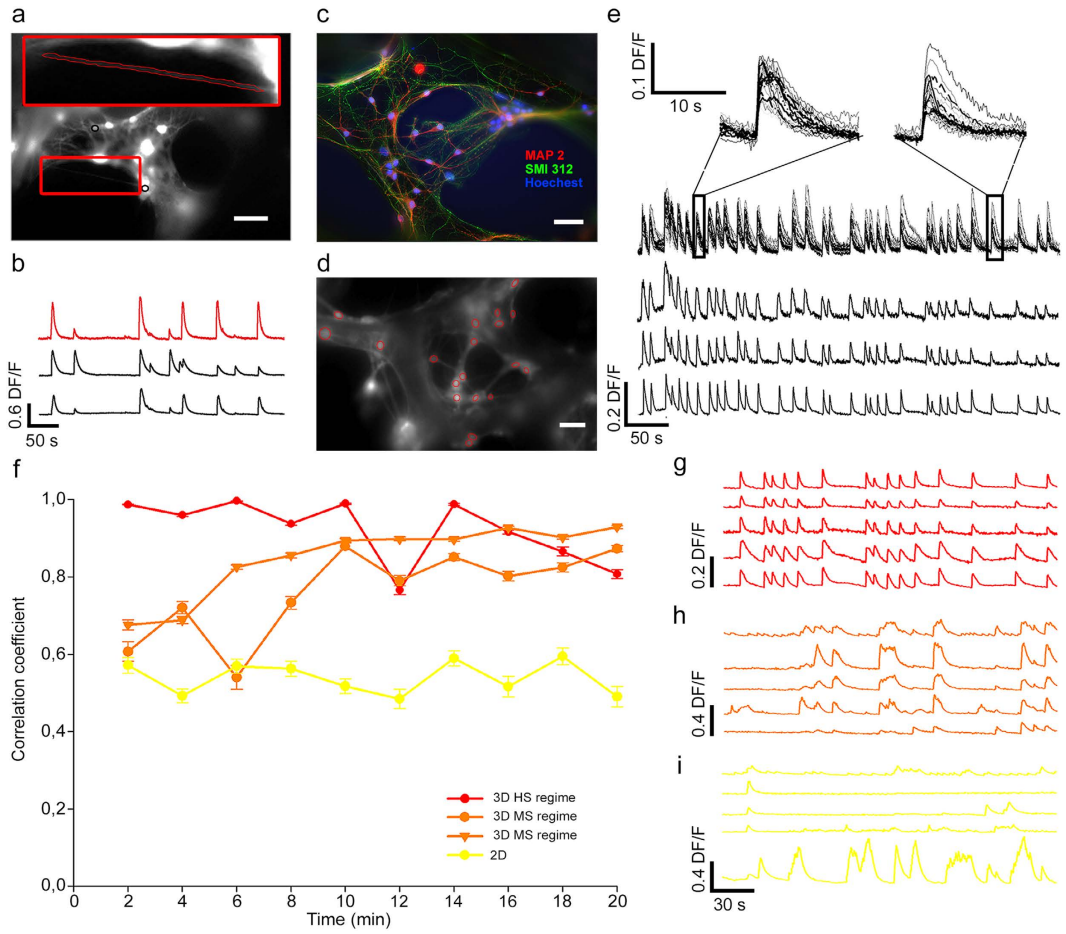

Figure 5. High connectivity leads to HS regime. (**a**) Fluorescent image of a neuronal culture grown on a 3D-GF loaded with Fluo-4 AM; a crossing neurite (inset) and two examples of ROIs (black circles) are shown. (**b**) Optical traces from the crossing neurite shown in a (red trace) and from two neighbouring neurons (black traces) obtained from the two ROIs indicated in a. (**c**) Fluorescence image of a neuronal culture grown on a 3D-GF where neurons cross and fill a pore of the scaffold with both neurites and cell bodies. Cells were stained for the somatodendritic neuronal marker MAP2 (red), axonal marker SMI 312 (green) and Hoechst 33342 nuclear stain (blue). (**d**) Example of a highly connected network as in c but loaded with Fluo-4 AM exhibiting the HS regime. (**e**) 24 superimposed optical traces (3 of them are shown separately in the bottom part) obtained from the 3D neuronal network shown in d; the rising phase of calcium transients is almost perfectly synchronized, as shown in the insets. (**f**) Time evolution of the correlation coefficient cc computed over a bin width of 2 minutes for 3D neuronal networks in the MS and HS regime and for 2D neuronal networks. (**g–i**) are examples of optical traces for each type of regime with the same colour code as in (**f**). Scale bar, 50 μm.

of cc close to 0.8) and episodes of complete lack of synchrony (value of cc below 0.2). The overall degree of synchrony among all neurons varied significantly in time (Fig. 6k yellow line) and was slightly higher than that of pairs of neurons from distinct focal planes.

Maturation of 3D neuronal networks. We investigated also changes of the spontaneous activity of 3D neuronal cultures during the maturation. We compared neuronal cultures obtained from the same batch of dissociated hippocampal neurons after one week (8–9 DIV) and two weeks (15–16 DIV) of culture. Calcium transients after one week of culture were rather synchronous (Fig. 7a) and the degree of synchrony decreased after two weeks (Fig. 7b). The mean IEI increased its value from 32.8 ± 3.0 to 46.8 ± 10.5 seconds (Fig. 7c). The value of the cc, instead, decreased from 0.82 ± 0.005 (8–9 DIV) to 0.53 ± 0.02 (15–16 DIV) in 3D-GFs and this change was statistically significant (Fig. 7d; *Mann-Whitney test*). The decreased correlation between calcium transients was more evident for pairs of neurons separated by a distance larger than 100 μm (Fig. 7e). The degree of synchrony, quantified by the value of cc, fluctuated similarly for 3D neuronal networks after one and two weeks of culture (Fig. 7f) and episodes of high synchrony (value of cc close to 0.9) were interspersed with periods of low synchrony (cc around 0.6). This reduction is very similar to what observed during maturation in the rat cortex[19] where synchronization of calcium transients decreases at the second week of maturation. It is possible that the observed decrease of synchrony in our 3D neuronal cultures and in cortical networks have a similar origin associated to maturation.

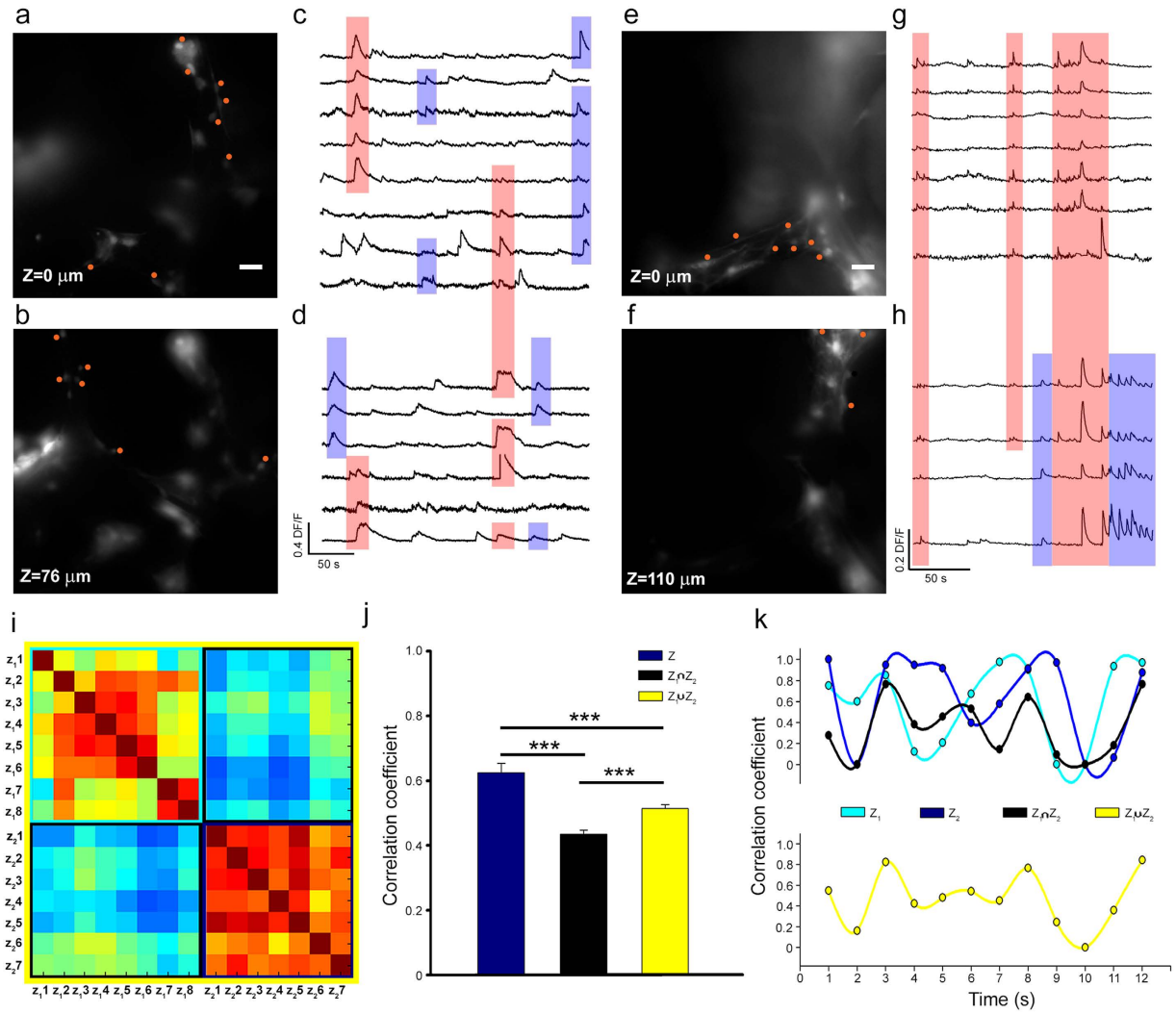

Figure 6. Assemblies of neurons firing in synchrony are dynamic and change both in space and time. (**a**,**b**,**e**,**f**) Fluorescent images of neuronal networks stained by Fluo-4-AM at two focal planes of the same 3D neuronal networks at different z heights (0–76 and 0–110 μm respectively). Calcium transients were obtained from identified neurons indicated by the red circles. (**c**,**d**,**g**,**h**) Traces obtained from neurons in (**a**,**b**,**e**,**f**) respectively. Calcium transients in synchrony on both planes are framed by pink shadow bars and those in synchrony only on a single plane by blue shadow bars. (**i**) Cross-correlation Matrix of calcium transients $CT_{\mathcal{M}}$ obtained at 2 different focal planes (z_1 and z_2). Data from 8 (7) neurons at the focal plane z_1 (z_2). $CT_{\mathcal{M}}$ is partitioned in 4 regions, corresponding to the values of the cross-correlation among pairs of neurons in the same focal plane (the two squares along the diagonal, framed in light and dark blue) and among pairs of neurons in different focal planes (the two rectangles off the diagonal, framed in black). (**j**) The mean value of correlation coefficient for pairs of neurons on the same focal plane (blue), for pairs of neurons on different focal planes (black) and for all pairs of neurons (yellow). Collected data from 3 experiments (n = 79, 207 and 364 pairs of neurons, ***$p < 0.001$ ANOVA on ranks, Domm's post-hoc test). (**k**) Time evolution of the correlation coefficient cc computed over a bin width of 60 s for pairs of neurons on the same focal plane (light blue and blue line), for pairs of neurons on different focal planes (black line) and for all pairs of neurons (yellow line). Scale bar, 50 μm.

Discussion

The present manuscript demonstrates that the dynamics of 3D neuronal networks differ from those of 2D neuronal networks and better recapitulate what is observed *in vivo*[19,40]. This difference is due to a more extensive connectivity, which results in a more synchronous electrical activity[41] and frustrated synchrony. Our results extend and complete previous recent investigations[42,43], providing an experimental framework rationalizing theoretical results[9,10,23–25] and explaining why 2D and 3D neuronal networks have different properties. In addition to this, we show that graphene scaffolds are a solid and biocompatible support useful in biomedical applications.

We have identified two main regimes of spontaneous activity that depend on the degree of 3D connectivity: a high connectivity leads to an almost complete synchronization of the bursting activity (HS regime); in the presence of a less extensive connectivity, synchronous bursts coexist with local uncorrelated firing (MS regime).

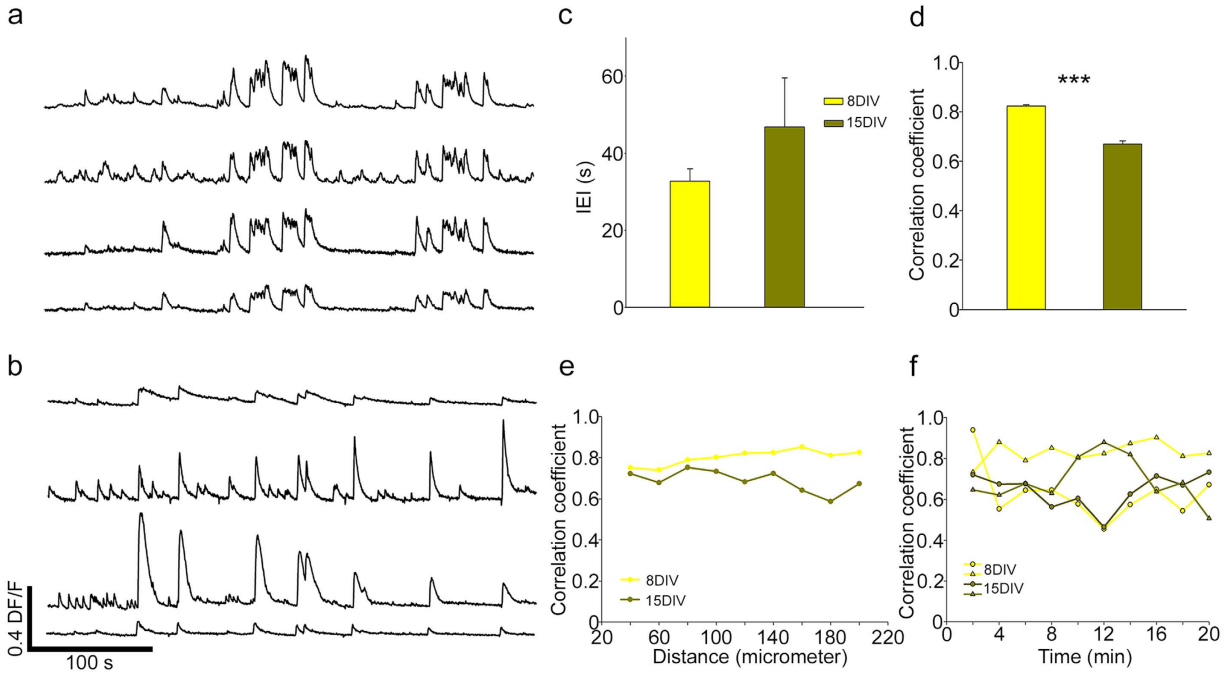

Figure 7. Changes of the degree of correlated activity of 3D neuronal networks during maturation. (**a**,**b**) Calcium transients of neurons cultured on 3D GF after 8DIV and 15 DIV respectively. (**c**) The mean value of IEI after 8DIV and 15DIV. (**d**) The correlation coefficient shows that there is a reduction in the network synchronization after 15DIV (***$p < 0.001$ Mann-Whitney test). (**e**) The correlation coefficient between pairs of neurons at different distances. While after 8DIV both near and far pairs of neurons are synchronous, at 15 DIV pairs of far neurons are less synchronous. (**f**) Time evolution of the correlation coefficient cc computed over a bin width of 2 minutes for 3D neuronal networks after 8DIV (yellow) and 15 DIV (green). The value of cc Correlation coefficient fluctuated similarly after 8 and 15DIV.

A recent approach allowed to study simultaneously the calcium activity of multiple layers of the mouse cortex with cellular resolution[44]; acquisition at two different fields of view separated by almost 300 μm showed that some neurons can have a highly correlated activity. Our almost simultaneous measurement of calcium transients on two different focal planes of the 3D-GF, vertically separated by 70–150 μm, allowed us to observe correlated activity both between neurons of the same focal plane and between neurons from different planes. These results also show that the degree of correlated electrical activity is modular and changes in size with time, in agreement with network theory[9,10,23–25] and experimental observations[19,40]. Therefore, neuronal networks grown on 3D-GFs recapitulate two basic properties of the complexity of the brain: firstly, the coexistence of local and global electrical activity (Fig. 4), and secondly, the existence of neuronal assembly with a degree of correlated electrical activity varying in space and time (Figs 1, 5 and 6). These two properties are not shared by 2D neuronal networks, and are the consequence of the dimensionality of networks grown on 3D-GFs.

Glial cells grown on 3D scaffolds maintain the *in vivo*-like complex morphology[2,45]. Almost 80% of astrocytes extended processes on our 3D-GFs, whereas glia with processes represented less than 40% of GFAP-positive cells on glass. The amount of "undifferentiated" astrocytes (i.e., lacking processes) reached almost 80% on 2D G, the opposite of what we observed on 3D-GFs. Therefore, the 3D topology, rather than graphene itself, promotes the extension of glial processes in all three dimensions, as it does *in vivo*[2,46].

The diameter of pores in 3D hydrogel scaffolds[47] and 3D nanofibers[2] are on the order of some tens of micrometres, varying from 20 to 60 μm. However, the pores in our 3D-GF scaffolds are larger by almost 1 order of magnitude. As shown in Fig. 5, neurites and even the cell bodies of neurons and glial cells could be found inside these holes. Crossings more often occurred near the edges of the holes, where the distance is shorter and more anchoring sites are present. Large pores lead to enhanced nutrient and oxygen diffusion[48] and the optimization of pore size is crucial.

Materials and Methods

Construction of the simulated 3D network and Kuramoto model. In order to construct the 3D network, first we place the nodes (neurons) along a 3D Pythagoras fractal tree.

This tree is formed by n = 8 number of iterations, it has a vector scale factor r = [0.5,0.8,0.8] a vector of azimuth angles of the fractal generator phi = [0,2*pi/3,4*pi/3], a vector of polar angles in fractal generator relative to the trunk chi = [pi/3,pi/3,pi/3], and coordinate of the trunk xb, yb and zb given by [0,0],[0,0],[0,1]. This tree can be generated with the FraktalT3D MATLAB code using the command

FraktalT3D (n,[0.5,0.8,0.8],[0,2*pi/3,4*pi/3],[pi/3,pi/3,pi/3],[0,0],[0,0],[0,1]).

Along the branches of the tree we place randomly the nodes (neurons) of the simulated network with an average density $\rho = 3$ neurons/unit length. We indicate with N the number of such neurons.

The simulated neuronal network is generated by placing short-range links between the neurons i and j with probability

$$p_{ij}^{SR} = e^{-d_{ij}/d_0^{SR}}, \tag{1}$$

and long-range links with probability

$$p_{ij}^{LR} = \delta \left(\frac{d_0^{LS}}{d_{ij}} \right)^{\alpha}, \tag{2}$$

where d_{ij} is the 3D distance between neuron i and neuron j, and d_0^{SR}, d_0^{LS}, δ and α are parameters determining the topology of the network.

For a wide range of parameter values the networks generated in this way are small world, have a modular structure and the distribution of the nodes is fractal.

On these networks we simulated a Kuramoto model of coupled oscillators, by numerically integrating the equations

$$\frac{d\theta_i}{dt} = \omega_i + \frac{K}{k_i} \sum_{j=1}^{N} a_{ij} \sin(\theta_j - \theta_i), \tag{3}$$

for $i = 1,2 \ldots N$, where θ_i is the phase of the oscillator i, K is the parameter determining the intensity of the coupling between the oscillators, ω_i is the intrinsic frequency of the oscillator i and is drawn randomly from a Gaussian distribution with zero average and unitary standard deviation, a_{ij} is the adjacency matrix of the network indication which neurons are connected together, and k_i is the degree of node i, i.e.

$$k_i = \sum_j a_{ij}.$$

In order to evaluate the synchronization property of the 3D network we have measured the order parameter R given by

$$R = \left| \frac{1}{N} \sum_{j=1N} e^{i\theta_j} \right| \tag{4}$$

which takes values between 0 and 1.

Large values of R indicate phase synchronizations while $R \approx 0$ indicates absence of synchronization.

We found, that for networks which are at the same time small world and fractal, three different phases of the synchronization dynamics occur as a function of the coupling K. These are: for high values of K, the fully synchronized phase characterized by large values of R which reach a steady state in time, for intermediate values of K, the frustrated synchronization characterized by intermediate values of R which do not reach a steady state in time, and for low values of K, the absence of synchronization characterized by very small values of R. These phases as described in the main text and typical simulations results are shown in Fig. 1e.

We note here that the network considered in Fig. 1d,e it is constructed by taking $d_0^{SR} = 0.025$, $d_0^{LS} = 0.01$, $\alpha = 2.5$ and a dynamics given by equation (3) with $K = 1$, $K = 9$ and $K = 25$.

Scaffold preparation. Graphene samples were synthesized using the chemical vapour deposition (CVD) method as described previously[14,49,50]. Briefly, the 3D-GFs were made via CVD using Ni foam as a template, whereas the 2D graphene films were prepared using a Cu foil as substrate. All heavy metal components were then chemically removed, and the substrates were rinsed with HNO_3, HCl and running water for at least 72 h to remove the etching agents. For sterilization, the scaffolds were treated with UV light for 20 min, followed by decreasing concentrations of ethanol (100%, 75%, 50% for 10 min). Finally, the scaffolds were rinsed with sterile deionized water (twice for 10 min).

Neuronal preparation and culture. Hippocampal neurons from Wistar rats (P2-P3) were prepared in accordance with the guidelines of the Italian Animal Welfare Act, and their use was approved by the Local Veterinary Service, the SISSA Ethics Committee board and the National Ministry of Health (Permit Number: 630-III/14) in accordance with the European Union guidelines for animal care (d.1.116/92; 86/609/C.E.). The animals were anaesthetized with CO_2 and sacrificed by decapitation, and all efforts were made to minimize suffering. All substrates (2D glass coverslips, 2D graphene films and 3D-GFs) were coated with 50 μg/ml poly-L-ornithine (Sigma-Aldrich, St. Louis, MO, USA) overnight, soaked in culture medium overnight and coated with Matrigel just before cells seeding (Corning, Tewksbury MA, USA). Dissociated cells were plated at a concentration of 6×10^5 cells/ml on 2D substrates and 2.4×10^6 cells/ml on 3D-GF in minimum essential medium (MEM) with GlutaMAX™ supplemented with 10% foetal bovine serum (FBS, all from Invitrogen, Life Technologies, Gaithersburg, MD, USA), 0.6% D-glucose, 15 mM Hepes, 0.1 mg/ml apo-transferrin, 30 μg/ml insulin, 0.1 μg/ml D-biotin, 1 μM vitamin B12 (all from Sigma-Aldrich), and 2.5 μg/ml gentamycin (Life Technologies). After 48 hours, 2 μM cytosine-β-D-arabinofuranoside (Ara-C; Sigma-Aldrich) was added to the culture medium to

block glial cell proliferation, and the concentration of FBS was decreased to 5%. Half of the medium was changed every 2–3 days. The neuronal cultures were maintained in an incubator at 37 °C, 5% CO_2 and 95% relative humidity. The cell concentration was adjusted to ensure comparable cell numbers on all substrates. Unlike the 2D substrates, on which all plated cells uniformly deposit on the surface, the 3D-GFs retain cells, which permeate the pores.

Calcium Imaging. The cells were loaded with a cell-permeable calcium dye Fluo4-AM (Life Technologies) by incubating them with 4 μM Fluo4-AM (dissolved in anhydrous DMSO (Sigma-Aldrich), stock solution 4 mM) and Pluronic F-127 20% solution in DMSO (Life Technologies) at a ratio of 1:1 in Ringer's solution (145 mM NaCl, 3 mM KCl, 1.5 mM $CaCl_2$, 1 mM $MgCl_2$, 10 mM glucose and 10 mM Hepes, pH 7.4) at 37 °C for 1 hour. After incubation, the cultures were washed and then transferred to the stage of a Nikon Eclipse Ti-U inverted microscope equipped with a piezoelectric table (Nano-ZI Series 500 μm range, Mad City Labs), an HBO 103 W/2 mercury short arc lamp (Osram, Munich, Germany), a mirror unit (exciter filter BP 465–495 nm, dichroic 505 nm, emission filter BP 515–555) and an Electron Multiplier CCD Camera C9100-13 (Hamamatsu Photonics, Japan). The experiments were performed at RT, and images were acquired using the NIS Element software (Nikon, Japan) with an S-Fluor 20x/0.75 NA objective at a sampling rate of 3–10 Hz with a spatial resolution of 256 × 256 pixels for 10–20 min. To avoid saturation of the signals, excitation light intensity was attenuated by ND4 and ND8 neutral density filters (Nikon).

Data Analysis. *Ca^{2+} imaging processing and analysis.* The initial video was processed with the ImageJ (U. S. National Institutes of Health, Bethesda, MA) software. The image sequences were then analysed as described previously[51]. Briefly, neurons were localized, and an appropriate region of interest (ROI) was selected to subtract the background. Appropriate ROIs around the cells bodies were then selected. The time course of the fluorescence intensity, $I_f(t)$, in this ROI was displayed, and any decay, which is a consequence of dye bleaching, was evaluated. The Ca^{2+} transients of each cell signal were extracted in a semi-automatic manner by selecting a threshold for the smallest detectable peak that was equal to three times the standard deviation of the baseline. Subsequently, the decay of $I_f(t)$ was fitted to a cubic spline interpolating $I_f(t)$ at 10 or 20 points. $I_f(t)$ was then fitted to the original optical signal to compensate for dye bleaching, and the fractional optical signal was calculated as follows: $DF/F = (Y(t)+I_f(t))/I_f(0)$, where $I_f(0)$ is the fluorescence intensity at the beginning of the recording.

Computation of raster plot and correlation coefficient of Ca^{2+} transient occurrence. The times, t_i, at which transient peaks occurred are presented in a conventional raster plot. To isolate the smaller transients from the larger ones, the single traces were considered independently. The amplitude distribution of peaks was calculated to separate the two different classes of events. Based on this distribution, a threshold was set to approximately 30% of the maximum amplitude. All peaks under the threshold were considered small, whereas all other peaks were considered to be large calcium transients.

The correlation coefficient of the calcium transients for neuron i and neuron j (σ_{CTij}) was computed as follows: The total recording time, T_{tot}, was divided into N intervals (1,..,n,…,N) of a duration Δt. Thus, if f_{in} and f_{jn} are the number of calcium transients of neuron i and neuron j in the time interval Δt_n, then

$$\sigma_{CT_{ij}} = \frac{\sum_n f_{in} f_{jn}}{\sqrt{(\sum_n f_{in}^2)(\sum_n f_{jn}^2)}} \tag{5}$$

such that σ_{CTij} depends on Δt and varies between 0 and 1. The range of explored values of Δt was 20 s.

Computation of cross-correlation of slow Ca^{2+} oscillation. Because we observed that Ca^{2+} transients can occur both during a positive phase and a negative phase of Ca^{2+} fluctuation, we also analysed and computed the correlation coefficient of slow Ca^{2+} oscillation. The correlation coefficient of this type of oscillation can be negative, whereas σ_{CTij} can only vary between 0 and 1. The correlation coefficient of slow Ca^{2+} oscillation obtained for neuron i and neuron j (σ_{SLOWij}) was computed as follows:

If s_{in} is the slow signal from neuron i at time t_n, its mean value, $\langle s_i \rangle$, is given by $\frac{\sum_n s_{in}}{N}$ where N is the total number of available samples.

$$\sigma_{SLOW_{ij}} = \frac{\sum_n (s_{in} - \langle s_i \rangle)(s_{jn} - \langle s_j \rangle)}{\sqrt{(\sum_n (s_{in} - \langle s_i \rangle)^2)(\sum_n (s_{jn} - \langle s_j \rangle)^2)}} \tag{6}$$

so that σ_{SLOWij} varies between −1 and 1 and σ_{SLOWij} was computed at the same time interval of σ_{CTij}.

Morphological and immunocytochemical analysis. Cells were fixed in 4% paraformaldehyde containing 0.15% picric acid in phosphate-buffered saline (PBS), saturated with 0.1 M glycine, permeabilized with 0.1% Triton X-100, saturated with 0.5% BSA (all from Sigma-Aldrich) in PBS and then incubated for 1 h with primary antibodies: mouse monoclonal glial fibrillary acidic protein (GFAP), rabbit polyclonal against MAP2 and GABA (all from Sigma-Aldrich), anti-β-tubulin III (TUJ1) and SMI 312 mouse monoclonal antibodies (Covance, Berkeley, CA). The secondary antibodies were goat anti-rabbit Alexa Fluor® 488, goat anti-mouse Alexa Fluor® 594, goat anti-mouse immunoglobulin (Ig) G_1 Alexa Fluor® 488, goat anti-mouse IgG_{2a} Alexa Fluor® 594, (all from Life Technologies) and the incubation time was 30 min. Nuclei were stained with 2 μg/ml in PBS Hoechst 33342 (Sigma-Aldrich) for 5 min. All the incubations were performed at room temperature (20–22 °C). The cells

were examined using a Leica DM6000 fluorescent microscope equipped with DIC and fluorescence optics, CCD camera and Volocity 5.4 3D imaging software (PerkinElmer, Coventry, UK). The fluorescence images were collected with a 20x magnification and 0.5 NA objective. For each image at least 30 slices were acquired with slice spacing of 0.5 μm. Image J by W. Rasband (developed at the U.S. National Institutes of Health and available at http://rsbweb.nih.gov/ij/) was used for image processing.

Statistical analysis. Data are shown as the mean ± s.e.m from at least three neuronal cultures. For the morphological analysis of immunofluorescence images (Fig. 2), n refers to the number of images analysed, and the number in brackets refers to total number of cells analysed. The quantified activity (IEI and Cross-correlation) and morphological data were analysed with the ANOVA test followed by post hoc comparisons using the software SygmaPlot 10.0. Differences among two groups were evaluated with Kolmogorov-Smirnov test, Student's-t test or Mann-Whitney test (Statistica 6.0 – StatSoft Italy). The number of replicates and statistical tests used for each experiment are mentioned in the respective figure legends or in the Results. Significance was set to $*p < 0.05$, $**p < 0.01$ and $***p < 0.001$.

References

1. Irons, H. R. *et al.* Three-dimensional neural constructs: a novel platform for neurophysiological investigation. *J. Neural Eng.* **5,** 333–341 (2008).
2. Puschmann, T. B. *et al.* Bioactive 3D cell culture system minimizes cellular stress and maintains the *in vivo*-like morphological complexity of astroglial cells. *Glia* **61,** 432–440 (2013).
3. Baker, B. M. & Chen, C. S. Deconstructing the third dimension: how 3D culture microenvironments alter cellular cues. *J. Cell Sci.* **125,** 3015–3024 (2012).
4. Sporns, O. Networks of the Brain. *MIT Press* (2010). Available at: https://mitpress.mit.edu/books/networks-brain. (Accessed: 3rd August 2015).
5. Buzsaki, G. Rhythms of the Brain - Gyorgy Buzsaki - Oxford University Press. (2006). Available at: https://global.oup.com/academic/product/rhythms-of-the-brain-9780199828234?cc=it&lang=en&. (Accessed: 3rd August 2015).
6. Bullmore, E. & Sporns, O. Complex brain networks: graph theoretical analysis of structural and functional systems. *Nat. Rev. Neurosci.* **10,** 186–198 (2009).
7. Bassett, D. S. & Bullmore, E. Small-World Brain Networks. *The Neuroscientist* **12,** 512–523 (2006).
8. Bullmore, E. T. & Bassett, D. S. Brain graphs: graphical models of the human brain connectome. *Annu. Rev. Clin. Psychol.* **7,** 113–140 (2011).
9. Villegas, P., Moretti, P. & Muñoz, M. A. Frustrated hierarchical synchronization and emergent complexity in the human connectome network. *Sci. Rep.* **4,** 5990 (2014).
10. Gallos, L. K., Makse, H. A. & Sigman, M. A small world of weak ties provides optimal global integration of self-similar modules in functional brain networks. *Proc. Natl. Acad. Sci. USA* **109,** 2825–2830 (2012).
11. Gilmour, A. D., Woolley, A. J., Poole-Warren, L. A., Thomson, C. E. & Green, R. A. A critical review of cell culture strategies for modelling intracortical brain implant material reactions. *Biomaterials* **91,** 23–43 (2016).
12. Aregueta-Robles, U. A., Woolley, A. J., Poole-Warren, L. A., Lovell, N. H. & Green, R. A. Organic electrode coatings for next-generation neural interfaces. *Front. Neuroengineering* **7,** 15 (2014).
13. Novoselov, K. S. *et al.* A roadmap for graphene. *Nature* **490,** 192–200 (2012).
14. Li, N. *et al.* Three-dimensional graphene foam as a biocompatible and conductive scaffold for neural stem cells. *Sci. Rep.* **3,** 1604 (2013).
15. Li, N. *et al.* The promotion of neurite sprouting and outgrowth of mouse hippocampal cells in culture by graphene substrates. *Biomaterials* **32,** 9374–9382 (2011).
16. Tang, M. *et al.* Enhancement of electrical signaling in neural networks on graphene films. *Biomaterials* **34,** 6402–6411 (2013).
17. Song, Q. *et al.* Anti-inflammatory effects of three-dimensional graphene foams cultured with microglial cells. *Biomaterials* **35,** 6930–6940 (2014).
18. Bando, Y. *et al.* Control of Spontaneous Ca2+ Transients Is Critical for Neuronal Maturation in the Developing Neocortex. *Cereb. Cortex N. Y. N 1991*, doi: 10.1093/cercor/bhu180 (2014).
19. Gonçalves, J. T., Anstey, J. E., Golshani, P. & Portera-Cailliau, C. Circuit level defects in the developing neocortex of Fragile X mice. *Nat. Neurosci.* **16,** 903–909 (2013).
20. Okamoto, K. *et al. Ex vivo* cultured neuronal networks emit *in vivo*-like spontaneous activity. *J. Physiol. Sci. JPS* **64,** 421–431 (2014).
21. Kirkby, L. A., Sack, G. S., Firl, A. & Feller, M. B. A role for correlated spontaneous activity in the assembly of neural circuits. *Neuron* **80,** 1129–1144 (2013).
22. Winnubst, J., Cheyne, J. E., Niculescu, D. & Lohmann, C. Spontaneous Activity Drives Local Synaptic Plasticity *In Vivo*. *Neuron* **87,** 399–410 (2015).
23. Barahona, M. & Pecora, L. M. Synchronization in Small-World Systems. *Phys. Rev. Lett.* **89,** 54101 (2002).
24. Chavez, M., Hwang, D.-U., Amann, A., Hentschel, H. G. E. & Boccaletti, S. Synchronization is enhanced in weighted complex networks. *Phys. Rev. Lett.* **94,** 218701 (2005).
25. Sorrentino, F., Di Bernardo, M., Cuellar, G. H. & Boccaletti, S. Synchronization in weighted scale-free networks with degree–degree correlation. *Phys. Nonlinear Phenom.* **224,** 123–129 (2006).
26. Arenas, A., Diaz-Guilera, A., Kurths, J., Moreno, Y. & Zhou, C. Synchronization in complex networks. *Phys. Rep.* **469,** 93–153 (2008).
27. Winfree, A. T. *The Geometry of Biological Time*. 12, (Springer New York, 2001).
28. Hong, H., Park, H. & Choi, M. Y. Collective phase synchronization in locally-coupled limit-cycle oscillators. *Phys. Rev. E* **70** (2004).
29. Hong, H., Chaté, H., Park, H. & Tang, L.-H. Entrainment transition in populations of random frequency oscillators. *Phys. Rev. Lett.* **99,** 184101 (2007).
30. Kalman, D., Gomperts, S. N., Hardy, S., Kitamura, M. & Bishop, J. M. Ras family GTPases control growth of astrocyte processes. *Mol. Biol. Cell* **10,** 1665–1683 (1999).
31. Verstraelen, P. *et al.* Pharmacological characterization of cultivated neuronal networks: relevance to synaptogenesis and synaptic connectivity. *Cell. Mol. Neurobiol.* **34,** 757–776 (2014).
32. Chamberland, S. & Topolnik, L. Inhibitory control of hippocampal inhibitory neurons. *Front. Neurosci.* **6,** 165 (2012).
33. Jinno, S. & Kosaka, T. Cellular architecture of the mouse hippocampus: a quantitative aspect of chemically defined GABAergic neurons with stereology. *Neurosci. Res.* **56,** 229–245 (2006).
34. Matyash, V. & Kettenmann, H. Heterogeneity in astrocyte morphology and physiology. *Brain Res. Rev.* **63,** 2–10 (2010).
35. Scemes, E. & Giaume, C. Astrocyte calcium waves: what they are and what they do. *Glia* **54,** 716–725 (2006).
36. Cellot, G. *et al.* Carbon nanotubes might improve neuronal performance by favouring electrical shortcuts. *Nat Nano* **4,** 126–133 (2009).
37. Fabbro, A. *et al.* Graphene-Based Interfaces Do Not Alter Target Nerve Cells. *ACS Nano* **10,** 615–623 (2016).

38. Cossart, R., Ikegaya, Y. & Yuste, R. Calcium imaging of cortical networks dynamics. *Cell Calcium* **37,** 451–457 (2005).
39. Pinato, G., Pegoraro, S., Iacono, G., Ruaro, M. E. & Torre, V. Calcium control of gene regulation in rat hippocampal neuronal cultures. *J. Cell. Physiol.* **220,** 727–747 (2009).
40. Golshani, P. *et al.* Internally mediated developmental desynchronization of neocortical network activity. *J. Neurosci. Off. J. Soc. Neurosci.* **29,** 10890–10899 (2009).
41. Takahashi, N., Sasaki, T., Matsumoto, W., Matsuki, N. & Ikegaya, Y. Circuit topology for synchronizing neurons in spontaneously active networks. *Proc. Natl. Acad. Sci. USA* **107,** 10244–10249 (2010).
42. Bosi, S. *et al.* From 2D to 3D: novel nanostructured scaffolds to investigate signalling in reconstructed neuronal networks. *Sci. Rep.* **5,** 9562 (2015).
43. Frega, M., Tedesco, M., Massobrio, P., Pesce, M. & Martinoia, S. Network dynamics of 3D engineered neuronal cultures: a new experimental model for *in-vitro* electrophysiology. *Sci. Rep.* **4,** 5489 (2014).
44. Yang, W. *et al.* Simultaneous Multi-plane Imaging of Neural Circuits. *Neuron* **89,** 269–284 (2016).
45. Puschmann, T. B., de Pablo, Y., Zandén, C., Liu, J. & Pekny, M. A novel method for three-dimensional culture of central nervous system neurons. *Tissue Eng. Part C Methods* **20,** 485–492 (2014).
46. Allaman, I., Bélanger, M. & Magistretti, P. J. Astrocyte-neuron metabolic relationships: for better and for worse. *Trends Neurosci.* **34,** 76–87 (2011).
47. Hanson Shepherd, J. N. *et al.* 3D Microperiodic Hydrogel Scaffolds for Robust Neuronal Cultures. *Adv. Funct. Mater.* **21,** 47–54 (2011).
48. Li, H., Wijekoon, A. & Leipzig, N. D. 3D differentiation of neural stem cells in macroporous photopolymerizable hydrogel scaffolds. *PloS One* **7,** e48824 (2012).
49. Li, X. *et al.* Large-area synthesis of high-quality and uniform graphene films on copper foils. *Science* **324,** 1312–1314 (2009).
50. Tang, M. *et al.* Enhancement of electrical signaling in neural networks on graphene films. *Biomaterials* **34,** 6402–6411 (2013).
51. Moshtagh-Khorasani, M., Miller, E. W. & Torre, V. The spontaneous electrical activity of neurons in leech ganglia. *Physiol. Rep.* **1,** e00089 (2013).

Acknowledgements

The research leading to these results has received funding from the European Union's Seventh Framework Programme under grant agreement FP7 ICT 2011 – 284553 (Acronym: Si-CODE), the NEUROSCAFFOLDS Project n. 604263, the National Natural Science Foundation of China (Grant number: 51361130033) and the Ministry of Science and Technology of China (973 Grant number: 2014CB965003). We thank Beatrice Pastore for technical assistance, Giulietta Pinato for useful discussions and Rossana Rauti for help with the statistical analysis and Manuela Schipizza Lough for carefully reading the manuscript.

Author Contributions

F.P.U.S. prepared the cultures, performed calcium imaging experiments with Q.S. and M.T. and analyzed the data. J.B. performed immunofluorescence experiments and morphological analysis. Q.S., M.T. and G.C. provided 2D graphene films and 3D graphene scaffolds. G.B. prepared network model. V.T. planned the experiments and wrote the paper with F.P.U.S., J.B. and G.B. All other authors read and commented on the manuscript.

Additional Information

Supplementary information accompanies this paper at http://www.nature.com/srep

Competing financial interests: The authors declare no competing financial interests.

How to cite this article: Ulloa Severino, F. P. *et al.* The role of dimensionality in neuronal network dynamics. *Sci. Rep.* **6**, 29640; doi: 10.1038/srep29640 (2016).

Supplementary Information

The role of dimensionality in neuronal network dynamics

Francesco Paolo Ulloa Severino[1†], Jelena Ban[1†], Qin Song[2], Mingliang Tang[3], Ginestra Bianconi[4], Guosheng Cheng[2*] and Vincent Torre[1*]

[1]Neurobiology Sector, International School for Advanced Studies (SISSA), via Bonomea, 265, 34136 Trieste, Italy

[2]Key Laboratory of Nano-Bio Interface, Suzhou Institute of Nano-tech and Nano-bionics, Chinese Academy of Sciences, 398 Ruoshui Road, Jiangsu 215123, China

[3]Institute of Life Sciences, Southeast University, Sipailou 2, Nanjing 210096, China

[4]School of Mathematical Sciences, Queen Mary University of London, Mile End Rd, London E1 4NS, United Kingdom

†These authors contributed equally

* Corresponding authors:

Vincent Torre, email: torre@sissa.it

Cheng Guosheng, email: gscheng2006@sinano.ac.cn

Supplementary Figure S1

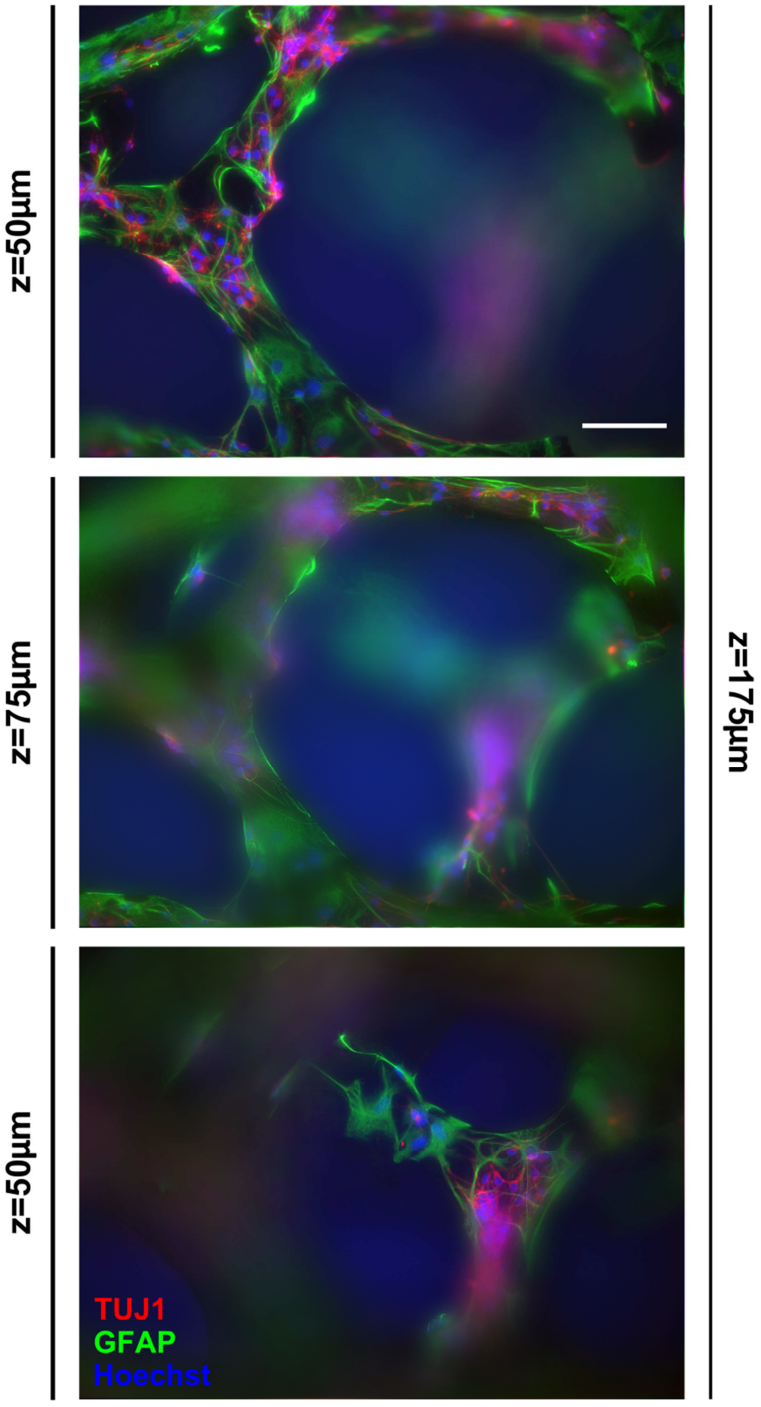

Supplementary Figure S1. Neuronal network is continuous throughout the 3D-GF backbone. From top to bottom: three consecutive z-projections for the 175 µm thick z-stack. The thickness of each sub-stack is indicated on the left and the total z-stack thickness is indicated on the right. Images were acquired with slice spacing of 0.5 µm and derive from the neuronal culture grown for 7 DIV on 3D-GFs and stained for β-tubulin III (TUJ1, red), glial fibrillary acidic protein (GFAP, green) and Hoechst 33342 nuclear stain (blue). Scale bar, 100 µm.

Supplementary Figure S2

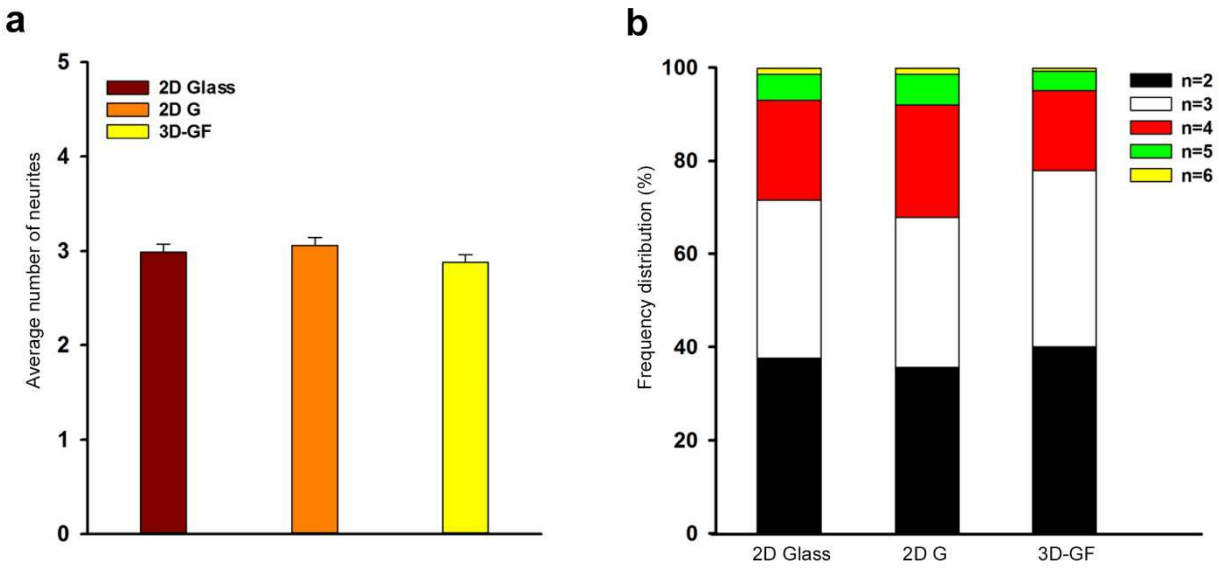

Supplementary Figure S2. Neurite outgrowth is similar between 2D and 3D neuronal networks. (a) The average number of neurite per neuron was obtained from fluorescence images of neurons stained for MAP2 at 7 DIV. (b) Frequency distribution of neurite numbers for glass, 2D-G and 3D-GFs. n refers to number of neurites per neuron.

Supplementary Figure S3

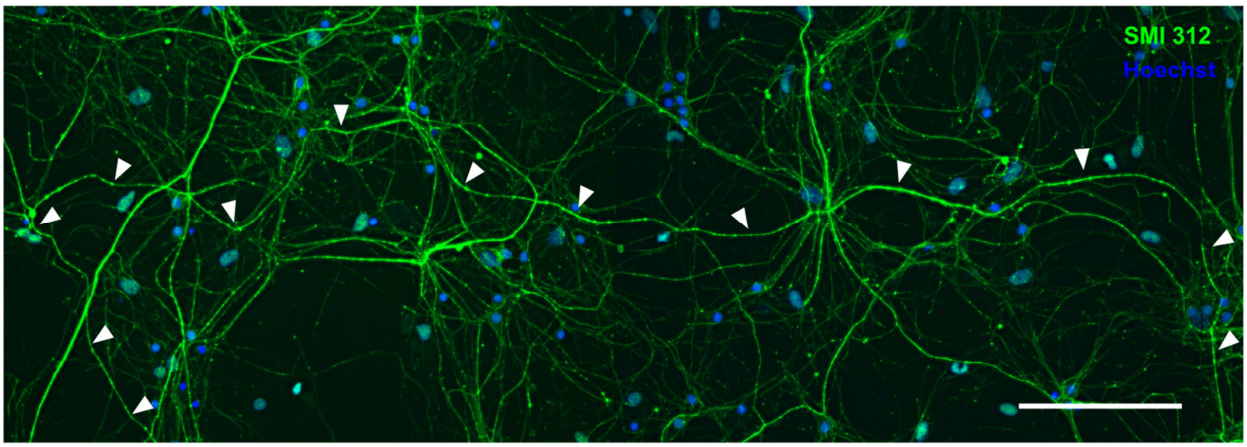

Supplementary Figure S3. After two weeks of culture axons can reach millimeter length. Fluorescent image of hippocampal culture at 14 DIV cultured on glass and stained for axonal marker SMI 312. Cell nuclei were marked by Hoechst 33342. Arrowheads follow the axon that extends for several hundreds of micrometer reaching millimeter length. Similar axon outgrowth was observed also on 2D-G and 3D-GFs. Scale bar, 100 µm.

Supplementary Figure S4

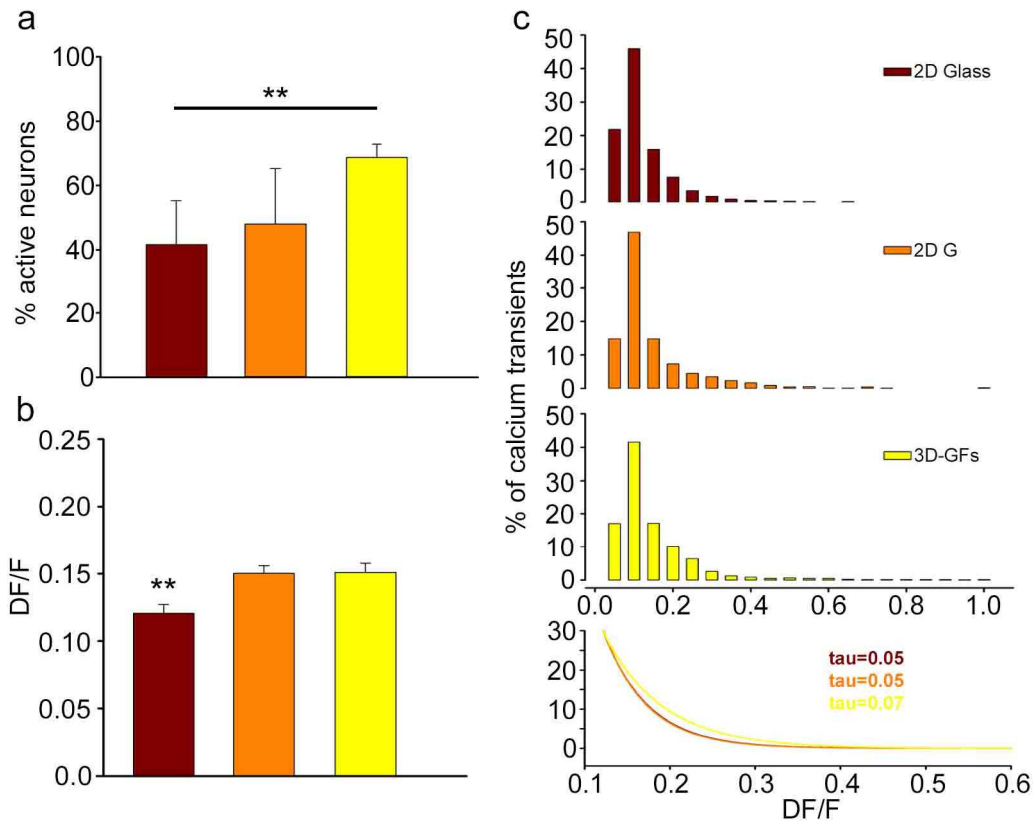

Supplementary Figure S4. Standard analysis of network activity. (a) Percentage of active neurons for 2D Glass, 2D-G and 3D-GFs respectively. Significant difference is reported comparing 2D Glass and 3D-GFs (**=p<0.01 ANOVA on ranks, Domm's post-hoc test). (b) Weighted mean of Ca^{2+}-transients amplitude (averaged over the single neurons). 2D-G and 3D-GFs have comparable values, neurons on 2D Glass show a significant reduction (**=p<0.01 ANOVA on ranks, Domm's post-hoc test). (c) Frequency distribution of the amplitudes for the three conditions. The bottom panel show the exponential fitting curve used to evaluate the decay time of the chart.

Supplementary Information 1

Comparison of the 2D cultures

In this work we used two different experimental controls: glass coverslip (2D Glass) and 2D graphene films (2D-G). Standard 2D neuronal networks are most commonly cultured on glass, while graphene films (see Methods) represent an additional control for material. In order to understand if the differences observed with neuronal networks on 3D scaffolds are due to graphene or 3D arrangement, we performed additional morphological and functional analysis in which we compared 2D cultures.

Supplementary Figure S5 shows that after 7 DIV - although glia to neuron ratio is similar between 2D cultures (see Figure 2 of the manuscript) - astrocytes on 2D-G are larger, have less processes and cover completely the substrate (see Supplementary Fig. S5b). These differences were even more pronounced after 14 DIV where cell-free regions on glass surface increase while on 2D-G astrocytes retain their morphology and cover completely the surface (compare panel c and d of Supplementary Fig. S5). Similarly, after 14 DIV we observe a denser neuronal network on 2D-G, as shown by the staining of axons with SMI 312 (Supplementary Figure S5e-f). All these observations indicate that on 2D-G cells survive better than on glass.

The observed differences could be related to the roughness of the graphene films surface that could enhance cell adhesion[1]. Further investigations are required using adhesion markers such as integrin, paxillin or vinculin.

Morphological observations can be confirmed by the functional data. We observed that graphene itself does not affect the rate of activity (see Figure 3j), but higher density of neurites could have some effect on the synchronization (see Figure 3m). However, it still remains significantly different (i.e. lower) to what observed for 3D cultures.

Moreover, we specify that the electrical conductivity of the materials alone, as well as their nanostructure, have been reported not to affect the excitability of neurons suggesting the synergy of multiple properties as a key factor[2]. In addition, few-layer graphene does not affect the frequency of the neuronal activity[3].

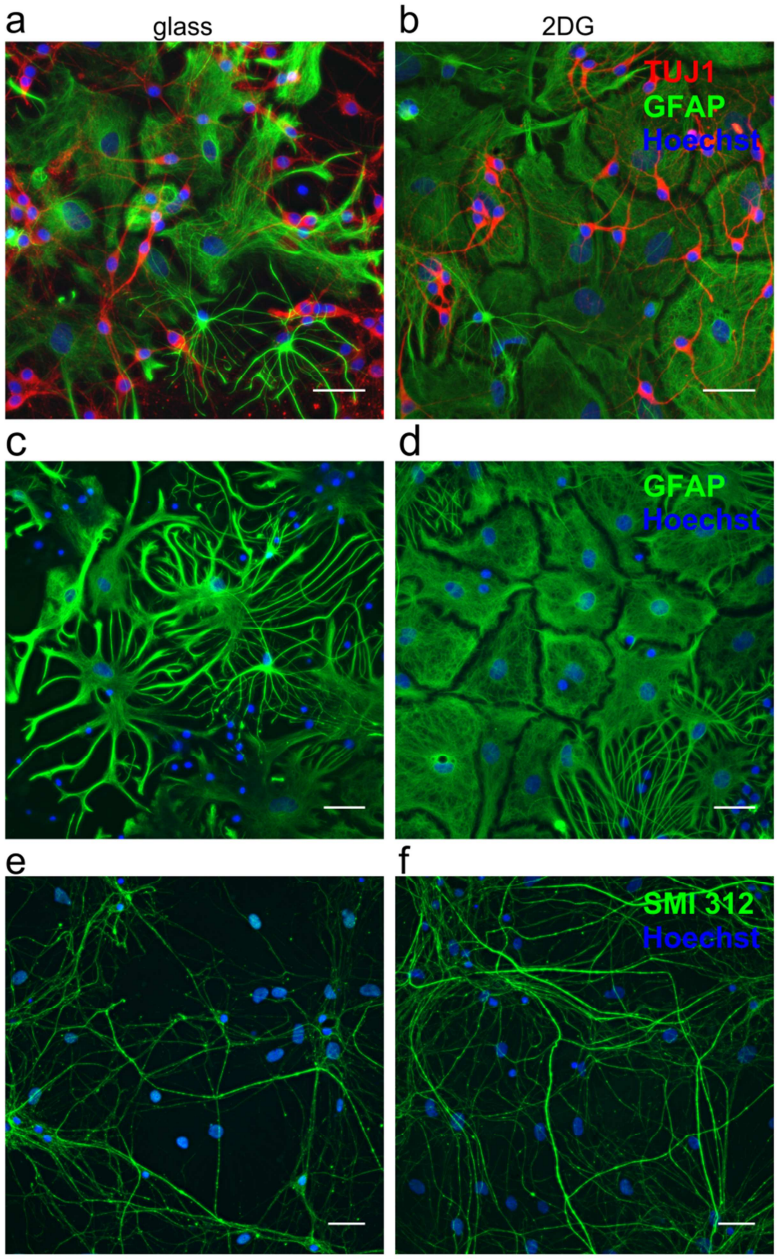

Supplementary Figure S5. Morphological comparison of 2D cultures. Hippocampal culture at 7 DIV on glass (a) and 2D-G (b) stained for β-tubulin III (TUJ1, red) and glial fibrillary acidic protein (GFAP, green). (c-d) GFAP-positive astrocytes (green) and (e-f) SMI 312-positive axons (green) after 14 DIV on glass (left) and 2D-G (right) respectively. Nuclei were stained with Hoechst 33342 nuclear stain (blue). Scale bar, 50µm.

1. Lorenzoni, M., Brandi, F., Dante, S., Giugni, A. & Torre, B. Simple and effective graphene laser processing for neuron patterning application. *Sci. Rep.* **3,** 1954 (2013).
2. Cellot, G. *et al.* Carbon nanotubes might improve neuronal performance by favouring electrical shortcuts. *Nat Nano* **4,** 126–133 (2009).
3. Fabbro, A. *et al.* Graphene-Based Interfaces Do Not Alter Target Nerve Cells. *ACS Nano* **10,** 615–623 (2016).

Supplementary Videos

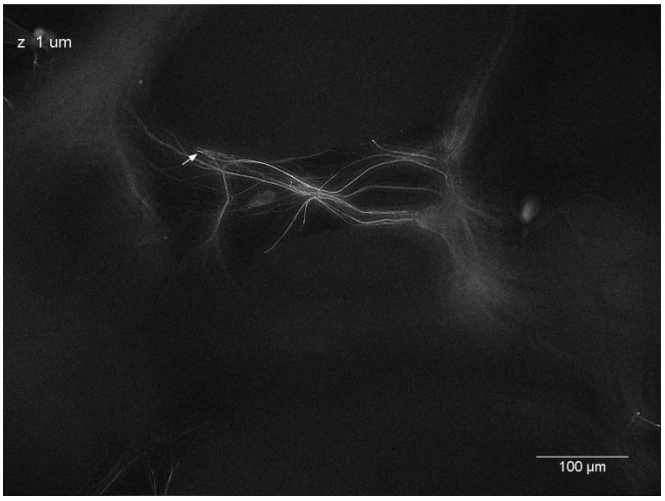

Supplementary Video S1. Axonal projection in 3D space. Axons on 3D-GFs project in all three dimensions connecting the different layers and extending for several hundreds of micrometers. Images were acquired with 20x and 0,5 NA objective for a total thickness of 95 µm with slice spacing of 1 µm. Cells were cultured for 2 weeks on 3D-GFs and stained with axonal marker SMI 312. The arrow follows the axon that connects different planes of the scaffold.

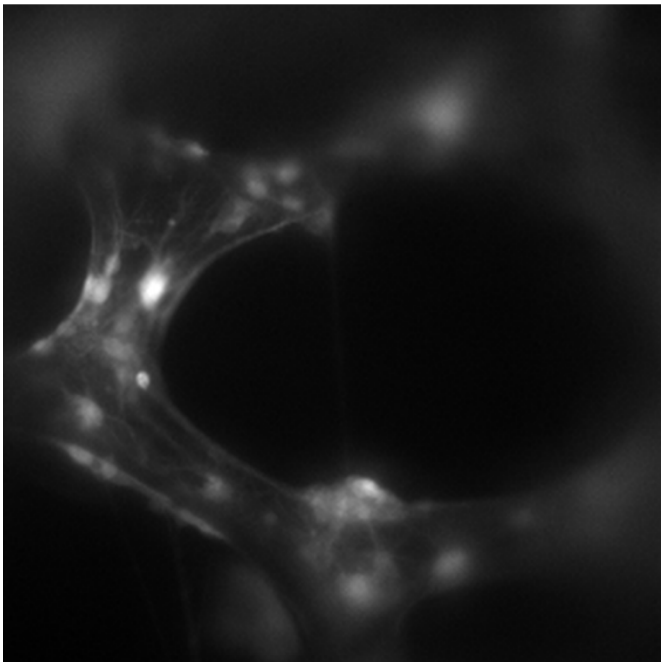

Supplementary Video S2. Calcium imaging. Neuronal culture loaded with 4µM Fluo-4-AM calcium indicator on 3D-GF. Images were acquired with 20x and 0,75 NA objective, 5 Hz, a spatial resolution of 256 × 256 pixels and for 10 min. The movie reproduction has been made using 25 frames per second.

5. CONCLUSIONS AND PERSPECTIVES

Two-dimensional *in vitro* models remain the predominant culture method, but it is now clear that we need a more realistic system to investigate physiological processes *in vitro*. This concept is true for the nervous system as well as for any other organ and tissue.
One of the most recent methodologies is the creation of organoids[1,2], which rely on the application of the stem cell technology to have self-organized structures that can be used to investigate developmental processes or diseases[3–5]. However, there are still limitations to deal with and we can tackle those limitations using biocompatible materials and developing scaffolds as support for cell growth and development.

All together, the results obtained during my Ph.D. training, show that to achieve complex connectivity among neurons, 3D scaffolds with distinct electric and topographic properties can be applied. Our aim was to improve our knowledge on how scaffold-based three-dimensional neuronal networks work and what kind of recent technology may be used to build them in such a way that mimics the *in vivo* condition. I developed and tested a series of scaffolds made of different materials and geometries as a platform technology to be applied to different scientific purposes. Herein, I explored their use in neurobiology and neuronal network studies.
Starting from easy handling substrates designed as an annulus with a honeycomb structure of PEGDA covered by a gold film to support the electrospinning of gelatin nanofibers, we built a soft structure that provides the topographical cues of a three-dimensional environment. Grown under such conditions, neurons and astrocytes show different properties in terms of activity and morphology. The increased connectivity among neurons, the ramified shape of astrocytes, the possibility to be surrounded by nutrients, the stiffness and/or the topology of the substrate are all possible reasons for the higher firing frequency of neurons as compared to standard culture conditions. Although this patch method lacks of vertical connections among neurons, it represents a good model for electrophysiological, live cell imaging and cell-material interaction studies. Moreover, it is possible to apply electrical stimuli to the gold film and investigate the evoked cellular responses, as well as the effects of the overexcitation on developing neurons, opening the possibilities to use this device also in biomedicine.

Then, the development of a 3D patterning process based on conventional photolithography techniques, made it possible to produce 3D lattice-type scaffolds made of PDMS with defined mechanical properties and geometric parameters. We tested different parameters for the lattices (i.e. heights, thickness, node-to-node space) to exploit all the possible configurations and find the most appropriate conditions to culture primary neurons. By using this approach, we could increase the dimensionality of our network, having cells on different heights on a soft substrate like PDMS, and have connections in vertical dimension. We could obtain a culture with a good cell-material interaction and similar *in vivo*-like properties, as observed on the nanofiber patch. Moreover, the control of the lithography parameters allowed us to separate the PDMS lattice from the substrate, which shows its potential to the application in tissue engineering and transplantation, as already proposed[6]. However, there were still limitations in this approach, such as the limited maximum heights of the PDMS pillars.

We went a step forward and realized a real three-dimensional scaffold-based culture using graphene foams. This biocompatible structure was already used to culture NSCs and microglia[7,8], so we used it to grow a network of primary hippocampal cells. We were unexpectedly able to build a neuronal network through the entire scaffold height (1-1.5 mm) and keep it alive for weeks. This opened new opportunity to study the neuronal activity of 3D networks. We found out that the morphology and the dynamics of 3D neuronal networks differ from those of 2D neuronal networks and better recapitulate what is observed *in vivo*; we also have evidences supporting the hypothesis that these dynamic changes are due to a more extensive connectivity.

We could identify two main regimes of spontaneous activity depending on the degree of 3D connectivity: a high connectivity leads to an almost complete synchronization of the bursting activity (HS regime); in the presence of a less extensive connectivity, synchronous bursts coexist with local uncorrelated firing (MS regime). Overall, the activity of the network has a high level of synchronization that oscillates between different focal planes and decreases with the maturation of the network. The use of graphene, with its peculiar properties, to build the 3D scaffold can lead to many possible applications, from brain implants to the construction of stimulating devices for *in vitro* and *in vivo* applications.

What is the next step toward the improvement of 3D scaffold-based cultures? There is not a single answer to address this question. Aiming at creating an even more real 3D culture, we are now working to have cortical cells growing in suspension in an innovative structure

made of graphene foam and carbon nanotubes that supports the growth of neuronal processes through the pores of the structure and hosts a higher number of cells. This will allow us to reproduce an almost full piece of brain tissue, having the space for the nutrients and oxygen circulation, which are necessary for survival[9]. Moreover, we are using this new scaffold for glioblastoma invasion studies in 3D, both in the absence and presence of cortical neurons.

A relevant issue to better understand 3D cultures is to compare a 3D scaffold-based *in vitro* model to a positive control, such as organotypic cultures or acute slices, in order to understand how close we are to the network dynamics of an *in-vivo* preparation. Moreover, it could be interesting to investigate in more detail the reasons behind the more elevated frequency and synchronization of 3D neuronal networks. It is possible that the different morphology of astrocytes or a different time of maturation of the network or, finally, the presence of more and longer connections can affect the neuronal spontaneous activity.

Even though we use all our efforts to reconstruct a scaffold-based 3D culture, we still have limitations if we aim to mimic the real tissue. The cortex, for instance, is made by six well organized layers to carry out peculiar functions; here we can only have a randomly organized neuronal network since there is no control on the position of any cell type.. There are some attempt to overcome this limitation[10], but they still rely on expedients. What would be useful is the development of combined scaffolds that allows the controlled release of molecules to differentiate neural progenitor cells in specific kind of neurons and have self-organized 3D scaffold-based cultures. The joint application of biomaterials and stem cell technology will provide us a new concept of lab-on-a-chip[11,12], where we could support the culture structure, control the release of molecules for cell self-organization and differentiation, as well as for vascular infiltration (for *in vivo* applications), reduce the use of animals in basic research and finally use host's cells for possible implants.

1. Xinaris, C., Brizi, V. & Remuzzi, G. Organoid Models and Applications in Biomedical Research. *NEF* **130,** 191–199 (2015).

2. Lancaster, M. A. & Knoblich, J. A. Generation of cerebral organoids from human pluripotent stem cells. *Nat Protoc* **9,** 2329–2340 (2014).

3. Lancaster, M. A. *et al.* Cerebral organoids model human brain development and microcephaly. *Nature* **501,** 373–379 (2013).
4. Watanabe, M. *et al.* Self-Organized Cerebral Organoids with Human-Specific Features Predict Effective Drugs to Combat Zika Virus Infection. *Cell Reports* **21,** 517–532 (2017).
5. Mariani, J. *et al.* FOXG1-Dependent Dysregulation of GABA/Glutamate Neuron Differentiation in Autism Spectrum Disorders. *Cell* **162,** 375–390 (2015).
6. Vaysse, L., Beduer, A., Sol, J. C., Vieu, C. & Loubinoux, I. Micropatterned bioimplant with guided neuronal cells to promote tissue reconstruction and improve functional recovery after primary motor cortex insult. *Biomaterials* **58,** 46–53 (2015).
7. Li, N. *et al.* Three-dimensional graphene foam as a biocompatible and conductive scaffold for neural stem cells. *Sci Rep* **3,** 1604 (2013).
8. Song, Q. *et al.* Anti-inflammatory effects of three-dimensional graphene foams cultured with microglial cells. *Biomaterials* **35,** 6930–6940 (2014).
9. Ahn, G. *et al.* Effect of pore architecture on oxygen diffusion in 3D scaffolds for tissue engineering. *J Biomech Eng* **132,** 104506 (2010).
10. Tang-Schomer, M. D. *et al.* Bioengineered functional brain-like cortical tissue. *Proc. Natl. Acad. Sci. U.S.A.* **111,** 13811–13816 (2014).
11. Gupta, K. *et al.* Lab-on-a-chip devices as an emerging platform for stem cell biology. *Lab Chip* **10,** 2019–2031 (2010).
12. Young, E. W. K. & Beebe, D. J. Fundamentals of microfluidic cell culture in controlled microenvironments. *Chem. Soc. Rev.* **39,** 1036–1048 (2010).

6

SUPPLEMENTARY PUBLICATIONS

6.1

Graphene oxide nanosheets reshape synaptic function in cultured brain networks

R. Rauti, N. Lozano, V. León, D. Scaini, M. Musto, I. Rago, F. P. Ulloa Severino, A. Fabbro, L. Casalis, E. Vázquez, K. Kostarelos, M. Prato, and L. Ballerini

ACS Nano

ACSNANO
www.acsnano.org
ARTICLE

Graphene Oxide Nanosheets Reshape Synaptic Function in Cultured Brain Networks

Rossana Rauti,[†] Neus Lozano,[‡] Veronica León,[§] Denis Scaini,[†,⊥] Mattia Musto,[∥] Ilaria Rago,[⊥] Francesco P. Ulloa Severino,[∥] Alessandra Fabbro,[¶] Loredana Casalis,[⊥] Ester Vázquez,[§] Kostas Kostarelos,[‡] Maurizio Prato,[*,¶,#,△] and Laura Ballerini[*,†,∥]

[†]Life Science Department, University of Trieste, 34127 Trieste, Italy

[‡]Nanomedicine Lab, School of Medicine and National Graphene Institute, Faculty of Medical & Human Sciences, University of Manchester, M13 9PL Manchester, United Kingdom

[§]Departamento de Química Orgánica, Facultad de Ciencias y Tecnologías Químicas-IRICA, Universidad de Castilla La Mancha, 13071 Ciudad Real, Spain

[⊥]ELETTRA Synchrotron Light Source, 34149 Trieste, Italy

[∥]International School for Advanced Studies (SISSA), 34136 Trieste, Italy

[¶]Department of Chemical and Pharmaceutical Sciences, University of Trieste, 34127 Trieste, Italy

[#]CIC BiomaGUNE, Parque Tecnológico de San Sebastián, Paseo Miramón, 182, 20009 San Sebastián, Guipúzcoa, Spain

[△]Basque Foundation for Science, Ikerbasque, Bilbao 48013, Spain

Supporting Information

ABSTRACT: **Graphene offers promising advantages for biomedical applications. However, adoption of graphene technology in biomedicine also poses important challenges in terms of understanding cell responses, cellular uptake, or the intracellular fate of soluble graphene derivatives. In the biological microenvironment, graphene nanosheets might interact with exposed cellular and subcellular structures, resulting in unexpected regulation of sophisticated biological signaling. More broadly, biomedical devices based on the design of these 2D planar nanostructures for interventions in the central nervous system require an accurate understanding of their interactions with the neuronal milieu. Here, we describe the ability of graphene oxide nanosheets to down-regulate neuronal signaling without affecting cell viability.**

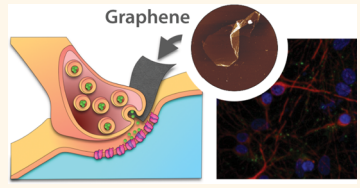

KEYWORDS: *nanotechnology, graphene, patch-clamp, synaptic terminals, exocytosis, FMI-43, microvesicles*

Graphene is a 2D plate-like material consisting of sp^2-hybridized carbon atoms organized in a hexagonal lattice and characterized by, among other properties, high electron mobility and mechanical flexibility.[1−3] In addition to the successful exploitation of graphene and graphene-based materials in an increasing number of industrial products, current applications of graphene hold the potential to revolutionize specific areas of medicine.[2−6] Biomedical developments, in general, in neurology, in particular, are focusing on few-layer graphene sheets to manufacture novel biodevices, including biosensors, interfaces, tissue scaffolds, drug delivery, and gene therapy vector systems.[4] The successful design of multifunctional graphene-based neurodevices will expose brain cells and neuronal circuits directly to this material by injection or implantation.[4,7] In this context, the exploration of the interactions between graphene nano- and microsheets with the sophisticated signaling machinery of nerve cells, with a particular focus on potential graphene flake interactions with the hydrophobic membrane domains, is of great importance.[1,8,9] Such interactions may favor graphene translocation or adhesion to cell membranes,[8,10] potentially interfering with exquisite membrane activities, such as the exocytic and endocytic trafficking systems, which are crucial to physiological synaptic transmission.[8,11]

Here, we explore by patch clamp and fluorescence imaging the ability of graphene (GR) and graphene oxide (GO) nanosheets to interfere with synaptic signaling once hippocampal cultured neurons are exposed for 1 week to a growth medium containing thin sheets of such materials at 1 or 10 μg/mL (concentrations reported not to induce cell death[12−14]). We further investigated whether, in the absence of explicit cell toxicity, such materials affected the ability of astrocytes to release synaptic-like microvesicles[15] (MVs) in pure glial cultures. Our results describe the potential of GO nanosheets to alter different modes of interneuronal communication systems in the central nervous system (CNS), hinting at

Received: January 7, 2016
Accepted: March 31, 2016
Published: March 31, 2016

DOI: 10.1021/acsnano.6b00130
ACS Nano 2016, 10, 4459−4471

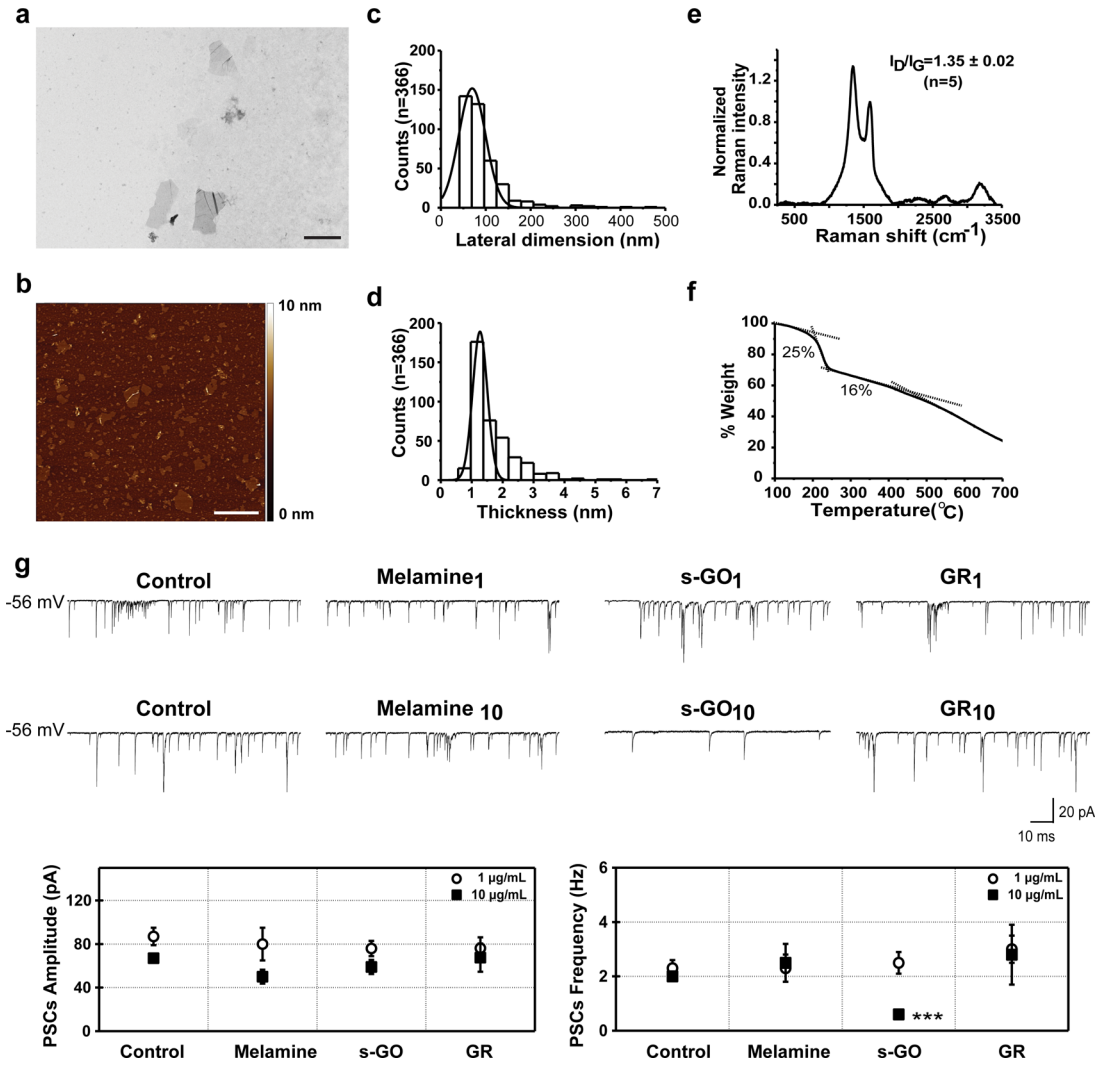

Figure 1. Characterization of small graphene oxide (s-GO) of biological grade; graphene oxide exposure at high concentration influences synaptic function. (a–f) Physicochemical characterization of s-GO: (a) TEM micrograph (scale bar 1 μm), (b) AFM height image (scale bar 1 μm), (c) lateral dimension distribution, and (d) thickness distribution analysis; (e) normalized Raman spectrum and (f) TGA analysis. (g) Graphene oxide exposure at high concentration influences synaptic function. Spontaneous synaptic activity recorded from hippocampal cultures in control, melamine, s-GO, and GR-treated cultures at 1 μg/mL (top traces) and 10 μg/mL (bottom traces) grown for 8–10 days *in vitro*. Postsynaptic currents (PSCs) were detected at −56 mV holding potential. Bottom plots represent pooled data and summarize average PSC amplitude and frequency; note the reduction in s-GO treatment (10 μg/mL, final concentration) of PSC frequency (* = $P < 0.001$ Student's *t* test; data are mean ± SEM).**

opportunities for neuromodulatory applications or highlighting subtle, but potentially unwanted, subcellular interactions.

RESULTS AND DISCUSSION

To address the issue of prolonged exposure of a functional brain network to graphene sheets, we used different materials. Graphene oxide sheets of large and small lateral dimensions (l-GO and s-GO, respectively) were synthesized using a modified Hummers method (see Methods). Following the reaction, the GO gel-like top layer was extracted carefully by using warm water, resulting in the large GO (l-GO). Final concentrations ranging between 1 and 2 mg/mL were obtained with a yield of *ca.* 10%. l-GO was freeze-dried, reconstituted in water for injection, sonicated for 5 min, and centrifuged at room temperature to generate the small GO (s-GO).The lateral dimension of the GO sheets was controlled by drying and sonicating the l-GO to obtain the s-GO sheets, which were always at least 1 order of magnitude smaller, without introducing any significant changes among their surface properties (see Table S1 in the Supporting Information).

The GO dispersions in aqueous media were homogeneous, of brownish color, and stable at room temperature for more than 6 months. The physicochemical characterization of the l-GO and s-GO dispersions is shown in Figure 1a–f and in the Supporting Information Figures S1 and S2. The structural properties (lateral dimension and thickness) were studied by optical microscopy, transmission electron microscopy (TEM), and atomic force microscopy (AFM). Optical properties were studied by UV–vis and fluorescence spectroscopy. Raman spectroscopy and laser Doppler electrophoresis (measuring ζ-potential) were used to assess the surface properties of the GO materials. The Raman spectroscopic analysis revealed D and G bands at 1319 and 1596 cm^{-1}, respectively, characteristic of most polyaromatic hydrocarbons. The D to G band intensity ratio (I_D/I_G) was calculated to be 1.3, corresponding to the metric of disorder in the graphitic structure. The surface charge

DOI: 10.1021/acsnano.6b00130
ACS Nano 2016, 10, 4459–4471

measured with a Zetasizer instrument showed an average ζ-potential of −50 mV, indicating flakes of high negative surface charge. To elucidate the degree of surface functionalization, thermogravimetric analysis (TGA) and X-ray photoelectron spectroscopy (XPS) were performed to quantify the purity of the GO (>99%) and the C/O ratio. XPS high-resolution C 1s spectra were recorded to elucidate the contribution of individual functional groups such as carboxylic, carbonyl, epoxide, and hydroxyl (Table S2b). All fittings shown were performed using the CasaXPS software, and the different regions were assigned according to NIST's XPS and lasurface databases. Deconvolution XPS spectra and assignment of the functional groups indicated that hydroxyls were the least abundant species in the GO material (see Supporting Information Table S2a).

Aqueous dispersions of graphene flakes were prepared using ball-milling for the exfoliation of graphite through interaction with melamine, as previously described[16,17] (see Methods). Due to the GR preparation process, graphene dispersions can contain traces of melamine. In order to determine the exact amount of these traces, final graphene dispersions (0.09 mg/mL) were evaluated by elemental analysis, which indicated 0.9 ppm of melamine. Experiments that involved incubation in neurons also included controls exposed to equal amounts of melamine alone (see Methods). The physicochemical characterization of GR dispersions is shown in Figure S3. The lateral size, studied by TEM, was found to range between 500 nm and 3 μm (Figure S3a,b in the Supporting Information). Optical properties were studied by UV−vis absorption spectroscopy. Dispersions were diluted, and the respective UV−vis absorption spectra were recorded (Figure S3). The spectra are featureless in the vis−NIR region, as expected. The absorbance at 660 nm, divided by cell length, is plotted against the concentration, exhibiting Lambert−Beer behavior (Figure S3d). Raman spectroscopy revealed differences between the GO and GR. Graphene exhibits G and 2D modes around 1573 and 2700 cm^{-1} that satisfy Raman selection rules, while the D peak, around 1345 cm^{-1}, requires a defect for its activation (Figure S3e). The D to G band intensity ratio was calculated at different locations, giving a significantly low value (0.22) in comparison with that of GO. TGA was also used to quantify the functionalization degree of GR. The low weight loss observed in GR (7%) corroborated the low quantity of oxygen groups generated by the exfoliation process (Figure S3f).

We used hippocampal neurons isolated and cultured for 8−10 days *in vitro* (DIV). Primary neuronal cultures were incubated for 2 DIV in the presence of GR or s-GO (at 1 and 10 μg/mL; see Methods) and maintained for 6−8 days. Afterward, visually identified neurons were patch clamped under a voltage clamp. Hippocampal neuron maturation and viability were assessed using single-cell recordings (see Methods) to measure the cell passive membrane properties that are accepted indicators of neuronal health[18−20] that allowed comparison among the recorded cells. These parameters (membrane capacitance and input resistance) displayed similar values in all treatment conditions (summarized in Table 1).

To investigate synapse formation and activity after *in vitro* growth of neurons, we monitored the occurrence of spontaneous postsynaptic currents (PSCs). The appearance of PSCs provided clear evidence of functional synapse formation, and it is a widely accepted index of network efficacy.[21,22]

Table 1. Neuronal Passive Membrane Properties upon GR and s-GO Exposure (1 and 10 μg/mL, Respectively)

	capacitance (pF)	input resistance (MΩ)
$control_1$ (n = 24)	59 ± 4	976 ± 138
$melamine_1$ (n = 28)	46 ± 5	1036 ± 132
$s\text{-}GO_1$ (n = 27)	62 ± 8	876 ± 145
GR_1 (n = 30)	50 ± 5	1029 ± 161
$control_{10}$ (n = 20)	57 ± 7	744 ± 82
$melamine_{10}$ (n = 25)	72 ± 16	717 ± 106
$s\text{-}GO_{10}$ (n = 18)	67 ± 6	997 ± 156
GR_{10} (n = 25)	59 ± 18	1223 ± 501

Figure 1g shows representative current tracings of the recorded electrical activity. In neurons exposed to low (1 μg/mL) s-GO and GR, spontaneous synaptic activity was not affected. In fact, measured PSC amplitude and frequency in s-GO and GR (79 ± 7 pA, 2.5 ± 0.4 Hz, n = 27 and 77 ± 8 pA, 3 ± 0.5 Hz, n = 30, respectively) were comparable to the corresponding control and control−melamine values (87 ± 8 pA and 2.3 ± 0.3 Hz, control, n = 24; 80 ± 15 pA and 2.3 ± 0.5 Hz melamine n = 28; plots in Figure 1g). In all tests, cell parameters measured in melamine were comparable to those expressed by control neurons (Figure 1g, bottom plots), thus the impact on cells of such a contaminant at the estimated concentration is negligible.

When investigating the impact of higher graphene doses (10 μg/mL), we detected a significant difference (P < 0.001; Student's t test) in PSC frequency when comparing control neurons (2.0 ± 0.1 Hz control, n = 20) with s-GO-treated ones (0.6 ± 0.1 Hz, n = 18), while in melamine and GR, PSC frequency values remained unchanged (2.5 ± 0.7 Hz, n = 25 for melamine and 2.8 ± 1.1 Hz, n = 25 for GR). In all treatments studied, the amplitude values of the PSCs were never affected (data are summarized in Figure 1g plots). We further tested synaptic responses when neurons were treated (1 and 10 μg/mL) with a commercially available GO provided by an industrial partner (A-GO; Supporting Information and Figure S4). Similar reduction in PSC frequency (Figure S5) was detected that validated the observation that GO nanosheets, differently than GR flakes, specifically interfered with synapses in cultured neurons, regardless of the starting material.

The impact of 10 μg/mL s-GO on synaptic activity was not related to a decreased number of surviving neurons in the presence of s-GO. In fact, we determined the cellular composition of control and s-GO-treated hippocampal cultures using immunofluorescence markers[23] for astrocytes (GFAP) and neurons (β-tubulin III). We observed both β-tubulin III and GFAP immunoreactive cells in all growing conditions (Figure 2a), and both cell groups were represented in a comparable proportion in all treatment groups (quantified by measuring the cell density in Figure 2a; n = 13 visual field per condition, three different culture series). Thus, s-GO at higher concentrations specifically altered synapse formation and/or function without affecting cell survival or the global network size.

To gain more insight into such processes, we further investigated s-GO-treated (10 μg/mL) cultures. We specifically addressed the distribution of neuronal excitation by measuring the activity of small clusters of neurons with fluorescence calcium imaging.[23−25] On average, 7 ± 2 fluorescent neurons (n = 26 fields), stained with the membrane-permeable Ca^{2+} dye Fura-2-AM (see Methods), were simultaneously visualized in

DOI: 10.1021/acsnano.6b00130
ACS Nano 2016, 10, 4459−4471

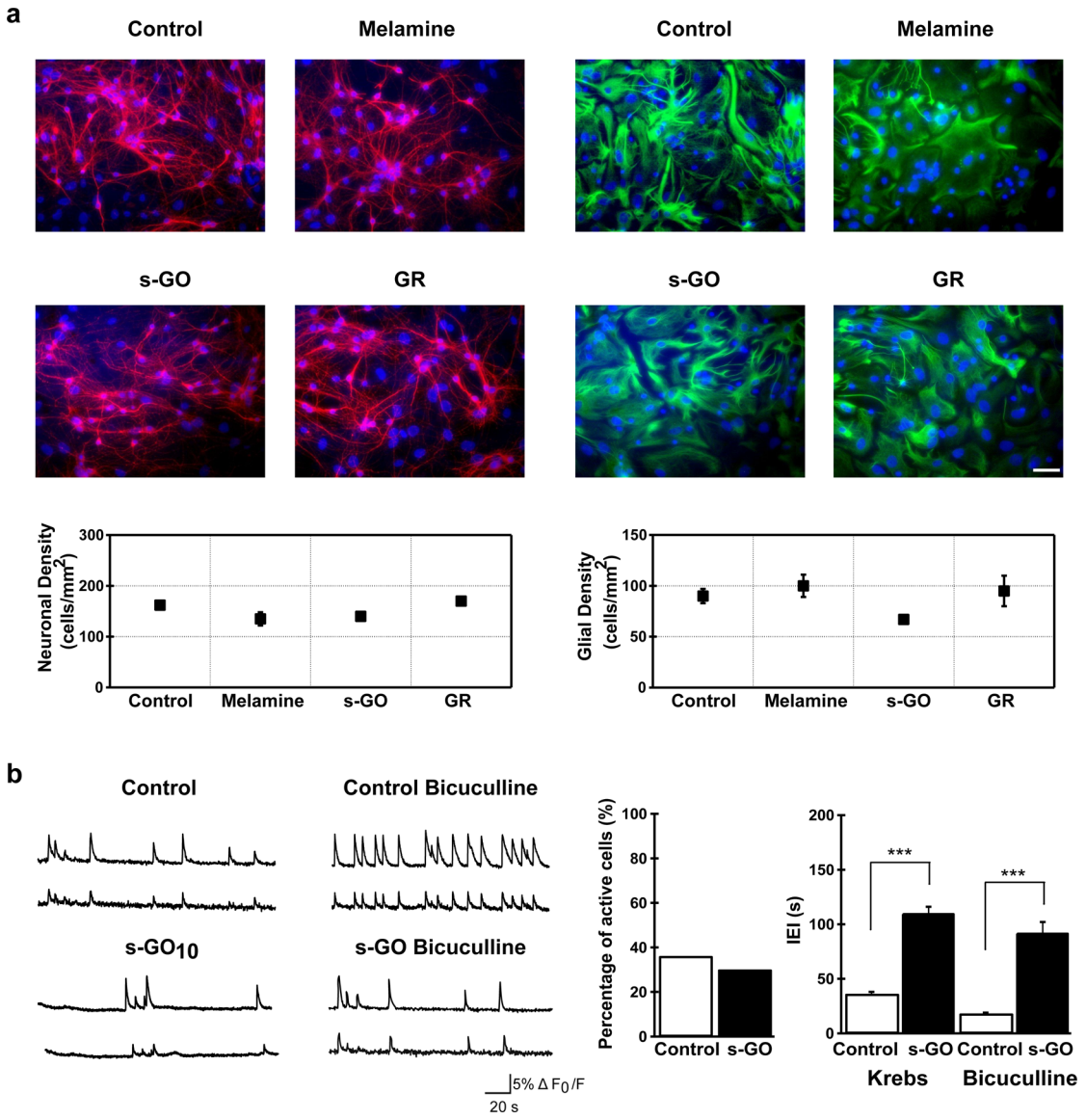

Figure 2. s-GO exposure at high concentration impaired network activity without changing network size. (a) Immunofluorescence images are shown to visualize neurons and glial cells in four different conditions (anti-β-tubulin III, in red, left panels; anti-GFAP, in green, right panels; in all, nuclei are visualized by DAPI in blue) (samples are for the 10 μg/mL protocol; scale bar 50 μm). The plots summarize neuronal (left) and glial (right) densities in all conditions. (b) Repetitive spontaneous Ca^{2+} (left panel) or bicuculline-induced (right panel) oscillations recorded in hippocampal cultures at 8−10 DIV (from each field sample, recordings of two cells were selected). Histograms summarize the percentage of spontaneous active cells (middle) and the average values of the interevent interval (IEI; right) in standard saline (Krebs) and in the presence of bicuculline (* = $P < 0.001$ Student's t test; data are mean ± SEM).**

the recorded field (120 × 160 μm^2). We compared and characterized the cell ability to generate repetitive Ca^{2+} oscillations.[23−25] In control conditions, all recorded fields (n = 8) displayed active cells, while in s-GO-treated cells, 56% (n = 10 out of 18) of the recorded fields did not display detectable cell activity. However, in the remaining s-GO fields (n = 8), we found an amount of neurons that were spontaneously generating repetitive Ca^{2+} oscillations comparable to that measured in controls (Figure 2b; 36% in control, 20 out of 56 neurons, n = 8 active fields and 30% in s-GO-treated, 18 out of 60 neurons, n = 8 active fields).

Figure 2b traces represent fluorescence recordings from active fields in control and s-GO-treated cultures (two sampled cells in each field). Episodes usually comprised spontaneous bursts of activity, fully blocked by tetrodotoxin (TTX, a blocker of voltage-gated, fast Na^+ channels) applications (1 μM; n = 8 fields, control and s-GO-treated; not shown). Control Ca^{2+} oscillations displayed an interevent interval (IEI) of 36 ± 2 s (n = 20 cells) that was significantly lower ($P < 0.001$; Student's t test) than that measured in s-GO-treated networks (110 ± 6 s, n = 18 cells, right plot in Figure 2b). When $GABA_A$ receptors were pharmacologically blocked by bicuculline (20 μM, 20 min), an antagonist of inhibitory connections known to potentiate rhythmic activity patterns,[23,26,27] the control IEI average value was still significantly lower ($P < 0.001$; Student's t test) than that measured in s-GO neurons in the presence of the $GABA_A$ receptor antagonist (18 ± 1 s, n = 20 in control cells *vs* 92 ± 10 s, n = 18 in s-GO cells; plot in Figure 2b, right). This indicated a direct reduction in the excitatory activity due to s-GO exposure.

DOI: 10.1021/acsnano.6b00130
ACS Nano 2016, 10, 4459−4471

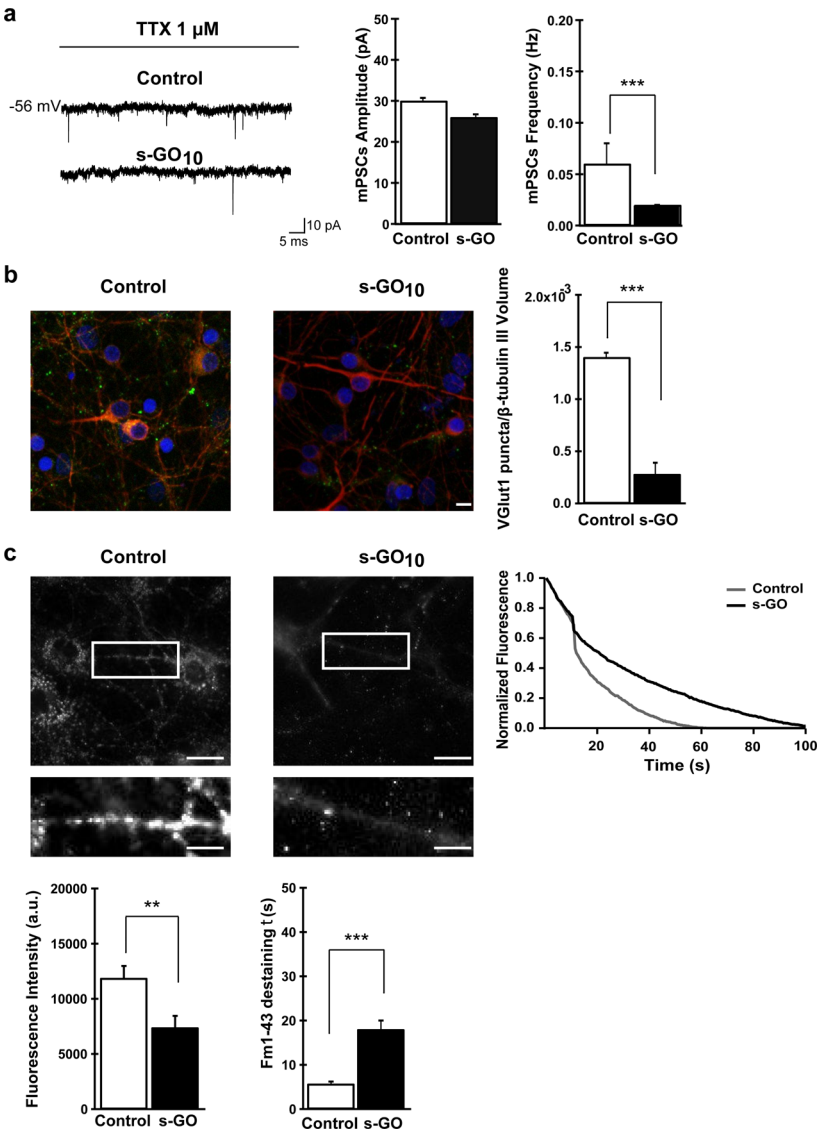

Figure 3. s-GO exposure at high concentration impaired excitatory synapses. (a) Sample tracings of mPSCs recorded in control and s-GO-treated cultures (left panel). Right panel: plots reporting mPSC amplitude and frequency values. s-GO treatment significantly decreased the frequency of mPSCs (* = $P < 0.001$ Student's t test). (b) Confocal reconstruction of control and s-GO-treated neurons immunolabeled for the vesicular glutamate transporter 1 (VGLUT1, green) and counterstained for cytoskeletal component β- tubulin III (red; nuclei are visualized by DAPI in blue; scale bar 10 μm). The plot shows the significant decrease of VGLUT1-positive puncta in s-GO-treated cultures (*** = $P < 0.001$ Student's t test). (c) Top: fluorescence images following staining with FM1-43, control, and s-GO-treated. Scale bar 50 μm. The areas in the boxes are higher magnifications to highlight the difference in vesicular staining between the two conditions (scale bar 100 μm). The plot (top right) reproduces the representative (control and s-GO) traces of FM1-43 destaining (please note that each trace has been normalized to the maximum fluorescence detected). Bottom: left plot summarizes the initial raw fluorescent intensities of hippocampal terminals from control and s-GO-treated cultures (** = $P < 0.01$ Mann–Whitney test); the right plot summarizes the decay time constant τ of FM1-43 destaining in the two conditions (*** = $P < 0.001$, Mann–Whitney test).**

Next, we recorded single-cell synaptic activity in the presence of TTX (1 μM, Figure 3a). Under these experimental conditions, synaptic currents, termed miniature PSCs (mPSCs), do not depend on action potential generation. mPSCs are due to the stochastic fusion of neurotransmitter vesicles at the presynaptic membrane, and their frequency is proportional to the number of synaptic contacts.[28] Despite the fact that in the recorded hippocampal neurons spontaneous synaptic activity was manifested as inward currents (in our recording conditions, see Methods[21]) made up by a mixed population of inhibitory ($GABA_A$ receptor-mediated) and excitatory (AMPA glutamate receptor-mediated) PSCs, virtually all mPSCs, as previously reported,[22] were identified as excitatory by their fast kinetics (decay time constant $\tau = 4 \pm 0.3$ ms; see Methods[22]). Notably, s-GO significantly decreased ($P < 0.001$, Student's t test; see plots in Figure 3a) the frequency of mPSCs without affecting their amplitude (0.06 ± 0.02 Hz and 30 ± 0.7 pA, control, $n = 15$; 0.02 ± 0.001 Hz and 26 ± 0.7 pA, s-GO-treated, $n = 9$; summarized in Figure 3a). To ascertain whether the s-GO interference with synaptic activity was selective on glutamate-mediated fast synaptic transmission, we tested the occurrence of evoked inhibitory PSCs by pair recordings of monosynaptically coupled neurons[22] (Methods and Figure S6a), and we observed that s-GO apparently did not impair $GABA_A$-mediated connections.

DOI: 10.1021/acsnano.6b00130
ACS Nano 2016, 10, 4459–4471

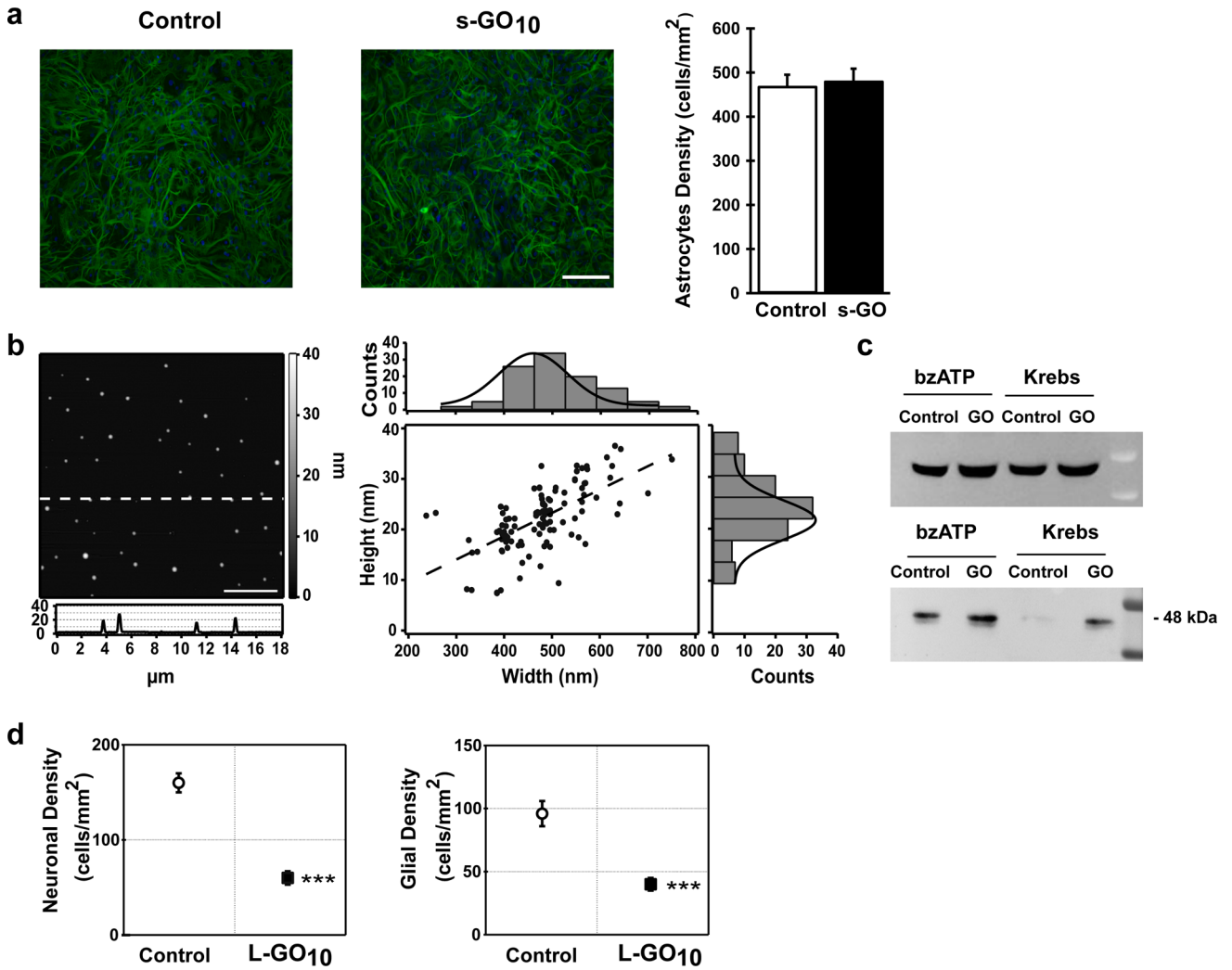

Figure 4. s-GO exposure and microvesicle release in glial cells. (a) Immunolabeling of primary rat astrocytes (3 weeks) in control and s-GO-treated cells (10 μg/mL, 6−8 days). Both cultures were immunostained for GFAP (green) and nuclei visualized by DAPI (blue; scale bar 100 μm). No statistical significance was found between the two conditions (top right). (b) AFM image of fixed MVs, where the differences in color are representative of height differences (brighter means higher). A representative height profile crossing three MVs is reported. The scatter plot (right) shows MV width *versus* height distribution and is fitted with a regression line represented by the equation $y = 0.046x + 0.218$. A frequency histogram, built upon experimental measurements of both width and height, was plotted over each axis of the scatter graph and fitted with Gaussian distributions. The frequency histograms revealed the highest number of occurrences to be about 490 and 24 nm for width and height, respectively. (c) Western blotting of the pellets (bottom row) and cell lysates (top row) for the MV marker flotillin-1. Pellets were obtained from the medium of glial cultures treated or untreated with s-GO under two different conditions: stimulated and not stimulated (Krebs) by 100 μM bzATP. Note the marked increase of the band for flotillin-1 in s-GO-treated cells. (d) Plots summarizing the decreased density of hippocampal cells when treated with l-GO (~10 μm lateral size; 10 μg/mL final concentration).

To determine whether changes in excitatory synaptic density may account for the reduction in fast mPSC frequency detected in s-GO-treated cultures, neurons were co-immunostained for β-tubulin III and the vesicular glutamate transporter (VGLUT1), a transmembrane protein localized at the glutamatergic presynaptic terminals.[29] Antibody to VGLUT1 labeled presynaptic boutons under both conditions (Figure 3b). Using β-tubulin III labeling to identify neuronal bodies and dendrites, we quantified VGLUT1-positive puncta, detecting a significant ($P < 0.001$; Student's t test) reduction in their density in s-GO-treated samples ($1.4 \times 10^{-3} \pm 0.045 \times 10^{-3}$, $n = 6$ fields for control and $0.28 \times 10^{-3} \pm 0.11 \times 10^{-3}$, $n = 6$ fields for s-GO; plot in Figure 3b). Parallel experiments were performed to quantify GABAergic synapses, by similar co-staining but for the vesicular GABA transporter (VGAT) to localize presynaptic GABAergic terminals.[22,30] These studies indicated that s-GO incubation did not alter the inhibitory connection density (Supporting Information and Figure S6b).

In the next set of experiments, we measured the kinetics of synaptic vesicle release by real-time imaging of vesicles labeled with FM dye to monitor the rate of presynaptic vesicle recycling from hippocampal neurons treated or untreated with s-GO. After being stained with the lipophilic dye FM1-43,[31−33] clusters of presynaptic terminals were visible as bright fluorescent spots (Figure 3c). The fluorescence intensity measured on FM-positive puncta following high KCl (50 mM[34]) depolarization is proportional to the number of vesicles endocytosed during synaptic vesicle recycling and thus allows estimation of the size of the recycling vesicle pool.[34] In s-GO-treated cells, upon a high-K^+-loading protocol, we detected a significant ($P < 0.01$; Mann−Whitney test) reduction in the raw fluorescence intensity of FM1-43-positive hippocampal

DOI: 10.1021/acsnano.6b00130
ACS Nano 2016, 10, 4459−4471

terminals (11876 ± 1100 arbitrary units (au), n = 7 fields for control and 7400 ± 1057 au, n = 6 fields for s-GO; three different culture series; Figure 3c), suggesting that chronic incubation with s-GO decreased the recycling vesicle pool. When analyzing the decay time constant (τ) of the FM1-43 fluorescence destaining profiles during vesicle exocytosis, we observed a significant (P < 0.001; Mann−Whitney test) difference in the kinetics displayed by control (τ = 5.7 ± 0.5 s, n = 205 terminals) and s-GO-treated (τ = 18 ± 2 s, n = 85 terminals) cells, as summarized in Figure 3c. In reference experiments, the image series captured on FM1-43-stained cells, but without the high-K^+ destaining stimulus, produced a baseline reference plot (not shown). Taken together, these results support the specific ability of chronic exposure to s-GO flakes to reduce the amount of excitatory synaptic contacts and to interfere with presynaptic vesicle recycling.

To test the ability of s-GO to impair cell membrane dynamics, in general, we investigated whether s-GO (10 μg/mL) was also reducing exocytosis and recycling of synaptic-like microvesicles[15] from cultured primary glial cells (see Methods). MVs are released into the extracellular space by direct budding from the plasma membrane of astrocytes and have been shown to contribute to intercellular communication.[15,35,36] We treated pure glial cell cultures with s-GO (10 μg/mL) for 6−8 days. In Figure 4a, immunofluorescence staining of control and s-GO-treated GFAP-positive cells are shown. s-GO incubation did not affect astrocyte density (Figure 4a, right histograms; n = 20 fields for both conditions), excluding any cytotoxic effect. In glial cultures, MV release was induced by bzATP incubation (100 μM, 30 min, n = 3 different series of cultures[37−39]), and MV release was detected and quantified by immunoblot analysis of the collected supernatant. In control, bzATP stimulation induced the appearance of the band corresponding to flotillin-1 (Figure 4c, bottom blot), a signature of MV release.[40−42] Surprisingly, in s-GO-treated astrocytes, the bzATP stimulation induced a marked increase in the size of the flotillin-1 band. This band was also detected in the absence of stimulation (Figure 4c, bottom blot), suggesting that s-GO *per se* induced the MVs' constitutive release.

AFM micrographs in Figure 4b (left panel) show the presence of vesicles in the stimulated control supernatant appearing as circular spots protruding from the ultraflat mica surface. For each of them, width and height were independently measured from particle crossing height profiles, and the resulting distributions were plotted (Figure 4b, right panel). Intriguingly, similar experiments with GR (10 μg/mL) did not induce shedding of MVs in glial cell cultures (Supporting Information and Figure S7).

We also attempted to investigate the effect of increased lateral size of GO (l-GO, with a lateral dimension in the few micromter range; 10 μg/mL final concentration) on cultured hippocampal cells. However, after 6−8 days of incubation, we measured a significant (P < 0.001; Student's t test; Figure 4d) reduction in both neuron and glial cell densities (160 ± 10 neurons/mm^2 and 96 ± 10 astrocytes/mm^2 for control and 96 ± 10 neurons/mm^2 and 40 ± 7 astrocytes/mm^2 for l-GO; n = 10 visual fields each, three series of cultures; Figure 4d), indicating cell toxicity that prevented any further functional measurements. We believe further investigations are warranted to explore such lateral size-dependent cytotoxic responses.

We report here the ability of s-GO nanosheets to interfere specifically with neuronal synapses, without affecting cell viability. In particular, in cultured neuronal networks, upon chronic s-GO exposure, glutamatergic release sites were sized down. This was shown by (i) the reduction in frequency of spontaneous synaptic activity (PSCs and mPSCs) together with the marked reduction in VGLUT1-positive labeling,[43] (ii) the reduced probability of finding active neurons when networks were explored by Ca^{2+} imaging,[23,44] and (iii) the decreased recycle vesicle pool quantified by FM1-43 measurements together with the altered kinetics of vesicle recycling.[34] This down-regulation of glutamate-mediated synapses was apparently not due to a general cell membrane disruption or to neuronal cell loss. In fact, we never detected alterations in basic electrophysiological parameters, reflecting neuronal health and membrane integrity.[18−20]

In addition, cell densities in treated cultures were comparable to control ones. The survival of GFAP-positive glial cells was also not affected by s-GO exposure, both in mixed neuronal and in pure neuroglial cultures. In the latter condition, MV release was indirectly monitored by the blot analysis of flotillin-1 protein,[40,41] and MV presence was confirmed by direct AFM measures. In these cultures, exposure to s-GO stimulated the basal release of shed vesicles and augmented the bzATP-induced one.[37−39] s-GO increase in MV release from neuroglia cells might be related to a general cell-stress condition[15] ultimately due to s-GO glial−membrane interactions or even internalization, depending on the flakes' shape, lateral dimension, and oxidization degree,[10] as well as the degree of protein adsorption from the culturing milieu.[45]

Based on our experimental evidence, we cannot rule out that treatment with s-GO down-regulated the synaptic function (in particular, presynaptic release) *via* MVs released in mixed neuronal−glial cultures, thus excluding a direct, membrane interference of s-GO nanosheets at the presynaptic glutamatergic terminals. MVs have long been reported as active messengers of intercellular communication, rather than mere inert debris;[37] however, to our knowledge, there are no reports of astrocyte shedding MVs acting as regulators of synaptic activity. On the contrary, MVs released by microglia have been reported to affect synaptic activity, mainly acting at the presynaptic site of the excitatory synapses, but increasing synaptic activity and release in primary cultures.[37] Against this neuroglial cell-mediated response to s-GO is also the fact that astrocyte density in mixed cultures is artificially kept at a low level by the culturing procedure itself, while the surviving microglia are even fewer.[46]

In contrast to s-GO, the inert nature of GR flakes regarding synaptic activity and MV release by glia is also of interest. This could be due to differences in shape and lateral size affecting flake−membrane interactions.[10] It is also interesting to consider that GR has a much less hydrophilic surface characteristic and overall poorer dispersibility in cell culture media[45] that may lead to the formation of aggregates potentially unable to interact with submicroscopic structures (such as the synaptic clefts).

The apparent selectivity in terms of the presynaptic terminals targeted by s-GO was also notable, with the inhibitory GABAergic ones that remained unaffected, as evidenced by pair recordings and the VGAT labeling.[22] Given the ability of graphene flakes to undergo motion and vibration that can lead to interaction with and possible piercing of lipid bilayers,[8] we propose an alternative mechanistic interpretation of our synaptic results. s-GO flakes may prevent the synaptic vesicle endocytotic cycle because their dimensions allow them to interact with the presynaptic cell membrane at the periphery of

DOI: 10.1021/acsnano.6b00130
ACS Nano 2016, 10, 4459−4471

the synaptic cleft and then be taken up by vesicles. In this process, the flakes may transiently trap vesicles in an open mode and prevent their closing and the subsequent endocytosis. This could affect synaptic release in the short term, inducing, in the long term, a down-regulation of glutamatergic release sites and synapses. Note that glutamatergic synaptic activity is specifically, and reversibly, affected also when neurons are transiently exposed to s-GO, with a short-term up-regulation of release, turned into a down-regulation within the first 3 days of chronic exposure (Figure S8 in Supporting Information). This observation further supports the hypothesis of the ability of s-GO to directly target synapses. The mechanism of such interaction among s-GO flakes and vesicles (including extra-synaptic ones) could be similar to what has been previously described for dispersed single-walled carbon nanotubes.[47] In this context, the unlikeliness of affecting GABAergic terminals may reside in the different dimensions of the excitatory (16 nm) and inhibitory (10 nm) synaptic clefts.[48] The latter are reported to be narrowed to 6 nm at the periphery of the clefts due to transcleft elements, while docked vesicles are concentrated at the central cleft domain.[48] On the contrary, docked vesicles in excitatory synapses are distributed evenly over the synaptic cleft.[48] It is tempting to speculate that these synaptic ultrastructural differences might explain why glutamatergic terminals became ideal targets of s-GO interactions. This selectivity is supported by the notion that, even when transiently exposed to s-GO *via* pressure-ejected brief pulses, GABAergic synapses are unaffected (see Supporting Information and Figure S8).

CONCLUSIONS

Regardless of the mechanisms involved, the described ability of s-GO to alter synapses and induce glial cell reaction has not been previously documented. This might compromise neuronal signaling and CNS functions and seems crucially dependent on the GO sheet dimensions since larger flakes were found unequivocally cytotoxic. In our experiments, 6 days of exposure of cultures to equal amounts of dispersed l-GO induced unequivocal hippocampal cell loss, both neuroglia and neurons, thus hampering any further evaluation of membrane/flake interactions.

These observations deserve further studies; in fact, altering synapses and inducing glia reactivity may raise concerns from a safety and nanotoxicity point of view.[49]

Beyond the safe design of nanomaterials, such a subtle interference affecting exquisite CNS signaling may offer possibilities in neuropharmacology when specific targeting of excitatory synapses is desired.[50−52] The use of nanoparticles as therapeutics is, in fact, fueled by their ability to circumvent biological barriers,[53] and targeting of synapses has created the basis for theranostics applications.[54] Our observations with thin s-GO flakes illustrate the potential of 2D nanosheet physical properties to engineer specific glutamate transmission modulators.

It is also relevant to note that synapse formation and function in neuronal networks, when interfaced to planar graphene-based materials, are not affected.[55] This strengthens the notion that when exploring the application of graphene in biology, studies should be performed with well-characterized types of materials because the materials' physical−chemical features, including geometry, are governing the potential interactions with specific biological components.[2]

METHODS

Synthesis and Characterization of Biological-Grade Thin Graphene Oxide of Different Lateral Size Distribution. For graphene oxide preparation, graphite flakes (Graflake 9580) were obtained from Nacional Grafite Ltd. (Brazil) and used for the preparation of large and small graphene oxide. Nitric acid 70%, sodium nitrate, potassium permanganate, sulfuric acid 99.999%, and hydrogen peroxide 30% were purchased from Sigma-Aldrich. Water for injection was obtained from Fresenius Kabi.

Graphene oxide sheets were synthesized using the modified Hummers method previously described[56] and under endotoxin-free conditions by using a laminar flow hood, water for injection, gloves, nonpyrogenic plastic containers, and depyrogenated glassware.[57] Briefly, 0.8 g of graphite flakes was mixed with 0.4 g of sodium nitrate in a round-bottom flask, and then 18.4 mL of sulfuric acid 99.999% was added slowly to the mixture. After a homogenized mixture was obtained, 2.4 g of potassium permanganate was slowly added and the mixture was maintained for 30 min. Next, 37 mL of water for injection was added dropwise due to the violent exothermic reaction, and the temperature was continuously monitored and kept at 98 °C for 30 min. The mixture was further diluted with 112 mL of water for injection, and 30% hydrogen peroxide was added for the reduction of the residual potassium permanganate, manganese dioxide, and manganese heptoxide to soluble manganese sulfate salts. The resulting mixture was purified by several centrifugation steps at 9000 rpm for 20 min until a viscous orange/brown layer of pure GO started to appear on top of the oxidation byproducts at neutral pH.[58]

This GO gel-like layer was extracted carefully with warm water, resulting in the large GO. Final concentrations ranging between 1 and 2 mg/mL were obtained with a yield of *ca.* 10%. l-GO was freeze-dried, reconstituted in water for injection, sonicated in a bath sonicator (VWR, 80W) for 5 min, and centrifuged at 13 000 rpm for 5 min at room temperature to prepare the s-GO. Structural properties such as lateral dimension and thickness of the GO materials have been studied by optical microscopy, TEM, and AFM. Optical properties such as absorbance and fluorescence have been studied by using UV−vis and fluorescence spectroscopy, respectively. Surface properties have also been studied by Raman spectroscopy and ζ-potential measurements. To elucidate the functionalization degree of the GO sheets, TGA was performed. X-ray photoelectron spectroscopy has been used to quantify the chemical composition of the GO sheets, C/O ratio, and the contribution of each individual functional group such as carboxylic, carbonyl, and epoxides.

Optical Microscopy. Bright-field microscopy using a Zeiss Primovert microscope was used to assess the lateral dimension distribution of the l-GO and to verify the size reduction of the s-GO.

Transmission Electron Microscopy. TEM was performed using a FEI Tecnai 12 Biotwin microscope (FEI, The Netherlands) at an acceleration voltage of 100 kV. Images were taken with Gatan Orius SC1000 CCD camera (GATAN, UK). One drop of sample was placed on a Formvar/carbon-coated copper grid. Filter paper was used to remove the excess material.

Atomic Force Microscopy. A multimode AFM was used on the tapping-mode with a J-type scanner, Nanoscope V8 controller (Veeco, Cambridge, UK), and an OTESPA silicon probe (Bruker, UK). Images were taken in air by depositing 20 μL of 100 μg/mL of GO on a freshly cleaved mica surface (Agar Scientific, Essex, UK) coated with poly-L-lysine 0.01% (Sigma-Aldrich, UK) and allowed to adsorb for 5 min. Excess unbound material was removed by washing with Milli-Q water and then allowed to dry in air; this step was repeated once. Lateral dimension and thickness distributions of GO were carried out using NanoScope Analysis software (version 1.40 Bruker, UK).

UV/Visible Spectroscopy. UV/visible absorbance spectra were obtained for GO samples from 7.5 to 20 μg/mL using a Varian Cary winUV 50 Bio spectrophotometer. Dual beam mode and baseline correction were used throughout the measurements to scan the peak wavelength and maximum absorbance between 200 and 800 nm.

Fluorescence Spectroscopy. Fluorescence emission spectroscopy was performed for GO samples from 75 to 200 μg/mL using a LS-50B

DOI: 10.1021/acsnano.6b00130
ACS Nano 2016, 10, 4459−4471

PerkinElmer spectrofluorimeter at the excitation wavelength of 525 nm, with both excitation and emission slits set at 20.

Raman Spectroscopy. Raman spectra were recorded for GO (20 μL of 100 μg/mL) on glass slides after complete evaporation of the water. Measurements were carried out using a 50× objective at 633 nm laser excitation using a micro-Raman spectrometer (ThermoScientific, UK). An average of five different locations within each sample was measured to calculate the I_D/I_G ratio.

Zeta-Potential Measurements. Electrophoretic mobility (μ) was measured by Malvern Zetasizer Nano ZS (UK) after dilution of samples with water in disposable Zetasizer cuvettes (Malvern Instruments). Default instrument settings and automatic analysis were used for all measurements, where the μ was converted automatically by the equipment software to zeta-potential (ζ) values as it is directly related to ζ-potential by Henry's equation. All values for samples prepared are triplicate measurements, and values were mean ± SD.

Thermogravimetric Analysis. The weight loss of GO samples was performed by TGA using a Pyris 6, PerkinElmer Ltd. GO (1−2 mg) was weighed into a ceramic crucible and analyzed from 100 to 995 °C at 10 °C/min with a nitrogen flow of 20 mL/min.

X-ray Photoelectron Spectroscopy. The composition of GO surfaces was studied by XPS at the NEXUS facility (the UK's National EPSRC XPS Users' Service, hosted by nanoLAB in Newcastle-upon-Tyne). XPS was recorded using a Thermo Theta Probe XPS spectrometer with a monochromatic Al Kα source of 1486.68 eV. The survey XPS spectra were acquired with pass energy (PE) of 200 eV, 1 eV step size, 50 ms dwell time, and averaged over five scans. The etching was 90 s. High-resolution C 1s XPS spectra were acquired with PE of 40 eV, 0.1 eV step size, 100 ms dwell time, and averaged over 20 scans. Spectra from insulating samples have been charge-corrected by shifting all peaks to the adventitious carbon C 1s spectral component binding energy set to 284.6 eV. CasaXPS software was used to process the spectra acquired at NEXUS. For the deconvolution of the different components, the CasaXPS software was used and the different regions were assigned according to NIST's XPS and lasurface databases:

$\pi-\pi^*$: 290.9−289.7
O−C═O: 288.8−288.0 eV
C═O: 287.6−286.6 eV
C−O−C: 286.7−286.3 eV
C−OH: 285.9−285.3 eV
C−C and C═C: 284.6 eV

For graphite samples, the CasaXPS software was able to properly fit the hydroxyl component at 285.6 eV, but for graphene oxide samples, it was not possible to fit six components where we should expect to have the epoxide and hydroxyl contributions separately. The amount of hydroxyls in the graphene oxide samples depends on the degree of oxidation, with the hydroxyl groups being the least oxidized, followed by epoxide, carbonyl, and carboxylic groups (the latter being the most oxidized).

Synthesis and Characterization of Pristine Graphene. The pristine graphene flakes used in this study were obtained by a methodology[16] that uses mechanochemical activation by ball-milling to exfoliate graphite through interactions with melamine (2,4,6-triamine-1,3,5-triazine) in solvent-free conditions. In a typical experiment, 7.5 mg of graphite (purchased from Bay Carbon, Inc. SP-1 graphite powder) and 0.16 mmol of melamine were ball-milled in a Retch PM100 planetary mill at 100 rpm for 30 min in air atmosphere. The resulting solid mixtures were dispersed in 20 mL of water to produce stable black suspensions. The as-prepared dispersions can be filtered and washed in hot water to remove melamine. Graphene water dispersions were obtained with a final concentration of 0.09 mg/mL in Milli-Q water. Melamine traces in the dispersions were analyzed by elemental analysis (LECO CHNS-932, model no. 601-800-500), giving 0.9 ppm of melamine. For TEM analyses, water dispersions were placed on a copper grid (3.00 mm, 200 mesh, coated with carbon film), and samples were investigated by high-resolution transmission electron microscopy (HRTEM) on a JEOL 2100. Lateral dimension distribution was carried out using Fiji-win32. UV−vis−NIR absorbance was performed for GR samples from 2.4 to 14.2 μg/mL using a 1 cm quartz cuvettes on a Cary 5000 UV−vis−NIR spectrophotometer. For Raman spectroscopy, the water dispersions are drop-cast onto a silicon surface (Si-Mat silicon wafers, CZ). Measurements were carried out using a 100× objective at 532 nm laser excitation using a SENTERRA Raman microscope. An average I_D/I_G ratio was measured from different locations in the sample. Thermogravimetric analyses were performed with a TGA Q50 (TA Instruments) at 10 °C/min in a nitrogen atmosphere.

Commercially Sourced Graphene Oxide. The graphene oxide was prepared by stirring powdered carbon fibers (GANF helical-ribbon carbon nanofibers manufactured by the Grupo Antolin Ingeniería, GANF) and sodium nitrate in sulfuric acid at 0 °C. While vigorous agitation was maintained, potassium permanganate was added to the suspension. After 30 min, water was slowly stirred into the paste. Then, the suspension was filtered and rinsed with copious amounts of water to remove the presence of acids.[59] For TEM analyses, water dispersions were placed on a copper grid (3.00 mm, 200 mesh, coated with carbon film). Samples were investigated by HRTEM on a JEOL 2100. Lateral dimension distribution was carried out using Fiji-win32. UV−vis−NIR absorbance was performed for GO samples from 7.5 to 20 μg/mL using a 1 cm quartz cuvettes on a Cary 5000 UV−vis−NIR spectrophotometer. For Raman spectroscopy, the water dispersions were drop-cast onto a silicon surface (Si-Mat silicon wafers, CZ). Measurements were carried out using a 100× objective at 532 nm laser excitation using a SENTERRA Raman microscope. An average I_D/I_G ratio was measured from different locations in the sample. The thermogravimetric analyses were performed with a TGA Q50 (TA Instruments) at 10 °C/min in a nitrogen atmosphere.

Preparation of Primary Cultures. Primary hippocampal cultures were prepared from 2 to 3 days postnatal (P_2-P_3) rats as previously reported.[21,22,60] All procedures were approved by the local veterinary authorities and performed in accordance with the Italian law (decree 116/92) and the UE guidelines (86/609/CE, 2007/526/CE, and 2010/63/UE). The animal use was approved by the Italian Ministry of Health. All efforts were made to minimize suffering and to reduce the number of animals used. All chemicals were purchased by Sigma unless stated otherwise. Briefly, enzymatically dissociated hippocampal neurons[21,22,60] were plated on poly-L-ornithine-coated glass coverslips (Kindler, EU) at a density of 200 000 ± 16 000 cells/mL (measure by sampling n = 4 culture series). Cultures were incubated (37 °C, 5% CO_2) in medium consisting of either 1× MEM (Gibco) or 10× MEM (Gibco) to compensate the volume of the added GR and GO water dispersion when treating cells at higher flakes concentrations (*i.e.*, 10 μg/mL). In both cases, the MEM was supplemented to reach 35 mM glucose, 1 mM Apo-transferrin, 15 mM HEPES, 48 μM insulin, 3 μM biotin, 1 mM vitamin B12, 500 nM gentamicin, and 10% fetal bovine serum (FBS; Invitrogen). For experiments involving chronic treatments, cultures were incubated at 2 DIV, with a medium containing 1 or 10 μg/mL of GR, either s-GO and A-GO, or l-GO, and controls were subjected to the same medium changes with addition of equivalent volumes of Milli-Q water or melamine alone. Cultures were used at days 8−10 (after 6−8 days of incubation).

Primary cortical glial cultures were prepared from P_2-P_3 rats as described in Calegari *et al.*[61] Briefly, dissociated cells were plated into plastic 75 cm^2 flasks, incubated (37 °C; 5% CO_2) in culture medium consisting of DMEM (Gibco), supplemented with 10% FBS, 100 IU/mL penicillin, and 10 mg/mL streptomycin. At 21 DIV, GR or s-GO (10 μg/mL) was added to the culture medium and cultures were used after 6−8 days of incubation.

Electrophysiological Recordings. Single and paired whole-cell recordings were obtained at room temperature (RT) with pipettes (5−7 MΩ) containing (in mM) 120 K gluconate, 20 KCl, 10 HEPES, 10 EGTA, 2 $MgCl_2$, 2 Na_2ATP, pH 7.3; osmolarity was adjusted to 300 mOsm. The extracellular solution contained (in mM) 150 NaCl, 4 KCl, 1 $MgCl_2$, 2 $CaCl_2$, 1 $MgCl_2$, 10 HEPES, 10 glucose (all Sigma), pH 7.4. Coverslips with cultures were positioned in a Perspex chamber mounted on an inverted microscope (Eclipse TE-200, Nikon, Japan). Data were collected by Multiclamp 700B patch amplifier (Axon CNS, Molecular Devices) and digitized at 10 kHz with the pClamp 10.2

DOI: 10.1021/acsnano.6b00130
ACS Nano 2016, 10, 4459−4471

acquisition software (Molecular Devices LLC, USA). The spontaneous synaptic activity was recorded by clamping the membrane voltage at −56 mV holding potential (not corrected for liquid junction potential, which was 14 mV). In paired recordings, the presynaptic neuron was held under current clamp mode at −70 mV (≤0.02 nA negative current injection), and action potentials were elicited by injecting short (4 ms) square current pulses (1 nA). The postsynaptic cell was voltage clamped usually at −56 mV holding potential. Monosynaptic connections were recognized by their short latency (<5 ms[62]), measured between the peak of the evoked action potential and the onset of the postsynaptic current response. All recorded events were analyzed offline with the AxoGraph 1.4.4 (Axon Instrument) event detection software (Axon CNS, Molecular Devices).

Calcium Imaging. Cultures were loaded for 1 h at RT with cell-permeable Fura-2-AM (2 μM) in the extracellular recording solution supplemented with 0.5% bovine serum albumin. The Fura-2-loaded cultures were observed with a 40× objective (0.6 NA, Nikon, Japan), and recordings were performed from visual fields (120 × 160 μm^2) containing on average 7 ± 2 neurons. Prior to recording Ca^{2+} signals, we selected the cells by drawing regions of interest (ROI) around their bodies to reduce any background.[23] Samples were excited at wavelengths of 340 and 380 nm generated by a monochromator device equipped with integrated light source (Polychrome IV, Till Photonics). Excitation light was separated from the light emitted from the sample using a 395 nm dichroic mirror. Images of emitted fluorescence >510 nm were acquired continuously for a maximum of 2400 s (200 ms individual exposure time) by a cooled slow-scan interline transfer camera (IMAGO CCD camera; Till Photonics). The camera was operated on 8 × 8 pixel binning mode, and the imaging system was controlled by an integrating imaging software package (TILLvisION; Till Photonics). To induce rhythmic bursts, 20 μM bicuculline methiodide was bath-applied after 15 min recording;[23] at the end of each experiment, tetrodotoxin (1 μM; Latoxan) was applied to confirm the neuronal nature of the recorded signals.[23] Recorded images were analyzed offline by Clampfit software (pClamp suite, 10.2 version; Molecular Devices LLC, US) and Igor Pro software (6.32A version; WaveMetrics, Lake Oswego, Oregon, USA). Intracellular Ca^{2+} transients were expressed as fractional amplitude increase ($\Delta F/F_0$, where F_0 is the baseline fluorescence level and ΔF is the rise over the baseline); elevations in calcium level were considered significant if they exceeded 5 times the standard deviation of the noise. We then computed the difference between consecutive onset times to obtain the IEI. Hence, after the IEI values were obtained from each active cell in the field, data were pooled for all fields recorded under the same experimental conditions and averaged for further comparison.

FM1-43 Loading and Destaining. Depolarization-dependent staining of synaptic terminals with the styryl dye *N*-(3-triethylammoniumpropyl)-4-(4-(dibutylamino)styryl)pyridinium dibromide (FM1-43, Molecular Probes, Life Technology) was obtained by incubating cultures (after 10 min saline buffer wash at RT) for 120 s with 50 mM KCl and FM1-43 (15 μM). The buffer was replaced with 2 mL of normal saline containing FM1-43, and cells were left to recover for 10 min to ensure complete recycling of the vesicles[63] and then incubated for 10 min with saline containing 6-cyano-7-nitroquinoxaline-2,3-dione (10 μM) and 2-aminophosphonovaleric acid (50 μM) to prevent network activity altering the rate of FM release. These antagonists were present throughout the experiment. After incubation with FM1-43 dye, cultures were transferred to the stage of a Nikon Eclipse Ti−U inverted microscope equipped with a piezoelectric table (Nano-ZI Series 500 μm range, Mad City Laboratories), HBO 103 W/2 mercury short lamp (Osram, Munich, Germany), mirror unit (exciter filter BP 465−495 nm, dichroic 505 nm, emission filter BP 515−555), and electron multiplier CCD camera C9100-13 (Hamamatsu Photonics, Japan). Images were acquired with an oil-immersion Plan Apo 100× (1.4 NA, Nikon, Japan) objective at a sampling of 2 Hz with a spatial resolution of 256 × 256 pixels. All experiments were performed at RT. Application of 50 mM KCl (5 s), followed by a 2 min washout, was used to stimulate vesicle exocytosis from the dye-containing terminals, measured as a fluorescence loss. The imaging system was controlled by an integrating imaging software package (NIS Element, Nikon, Japan). Offline analysis was performed on the image sequence with the image-processing package Fiji.[64] After background subtraction, images were analyzed using rounded ROIs of 4 pixels in diameter drawn on neural processes. Endocytosed vesicles during FM1-43 loading were measured by estimating the brightness of the total vesicle pool puncta (raw fluorescence intensity) in GO-treated and untreated cultures before the unloading stimulus. The decay time constant, τ, was measured by pClamp 10.2 software (Molecular Devices LLC, USA). To avoid imaging nonselective FM staining, only puncta that showed stimulus-dependent destaining were included in the analyses.

Immunofluorescence Labeling. Hippocampal neurons or glial cells, treated and untreated, were fixed in PBS containing 4% PFA for 20 min at RT. Cells were permeabilized with 1% Triton X-100 for 30 min, blocked with 5% FBS in PBS for 30 min at RT, and incubated with primary antibodies for 30 min. The primary antibodies used were rabbit polyclonal anti-β-tubulin III (Sigma T2200, 1:250 dilution), mouse monoclonal anti-GFAP (Sigma-Aldrich, 1:500 dilution), and guinea pig polyclonal antivesicular glutamate transporter (Millipore AB5905, dilution 1:2000). After the primary incubation and PBS washes, neurons were incubated for 30 min with the secondary antibodies AlexaFluor 594 goat anti-rabbit (Invitrogen, dilution 1:500), AlexaFluor 488 goat anti-mouse (Invitrogen, dilution 1:500), AlexaFluor 488 goat anti-guinea pig (Invitrogen, dilution 1:500), and DAPI (Invitrogen, dilution 1:200) to stain the nuclei. Samples were mounted in Vectashield (Vector Laboratories) on 1 mm thick coverslips. Cell densities were quantified at 20× (0.5 NA) magnification using a DM6000 Leica microscope (Leica Microsystems GmbH, Wetzlar, Germany), with random sampling of seven to ten fields (713 × 532 μm; control and treated, n = 3 culture series). For VGLUT1-positive terminals, image acquisition was performed using a confocal microscope (Leica Microsystems GmbH, Wetzlar, Germany) with 63× (1.4 NA) magnification (*Z*-stacks were acquired every 300 nm; 12 fields for control and untreated conditions). Offline analysis was performed using Volocity software (Volocity 3D image analysis software, PerkinElmer, USA). For each set of experiments, the images were acquired using identical exposure settings. The ROIs for the quantification were blindly chosen using the tubulin channel. For each analyzed field, we used the *Z*-stacks to quantify VGLUT1 puncta as 3D objects. The resulting numbers were normalized to the relative cellular volume calculated on the basis of β-tubulin III labeling.

Micovesicle Isolation and Characterization. Microvesicle shedding was induced in 21 DIV confluent glial cells (after washing in PBS, 37 °C) upon exposure to benzoyl-ATP (bzATP; 100 μM) in Krebs−Ringer solution with the following composition: 125 mM NaCl, 5 mM KCl, 1.2 mM $MgSO_4$, 1.2 mM KH_2PO_4, 2 mM $CaCl_2$, 6 mM D-glucose, and 25 mM HEPES/NaOH (pH adjusted to 7.4), for 30 min at 37 °C and 5% CO_2.[39] MVs were pelleted by centrifugation as described in Bianco *et al.*[39] Negative controls were incubated with Krebs−Ringer solution without the presence of bzATP. MVs isolated from confluent mixed glial cells were resuspended in lysis buffer (50 mM Tris-HCl, pH 8.0, 150 mM NaCl, 1% NP40, 0.1% SDS), sonicated 3 × 10 s, and then boiled at 95 °C for 5 min. Samples were run on a 10% polyacrylamide gel and were blotted onto nitrocellulose filters (Millipore, Italy). Filters were then blocked in PBS-Tween-20 (0.1%) plus 5% nonfat dry milk and incubated with the primary antibody antiflotillin-1 (dilution 1:1000) for 16 h at 4 °C. Specific MV marker flotillin-1[40,41] was detected with mouse monoclonal anti-flotillin-1 (dilution 1:1000). After three washes with PBS-Tween, filters were incubated with peroxidase-conjugated anti-mouse secondary antibody (dilution 1:1000). Optical density of immunolabeled ECL-exposed protein bands was measured with UVI-1D software.

For the AFM characterization, MVs were diluted 1:10 in PBS buffer solution and processed as described in Junker *et al.*[65] Briefly, a 15 μL drop of sample solution was placed and left to adsorb (15 min) onto a freshly peeled mica substrate, thereafter rinsed with PBS. In order to reduce vesicle collapsing during AFM analysis, vesicles were fixed with 1% formaldehyde for 1 h (RT). MVs were then washed with PBS and dried under a gentle stream of nitrogen. AFM was used in semicontact mode at RT in air using a commercial instrument (Solver Pro, NT-MDT, RU). Silicon tips (NSC36/CR-AU, MikroMash, USA) with a

DOI: 10.1021/acsnano.6b00130
ACS Nano 2016, 10, 4459−4471

typical force constant of 0.6 nN/nm and a resonance frequency of about 65 kHz were employed. Topographic height and phase images were recorded at 512 × 512 pixels at a scan rate of 0.5 Hz. Image processing was performed using Gwyddion freeware AFM analysis software, version 2.40.[66] For statistical analysis, 107 individual MVs were imaged in seven different fields and measured. In particular, width and height of each vesicle were evaluated from cross-line profiles, and results were statistically analyzed using Igor Pro software (Wavemetrics. USA).

ASSOCIATED CONTENT

Supporting Information

The Supporting Information is available free of charge on the ACS Publications website at DOI: 10.1021/acsnano.6b00130.

Supporting results, Figures S1−S8, and Tables S1 and S2 (PDF)

AUTHOR INFORMATION

Corresponding Authors

*E-mail: prato@units.it.

*E-mail: laura.ballerini@sissa.it.

Author Contributions

R.R. and A.F. performed cell biology, electrophysiology, and immunofluorescence experiments and analysis; R.R. and F.P.U.S. designed and performed imaging and real-time imaging experiments and analysis; N.L. and K.K. contributed to the synthesis and characterization of thin graphene oxide (l-GO and s-GO) of biological grade; V.L. and E.V. contributed to the synthesis and characterization of pristine graphene; M.M. performed glial cell experiments, immunofluorescence, and Western blot; D.S., I.R., and L.C. designed and performed the AFM experiments; L.B. and M.P. conceived the study; L.B. conceived the experimental design and contributed to the analysis of data; L.B. wrote the manuscript.

Notes

The authors declare no competing financial interest.

ACKNOWLEDGMENTS

We are especially grateful to Micaela Grandolfo, Jessica Franzot, and Beatrice Pastore for supervising the synaptic immune staining and quantification, the glial cell culturing, and Western Blot experiments. IOM-TASC National Laboratory (Trieste) is also gratefully acknowledged for AFM assistance. N.L. acknowledges Leon Newman for assistance with the TEM and Raman instrumentation. The authors acknowledge the staff in the Faculty of Life Sciences EM Facility and the Wellcome Trust for equipment grant support to the EM Facility. The University of Manchester Bioimaging Facility microscopes used in this study were purchased with grants from the BBSRC, Wellcome Trust, and the University of Manchester Strategic Fund. X-ray photoelectron spectroscopy was performed at the National EPSRC XPS User's Service (NEXUS) at Newcastle University, an EPSRC Mid-Range Facility. The Antolin group is also acknowledged for the provision of the commercial material. We acknowledge financial support from the EU FP7-ICT-2013-FET-F GRAPHENE Flagship project (No. 604391) from the NEUROSCAFFOLDS-FP7-NMP-604263 and PRIN-MIUR No. 2012MYESZW.

REFERENCES

(1) Sanchez, V. C.; Jachak, A.; Hurt, R. H.; Kane, A. B. Biological Interactions of Graphene-Family Nanomaterials: An Interdisciplinary Review. *Chem. Res. Toxicol.* **2012**, *25*, 15−34.

(2) Kostarelos, K.; Novoselov, K. S. Materials Science. Exploring the Interface of Graphene and Biology. *Science* **2014**, *344*, 261−263.

(3) Mao, H. Y.; Laurent, S.; Chen, W.; Akhavan, O.; Imani, M.; Ashkarran, A. A.; Mahmoudi, M. Graphene: Promises, Facts, Opportunities, and Challenges in Nanomedicine. *Chem. Rev.* **2013**, *113*, 3407−3424.

(4) Bitounis, D.; Ali-Boucetta, H.; Hong, B. H.; Min, D. H.; Kostarelos, K. Prospects and Challenges of Graphene in Biomedical Applications. *Adv. Mater.* **2013**, *25*, 2258−2268.

(5) Krishna, K. V.; Ménard-Moyon, C.; Verma, S.; Bianco, A. Graphene-Based Nanomaterials for Nanobiotechnology and Biomedical Applications. *Nanomedicine (London, U. K.)* **2013**, *8*, 1669−1688.

(6) Wang, Y.; Li, Z.; Wang, J.; Li, J.; Lin, Y. Graphene and Graphene Oxide: Biofunctionalization and Applications in Biotechnology. *Trends Biotechnol.* **2011**, *29*, 205−212.

(7) Kuzum, D.; Takano, H.; Shim, E.; Reed, J. C.; Juul, H.; Richardson, A. G.; de Vries, J.; Bink, H.; Dichter, M. A.; Lucas, T. H.; Coulter, D. A.; Cubukcu, E.; Litt, B. Transparent and Flexible Low Noise Graphene Electrodes for Simultaneous Electrophysiology and Neuroimaging. *Nat. Commun.* **2015**, *5*, 5259−5263.

(8) Li, Y.; Yuan, H.; von dem Bussche, A.; Creighton, M.; Hurt, R. H.; Kane, A. B.; Gao, H. Graphene Microsheets Enter Cells Through Spontaneous Membrane Penetration at Edge Asperities and Corner Sites. *Proc. Natl. Acad. Sci. U. S. A.* **2013**, *110*, 12295−12300.

(9) Tu, Y.; Lv, M.; Xiu, P.; Huynh, T.; Zhang, M.; Castelli, M.; Liu, Z.; Huang, Q.; Fan, C.; Fang, H.; Zhou, R. Destructive Extraction of Phospholipids from Escherichia Coli Membranes by Graphene Nanosheets. *Nat. Nanotechnol.* **2013**, *8*, 594−601.

(10) Mao, J.; Guo, R.; Yan, L. Simulations and Analysis of Cellular Internalization Pathways and Membrane Perturbation for Graphene Nanosheets. *Biomaterials* **2014**, *35*, 6069−6077.

(11) Rizzoli, S. O. Synaptic Vesicle Recycling: Steps and Principles. *EMBO J.* **2014**, *33*, 788−822.

(12) Bianco, A. Graphene: Safe or Toxic? The Two Faces of the Medal. *Angew. Chem., Int. Ed.* **2013**, *52*, 4986−4997.

(13) Yang, D.; Li, T.; Xu, M.; Gao, F.; Yang, J.; Yang, Z.; Le, W. Graphene Oxide Promotes the Differentiation of Mouse Embryonic Stem Cells to Dopamine Neurons. *Nanomedicine (London, U. K.)* **2014**, *9*, 2445−2455.

(14) Zhang, Y.; Ali, S. F.; Dervishi, E.; Xu, Y.; Li, Z.; Casciano, D.; Biris, A. S. Cytotoxicity Effects of Graphene and Single-Wall Carbon Nanotubes in Neural Phaeochromocytoma-Derived PC12 Cells. *ACS Nano* **2010**, *4*, 3181−3186.

(15) Falchi, A. M.; Sogos, V.; Saba, F.; Piras, M.; Congiu, T.; Piludu, M. Astrocytes Shed Large Membrane Vesicles that Contain Mitochondria, Lipid Doplets and ATP. *Histochem. Cell Biol.* **2013**, *139*, 221−231.

(16) León, V.; Quintana, M.; Herrero, M. A.; Fierro, J. L.; de la Hoz, A.; Prato, M.; Vázquez, E. Few-Layer Graphenes from Ball-Milling of Graphite with Melamine. *Chem. Commun. (Cambridge, U. K.)* **2011**, *47*, 10936−10938.

(17) León, V.; Rodriguez, A. M.; Prieto, P.; Prato, M.; Vázquez, E. Exfoliation of Graphite with Triazine Derivatives under Ball-Milling Conditions: Preparation of Few-Layer Graphene *via* Selective Noncovalent Interactions. *ACS Nano* **2014**, *8*, 563−571.

(18) Carp, J. S. Physiological Properties of Primate Lumbar Motoneurons. *J. Neurophysiol.* **1992**, *68*, 1121−1132.

(19) Gao, Y.; Liu, L.; Li, Q.; Wang, Y. Differential Alterations in the Morphology and Electrophysiology of Layer II Pyramidal Cells in the Primary Visual Cortex of a Mouse Model Prenatally Exposed to LPS. *Neurosci. Lett.* **2015**, *591*, 138−143.

(20) Djuric, U.; Cheung, A. Y.; Zhang, W.; Mok, R. S.; Lai, W.; Piekna, A.; Hendry, J. A.; Ross, P. J.; Pasceri, P.; Kim, D. S.; Salter, M. W.; Ellis, J. MECP2e1 Isoform Mutation Affects the Form and Function of Neurons Derived from Rett Syndrome Patient iPS Cells. *Neurobiol. Dis.* **2015**, *76*, 37−45.

(21) Lovat, V.; Pantarotto, D.; Lagostena, L.; Cacciari, B.; Grandolfo, M.; Righi, M.; Spalluto, G.; Prato, M.; Ballerini, L. Carbon Nanotube

DOI: 10.1021/acsnano.6b00130
ACS Nano 2016, 10, 4459−4471

Substrates Boost Neuronal Electrical Signaling. *Nano Lett.* **2005**, *5*, 1107−1110.
(22) Cellot, G.; Toma, F. M.; Varley, Z. K.; Laishram, J.; Villari, A.; Quintana, M.; Cipollone, S.; Prato, M.; Ballerini, L. Carbon Nanotube Scaffolds Tune Synaptic Strenght in Cultured Neural Circuits: Novel Frontiers in Nanomaterials-Tissue Interactions. *J. Neurosci.* **2011**, *31*, 12945−12953.
(23) Bosi, S.; Rauti, R.; Laishram, J.; Turco, A.; Lonardoni, D.; Nieus, T.; Prato, M.; Scaini, D.; Ballerini, L. From 2D to 3D: Novel Nanostructured Scaffolds to Investigate Signaling in Reconstructed Neuronal Networks. *Sci. Rep.* **2015**, *5*, 9562.
(24) Stetter, O.; Battaglia, D.; Soriano, J.; Geisel, T. Model-Free Reconstruction of Excitatory Neuronal Connectivity from Calcium Imaging Signals. *PLoS Comput. Biol.* **2012**, *8*, e1002653.
(25) Fabbro, A.; Pastore, B.; Nistri, A.; Ballerini, L. Activity-Independent Intracellular Ca^{2+} Oscillations are Spontaneously Generated by Ventral Spinal Neurons during Development *in vitro*. *Cell Calcium* **2007**, *41*, 317−329.
(26) Tibau, E.; Valencia, M.; Soriano, J. Identification of Neuronal Network Properties from the Spectral Analysis of Calcium Imaging Signals in Neuronal Cultures. *Front. Neural Circuits* **2013**, *7*, 199.
(27) Sokal, D. M.; Mason, R.; Parker, T. L. Multi-Neuronal Recordings Reveal a Differential Effect of Thapsigargin on Bicuculline- or Gabazine-Induced Epileptiform Excitability in Rat Hippocampal Neuronal Networks. *Neuropharmacology* **2000**, *39*, 2408−2417.
(28) Raastad, M.; Storm, J. F.; Andersen, P. Putative Single Quantum and Single Fibre Excitatory Postsynaptic Currents Show Similar Amplitude Range and Variability in Rat Hippocampal Slices. *Eur. J. Neurosci.* **1992**, *4*, 113−117.
(29) Bellocchio, E. E.; Reimer, R. J.; Fremeau, R. T., Jr; Edwards, R. H. Uptake of Glutamate into Synaptic Vesicles by an Inorganic Phosphate Transporter. *Science* **2000**, *289*, 957−960.
(30) Moulder, K. L.; Jiang, X.; Taylor, A. A.; Shin, W.; Gillis, K. D.; Mennerick, S. Vesicle Pool Heterogeneity at Hippocampal Glutamate and GABA Synapses. *J. Neurosci.* **2007**, *27*, 9846−9854.
(31) Betz, W. J.; Bewick, G. S. Optical Analysis of Synaptic Vesicle Recycling at the Frog Neuromuscular Junction. *Science* **1992**, *255*, 200−203.
(32) Ryan, T. A.; Reuter, H.; Wendland, B.; Schweizer, F. E.; Tsien, R. W.; Smith, S. J. The Kinetics of Synaptic Vesicle Recycling Measured at Single Presynaptic Boutons. *Neuron* **1993**, *11*, 713−724.
(33) Betz, W.; Mao, F.; Smith, C. Imaging Exocytosis and Endocytosis. *Curr. Opin. Neurobiol.* **1996**, *6*, 365−371.
(34) Ryan, T. A. Presynaptic Imaging Techniques. *Curr. Opin. Neurobiol.* **2001**, *11*, 544−549.
(35) Turola, E.; Furlan, R.; Bianco, F.; Matteoli, M.; Verderio, C. Microglial Microvesicles Secretion and Intercellular Signaling. *Front. Physiol.* **2012**, *3*, 149.
(36) Frühbeis, C.; Fröhlich, D.; Kuo, W. P.; Krämer-Albers, E. M. Extracellular Vesicles as Mediators of Neuron-Glia Communication. *Front. Cell. Neurosci.* **2013**, *7*, 182.
(37) Antonucci, F.; Turola, E.; Riganti, L.; Caleo, M.; Gabrielli, M.; Perrotta, C.; Novellino, L.; Clementi, E.; Giussani, P.; Viani, P.; Matteoli, M.; Verderio, C. Microvesicles Released from Microglia Stimulate Synaptic Activity *via* Enhanced Sphingolipid Metabolism. *EMBO J.* **2012**, *31*, 1231−1240.
(38) Bianco, F.; Pravettoni, E.; Colombo, A.; Schenk, U.; Möller, T.; Matteoli, M.; Verderio, C. Astrocyte-Derived ATP Induces Vesicle Shedding and IL-1 Beta Release from Microglia. *J. Immunol.* **2005**, *174*, 7268−7277.
(39) Bianco, F.; Perrotta, C.; Novellino, L.; Francolini, M.; Riganti, L.; Menna, E.; Saglietti, L.; Schuchman, E. H.; Furlan, R.; Clementi, E.; Matteoli, M.; Verderio, C. Acid Sphingomyelinase Activity Triggers Microparticle Release from Glial Cells. *EMBO J.* **2009**, *28*, 1043−1054.
(40) Del Conde, I.; Shrimpton, C. N.; Thiagarajan, P.; López, J. A. Tissue-Factor-Bearing Microvesicles Arise from Lipid Drafts and Fuse with Activated Platelets to Initiate Coagulation. *Blood* **2005**, *106*, 1604−1611.
(41) Al-Nedawi, K.; Meehan, B.; Micallef, J.; Lhotak, V.; May, L.; Guha, A.; Rak, J. Intercellular Transfer of the Oncogenic Receptor EGFRvIII by Microvesicles Derived from Tumour Cells. *Nat. Cell Biol.* **2008**, *10*, 619−624.
(42) Antonyak, M. A.; Cerione, R. A. Microvesicles as Mediators of Intercellular Communication in Cancer. *Methods Mol. Biol.* **2014**, *1165*, 147−173.
(43) Toyoshima, D.; Mandai, K.; Maruo, T.; Supriyanto, I.; Togashi, H.; Inoue, T.; Mori, M.; Takai, Y. Afadin Regulates Puncta Adherentia Junction Formation and Presynaptic Differentiation in Hippocampal Neurons. *PLoS One* **2014**, *9*, e89763.
(44) Aguado, F.; Carmona, M. A.; Pozas, E.; Aguiló, A.; Martínez-Guijarro, F. J.; Alcantara, S.; Borrell, V.; Yuste, R.; Ibañez, C. F.; Soriano, E. BDNF Regulates Spontaneous Correlated Activity at Early Developmental Stages by Increasing Synaptogenesis and Expression of the K^+/Cl^- Co-Transporter KCC2. *Development* **2003**, *130*, 1267−1280.
(45) Chong, Y.; Ge, C.; Yang, Z.; Garate, J. A.; Gu, Z.; Weber, J. K.; Liu, J.; Zhou, R. Reduced Cytotoxicity of Graphene Nanosheets Mediated by Blood-Protein Coating. *ACS Nano* **2015**, *9*, 5713−5724.
(46) Fabbro, A.; Sucapane, A.; Toma, F. M.; Calura, E.; Rizzetto, L.; Carrieri, C.; Roncaglia, P.; Martinelli, V.; Scaini, D.; Masten, L.; Turco, A.; Gustincich, S.; Prato, M.; Ballerini, L. Adhesion to Carbon Nanotube Conductive Scaffolds Forces Action-Potential Appearance in Immature Rat Spinal Neurons. *PLoS One* **2013**, *8*, e73621.
(47) Malarkey, E. B.; Reyes, R. C.; Zhao, B.; Haddon, R. C.; Parpura, V. Water Soluble Single-Walled Carbon Nanotubes Inhibit Stimulated Endocytosis in Neurons. *Nano Lett.* **2008**, *8*, 3538−3542.
(48) High, B.; Cole, A. A.; Chen, X.; Reese, T. S. Electron Microscopic Tomography Reveals Discrete Transcleft Elements at Excitatory and Inhibitory Synapses. *Front. Synaptic Neurosci.* **2015**, *7*, 9.
(49) Fedorovich, S. V.; Alekseenko, A. V.; Waseem, T. V. Are Synapses Targets of Nanoparticles? *Biochem. Soc. Trans.* **2010**, *38*, 536−538.
(50) Grados, M. A.; Atkins, E. B.; Kovacikova, G. I.; McVicar, E. A Selective Review of Glutamate Pharmacological Therapy in Obsessive-Compulsive and Related Disorders. *Psychology Res. and Behavior Management PRBM* **2015**, *8*, 115−131.
(51) Gardoni, F.; Di Luca, M. Targeting Glutamatergic Synapses in Parkinson's Disease. *Curr. Opin. Pharmacol.* **2015**, *20*, 24−28.
(52) Stone, J. M. Glutamatergic Antipsychotic Drugs: a New Dawn in the Treatment of Schizophrenia? *Ther. Adv. Psychopharmacol.* **2011**, *1*, 5−18.
(53) Meyer, R. A.; Sunshine, J. C.; Green, J. J. Biomimetic Particles as Therapeutics. *Trends Biotechnol.* **2015**, *33*, 514−524.
(54) Borisova, T.; Nazarova, A.; Dekaliuk, M.; Krisanova, N.; Pozdnyakova, N.; Borysov, A.; Sivko, R.; Demchenko, A. P. Neuromodulatory Properties of Fluorescent Carbon Dots: Effect on Exocytotic Release, Uptake and Ambient Level of Glutamate and GABA in Brain Nerve Terminals. *Int. J. Biochem. Cell Biol.* **2015**, *59*, 203−215.
(55) Fabbro, A.; Scaini, D.; León, V.; Vázquez, E.; Cellot, G.; Privitera, G.; Lombardi, L.; Torrisi, F.; Tomarchio, F.; Bonaccorso, F.; Bosi, S.; Ferrari, A. C.; Ballerini, L.; Prato, M. Graphene-Based Interfaces Do Not Alter Target Nerve Cells. *ACS Nano* **2016**, *10*, 615−23.
(56) Ali-Boucetta, H.; Bitounis, D.; Raveendran-Nair, R.; Servant, A.; Van den Bossche, J.; Kostarelos, K. Purified Graphene Oxide Dispersions Lack *in vitro* Cytotoxicity and *in vivo* Pathogenicity. *Adv. Healthcare Mater.* **2013**, *2*, 433−441.
(57) Mukherjee, S. P.; Lozano, N.; Kucki, M.; Del-Rio Castillo, A. E.; Vázquez, E.; Kostarelos, K.; Wick, P.; Fadeel, B. Detection of Endotoxin Contamination of Graphene Oxide Using the TNF-α Expression Test and Guidelines for Endotoxin-Free Graphene Oxide Production. Submitted for publication.
(58) Jasim, D. A.; Lozano, N.; Kostarelos, K. Synthesis of Few-Layered, High-Purity Graphene Oxide Sheets from Different Graphite Sources for Biology. *2D Mater.* **2016**, *3*, 014006.

DOI: 10.1021/acsnano.6b00130
ACS Nano 2016, 10, 4459−4471

(59) Varela-Rizo, H.; Rodriguez-Pastor, I.; Merino, C.; Martin-Gullon, I. Highly Crystalline Graphene Oxide Nano-Platelets Produced From Helical-Ribbon Carbon Nanofibers. *Carbon* **2010**, *48*, 3640−3643.
(60) Cellot, G.; Cilia, E.; Cipollone, S.; Rancic, V.; Sucapane, A.; Giordani, S.; Gambazzi, L.; Markram, H.; Grandolfo, M.; Scaini, D.; Gelain, F.; Casalis, L.; Prato, M.; Giugliano, M.; Ballerini, L. Carbon Nanotubes Might Improve Neuronal Performance by Favouring Electrical Shortcuts. *Nat. Nanotechnol.* **2009**, *4*, 126−133.
(61) Calegari, F.; Coco, S.; Taverna, E.; Bassetti, M.; Verderio, C.; Corradi, N.; Matteoli, M.; Rosa, P. A Regulated Secretory Pathway in Cultured Hippocampal Astrocytes. *J. Biol. Chem.* **1999**, *274*, 22539−22547.
(62) Pavlidis, P.; Montgomery, J.; Madison, D. V. Presynaptic Protein Kinase Activity Supports Long-Term Potentiation at Synapses Between Individual Hippocampal Neurons. *J. Neurosci.* **2000**, *20*, 4497−4505.
(63) Hoopmann, P.; Rizzoli, S. O.; Betz, W. J. Imaging Synaptic Vesicle Recycling by Staining and Destaining Vesicles with FM Dyes. *Cold Spring Harbor Protoc.* **2012**, *1*, 77−83.
(64) Schindelin, J.; Arganda-Carreras, I.; Frise, E.; Kaynig, V.; Longair, M.; Pietzsch, T.; Preibisch, S.; Rueden, C.; Saalfeld, S.; Schmid, B.; Tinevez, J. Y.; White, D. J.; Hartenstein, V.; Eliceiri, K.; Tomancak, P.; Cardona, A. Fiji: An Open-Source Platform for Biological-Image Analysis. *Nat. Methods* **2012**, *9*, 676−682.
(65) Junker, J. P.; Rief, M. Single-Molecule Force Spectroscopy Distinguishes Target Binding Modes of Calmodulin. *Proc. Natl. Acad. Sci. U. S. A.* **2009**, *106*, 14361−14366.
(66) Klapetek, P.; Valtr, M.; Nečas, D.; Salyk, O.; Dzik, P. Atomic Force Microscopy Analysis of Nanoparticles in Non-Ideal Conditions. *Nanoscale Res. Lett.* **2011**, *6*, 514.

DOI: 10.1021/acsnano.6b00130
ACS Nano 2016, 10, 4459−4471

Graphene Oxide Nanosheets Reshape Synaptic Function in Cultured Brain Networks

Rossana Rauti[†], Neus Lozano[§], Veronica León[‡], Denis Scaini[†,#], Mattia Musto[ø], Ilaria Rago[#], Francesco P. Ulloa Severino[ø], Alessandra Fabbro[‖], Loredana Casalis[#], Ester Vázquez[‡], Kostas Kostarelos[§], Maurizio Prato[‖&¥] and Laura Ballerini[†,ø*]*

Supporting Results

Figure S1

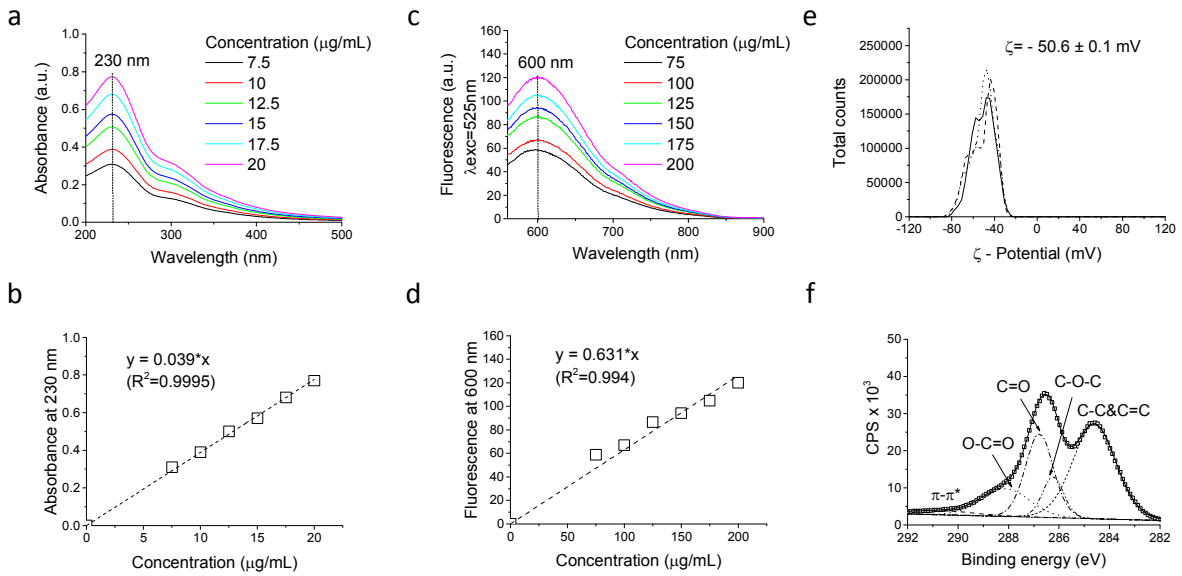

Figure S1. Physicochemical characterization of s-GO*. (a) UV-Vis absorption spectra and (b) maximum absorbance at 230nm. (c) Fluorescence spectra and (d) maximum fluorescence at 600nm. (e) Zeta-potential measurements. (f) High resolution C1s XPS spectrum.*

Figure S2

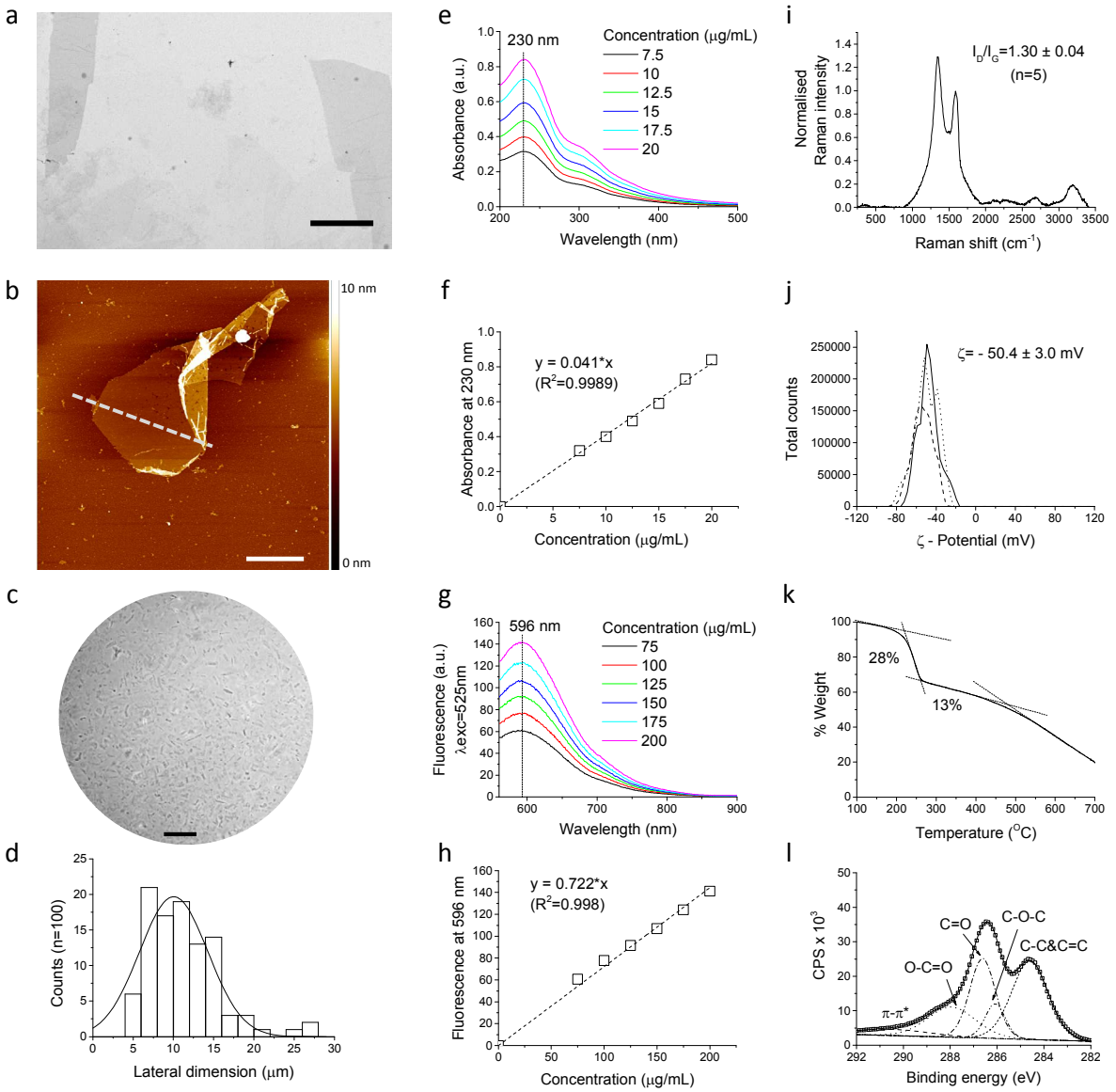

Figure S2. Physicochemical characterization of l-GO*. (a) TEM micrograph (scale bar 5μm). (b) AFM height image (scale bar 2 μm. (c) Bright field optical microscopy image (scale bar 50 μm) and (d) lateral dimension distribution analysis. (e) UV-Vis absorption spectra and (f) maximum absorbance at 230nm (g) Fluorescence spectra and (h) maximum fluorescence at 596nm. (i) Normalized Raman spectrum. (j) Zeta-potential measurements. (k) TGA analysis. (l) High resolution C1s XPS spectrum.*

Table S1. Summary of the physicochemical characterization of l-GO and s-GO

	Technique	***l*-GO**	***s*-GO**
Lateral dimension (*)	*Optical microscopy*	5 µm - 30 µm	-
	TEM	10 - 30 µm	200 nm - 1 µm
	AFM	10 - 15 µm	50 nm - 500 nm
Thickness	*AFM*	1 nm (1 layer)	1.3 ± 0.3 nm (1-2 layers)
Optical properties	*Absorbance*	A_{230}=0.041 * C_{GO} (µg/mL)	A_{230}=0.039 * C_{GO} (µg/mL)
	Fluorescence, λ_{exc} 525 nm	F_{596}=0.722 * C_{GO} (µg/mL)	F_{600}=0.631 * C_{GO} (µg/mL)
Degree of defects (I_D/I_G)	*Raman*	1.30 ± 0.04	1.35 ± 0.02
Surface charge	*ζ-potential*	-50.4 ± 3.0 mV	-50.6 ± 0.1 mV
Functionalization degree	*TGA*	41%	41%
Chemical composition (Purity)	*XPS*	C: 68.8%, O: 30.8%, N: 0.4% (99.6%)	C: 69.9%, O: 29.6%, N: 0.5% (99.5%)
C:O ratio	*XPS*	2.2	2.3
π-π*, O-C=O, C=O, C-O-C, C=C	*XPS*	4.3%, 13.2%, 18.7%, 6.4%, 26.2%	2.2%, 10.3%, 18.3%, 6.8%, 32.3%

(*) Lateral dimensions of l-GO and s-GO are reported as a range between the minimum and the maximum size detected.

Table S2. XPS analysis of graphite, l-GO and s-GO.

(a) XPS survey spectra for elemental analysis in O 1s, N 1s, C 1s and Si 2p regions and (b) XPS high resolution C1s spectra for the quantification of the π- π, O-C=O, C=O, C-O-C, C-OH and C-C&C=C contributions.*

a

System	***O 1s***	***N 1s***	***C 1s***	***Si 2p***	***Purity***	***C:O***
Graphite	3.0%	-	96.3%	0.7%	99.3%	32.1
l-GO	30.8%	0.4%	68.8%	-	99.6%	2.2
s-GO	29.6%	0.5%	69.9%	-	99.5%	2.3

b

System	***π- π****	***O-C=O***	***C=O***	***C-O-C***	***C-OH***	***C-C&C=C***
Graphite	289.9 eV 15.1%	-	-	-	285.6 eV 18.5%	284.6 eV 62.7%
l-GO	290.5 eV 4.3%	287.9 eV 13.2%	286.6 eV 18.7%	286.1 eV 6.4%	- -	284.6 eV 26.2%
s-GO	290.7 eV 2.2%	288.1 eV 10.3%	286.8 eV 18.3%	286.2 eV 6.8%	- -	284.6 eV 32.3%

Figure S3.

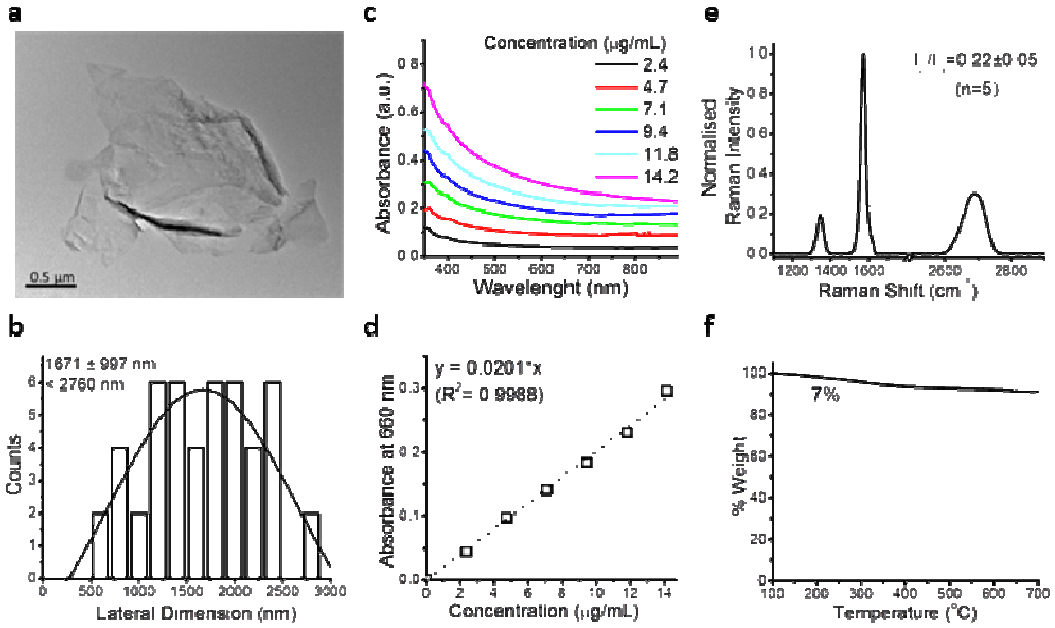

Figure S3. Physicochemical characterization of GR: *(a) TEM micrograph and (b) lateral dimension distribution analysis. (c) UV-Vis absorption spectra and (d) absorbance at 660nm. (e) Normalized Raman spectrum at 532 nm. (f) TGA analysis.*

Figure S4.

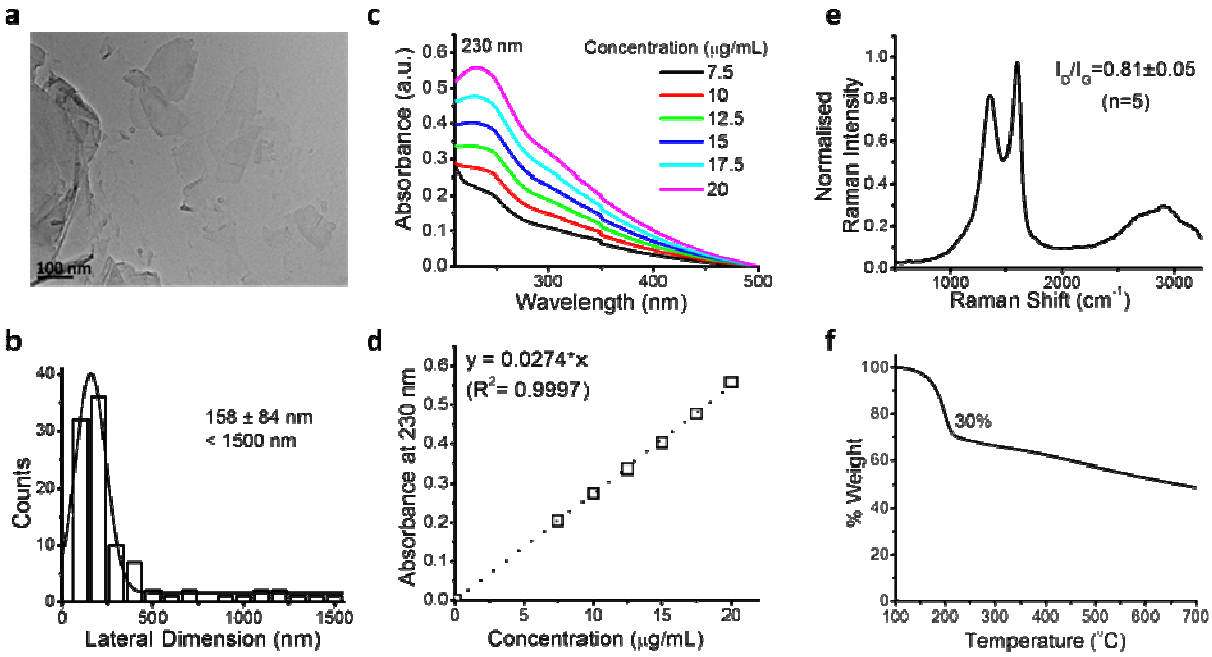

Figure S4. Physicochemical characterization of commercially-available GO (A-GO). *(a) TEM micrograph and (b) lateral dimension distribution. (c) UV-Vis absorption spectra and (d) maximum absorbance at 230nm. (e) Normalized Raman spectrum at 532 nm. (f) TGA analysis.*

A-GO effects on synaptic transmission

To validate our results on s-GO interference with synapses we tested the Antolin-GO (A-GO) in a separated set of experiments where hippocampal cultures were treated for 6-8 days with A-GO (1 μg/mL and 10 μg/mL). Membrane capacitance and input resistance displayed similar values in all the tested treatments, summarized in Table S2.

	Capacitance (pF)	Input Resistance (MΩ)
$Control_{1}$ n=17	47 ± 5	1078 ± 168
$A\text{-}GO_{1}$ n=22	49 ± 4	997 ± 158
$Control_{10}$ n=11	79 ± 11	679 ± 80
$A\text{-}GO_{10}$ n=22	70 ± 10	1011 ± 130

Figure S5 shows representative tracings of the recorded electrical activity. As for s-GO, also in this case, in neurons exposed to low (1 μg/mL) A-GO, the amplitude and frequency of PSCs were not affected compared to control cultures (71 ± 8 pA and 2.5 ± 0.3 Hz control, n= 17; 53 ± 5 pA and 2.7 ± 0.4 Hz for A-GO, n= 22; summarized in Figure S5 plots). When incubating neurons with higher A-GO concentrations (10 μg/mL), we detected a significant decrease ($P < 0.001$; Student's t-test) in PSCs frequency when compared to control cultures (0.4 ± 0.2 Hz, n= 22 in A-GO and 2.8 ± 0.5 Hz in control, n= 11). The PSCs amplitude was not significantly different between the two conditions (data are summarized in Figure S5, top plots).

Both neuronal and glial densities were not affected by 10 μg/mL A-GO (n=7 visual fields; see plots in Figure S5, bottom panel). Neuronal activity was then monitored by calcium imaging in 10 μg/mL A-GO condition. Like s-GO-treatment, in A-GO treated cultures the 50% (n= 2 out of 4) of the recorded fields didn't show any activity. In our recordings, spontaneous Ca^{2+} signaling is detected in 40% (6 out of 14 cells, control, n= 2 fields) and similarly, in 38% (6 out of 15 cells, A-GO, n= 2 fields) of the cells visualized in each field. Control Ca^{2+} oscillations displayed an IEI of 50 ± 5 s (n= 6 cells) that was significantly lower ($P<0.001$; Student's t-test) than that measured in A-GO treated cultures (168 ± 11 s, n= 6 cells). When we measured IEI in the presence of bicuculline (20 μM, 20 min), the control value was still significantly lower ($P<0.001$; Student's t-test) than that measured in A-GO treated cultures (26 ± 3 s, n= 6 control cells, *vs* 108 ± 10 s, n= 6 GO cells).

Figure S5

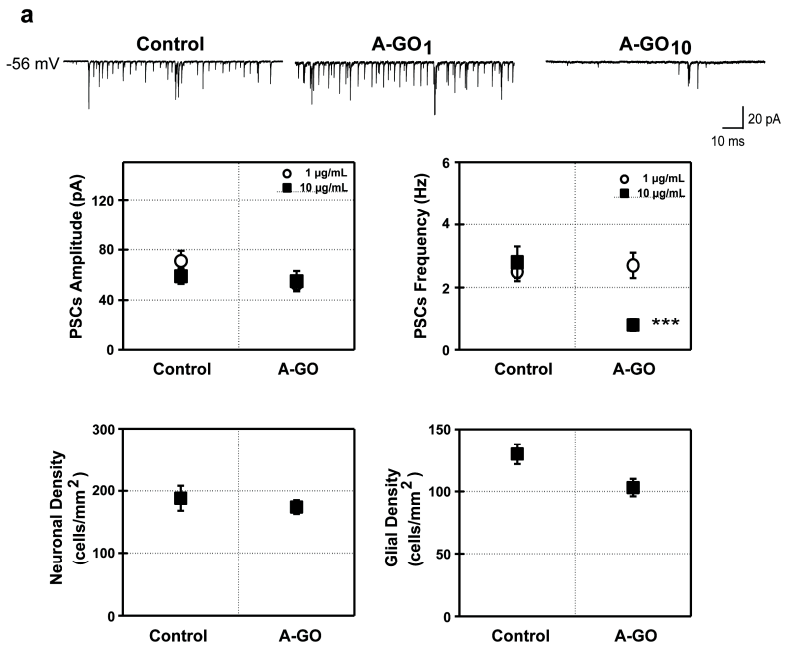

Figure S5. Spontaneous synaptic activity recorded from hippocampal neurons *in control and A-GO at 1 µg/mL and 10 µg/mL grown for 8 ÷ 10 DIV. PSCs were detected at -56 mV holding potential. Top plots represent pooled data and summarize average PSCs amplitude and frequency: note the reduction in A-GO-treatment (10 µg/mL, final concentration) of PSCs frequency (*** = P < 0.001 Student's test, data are mean ± SEM). Bottom plots summarize neuronal (left) and glial (right) densities in both conditions: no significant differences were detected.*

Inhibitory synaptic activity analysis

To determine how s-GO (10 µg/mL) treatment influenced GABAergic transmission we used simultaneous whole-cell recordings from pairs of closely located interconnected neurons (Figure S6[1]). The GABAergic nature of the evoked events was confirmed by the measured PSC slow decay ($\tau = 24 \pm 0.9$ ms, n= 16[1]) and sensitivity to bicuculline (20 µM) application (n=8). Apparently s-GO did not affect the density of inhibitory synapses, in fact the probability of finding monosynaptic coupled pairs was 70% (10 out of 14 pairs) in control and 66% in GO (6 out of 9 pairs). The similar GABAergic innervation was associated with similar amplitude of $GABA_A$ mediated events (on average the peak amplitude of evoked PSCs was 89 ± 16 pA and 96 ± 22 pA in control and s-GO treated neurons, respectively). We indirectly assessed the GABA release probability (p_r) in controls and s-GO treated pairs by measuring the paired-pulse (20 Hz) ratio [PPR, calculating the ratio between the mean peak amplitude of the second and the first PSC[2,3]]. In

both culture groups, pairs showed similar short-term depression (PPR 0.7 ± 0.12 and 0.5 ± 0.18, control and s-GO treated pairs, summarized in Figure S6a) thus ruling out gross differences in p_r.

Inhibitory synaptic density analysis

To further rule out s-GO (10 μg/mL) affecting inhibitory synapses, we examined and compared GABAergic synapses densities between control and s-GO treated cultures (8-10 DIV) by co-immunostaining for the vesicular GABA transporter (VGAT) and for neuronal cytoskeletal component β-tubulin III (Figure S6b). The following primary antibodies were used: rabbit polyclonal anti-β- tubulin III (Sigma T2200, 1:250 dilution) and mouse monoclonal antibody against the vesicular GABA transporter (VGAT, Synaptic Systems, 1:200 dilution). After the primary incubation, cultures were incubated with the secondary antibodies: Alexa 594 goat anti rabbit (Invitrogen, dilution 1:500) and Alexa 488 goat anti-mouse (Invitrogen, dilution 1:500). Confocal acquisition was performed at higher magnification (63x) and Z-stacks were acquired every 300 nm for both culture groups (n = 18 fields for control and s-GO). As for the measurements related to VGLUT1-staining, offline analysis was performed using Volocity software and for each set of experiments the cell images were acquired using identical exposure settings. As shown in the plot in Figure S6b, no significant differences in VGAT immunoreactivity were found: control and s-GO-treated neurons displayed a similar number of VGAT positive puncta (4.5 × 10-4 ± 2.6 × 10-5, control cultures; 4.0 × 10-4 ± 2.1 × 10-5, s-GO-treated cultures).

Figure S6

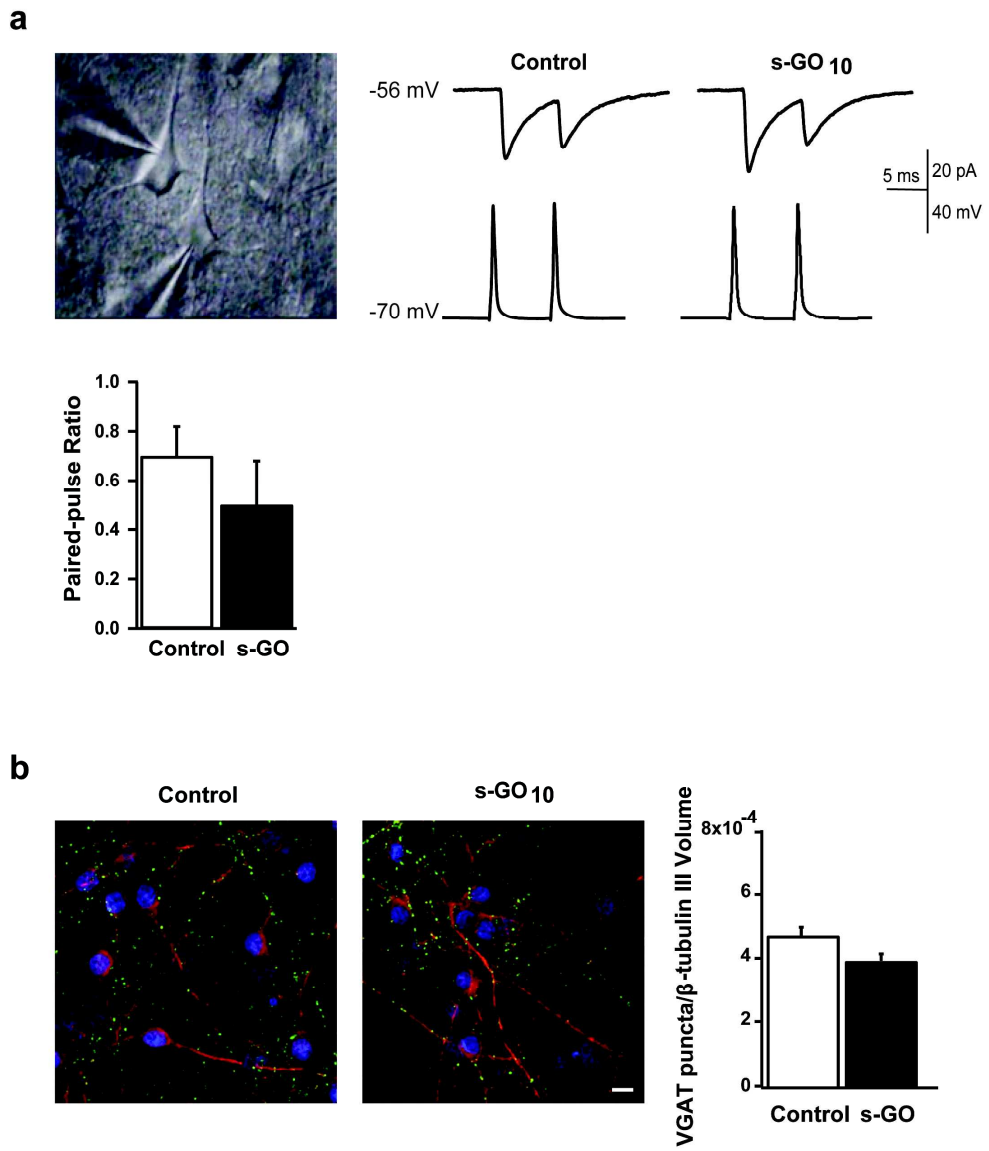

Figure S6 Representative bright field image depicts a pair of recorded neurons. *Left tracings represent presynaptic pairs of action potentials (bottom) and the corresponding monosynaptic GABAergic evoked currents (top) in control and in s-GO-treated cultures. In the plot, histograms summarize the PPR values recorded in control and s-GO-treated cultures. In (b) confocal reconstructions (n = 30 Z-stacks) showing hippocampal neurons treated and untreated with graphene oxide (10 μg/mL final concentration) immunostained for the vesicular GABA transporter (VGAT, green) and counterstained for cytoskeletal components β-tubulin III (red). Scale bar: 10 μm. The plot shows no significant difference in terms of VGAT positive puncta normalized to β-tubulin volume ($4.5 \times 10^{-4} \pm 2.6 \times 10^{-5}$, control cultures; $3.8 \times 10^{-4} \pm 2.1 \times 10^{-5}$, s-GO-treated cultures).*

Pristine Graphene and MVs release

Once we assessed the effect of s-GO on the release of the shedding MVs from glial cells, we decided to verify if also the pristine graphene (GR) could modulate it. We isolated MVs and quantify them by the analysis of the bands using western blot technique. Figure S7 shows the western blot analysis that was carried out on the P3 pellets purified from the supernatant collected from glial cultures previously incubated with GR (10 μg/mL). We have not found a positive signal from P3 pellet from glial cells incubated with GR and, as expected, no bands were obtained from P3 pellet purified from glial cultures not incubated (blot in Figure S7). We quantified astrocytes (GFAP positive cells; Figure S7 immunofluorescence images) density to determine cell survival (see Methods the Immunofluorescence staining paragraph for further details). We detected similar GFAP-positive cell densities in both GR treated and control groups (cell density GR: 855±23 cells/mm^2; cell density control: 819±23 cells/mm^2; summarized in the plot of Figure S7).

Figure S7

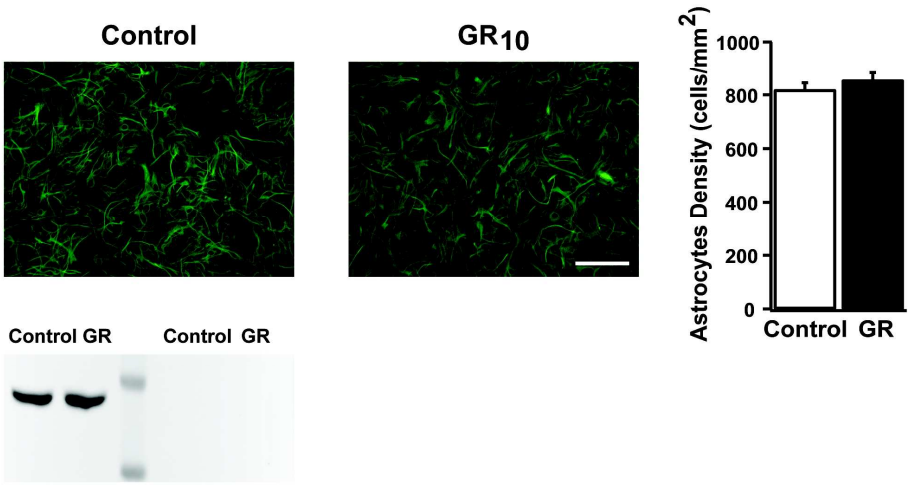

Figure S7. *Top panel: GFAP (in green) immunolabeling of primary rat astrocytes cultures (3 weeks) incubated for 6 days with graphene pristine (GR 10 μg/mL) and control untreated cultures. Scale bar: 100 μm. The histograms show astrocyte cell density in incubated and control cultures. No statistical significance was found between the two conditions. Bottom panel: Western blotting of P3 pellets (right side) and cell lysates (left side) for MVs marker flotillin-1. Pellets were obtained from the medium of glial cultures incubated with GR or not.*

s-GO flakes effects on synaptic activity in acute, 6-hours and 72-hours treatments

To elucidate the timeline of s-GO effects on synaptic activity, we patch-clamped neurons and we positioned a second pipette identical to that used for patch-clamp recording at a distance of 200 μm (under microscopy visual control) from the recorded cell. The second pipette was filled with standard saline solution (control, Krebs) or with s-GO (100 μg/mL in Krebs solution). An injection of pressurized air (500 ms duration, 8 PSI; by a Picospritzer PDES-02DX; NPI electronic GmbH, Germany) was used to deliver the s-GO acutely. The experimental settings were empirically tested.[4] In our experiments we have estimated that a long pulse of pressure as the one used combined with the relatively large pipette distance resulted in a local (i.e. on the recorded neuron) concentration of s-GO of at least 10% of that contained in the pipette. Baseline PSCs were recorded before (10 min) and after (10 min) the local injection, as shown in Figure S8a: top, control tracings, where standard saline (Krebs) was ejected and bottom, s-GO ones, where s-GO in saline solution was pressure ejected. In neurons exposed to Krebs applications, spontaneous PSCs frequency did not change (1.2 ± 0.35 Hz before the pipette saline-ejection and 1 ± 0.34 Hz after the pipette saline-ejection, n = 17; plot in Figure S8b). On the contrary, acute s-GO ejection significantly increased (***P < 0.001 Student's test) the PSCs frequency (from a baseline of 0.8 ± 0.35 Hz to a post injection frequency of 2.5 ± 0.6 Hz, n = 21, plot in Figure S8b). The increase in PSCs clearly emerged with a 10 s delay after the local s-GO ejection and was reversible, in fact PSCs frequency values returned to baseline values 7-8 min following the acute application. In all treatments, the PSCs amplitude was not affected. To note, GABAergic innervation recorded in pairs of closely located interconnected neurons was not affected by pressure ejection of s-GO applied under similar conditions (n=10; not shown).

The histograms in Figure S8c compare the frequency of PSCs when exposed to acute (pressure ejected) or to chronic s-GO (10 μg/mL). In the chronic experiments s-GO was added to the culturing medium and neuronal activity was recorded after 6-hours or after 72-hours. As shown in Figure S8c, after 6-hours we detected a slight increase in PSCs frequency when comparing control neurons (1.15 ± 0.4 Hz, n = 12) with s-GO treated ones (1.8 ± 0.5 Hz, n = 15). However, already after 72 hours treatment s-GO induced a significant decrease (**P < 0.01 Student's test) in PSCs frequency (0.7 ± 0.2 Hz) in treated neurons (n=17) when compared with untreated control cells (1.5 ± 0.36 Hz, n = 14).

These experiments confirm the ability of s-GO to specifically target synapses. It is tempting to speculate that, in the long term, this acute interference is translated in the documented decrease in synaptic activity (after 3 days) and reduction in synaptic vesicles and synaptic contacts (after 6 days).

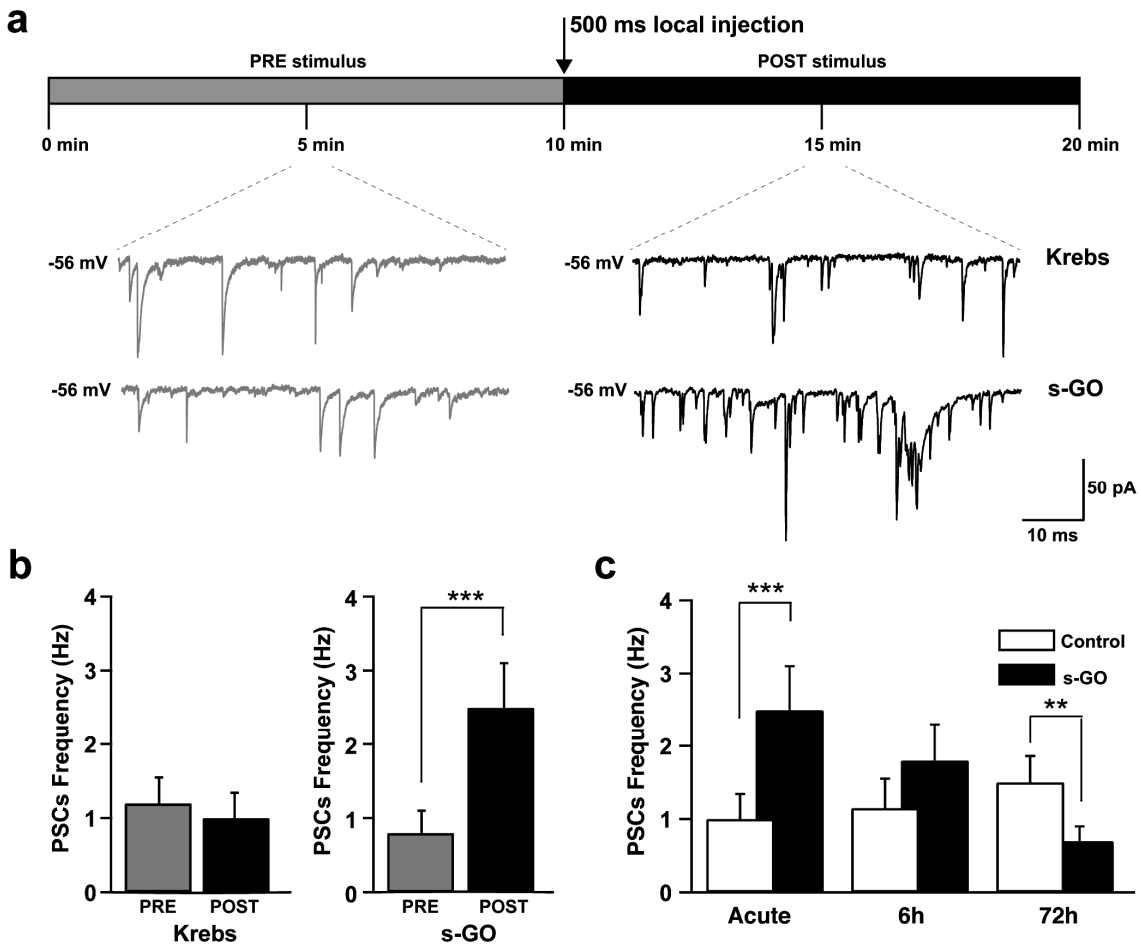

Figure S8. *In (a) schematic experimental protocol and representative tracings of spontaneous synaptic activity recorded 5 min before and 5 min after control Krebs (top) or s-GO (bottom) pulses (500 ms). In (b) plots represent pooled data and summarize average PSCs frequency before and after Krebs (left) and s-GO (right) pulses (***P < 0.001 Student's test). In (c) histograms of pooled data represent the average PSCs frequency after acute injection (as in b) or after 6h and 72h chronic exposure to s-GO (10 μg/mL final concentration) (**P < 0.01 Student's test).*

REFERENCES

1. Cellot, G.; Toma, F.M.; Varley, Z.K.; Laishram, J.; Villari, A.; Quintana, M.; Cipollone, S.; Prato, M.; Ballerini, L. Carbon Nanotube Scaffolds Tune Synaptic Strenght in Cultured Neural Circuits: Novel Frontiers in Nanomaterial-Tissue Interactions. *J Neurosci*. **2011***,* 31, 12945-12953.
2. Manabe, T.; Wyllie, D.J.; Perkel, D.J.; Nicoll, R.A. Modulation of Synaptic Transmission and Long-Term Potentiation: Effects on Paired Pulse Facilitation and EPSC Variance in the CA1 Region of the Hippocampus. *J Neurophysiol.* **1993** 70:1451-1459.
3. Debanne, D.; Guérineau, N.C.; Gähwiler, B.H.; Thompson, S.M. Paired-Pulse Facilitation and Depression at Unitary Synapses in Rat Hippocampus: Quantal Fluctuation Affects Subsequent Release. *J Physiol.* **1996** 491,163-76.
4. Smith D.V.; Uteshev V.V. Heterogeneity of Nicotininc Acetylcholine Receptor Expression in the Caudal Nucleus of the Solitary Tract. *Neuropharmacology* **2008** 54, 445-53.

6.2

Effective motor neuron differentiation of human induced pluripotent stem cells on a patch made of crosslinked monolayer gelatin nanofibers

Y. Tang, L. Liu, J. Li, L. Yu, F. P. Ulloa Severino, L. Wang, J. Shi, X. Tu, V. Torre, Y. Chen

Journal of Materials Chemistry B.

Journal of
Materials Chemistry B

PAPER

View Article Online
View Journal | View Issue

Cite this: J. Mater. Chem. B, 2016, 4, 3305

Effective motor neuron differentiation of hiPSCs on a patch made of crosslinked monolayer gelatin nanofibers†

Yadong Tang,[a] Li Liu,[b] Junjun Li,[b] Leqian Yu,[b] Francesco Paolo Ulloa Severino,[c] Li Wang,[a] Jian Shi,[a] Xiaolong Tu,[a] Vincent Torre[c] and Yong Chen*[abd]

Received 9th February 2016,
Accepted 29th March 2016

DOI: 10.1039/c6tb00351f

www.rsc.org/MaterialsB

Human induced pluripotent stem cells (hiPSCs) are differentiated into mature motor neurons by using a culture patch made of crosslinked monolayer gelatin nanofibers. Compared to the conventional culture dish method, the patch method is more effective for culture and differentiation of stem cells, because cells are supported by a net-like structure made of crosslinked monolayer nanofibers instead of a planar substrate. The pores of the net-like structure have sizes smaller than those of cells but large enough to minimize the exogenous cell–material contact and to increase the permeability as well as the efficiency of cell–cell interactions. As expected, the differentiated hiPSCs showed the up-regulation of the expression of neuron specific proteins and the signature of matured motor neurons, allowing plug-and-play with a commercial multi-electrode array for neuron spike recording.

1 Introduction

The *in vitro* study of neuron functions has great importance in biomedical research and in understanding information processing of central and peripheral nervous systems.[1,2] Previously, a large amount of investigations has been reported using primary neurons from animals,[3–6] which are interesting but the data obtained from animal cells would not be sufficient to understand the human neural functions. Recent studies showed advantages of using neurons derived from human pluripotent stem cells (hPSCs), including both embryonic stem cells (ESCs) and induced pluripotent stem cells (iPSCs).[7–11] Human iPSCs (hiPSCs) are in particular promising for the development of more systematic studies of neurons since they are obtained by reprogramming somatic cells and able to be differentiated into different types of neurons under standard laboratory conditions.[12,13] With hiPSCs, it is now possible to generate specific neurons carrying precise genetic variants from a patient for disease modeling, therapy and neural regeneration.[7,11,14] However, most of these studies have been focused on setting new protocols for differentiation of neurons of different types and less attention has been paid to the methodological development. Indeed, conventional methods relying on the use of planar culture dishes, flasks and multi-well plates allowed neuron differentiation, growth and characterization but they should not be ideal since they do provide neither the requested cellular microenvironment nor the desired flexibility for three-dimensional network formation and electrophysiological monitoring. When stem cells are plated in a planar dish, they have to adapt to a two-dimensional setting wherein cells are in contact with exogenous materials, lost the underneath permeability, and do not have sufficient freedom to self-organize. Furthermore, when electrophysiological measurements[15,16] are requested, planar culture requires laborious preparation and delicate operations with neurons on such as multi-electrode arrays (MEAs). Therefore, it is highly desirable to develop a new culture method which is able to recapitulate the *in vivo* setting of extracellular matrix proteins and soluble factors, and to facilitate robust manipulation of hiPSCs and the derived neurons.

Based on the results of our previous work for long term culture of hiPSCs on nanofibrous gelatin substrates,[17] we developed a culture patch method for effective neuron differentiation. Unlike the conventional dish method, hiPSCs are now differentiated directly on a net-like structure or a culture patch made of crosslinked monolayer gelatin nanofibers and poly(ethylene glycol) diacrylate (PEGDA) honeycomb microframes. The PEGDA frame was fabricated by soft-lithography and the monolayer nanofibers were produced by electrospinning. After crosslinking, nanofibers

[a] Ecole Normale Supérieure-PSL Research University, Département de Chimie, Sorbonne Universités – UPMC Univ Paris 06, CNRS UMR 8640 PASTEUR, 24, rue Lhomond, 75005 Paris, France. E-mail: yong.chen@ens.fr
[b] Institute for Integrated Cell–Material Science, Kyoto University, Kyoto 606-8507, Japan
[c] Scuola Internazionale Superiore di Studi Avanzati – via Bonomea, 265 – 34136 Trieste, Italy
[d] Center for Quantitative Biology and School of Physics, Peking University, Beijing, 100871, China

† Electronic supplementary information (ESI) available. See DOI: 10.1039/c6tb00351f

acquire a net structure with pore sizes smaller than cells but large enough for three-dimensional exposure of the differentiating stem cells to the culture medium and soluble factors. Flat and hemisphere hiPSC colonies were first generated in each of the honeycomb compartments and then directed to become motor neuron progenitors. After replating to another patch, mature motor neurons were obtained and used directly for electrophysiological measurements using a commercial MEA device, showing characteristic neuron activities. When the same procedures were repeated on planar glasses and MEAs, motor neurons expressed less specific proteins and no spontaneous firing was observed. Thus, the patch method is advantageous over the conventional dish method for both motor neuron differentiation and electrophysiological measurements, providing a novel and powerful way for neuron based assays for the benefit of plug-and-play users.

2 Experimental

2.1 Preparation of a patch frame

The patch frame made of PEGDA was fabricated by UV assisted molding using a polydimethylsiloxane (PDMS) mold. First, a chromium mask of the honeycomb network of a 500 μm period and a 50 μm line width was produced using a micro-pattern generator (μPG 101, Heidelberg Instruments, Germany). Then, the mask was spin coated with a 50 μm thick photoresist (AZ40XT, MicroChem, France) and backside exposed to UV light. After development, the mask with photoresist patterns was exposed to a vapor of trimethylchlorosilane (TMCS, Sigma, France) for anti-sticking treatment. A mixture of the PDMS pre-polymer and the cross-linker (GE RTV 615, GE, France) was prepared at a ratio of 10 : 1 and poured on the resist layer. After curing at 80 °C for 2 h, the PDMS layer was peeled off and placed on a glass slide. The PDMS-glass assembly was placed in a desiccator for degassing for 15 min. A PEGDA (average M_n = 250, Sigma, France) solution mixed with 1 v/v% Irgacure 2959 (Sigma, France) as a photo-initiator was prepared and dropped on glass at the edge of the PDMS mold to fill the cavity of the PDMS-glass assembly due to micro-aspiration. Then, a cured honeycomb frame of PEGDA was formed after UV exposure at 9.1 mW cm^{-2} for 30 s and peeling-off the PDMS mold. For easier handling, a 100 μm thick PEGDA ring of 13 mm outer diameter and 9 mm inner diameter was prepared in a similar manner and then mounted on the honeycomb frame using pre-cured PEGDA solution as a binder with UV curing. Finally, the PEGDA honeycomb frame was gently taken off with the ring using a scalpel.

2.2 Preparation of crosslinked monolayer nanofibers

Gelatin nanofibers were produced by electrospinning using the same protocol as previously described.[17] Briefly, 10 wt% gelatin powder (G2625, Sigma, France) was dissolved in a mixture of acetic acid, ethyl acetate and distilled water with a volume ratio of 21 : 14 : 10 before electrospinning. To collect the electrospun nanofibers more evenly, the backside of the supporting PEGDA network was sputtered with 10 nm thick Au to enhance the attachment of gelatin nanofibers and the PEGDA network. Then, the PEGDA substrate with a golden surface on top was taped onto a silicon wafer as a collector. After loading into a syringe, the gelatin solution was ejected to the collector at a distance of 10 cm, using a syringe pump (KD Scientific) at 0.2 mL h^{-1} pumping speed through a stainless steel 23-gauge needle. The spinneret was connected to the anode of high potential power supply (TechDempaz, Japan) with a bias voltage of 11 kV and the collector was connected to the cathode of the power supply. Afterward, the samples were dried in a vacuum overnight to eliminate the remaining solvent.

The crosslinking of electrospun gelatin nanofibers was obtained by soaking the sample in ethanol with 0.2 M 1-ethyl-3-(3-dimethylaminopropyl) carbodiimide hydrochloride (EDC, Sigma, France) and 0.2 M *N*-hydroxysuccinimide (NHS, Sigma, France) for 4 h. Then, the samples were rinsed with ethanol three times and dried in a vacuum overnight to remove the remaining ethanol, resulting in crosslinked monolayer nanofibers on the PEGDA honeycomb frame.

The pore size distribution and porosity of the crosslinked nanofibers were analyzed using commercial software imageJ. Three samples under the same conditions were analyzed. For each of them, no less than three areas at different locations were used to obtain the average value and the standard deviation of the porosity.

2.3 hiPSC culture

hiPSCs of the 253G1 cell line were prepared in complete E8 medium with a 1 : 100 diluted vitronectin (Life Technology, Japan) coated culture dish at 37 °C with 5% CO_2 supplementation. The medium was changed everyday until cells grew to 70–80% confluence. Cells were harvested with a solution of DPBS with 0.5 mM EDTA (Life Technologies, Japan). To obtain monolayer and hemisphere hiPSC aggregations, the patch was treated in a DPBS solution with 1 : 100 and 1 : 500 diluted vitronectin for 1 h at room temperature, respectively. Then, the patch was placed in a culture dish for cell seeding. hiPSCs at a cell density of 2×10^5 in 50 μL of E8 medium containing a 10 μM ROCK inhibitor (Y-27632; Wako Chemicals) were plated on the surface of the patch and the culture dish was transferred into an incubator for cell attachment for 1 h. Afterward, 2 mL of fresh E8 medium containing 10 μM ROCK inhibitor were gently added to the culture dish. Then, the culture medium was replaced by E8 medium without the ROCK inhibitor after 2 h and 24 h of incubation for hemisphere and monolayer hiPSC aggregation, respectively.

2.4 Motor neuron differentiation

Neuroectodermal induction. The induction medium was prepared with Knockout Serum Replacement (KSR) medium and N2 medium at different ratios. KSR medium contains 20% KSR, 2 mM Glutamax, 1% Non-Essential Amino Acid (NEAA), 4 ng mL^{-1} of basic fibroblast growth factor (bFGF) (all from Life Technologies) and 0.1 mM β-mercaptoethanol (Sigma, Japan) in DMEM/F12. N2 medium contains 1% N2 supplement (Life Technologies, Japan), 2 mM Glutamx and 1% NEAA in

DMEM/F12. The neuron induction of hiPSCs was done by using N2/KSR medium at a ratio of 0/100% (days 1–3), 25%/75% (day 4), 50%/50% (days 5–6), 75%/25% (day 7) and 100%/0 (day 8), respectively, together with 10 μM SB431542 and 0.1 μM LDN193189 (both from Sigma, Japan) for all days (for dual inhibition of SMAD signaling).

Motor neuron differentiation. From days 9 to 16, cells were treated with N2 medium containing 0.1 μM retinoic acid (RA, Sigma), 0.5 μM purmorphamine (Pur, Sigma) and 20 ng mL^{-1} of bFGF. The medium was changed every two days.

Motor neuron maturation. At day 17, motor neuron progenitors were digested with 1 mg mL^{-1} of Dispase (Life Technologies) and re-suspended in a maturation medium which is composed of a 1 : 1 mixture of N2 medium and B27 medium with a number of maturation factors. The B27 medium contains neurobasal medium (Life Technologies), 2% B27 supplement (Life Technologies), and 2 mM Glutamax. The maturation factors include 10 ng mL^{-1} of brain-derived neurotrophic factor (BDNF), 10 ng mL^{-1} of glial-derived neurotrophic factor (GDNF), 10 ng mL^{-1} of insulin-like growth factor 1 (IGF-1) (all from Life Technologies), 1 μM cyclic adenosine monophosphate (cAMP, Sigma), 0.2 μg mL^{-1} of ascorbic acid (AA, Sigma), 0.1 μM RA, and 1 μM Pur. Prior to cell seeding, the nanofiber patch was treated in a laminin solution (1 : 50 iMatrix511 diluted in PBS, Clontech) at 37 °C overnight, while glass slides and

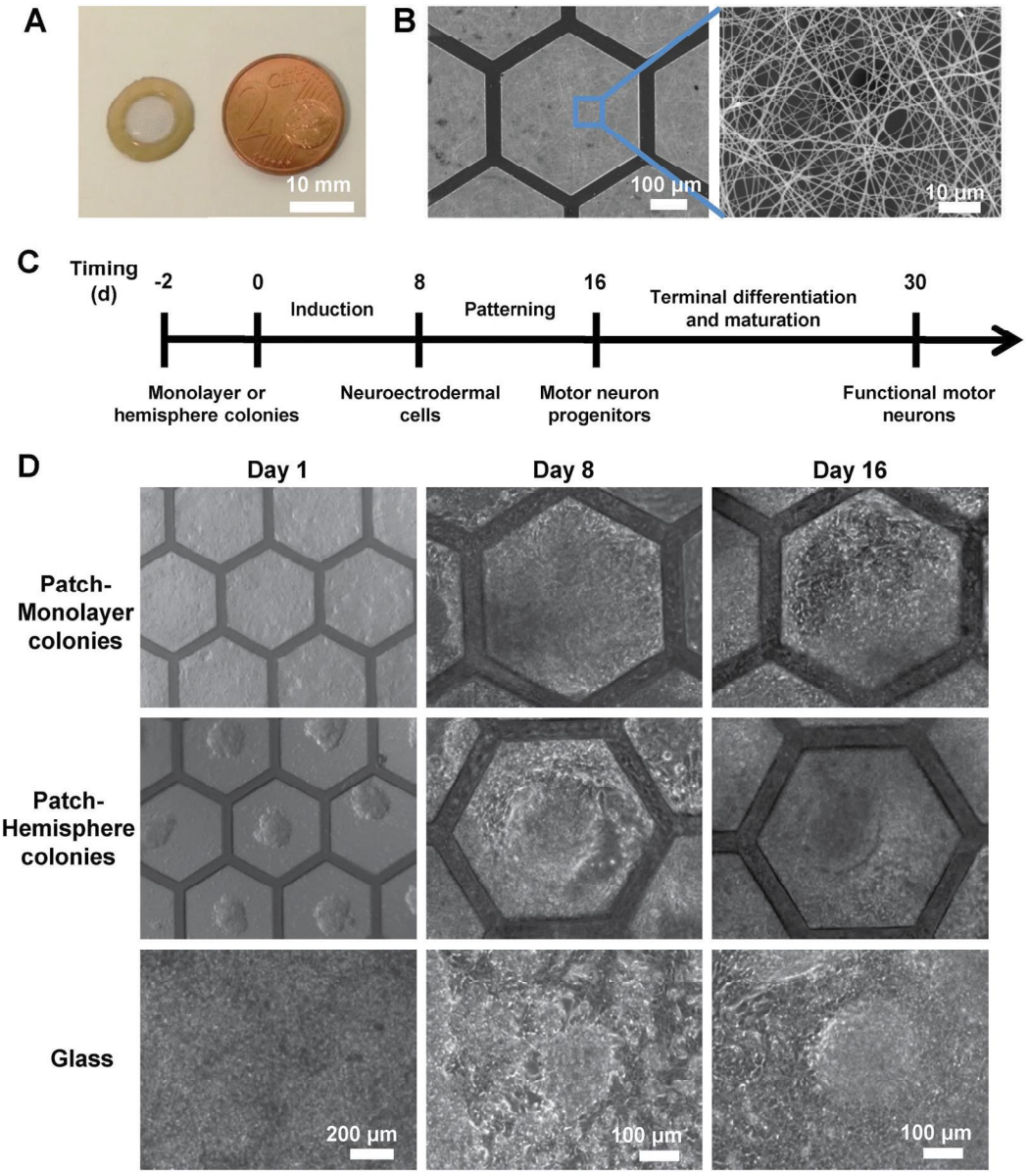

Fig. 1 (A) Photograph of a culture patch made of crosslinked monolayer gelatin nanofibers on a PEGDA honeycomb microframe; (B) SEM images of the patch, showing a net structure with pore sizes less than 8 μm; (C) schematic of motor neuron differentiation and maturation; (D) bright field images of differentiating hiPSCs toward motor neuron progenitors on two types of substrates (culture patch and glass) at days 1, 8 and 16. The shape of initial hiPSC colonies on the culture patch (day 1) was controlled by ROCK inhibitor treatment. Here, flat and hemisphere colonies were obtained by 24 h and 2 h ROCK inhibitor treatment, respectively.

multi-electrode array (MEA, Multichannel, Germany) samples were first treated in a solution of poly-ornithine (PO, Sigma) at 37 °C for 2 h and then in the laminin solution at 37 °C overnight. After cell reseeding, the medium was changed every two days.

2.5 Immunocytochemistry

For immunostaining, samples were rinsed with PBS to remove unattached cells and the remaining cells were fixed with 4% paraformaldehyde (PFA) diluted in PBS for 15 min. Then, cells were treated for permeabilization with 0.5% Triton X-100 in PBS at 4 °C overnight for antigens inside nuclei or 10 min at room temperature for antigens outside nuclei. Next, cells were incubated in a blocking solution containing 5% v/v normal goat serum, 5% v/v normal donkey serum, 3% v/v bovine serum albumin, and 0.1% v/v Tween 20 in D-PBS overnight at 4 °C to block out non-specific bindings. Afterward, cells were incubated with primary antibodies, *i.e.*, anti-Pax6 (1 : 100 diluted), anti-Nestin (1 : 200 diluted), anti-Olig2 (1 : 100 diluted), anti-β tubulin III (1 : 400 diluted) and anti-HB9 (1 : 100 diluted) in blocking solution (anti-Pax6, anti-Sox1, anti-Olig2 and anti-HB9 from Abcam, Japan; anti-Nestin and anti-β tubulin III from Sigma, Japan). After incubation at 4 °C overnight, cells were treated with secondary antibodies, *i.e.*, Alexa Fluor 488 Donkey anti-rabbit IgG (1 : 300 diluted) and Alexa Fluor 594 Donkey anti-mouse IgG (1 : 300 diluted) both from Jackson Immuno-Research in blocking buffer at room temperature for 1 h. For nuclei staining, cells were incubated with 300 ng mL^{-1} of 4′-6-diamidino-2-phenylindole (DAPI) for 30 min, and finally washed three times with PBS. The stained cells were observed using an inverted optical microscope (Axiovert 200, Zeiss, Germany) equipped with a digital CCD camera (Evolution QEI, US).

2.6 Quantitative RT-PCR

Total RNAs from derived neurons at day 8 and day 16 were harvested using an RNeasy Mini Kit (Qiagen, Valencia, CA) following the manufacturer's instructions. The RNA concentrations were determined using a NanoDrop1000 spectrophotometer (Thermo Fisher). Then RNAs were reverse transcribed using a RT First Strand Kit (Qiagen). The targeting cDNA was amplified and quantified using Power SYBR Green PCR MasterMix (Life Technologies). Briefly, cDNA solution was mixed with Power SYBR Green PCR MasterMix and applied to the PCR arrays. For amplification and quantification of cDNA, "hot start" PCRs were carried out with an initial incubation at 95 °C for 10 min, followed by 40 cycles of 95 °C for 15 s and then 60 °C for 3 min using an Applied Biosystems 7300 Real-Time PCR system (Life Technologies). Data analysis was carried out using Cluster 3.0 in combination with the TreeView 1.1.5 open-source software. The following primers were used: Nestin forward, 5′-ATC GCT CAG GTC CTG GAA GG-3′ and reverse, 5′-AAG CTG AGG GAA GTC TTG GAG-3′; Olig2 forward, 5′-GGG CCA CAA GTT AGT TGG AA-3′ and reverse, 5′-GAG GAA CGG CCA CAG TTC TA-3′; GAPDH (endogenous control) forward, 5′-AAC AGC CTC AAG ATC ATC AGC-3′ and reverse, 5′-GGT CTC TCT CTT CCT CTT GTG C-3′.

2.7 Field potential measurement

The culture patch with differentiated motor neurons was gently placed on the surface of MEAs to record the field potential (FP) of motor neurons by using a commercial MEA device and a data acquisition system (Multi Channel Systems, Germany). For a better contact of the patch and electrodes, a block of PDMS was used to gently press the patch against the MEA. For the neurons reseeded on the MEA, the field potential was recorded directly using a MEA system. The MEA is made of a 50 × 50 mm glass substrate with a 1.4 × 1.4 mm matrix of 60 silicon nitride insulated electrodes (30 μm diameter and 200 μm distance) imbedded in the center. The MEA chamber was filled with pre-warmed neuron maturation medium and maintained at 37 °C using a temperature controller. After 15 min of stabilization, the field potentials of 60 channels were obtained simultaneously at 20 kHz with 16-bit precision.

3 Results and discussion

3.1 Culture patch description

The culture patch was composed of gelatin nanofibers electrospun on a PEGDA microframe (Fig. 1). After crosslinking, the gelatin nanofibers formed a net-like structure with pore sizes less than 8 μm (Fig. S1, ESI†) and a porosity of 61.58 ± 2.06%, determined using imageJ. On such a net-like structure, cells could be cultured with minimum exogenous material contact and maximum exposure to the culture medium (Fig. 1B). The PEGDA frame has a honeycomb structure with 500 μm pitch size and 50 μm bandwidth (Fig. 1B). In addition, a PEGDA ring with a thickness of 100 μm and an inner and outer diameter of 9 and 13 mm, respectively, was mounted on the frame for easier handling and manipulation. Furthermore, the culture patch has a similar material density to that of culture medium, allowing an off-ground culture using or without using special handling devices.

3.2 Motor neuron differentiation

Motor neuron differentiation of hiPSCs can be achieved by using either embryoid bodies (EBs) or monolayer colonies.[18,19] We followed previous motor neuron differentiation protocols[20–22] but using the two types of colonies on the net-like structure (Fig. 1C) for a close comparison as well as a comparison with more conventional differentiation on glass (control).

Fig. 1D shows the bright field images of differentiating cells at different stages. After the formation of hiPSC hemisphere or monolayer colonies for 24 h, the hiPSCs were induced into neuroectodermal cells by inhibition of the dual Smad signaling pathway,[20] using TGF-β inhibitor SB431542 and BMP4 inhibitor LDN193189. Typical cell morphology changes can be observed at day 8. Meanwhile, cells started from hemisphere colonies migrated to the outside area of hemispheres and then connected to the neighboring ones. The results of immunostaining show that at day 8 most cells became both Pax6 and Nestin positive which are neuroectodermal specific transcription factor and common neural progenitor marker, respectively (Fig. 2A),

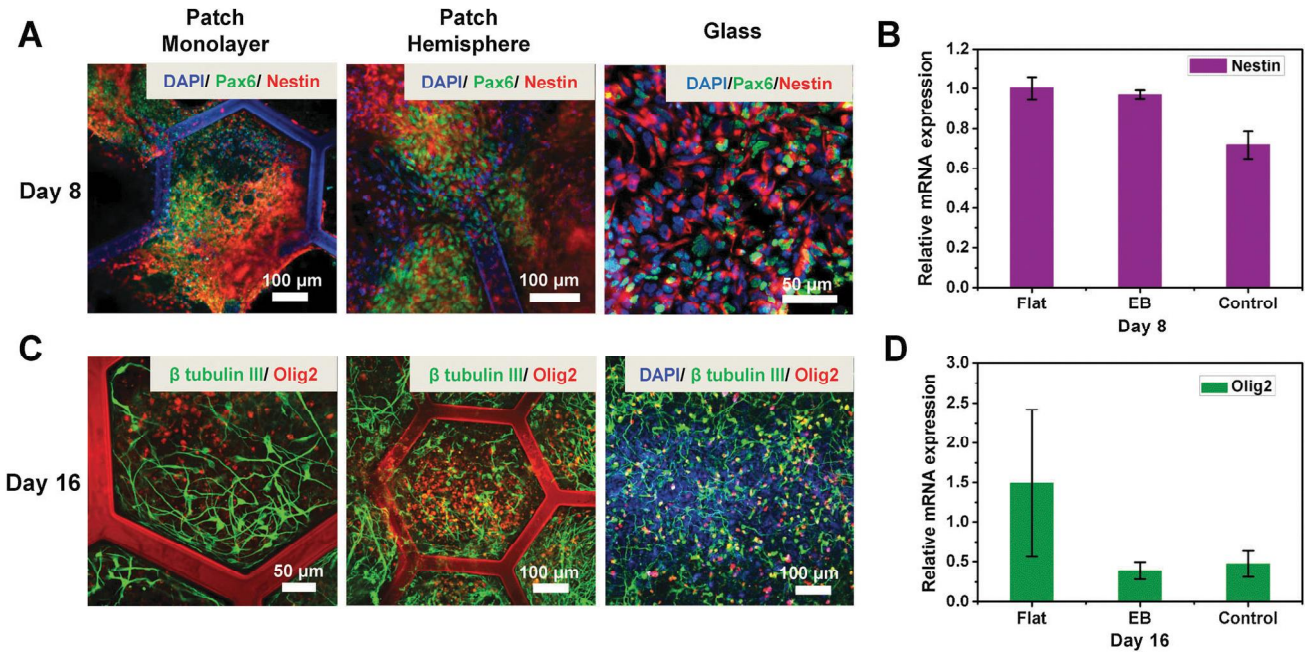

Fig. 2 (A) Immunofluorescence images of hiPSC-derived neuron stem cells at day 8 obtained on glass and the culture patch after 24 h (patch monolayer and glass) and 2 h (patch hemisphere) of Y-27632 treatment, respectively: nuclei stained with DAPI (blue), neuroectodermal cells with Pax6 (green), and neuron stem cells with Nestin (red); (B) relative mRNA expression of Nestin at day 8 of differentiating hiPSCs toward motor neuron progenitors, showing more Nestin expression for the cells differentiated on the patch than on glass; (C) immunofluorescence images of hiPSC-derived motor neuron progenitors at day 16, obtained on glass and the culture patch after 24 h (patch monolayer and glass) and 2 h (patch hemisphere) of Y-27632 treatment, respectively, showing more Olig2 positive motor neuron progenitors on the patch than on glass: nuclei stained with DAPI (blue), neural microtubules with β-tubulin III (green) and motor neuron progenitors with Olig2 (red); (D) relative mRNA expression of Olig2 at day 16 of differentiating hiPSCs toward motor neuron progenitors, showing more Olig2 expression for the cells differentiated from monolayer colonies on the patch than the other two situations.

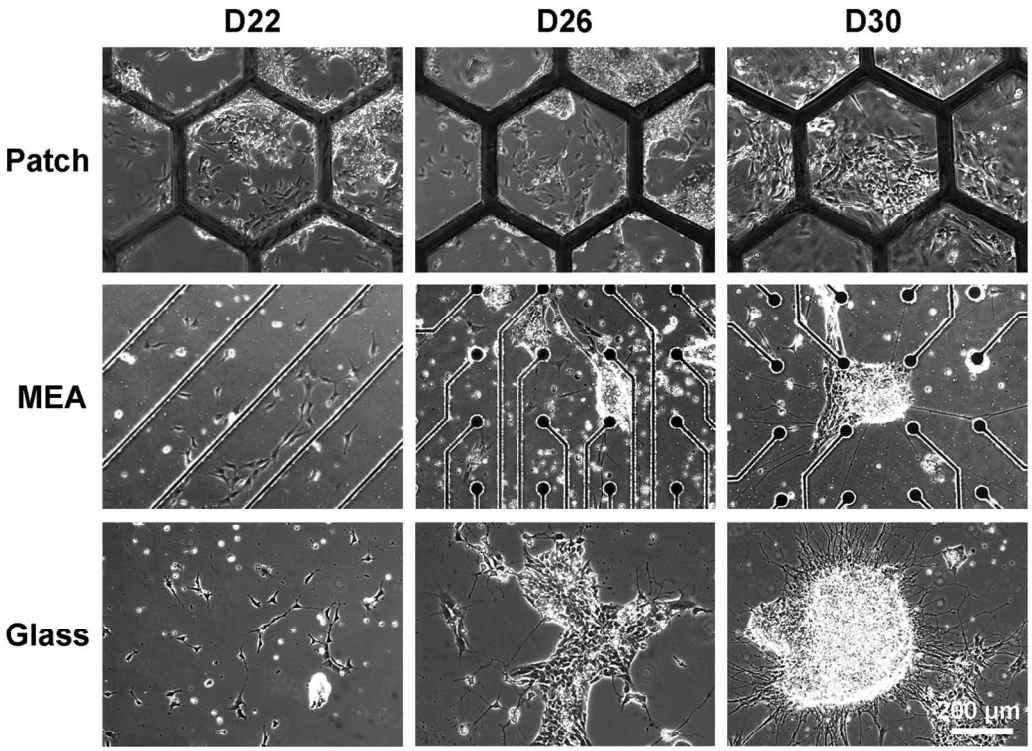

Fig. 3 Bright field images of motor neurons during maturation after reseeding on three types of substrates (culture patch, MEA and glass) at days 22, 26 and 30, showing the formation cell clusters and even neuron spheres on MEA and glass substrates.

while little difference could be observed from different groups. Then the results of q-PCR revealed a higher Nestin expression level of the cells on nanofibers than on glass, suggesting that the off-ground culture with crosslinked monolayer nanofibers leads to a better neuron induction of hiPSCs than conventional culture (Fig. 2B). After day 8, cells were exposed to soluble morphogens RA and Pur for motor neuron differentiation. At day 16, the immunofluorescence images show clearly neuron specific β-tubulin III positive microtubules and motor neuron progenitor specific transcription factor Olig2 (Fig. 2C). The expression of β-tubulin III showed clearly the elongated neurites with lengths of 100 to 200 μm, while there appeared more Olig2 positive motor neuron progenitors on the patch than on glass. Compared to the cells started from monolayer hiPSC colonies, cells differentiated from hemisphere colonies aggregated more in the center of each honeycomb compartment. However, the results of q-PCR show a much higher expression level of Olig2 for the cells started from monolayer colonies than those from hemisphere ones and on glass (Fig. 2D), suggesting that monolayer hiPSC colonies on the culture patch could be better directed to motor neurons.

3.3 Motor neuron maturation

After day 16, motor neuron progenitors derived from monolayer hiPSCs on the culture patch were digested and reseeded for maturation on three types of substrates, *i.e.*, pre-coated glass slide, MEA or culture patch. Fig. 3 shows the morphological changes of the cells at days 22, 26 and 30 on different culture supports. In the beginning, single neurons started to adhere on the substrate and showed neurite extension. Due to cell proliferation, neuron clusters and even neuron spheres (especially on the glass slide and the MEA) formed. Then, elongated axons (up to several hundred micrometers in length) appeared at day 30. However, significant differences in the cell/cluster morphology were observed with different culture supports. Apparently, neurons could not attach well on the MEA and a poor proliferation was observed. On MEAs and glass neurons often formed large clusters while they spread on culture patches presumably because of compartmentation and a lower stiffness of the substrate. Indeed, neurons are found in the relatively soft tissue of the nervous system *in vivo*, and thrived similarly on softer materials *in vitro*.[23,24] Compared to the environment of the nervous system *in vivo*, glass and MEAs (glass with titanium-nitride electrodes) are too rigid for

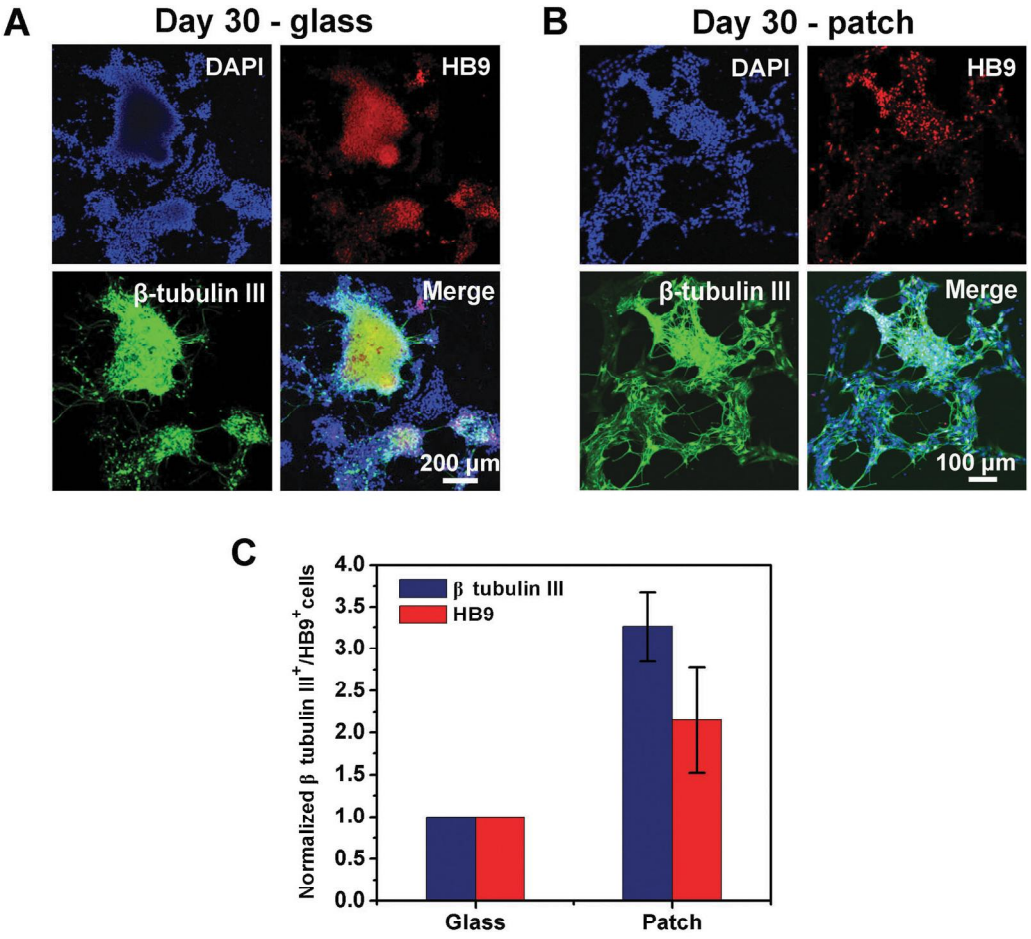

Fig. 4 (A and B) Immunostaining images of motor neurons on glass (A) and on the patch (B) during maturation at day 30: nuclei stained with DAPI (blue), motor neuron with HB9 (red) and neural microtubules with β-tubulin III (green); (C) bar plot showing the relative numbers of β-tubulin III and HB9 positive cells at day 30 on the patch normalized to the values on glass.

neuron culture, while the culture patch formed by crosslinked monolayer gelatin nanofibers provides a culture support more similar to the *in vivo* extracellular matrix. Finally, the immunostaining images show that at day 30 many neurons become HB9$^+$/β-tubulin III$^+$ motor neurons on both the glass and the patch (Fig. 4A and B). Here, HB9 is a motor neuron specific transcription factor and β-tubulin III is a neural microtubule marker. Again, large cell clusters were observed on glass due to the same reason as mentioned above. Cells on glass also showed less HB9 and β-tubulin III expression with respect to the cells on the patch. By measuring the fluorescence intensity ratio of HB9/β-tubulin III to DAPI using imageJ, the HB9/β-tubulin III positive cells on glass and the patch can be compared quantitatively. Not surprisingly, the maturation of neurons on the culture patch led to 3.26 and 2.15 fold increases in the numbers (and thus yields) of β-tubulin III$^+$ and HB9$^+$ cells, respectively, compared to that on glass (Fig. 4C). Such an increase could be contributed to the favorable conditions provided by off-ground culture of neurons on a patch.

3.4 Electrophysiological measurement

After day 30, maturing motor neurons on the culture patch were checked every two days, using a commercially available MEA, to verify their spontaneous activity (Fig. 5). At day 38, spikes were detected (Fig. 5C), indicating the maturation of the motor neurons and the formation of functional neural networks. In most of the experiments, clear electrical signals, which could be ascribed to spikes generated by neurons (Fig. 5D–F), were recorded by a dozen of electrodes over the available 64 of the MEA (Fig. 5C), presumably because of a bad electrical contact between neurons and the recording electrodes or the absence of neurons over the electrode. As can be seen, motor neurons fired spikes in bursts (Fig. 5E) or in an almost periodic fashion (Fig. 5D). We also observed extracellular spikes of different amplitudes from the same electrode (Fig. 5F). By using the spike sorting tool implemented in the MC_Rack software, these extracellular spikes could be categorized into two groups, due probably to the contribution of two neurons (Fig. 5G and H). Here, spikes of group 1 displayed a negative impulsion of 160–210 μV, while spikes of group 2 showed impulsions of 50–150 μV positive and 50–80 μV negative waveforms. Similar analyses were performed for other electrodes and we found that most of them could be attributed to 1 or 2 neurons. In this way in most of the experiments we monitored the electrical activity of some dozens of neurons, showing that the culture was healthy and neurons were generated properly. Occasionally we saw neurons firing almost in synchrony or with a reproducible pattern, proving that a functional network of neurons was formed. The duration of the spikes was about 1 ms, which is

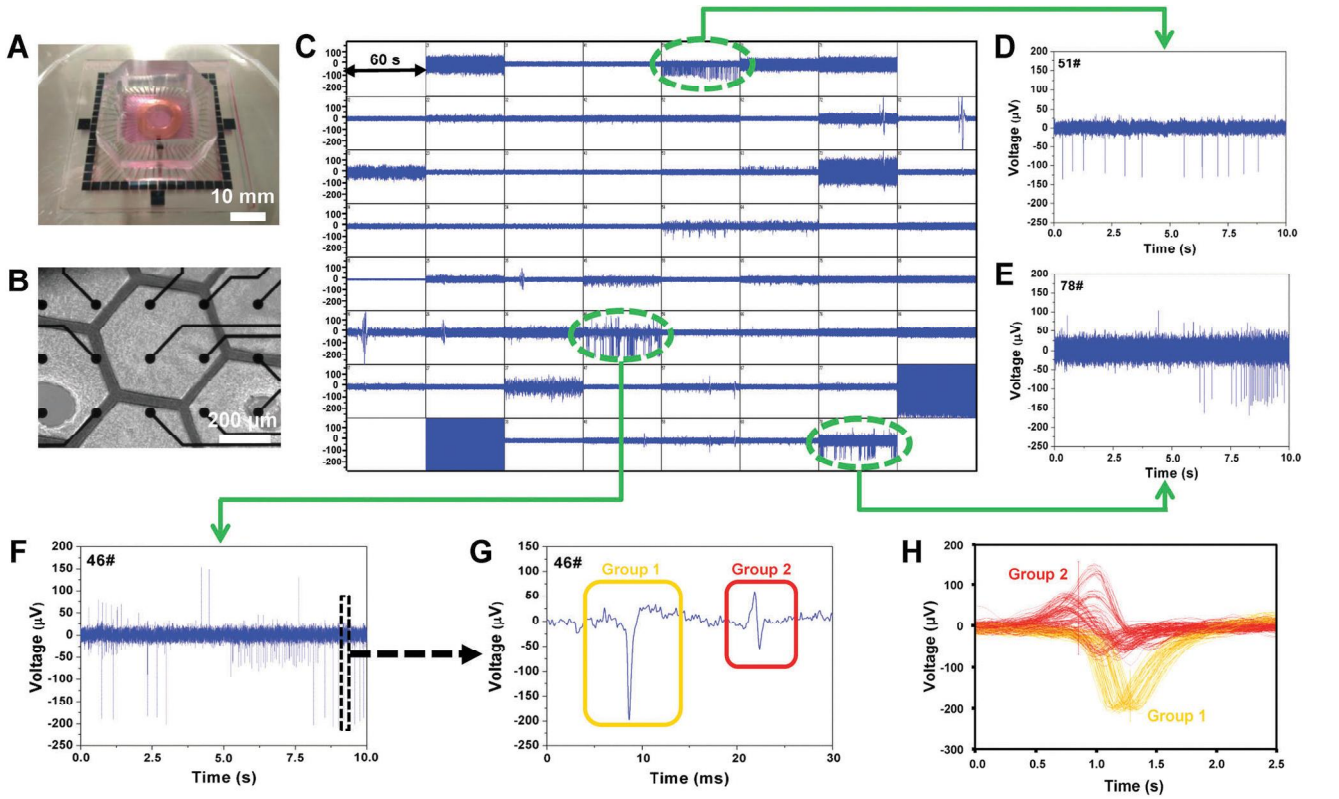

Fig. 5 Electrophysiological measurements of a motor-neuron patch using a commercial MEA device at day 38. (A) Neuron patch in the chamber of a MEA device filled with medium. (B) Bright field image of a neuron patch on the microelectrodes of MEAs. (C) Overall view of 60-channel recordings, showing spontaneous neuron activity. (D) Electrical signals detected by electrode 51# for 10 s. (E) Electrical signals detected by electrode 78# for 10 s. (F) Electrical signals detected on electrode 46# for 10 s. (G) Detailed view of (D) showing two typical types of neuron spikes. (H) Spike sorting results of electrical signals recorded by electrode 46#.

typical of neuron firing. For comparison, we also checked whether the neurons reseeded on the MEA provided similar electrical signals. We were not able to record any meaningful signals until day 50, suggesting that either the grown neurons were not mature enough or there was still no functional neural network. Therefore, motor neurons could be more easily matured and more effectively connected each other on a patch due to the mimic characteristics of the *in vivo* environment.

4 Conclusions

We fabricated a culture patch for off-ground culture and differentiation of hiPSCs. The patch was made of crosslinked monolayer gelatin nanofibers on a biodegradable PEGDA honeycomb frame to minimize the contact with the exogenous material and to maximize the accessibility of nutrients to the cells. Motor neuron progenitors were obtained and they expressed their characteristic proteins. After reseeding to different types of culture supports, electrical signals could be recorded at day 38 and the spontaneous firing of neurons was measured. No firing was detected for the neurons reseeded on the MEA device until day 50, indicating the advantage of off-ground culture for neuron network formation or maturation. Our results also show that the differentiation efficiency of hiPSCs to neurons is higher when started from flat hiPSC colonies than from hemispheres. The proposed culture patch can be used for advanced studies of neuronal differentiation and electrophysiological recordings. Compared to the more conventional culture dish methods, the use of a culture patch for neuron studies is more flexible and versatile, allowing reliable process optimization and a large variety of applications.

Acknowledgements

This work is partially supported by European commission through contract No. 604263 (Neuroscaffolds), French National Research Agency through grants ANR-12-RPIB-0015 (Cardiac-Patch) and ANR-13-NANO-0011-01 (Pillarcell) and Japan Society for the Promotion of Science (JSPS) for financial support: Challenging exploratory research (24651136 and 26630096).

References

1 P. Massobrio, J. Tessadori, M. Chiappalone and M. Ghirardi, *Neural Plast.*, 2015, **2015**, 1–18.
2 C. Bardy, M. van den Hurk, T. Eames, C. Marchand, R. V. Hernandez, M. Kellogg, M. Gorris, B. Galet, V. Palomares and J. Brown, *Proc. Natl. Acad. Sci. U. S. A.*, 2015, **112**, E2725–E2734.
3 G. Ju, T. Hökfelt, E. Brodin, J. Fahrenkrug, J. Fischer, P. Frey, R. Elde and J. Brown, *Cell Tissue Res.*, 1987, **247**, 417–431.
4 K. Moore, M. Macsween and M. Shoichet, *Tissue Eng.*, 2006, **12**, 267–278.
5 H. Runne, E. Régulier, A. Kuhn, D. Zala, O. Gokce, V. Perrin, B. Sick, P. Aebischer, N. Déglon and R. Luthi-Carter, *J. Neurosci.*, 2008, **28**, 9723–9731.
6 S. Prasad, M. Yang, X. Zhang, C. S. Ozkan and M. Ozkan, *Biomed. Microdevices*, 2003, **5**, 125–137.
7 J. T. Dimos, K. T. Rodolfa, K. K. Niakan, L. M. Weisenthal, H. Mitsumoto, W. Chung, G. F. Croft, G. Saphier, R. Leibel and R. Goland, *Science*, 2008, **321**, 1218–1221.
8 S. H. Choi, Y. H. Kim, M. Hebisch, C. Sliwinski, S. Lee, C. D'Avanzo, H. Chen, B. Hooli, C. Asselin, J. Muffat, J. B. Klee, C. Zhang, B. J. Wainger, M. Peitz, D. M. Kovacs, C. J. Woolf, S. L. Wagner, R. E. Tanzi and D. Y. Kim, *Nature*, 2014, **515**, 274–278.
9 A. Kirkeby, S. Grealish, D. A. Wolf, J. Nelander, J. Wood, M. Lundblad, O. Lindvall and M. Parmar, *Cell Rep.*, 2012, **1**, 703–714.
10 M. A. Lancaster and J. A. Knoblich, *Nat. Protoc.*, 2014, **9**, 2329–2340.
11 J. Sandoe and K. Eggan, *Nat. Neurosci.*, 2013, **16**, 780–789.
12 J. Yu, M. A. Vodyanik, K. Smuga-Otto, J. Antosiewicz-Bourget, J. L. Frane, S. Tian, J. Nie, G. A. Jonsdottir, V. Ruotti and R. Stewart, *Science*, 2007, **318**, 1917–1920.
13 S. V. Liu, *Stem Cells Dev.*, 2008, **17**, 391–398.
14 M. Bellin, M. C. Marchetto, F. H. Gage and C. L. Mummery, *Nat. Rev. Mol. Cell Biol.*, 2012, **13**, 713–726.
15 A. Odawara, Y. Saitoh, A. Alhebshi, M. Gotoh and I. Suzuki, *Biochem. Biophys. Res. Commun.*, 2014, **443**, 1176–1181.
16 T. J. O'Shaughnessy, J. L. Liu and W. Ma, *Biosens. Bioelectron.*, 2009, **24**, 2365–2370.
17 L. Liu, M. Yoshioka, M. Nakajima, A. Ogasawara, J. Liu, K. Hasegawa, S. Li, J. Zou, N. Nakatsuji, K.-I. Kamei and Y. Chen, *Biomaterials*, 2014, **35**, 6259–6267.
18 K. Watanabe, D. Kamiya, A. Nishiyama, T. Katayama, S. Nozaki, H. Kawasaki, Y. Watanabe, K. Mizuseki and Y. Sasai, *Nat. Neurosci.*, 2005, **8**, 288–296.
19 S.-C. Zhang, M. Wernig, I. D. Duncan, O. Brüstle and J. A. Thomson, *Nat. Biotechnol.*, 2001, **19**, 1129–1133.
20 S. M. Chambers, C. A. Fasano, E. P. Papapetrou, M. Tomishima, M. Sadelain and L. Studer, *Nat. Biotechnol.*, 2009, **27**, 275–280.
21 Y. Sun, K. M. Yong, L. G. Villa-Diaz, X. Zhang, W. Chen, R. Philson, S. Weng, H. Xu, P. H. Krebsbach and J. Fu, *Nat. Mater.*, 2014, **13**, 599–604.
22 W. Hu, Y. He, Y. Xiong, H. Lu, H. Chen, L. Hou, Z. Qiu, Y. Fang and S. Zhang, *Mol. Neurobiol.*, 2015, **53**, 1589–1600.
23 M. Tessier-Lavigne and C. S. Goodman, *Science*, 1996, **274**, 1123–1133.
24 A. Balgude, X. Yu, A. Szymanski and R. Bellamkonda, *Biomaterials*, 2001, **22**, 1077–1084.

6.3

Fabrication of PLGA nanofibers on PDMS micropillars for neuron culture studies

J. Wei+, D. Pozzi+, F.P. Ulloa Severino, V. Torre, Y. Chen

Microelectronic Engineering

Microelectronic Engineering 175 (2017) 67–72

Contents lists available at ScienceDirect

Microelectronic Engineering

journal homepage: www.elsevier.com/locate/mee

Research paper

Fabrication of PLGA nanofibers on PDMS micropillars for neuron culture studies

Jin Wei [a,1], Diletta Pozzi [b,1], Francesco Paolo Ulloa Severino [b], Vincent Torre [b,*], Yong Chen [a,c,d,**]

[a] Ecole Normale Supérieure, PSL Research University, Département de Chimie, CNRS UMR 8640 PASTEUR, 75005 Paris, France
[b] International School for Advanced Studies (SISSA),34100 Trieste, Italy
[c] Institute for Integrated Cell-Material Sciences, Kyoto University, Kyoto 606-8507, Japan
[d] Institute for Interdisciplinary Research, Jianghan University, Wuhan 430056, China

ARTICLE INFO

Article history:
Received 11 October 2016
Received in revised form 9 January 2017
Accepted 13 January 2017
Available online 22 January 2017

Keywords:
Micropillars array
Nanofiber
Neuron culture

ABSTRACT

We fabricated a nanocomposite substrate made of nanofibers on micropillar arrays by photolithography, soft lithography and electrospinning for cell culture studies. This nanocomposite substrate combines the advantage of the extra-cellular matrix (ECM)-like surface morphology and high porosity and low stiffness of underneath supporting material. For neuronal culture studies, we used nanofibers of poly (lactic-*co*-glycolic acid) (PLGA) on high aspect ratio micropillars of polydimethylsiloxane (PDMS). Our results showed that primary hippocampal neurons on such a nanocomposite substrate have different cell morphology than on flat surfaces and they showed more electric activities. Thus, the nanofiber-micropillar composite substrates were shown to be useful for neuron culture studies.

1. Introduction

Improvement of cell culture conditions is important for biomedical research as well as advanced applications such as tissue engineering, disease modeling and cancer treatment [1–3]. Among many others, the physical and biochemical properties of the culture substrate are critical issues in cell culture studies [4–5]. While cell adhesion and migration are dictated by topographical cues [6], the cell fate decision is clearly substrate stiffness dependent [7]. More specifically, the expression of neuronal markers and the formation of neural networks are both affected by the stiffness and the surface morphology of the culture substrate [8–10], in addition to the influence of the substrate surface coatings [11,12].

In order to simultaneously modulate the stiffness and the surface morphology of the substrate for primary neuron culture, we developed a new type of nanocomposite substrates by electrospinning poly-lactic-*co*-glycolic acid (PLGA) on polydimethylsiloxane (PDMS) pillars of high aspect ratio and small diameters. Previously, PDMS pillars have been repeatedly used for measurements of cell contracile forces [13]. PDMS pillars have also been used to facilitate stem cell differentiation toward neurons [14,15]. On the other hand, the morphology of electrospun nanofibers can be in-vivo extracellular matrix (ECM)-like so that they are prominent to cell culture studies [16,17]. While PDMS pillars of high aspect ratio and small feature sizes can serve as supporting structure with low effective Young's modules, PLGA nanofibers are highly biocompatible [18] so that such a nanocomposite substrate provides unique characteristic to guide neuronal growth and to enhance cell-medium exchange due to large free spaces underneath the fibers. Preliminary results of neuron culture and calcium imaging will be shown to illustrate the high potential of this approach.

2. Fabrication of PLGA nanofibers on PDMS micropillars

2.1. Materials

Blank chromium mask (Nanofilm Inc) and resist developer AZ726 (AZ Electronic Materials) were purchased from Cipec (France). Chrome Etch N°1 was purchased from Technic Inc. (France). SU8 photoresists (SU8-3025) and SU8 developer were obtained from CTS (France). Polydimethylsiloxane (PDMS) was purchased from Eleco-EFD (France). Dimethylformamide (DMF), tetrahydrofuran (THF) and D,L-lactide-*co*-glycolide (PLGA) were obtained from Sigma (France). Trimethylsilylchloride (TMCS) was purchased from Sigma (France).

2.2. Fabrication of micropillars

Micropillar arrays used in this work were obtained by casting PDMS on a PDMS mold with holes, whereas the PDMS mold was initially

* Corresponding author.
** Correspondence to: Y. Chen, Ecole Normale Supérieure, PSL Research University, Département de Chimie, CNRS UMR 8640 PASTEUR, 75005 Paris, France.
E-mail addresses: vincent.torre@sissa.it (V. Torre), yong.chen@ens.fr (Y. Chen).
[1] These authors contributed equally to this work.

http://dx.doi.org/10.1016/j.mee.2017.01.015
0167-9317/

obtained by PDMS casting on a photoresist mold (master) fabricated by photolithography (Fig. 1). Firstly, micro-hole arrays were patterned on the Cr mask using a micro pattern generator (μPG101, Heidelberg, Germany). Then, a 25-μm-thick negative resist layer (SU8-3025) was spin-coated on the mask and back-side ultraviolet (UV) exposed. After development, SU8 pillars of 25 μm height, 5 μm diameter and 20 μm spacing were obtained (Fig. 2a) and used as mold features to cast a mixture of PDMS pre-polymer and crosslink agent at ratio of 10:1. Before casting, the mold was treated in oxygen plasma for 2 min and then in TMSC vapor for 30 min. After PDMS casting and curing at 80 °C for 2 h, the PDMS layer was peeled-off, resulted in a negative replica of the mold features. Next, 0.2-μm thick Parylene C was deposited on the PDMS layer with a vacuum deposition system (SCS Labcoter 2, SCS ltd, UK). Afterward, a positive-tone replica of the master was finally obtained by casting PDMS on the PDMS mold using the same casting process. Comparing to the other fabrication processes, the present double casting technique is advantageous to achieve high quality PDMS pillar arrays, since it is relatively easy to obtain high resolution, high density and high aspect ratio SU8 pillars. It is also relatively easy to peel-off the PDMS layer from the fabricated resist pillars and then to replicate the same feature of the master due to the relative low Young's modules of PDMS. Previously, we have shown that it was convenient to use PDMS mold for replication of pillar structures with different types of polymers such as PDMS, PLGA and T-Flex [19]. Here, the PDMS mold was coated with a thin film of Parylene C, which further facilitated the replication due to the low surface energy of Parylene C. As results, this double casting procedure allowed us producing reproducibly high density and high aspect ratio PDMS pillar arrays (Fig. 2b).

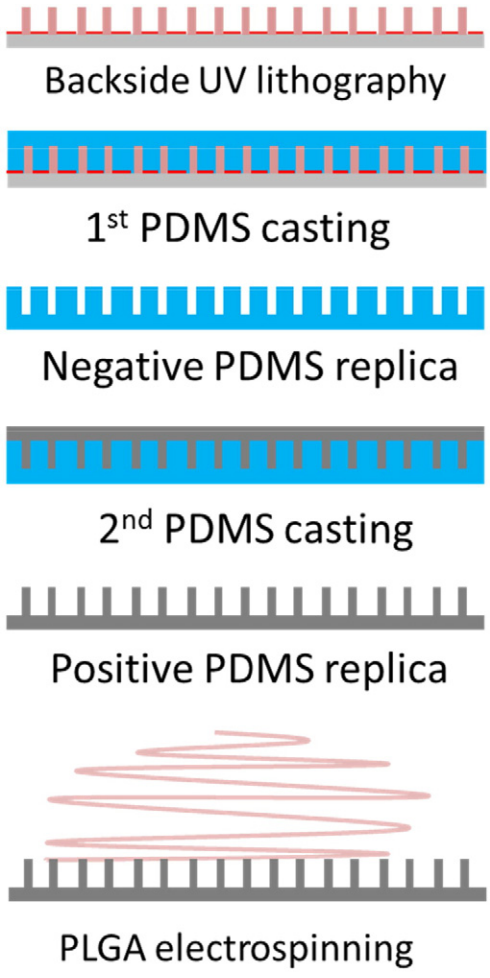

Fig. 1. Schematic diagram of the fabrication process of electrospun nanofibers on elastomer micropillars.

2.3. Electrospinning of nanofibers

Solution of PLGA (Mw 76,000–115,000) at lactide to glycolide ratio 75:25 were prepared by dissolving PLGA in THF (with higher volatility) and DMF mixed solvent with ratio 2:3. The concentration of PLGA solution was 20 wt%. For deposition of smooth and beads-free nanofibers, ionic surfactant sodium dodecyl sulphate (SDS, Sigma, France) dissolved in ethanol was admixed into the polymer solution to a final concentration of 1 mg/ml.

The PLGA solution was kept in a 1-ml-syringe and spinneret tip that connected to the anode of a high voltage (Heinzinger, Germany) of 12 kV. The cathode was connected to the grounded aluminum wafer collector. The solution was supplied by a syringe pump (KD Scientific, USA) at a rate of 0.2 ml/h. The vertical distance between spinneret tip and the collector was 10 cm. Random PLGA nanofibers were collected for 3 min on the aluminum wafer, on which the micro pillar supporter was attached. After electrospinning, the sample was put into a vacuum chamber to volatilize the solvent overnight. As expected, we obtained a new type of culture substrate made of PLGA nanofibers on PDMS pillar arrays (Fig. 2c). By using freeware Image-J and SEM images of the fabricated samples, the diameter of the nanofibers could be measured, showing that 84.0% fibers have diameters in the range of 500–900 nm (Fig. 2d) and <0.2% (2.5%) fibers have diameters smaller (larger) than100 nm (1000 nm).

3. Cell culture

3.1. Substrate preparation

One day before cells seeding, the PLGA/PDMS and PDMS (control) microarrays were exposed to plasma treatment for 2 min and sterilized with UV light for 20 min. Subsequently, the substrates were left in ethanol 70% for 1 h and rinsed with sterile water. For the conventional and two-dimensional culture, glass coverslips (15 mm diameter) were used and dry-heat sterilized. For U87 cells, all the substrates were coated with fibronectin at 25 °C for 2 h in a fume hood, in order to improve the adhesion of cells. For hippocampal cells, all the samples were coated with 50 μg/ml poly-L-ornithine (Sigma-Aldrich, St. Louis, MO, USA) for overnight incubation at 37 °C. An additional coating with Matrigel (diluted 1:50 with culture medium; Corning, Tewksbury MA, USA) was performed on the substrates 20 min before cells plating.

3.2. U87 culture

U87 cells were prepared in Dulbecco's modified eagle medium (DMEM) with 10% fetal bovine serum (FBS) and 1% penicillin/streptomycin. The cells prepared in flasks were trypsinized, centrifuged and re-suspended with cell density ~104 cell/ml. 50-μl solution (cells in medium) was dropped on each substrate. After 1 h incubation for cell attachment, fresh culture medium was added and the samples were placed in an incubator (37 °C, 5% CO2).

3.3. Hippocampal culture

Hippocampal neurons from Wistar rats (P2–P3) were prepared in accordance with the guidelines of the Italian Animal Welfare Act, and their use was approved by the Local Veterinary Service, the SISSA Ethics Committee board and the National Ministry of Health (Permit Number: 630-III/14) in accordance with the European Union guidelines for animal care (d.1.116/92; 86/609/C.E.). The animals were anaesthetized with CO_2 and sacrificed by decapitation, and all efforts were made to minimize suffering. After isolation of the hippocampi, cells were enzymatically dissociated and resuspended in minimum essential medium

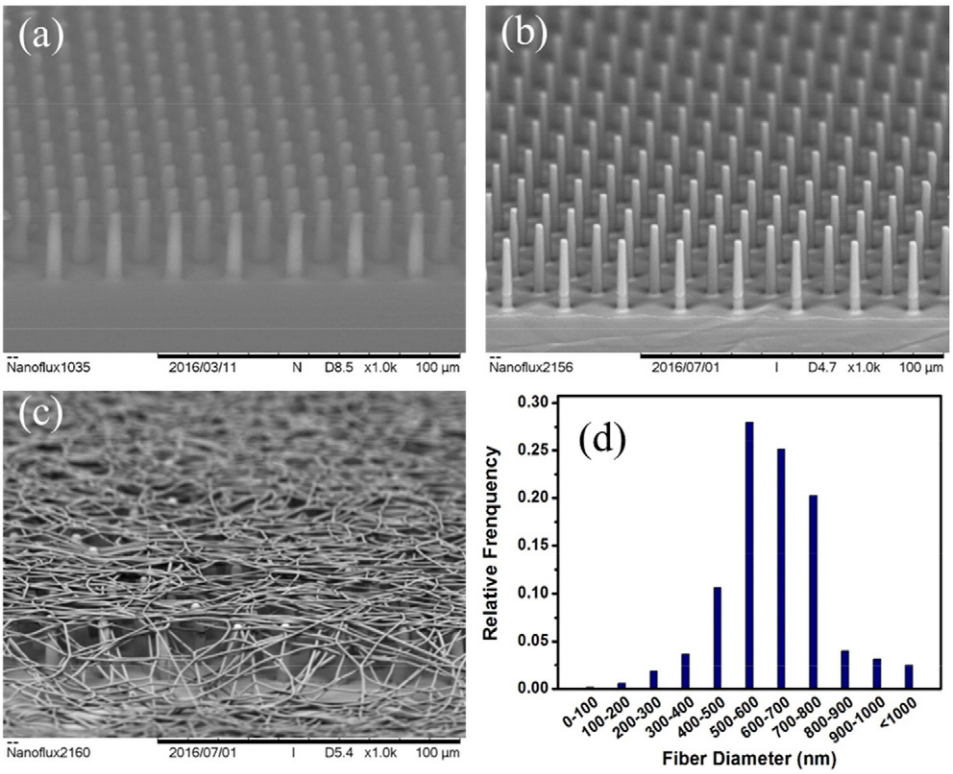

Fig. 2. SEM images of SU8 mold with a micropillar array (a), positive replica of the mold into PDMS (b), PLGA nanofibers electrospun on PDMS pillars (c). Statistic distribution of the PLGA nanofibers (d).

(MEM) with GlutaMAX™ supplemented with 10% dialyzed fetal bovine serum (FBS, all from Thermo Fisher Scientific, Waltham, MA, USA), 0.6% D-glucose, 15 mM Hepes, 0.1 mg/ml apo-transferrin, 30 µg/ml insulin, 0.1 µg/ml D-biotin, 1 µM vitamin B12 and 2.5 µg/ml gentamycin (all from Sigma-Aldrich). 48 h after cells' plating, half of the medium was changed with the addition of 2 µM cytosine-β-D-arabinofuranoside (Ara-C; Sigma-Aldrich). Subsequently, half of the medium was changed twice per week. The neuronal cultures were maintained in an incubator at 37 °C, 5% CO_2 and 95% relative humidity.

3.4. Immunocytochemistry and imaging

Cells were fixed in 4% paraformaldehyde containing 0.15% picric acid in phosphate-buffered saline (PBS), saturated with 0.1 M glycine, permeabilized with 0.1% Triton X-100, saturated with 0.5% BSA (all from Sigma-Aldrich) in PBS and then incubated for 1 h with primary mouse monoclonal antibodies: glial fibrillary acidic protein (GFAP, Sigma-Aldrich) and anti-β-tubulin III (TUJ1, Covance, Berkeley, CA). The secondary antibodies were goat anti-mouse Alexa Fluor® 594, goat anti-mouse immunoglobulin (Ig) G_1 Alexa Fluor® 488 and goat anti-mouse IgG_{2a} Alexa Fluor® 594. F-actin was marked with Alexa Fluor 488® phalloidin (all from Thermo Fisher Scientific) and the incubation time was 30 min. Nuclei were stained with 2 µg/ml in PBS Hoechst 33342 (Sigma-Aldrich) for 5 min. All the incubation steps were performed at room temperature (20–22 °C). Images were acquired using a Leica DM6000 fluorescent microscope equipped with differential interference contrast (DIC) and fluorescence optics, charge-coupled device (CCD) camera and Volocity 5.4 3D imaging software (PerkinElmer, Coventry, UK). The fluorescence images were collected with a 20× and a 40× magnification (0.5 NA) objective. Image J by W. Rasband (developed at the U.S. National Institutes of Health and available at http://rsbweb.nih.gov/ij/) was used for image processing.

3.5. Calcium imaging

The cells were incubated with the non-ratiometric calcium dye Oregon Green® 488 BAPTA-1, AM, (Thermo Fisher Scientific) dissolved in anhydrous dimethyl sulfoxide (DMSO) (Sigma-Aldrich) at a concentration of 4 mM (stock solution), with the addition of Pluronic F-127 20% solution in DMSO (Thermo Fisher Scientific) for increasing the cell's permeability. The two components were dissolved at a ratio of 1:1 in Ringer's solution (145 mM NaCl, 3 mM KCl, 1.5 mM $CaCl_2$, 1 mM $MgCl_2$, 10 mM glucose and 10 mM Hepes, pH 7.4) to give a final dye concentration of 4 µM, and incubated at 37 °C for 1 h. The cultures were then transferred to a glass-bottom Petri dish to allow visualization in a Nikon Eclipse Ti-U inverted microscope equipped with an HBO 103 W/2 mercury short arc lamp (Osram, Munich, Germany), a mirror unit (exciter filter BP 465–495 nm, dichroic 505 nm, emission filter BP 515–555) and an Electron Multiplier CCD Camera C9100-13 (Hamamatsu Photonics, Japan). The experiments were performed at room temperature for maximally 20 min/sample. Images were acquired using the NIS Element software (Nikon, Japan) with an S-Fluor 20×/0.75 NA objective at a sampling rate of 3–10 Hz. The spatial resolution was 256 × 256 pixels. To avoid saturation of the signals, excitation light intensity was attenuated by ND4 and ND8 neutral density filters (Nikon).

As described in our previous work [20,21], the initial video was processed with the ImageJ (U. S. National Institutes of Health, Bethesda, MA) software. Briefly, neurons were localized, and an appropriate region of interest (ROI) was selected to subtract the background. Appropriate ROIs around the cells bodies were then selected and the fluorescence intensity was measured for each ROI and expressed as a function of time or If(t). Then, the dye bleaching decay was evaluated. The Ca^{2+} transients of each cell signal were extracted in a semi-automatic manner by selecting a threshold for the smallest detectable peak that was equal three times the standard deviation of the baseline. Subsequently, the decay of If(t) was fitted to a cubic spline interpolating If(t) at 10 or

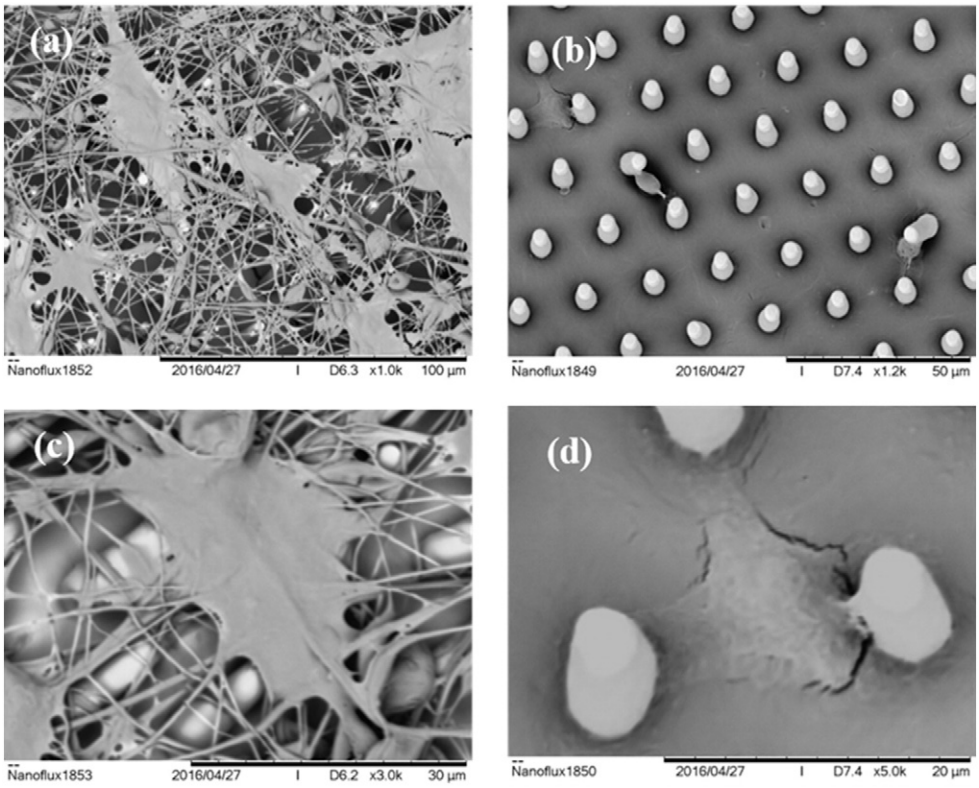

Fig. 3. SEM images of U87 cells cultured on a nanocomposite substrate of PLGA nanofibers on PDMS pillars (a and c) and PDMS flat layer (b and d) after 48 h incubation.

20 points. If(t) was then fitted to the original optical signal to compensate for dye bleaching, and the fractional optical signal was calculated as follows: $DF/F = (If(t) - If(t_0)) / If(t_0)$, where $If(t_0)$ is the fluorescence intensity at the beginning of the recording.

4. Results and discussion

As a preliminary test, the proposed substrate was used for culture of U87, a human glioblastoma cell line. Fixation of U87 cells were performed 48 h after cell seeding. Fig. 3a and c show SEM images of low and high magnitudes of U87 cells on a nanocomposite substrate of PLGA nanofibers on PDMS pillars, which are significant different from that on a substrate made of PDMS pillars alone. Clearly, cells spread over a large area on the fibers and fall down onto the bottom of pillar substrate due to relative large spacing between pillars (Fig. 3b and d). Due to the differences in supporting material, cells exhibited different behaviors in adhesion and spreading. In addition, the both sides of the cells were exposed to the culture medium in the suspended areas of the nanofibers, allowing more efficient exchange of the nutrients and metabolites of cells.

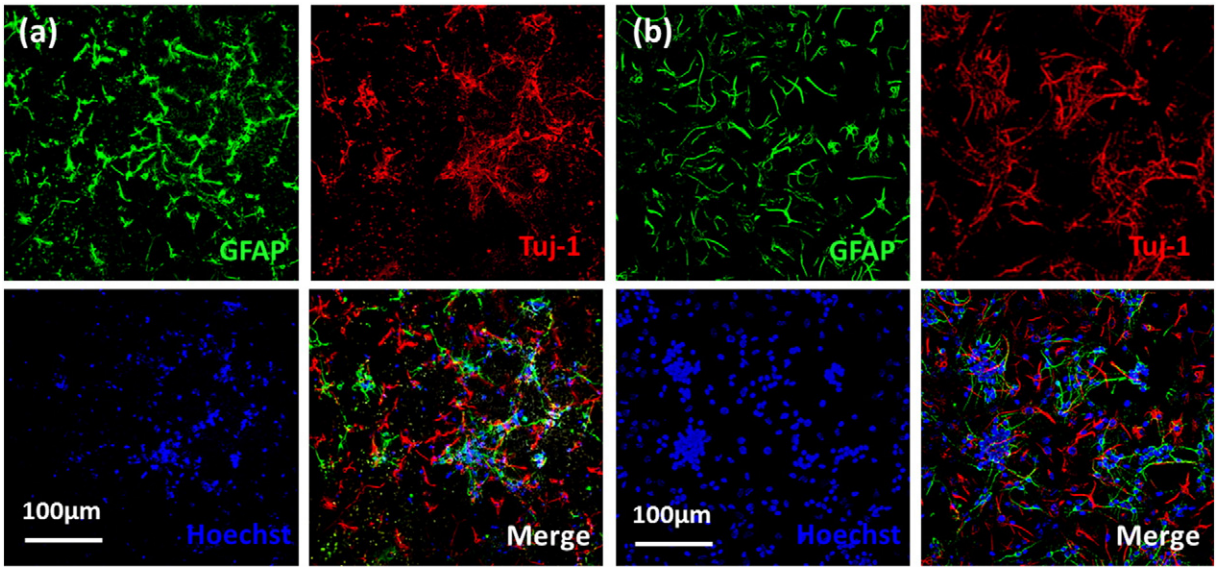

Fig. 4. Immunofluorescence images of neurons and astrocytes on a nanocomposite substrate of PLGA nanofibers on PDMS pillars (a) and a glass coverslip (b) after 48 h incubation. Astrocytes related glial fibrillary acidic protein is stained by GFAP (green). Neuron-specific class III β-tubulin is stained by TUJ1 (red). Cell nuclei were stained by Hoechst (blue). (For interpretation of the references to color in this figure legend, the reader is referred to the web version of this article.)

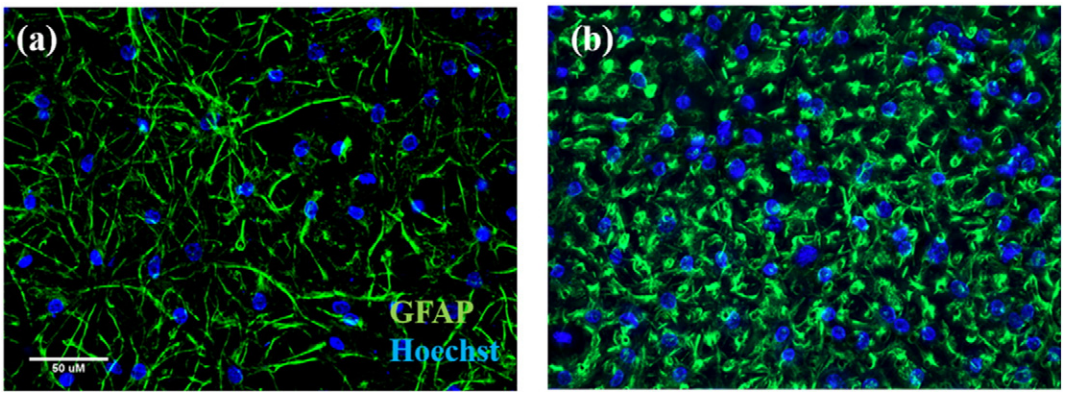

Fig. 5. Immunofluorescence images of astrocytes (green) on a nanocomposite substrate of PLGA nanofibers on PDMS pillars (a) and a glass coverslip (b) after one week incubation. (For interpretation of the references to color in this figure legend, the reader is referred to the web version of this article.)

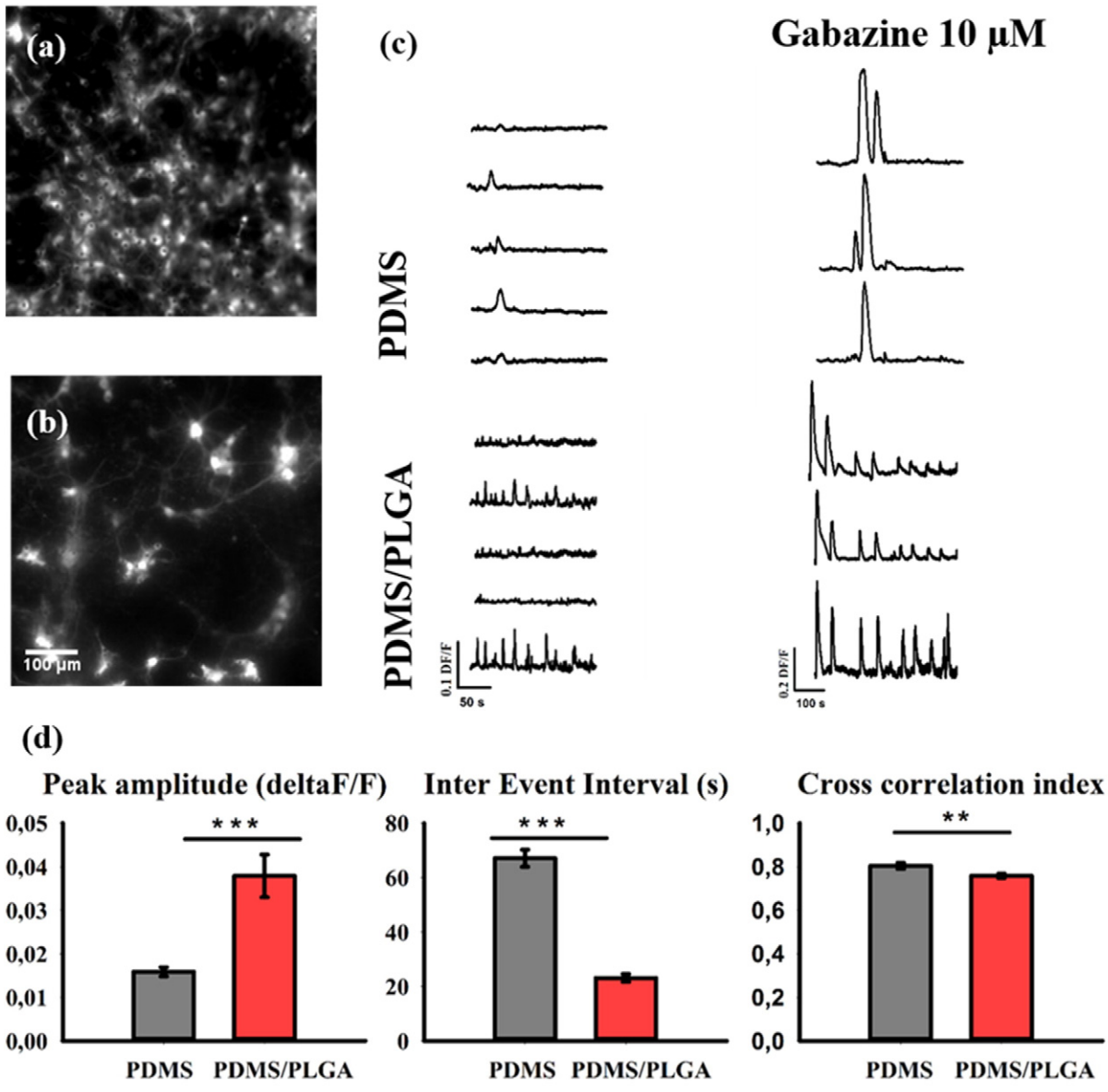

Fig. 6. Hippocampal neurons loaded with Oregon Green® 488 BAPTA-1, AM after two weeks of growth on PDMS (a) and PLGA/PDMS (b) substrates. Images of spontaneous and Gabazine induced calcium transients over time are also shown (c). Average amplitude, inter event interval and cross correlation index of spontaneous calcium transients on PLGA/PDMS vs PDMS substrates (n = 12 neurons for PLGA/PDMS, n = 16 neurons for PDMS - control; **p < 0.01 ***p < 0.001 One-way ANOVA, Tukey post-hoc test).

Next, primary hippocampal neurons were plated on the nanocomposite substrate of PLGA nanofibers on PDMS micropillars at a density of 300,000 cells/sample. Fixation and staining with the neuronal marker α-tubulin I, astrocytic marker GFAP and nuclear marker Hoechst were performed 48 h after cell seeding. At this stage, attachment and survival of neurons (red) and astrocytes (green) on PLGA/PDMS nanocomposite substrate (Fig. 4a) were found to be similar to that on a glass coverslip (Fig. 4b). However, after one week culture, the morphology of astrocytes plated on different types of substrates became significantly different. On the PLGA/PDMS substrate, the astrocytes showed a complex morphology with many cellular protrusions (Fig. 5a), similar to that of in vivo systems [22], whereas a flattened shape was observed for the cells on flat PDMS (Fig. 5b) [23]. This would suggest the importance of both surface morphology of the PLGA nanofibers and elastomeric material supporting and the PDMS pillars.

Once verified the neuronal attachment and survival, a functional test was performed on primary hippocampal cell cultures grown on the microarrays. The spontaneous and pharmacologically induced electrical activity of neurons was measured after two weeks of culture. At this time point, the neuronal network grown in vitro represents a mature stage of development. We chose an optical recording technique that allows the simultaneous imaging of many neurons. Specifically, we measured the fluctuations in the concentration of intracellular calcium ions by use of fluorescent calcium binding dye. Calcium ions are intracellular signals that regulate a large variety of cellular functions, such as genetic expression, neurotransmitter release and neuron-to-glia communication. The analysis of spontaneous calcium transients optically recorded from single cells allows comparing the functionality of the neuronal network grown on the PLGA/PDMS nanocomposite vs PDMS (control) substrates (Fig. 6).

On PDMS, we observed a few active neurons similar to the PLGA/PDMS substrates. Moreover, the calcium signals from glial cells were clearly visible on the micropillars, and distinguishable from neuronal signals because of their slower rates of rise and decay (Supplementary Video 1).

The average amplitude of neuronal calcium transients was significantly increased on the nanocomposite substrate vs control while the inter event interval was decreased, meaning that the neurons grown on nanofibers have more frequent and more homogeneously distributed calcium signals over time comparing to controls. The synchronization of calcium transients over time, measured as average cross correlation index, was slightly increased on PDMS (control) comparing to PLGA/PDMS as shown in Fig. 6d.

The average amplitude of neuronal calcium transients was significantly increased on the nanocomposite substrate (0.038 ± 0.004 DF/F) vs control (0.016 ± 0.001 DF/F); an elevation of intracellular calcium above a certain threshold is known to induce long-term potentiation of neuronal synapses [24]. The Inter Event Interval was instead decreased on the nanocomposite substrate vs control (23.13 ± 1.45 vs 67.07 ± 3.14 s), meaning that the neurons grown on nanofibers have more frequent and more homogeneously distributed calcium signals over time comparing to controls. The synchronization of calcium transients over time, measured as average cross correlation index between all the neuronal signals in the same field of view, was slightly increased on PDMS (0.80 ± 0.01) comparing to PLGA/PDMS (0.76 ± 0.01) as shown in Fig. 6g.

In addition, we stimulated the neuronal cultures with Gabazine 10 μM (Sigma-Aldrich), a specific GABAA receptor antagonist, and observed an increase in the amplitude and synchronization of calcium transients in both PLGA/PDMS and PDMS (control) substrates (Fig. 6c), as expected by neuronal physiology.

5. Conclusion

We proposed a new type of culture substrates made of electrospun nanofibers on elastomeric micropillars. The advantage of such an approach relies on the ECM-like surface morphology and the low effective Young's module of the under layer as well as the high porosity of the fiber-pillar assembly. Our preliminary results on culture of neurons and glial cells have shown improved cell morphology and electric activity compared to other types of substrates. Our further goal is to optimize the density and the stiffness of the nanofibers for improved culture of neurons as well as control stem cell differentiation toward functional neural networks.

Supplementary data to this article can be found online at http://dx.doi.org/10.1016/j.mee.2017.01.015.

Acknowledgements

This work was supported by Agence de Recherche Nationale under contract No. ANR-13-NANO-0011-01 (Pillarcell). J. Wei is grateful to China Scholarship Council (CSC) for grant.

References

[1] M.P. Lutolf, J.A. Hubbell, Nat. Biotechnol. 23 (1) (2005) 47–55.
[2] P. Friedl, K. Wolf, Nat. Rev. Cancer 3 (5) (2003) 362–374.
[3] F.B. Kai, H. Laklai, V.M. Weaver, Trends Cell Biol. 26 (7) (2016) 486–497.
[4] D.A. Lauffenburger, A.F. Horwitz, Cell 84 (3) (1996) 359–369.
[5] A.D. Doyle, M.L. Kutys, M.A. Conti, et al., J. Cell Sci. 125 (9) (2012) 2244–2256.
[6] D.H. Kim, C.H. Seo, K. Han, et al., Adv. Funct. Mater. 19 (10) (2009) 1579–1586.
[7] M. Gupta, B.R. Sarangi, J. Deschamps, et al., Nat. Commun. 6 (2015) 7525.
[8] S. Megelski, J.S. Stephens, D.B. Chase, et al., Macromolecules 35 (22) (2002) 8456–8466.
[9] E.K.F. Yim, S.W. Pang, K.W. Leong, Exp. Cell Res. 313 (9) (2007) 1820–1829.
[10] J. Xie, W. Liu, M.R. MacEwan, et al., Small 7 (2011) 293.
[11] S.H. Ku, J. Ryu, S.K. Hong, et al., Biomaterials 31 (9) (2010) 2535–2541.
[12] M.A. Cole, N.H. Voelcker, H. Thissen, et al., Biomaterials 30 (9) (2009) 1827–1850.
[13] J. Fu, Y.K. Wang, M.T. Yang, et al., Nat. Methods 7 (2010) 733.
[14] A. Higuchi, Q.D. Ling, Y. Chang, et al., Chem. Rev. 113 (5) (2013) 3297–3328.
[15] Y. Sun, K.M.A. Yong, L.G. Villa-Diaz, et al., Nat. Mater. 13 (6) (2014) 599–604.
[16] Y. Tang, L. Liu, J. Li, et al., J. Mater. Chem. B 4 (19) (2016) 3305–3312.
[17] M. Schindler, I. Ahmed, J. Kamal, et al., Biomaterials 26 (28) (2005) 5624–5631.
[18] J.Y. Lee, C.A. Bashur, A.S. Goldstein, et al., Biomaterials 30 (26) (2009) 4325–4335.
[19] J. Wei, J. Shi, et al., Microelectron. Eng. 158 (2016) 22–25.
[20] M. Moshtagh-Khorasani, E.W. Miller, V. Torre, Physiol. Rep. 1 (5) (2013) e00089.
[21] F.P. Ulloa Severino, et al., Sci. Rep. 6 (2016) 29640.
[22] T.B. Puschmann, et al., Glia 61 (2013) 432.
[23] D.M. Landis, L.A. Weinstein, C.J. Skordeles, Glia 3 (1990) 212.
[24] R.A. Zalutsky, R.A. Nicoll, Science 248 (4963) (1990) 1619–1624.